UNIVERSIDAD NACIONAL AUTÓNOMA DE MÉXICO
POSGRADO EN CIENCIAS FÍSICAS
INSTITUTO DE CIENCIAS NUCLEARES

CHAOS, SCARRING AND LOCALIZATION IN A SPIN-BOSON SYSTEM

TESIS
QUE PARA OPTAR POR EL GRADO DE:
DOCTOR EN CIENCIAS (FÍSICA)

PRESENTA:
DAVID BENJAMÍN VILLASEÑOR PÉREZ

TUTOR PRINCIPAL:
DR. JORGE GUSTAVO HIRSCH GANIEVICH
INSTITUTO DE CIENCIAS NUCLEARES, UNAM

MIEMBROS DEL COMITÉ TUTOR:
DR. PABLO BARBERIS BLOSTEIN
INSTITUTO DE INVESTIGACIONES EN MATEMÁTICAS APLICADAS Y EN SISTEMAS, UNAM

DR. RAMÓN LÓPEZ PEÑA
INSTITUTO DE CIENCIAS NUCLEARES, UNAM

CIUDAD DE MÉXICO, MÉXICO, JULIO 2022

Universidad Nacional Autónoma de México

Posgrado en Ciencias Físicas

Instituto de Ciencias Nucleares

Chaos, Scarring and Localization in a Spin-Boson System

David Benjamín Villaseñor Pérez

"POR MI RAZA HABLARÁ EL ESPÍRITU"
Ciudad Universitaria, Ciudad de México, Julio de 2022

To my Mother,

because without her support

this would not have been possible.

Acknowledgments

My approach to physics was almost an unnecessary incident. That little voice of curiosity that asks you -what is the reason of this?- or -why is that happening?-, and which does not let you sleep at night, was the reason of this great step in my professional training. At that time my understanding of the world and nature was a pragmatic approach, and the change from my original branch of study, the chemical engineering, to this new discipline was really difficult and challenging for me. Along the way to achieve the final work, which today I present to you in these pages, many people have helped me to make it possible.

First of all, I would like to thank my supervisor Jorge Hirsch his availability to work with me and guide me. I want to thank him his patience, empathy, and friendship. I have enriched myself very much as a scientist due to his wisdom. Furthermore, I want to thank the help provided by the researchers Lea Santos, Sergio Lerma, and Miguel Bastarrachea, and for letting me collaborate with them in this long journey through my doctoral research. From them I have learned that science is not a lonely way, and that friendship is an essential tool to reach goals. A special mention goes for the future researcher Saúl Pilatowsky, since many of the results presented in this Thesis were possible because of his computational skills. I had the fortune to collaborate with him and I learned a lot from him throughout this work. Another mention, but not less important, goes for the researcher Jorge Chávez, who guided me in the beginning of my research with technical aspects of some numerical techniques implemented in this work.

All these people have helped me directly or indirectly to complete this Thesis, we have colloquially called ourselves *The Dicke Team* and I am very grateful to all of them.

Abstract

The present Thesis compiles interesting results on different phenomenology displayed by an elemental quantum system where light and matter interact. The last type of quantum system is the cornerstone for the emergent quantum technologies, which promise a dream world only thought of in science fiction stories. The considered system is the Dicke model, a spin-boson system that represents in a simple way the interaction between a set of atoms (matter) and an electromagnetic radiation field (light, photons) within a cavity. Despite the simplicity of the model, a vast extension of phenomena arises from it, ranging from chaos, phase transitions and entanglement to equilibration and thermalization. Furthermore, the model also shows phenomena as peculiar as scarring and localization. In this regard, three main quantum phenomena were investigated in detail in this Thesis: Chaos, scarring and localization.

Chaos was studied in the Dicke model with an unconventional indicator called correlation hole, which captures spectral correlations and can be detected in the time evolution of a quantum observable. The correlation hole is a dynamical manifestation of the chaotic behavior of the model, which can be confirmed with conventional static indicators that consider spectral fluctuations. Additional studies on classical and quantum dynamics with coherent states were also performed in the model. This classical-quantum correspondence allowed to differentiate effects that are purely quantum and categorize universal behaviors (correlations from random matrix theory) from particular ones (scarring from unstable periodic orbits).

Scarring was detected for all eigenstates of the Dicke model, an unexpected result, since scarred states were thought for long time as small sets of states with special characteristics. Scarring can be seen in a primitive way as a form of localization, in the sense that it prevents the uniform distribution of a quantum state in phase space for a chaotic regime. Thus, additional studies trying to differentiate both phenomena were done, leading to a definition of quantum ergodicity only achievable as an ensemble property, after temporal averages are performed. A detailed study of the fundamental families of periodic orbits that cause this ubiquitous scarring of the model was also performed.

Finally, localization understood as the exponential of an entropy was studied under the formalism of the generalized Rényi entropy for continuous spaces. The last allowed to define generalized localization measures in the unbounded phase space of the Dicke model that can be used to detect unstable periodic orbits, which are the cause of quantum scarring. On the way to define these localization measures in unbounded continuous spaces the selection of a bounded subspace is needed, implying that there is no universal way to define such measures in this kind of spaces.

Publications

- **Publications Derived from this Thesis**

  1. S. Lerma-Hernández, D. Villaseñor, M. A. Bastarrachea-Magnani, E. J. Torres-Herrera, L. F. Santos, and J. G. Hirsch, *Dynamical signatures of quantum chaos and relaxation time scales in a spin-boson system*, Phys. Rev. E **100**, 012218 (2019).
  2. D Villaseñor, S Pilatowsky-Cameo, M A Bastarrachea-Magnani, S Lerma-Hernández, L F Santos, and J G Hirsch, *Quantum vs classical dynamics in a spin-boson system: manifestations of spectral correlations and scarring*, New J. Phys. **22**, 063036 (2020).
  3. Saúl Pilatowsky-Cameo, David Villaseñor, Miguel A. Bastarrachea-Magnani, Sergio Lerma-Hernández, Lea F. Santos, and Jorge G. Hirsch, *Ubiquitous quantum scarring does not prevent ergodicity*, Nat. Comm. **12**, 852 (2021).
  4. Saúl Pilatowsky-Cameo, David Villaseñor, Miguel A Bastarrachea-Magnani, Sergio Lerma-Hernández, Lea F Santos, and Jorge G Hirsch, *Quantum scarring in a spin-boson system: fundamental families of periodic orbits*, New J. Phys. **23**, 033045 (2021).
  5. D. Villaseñor, S. Pilatowsky-Cameo, M. A. Bastarrachea-Magnani, S. Lerma-Hernández, and J. G. Hirsch, *Quantum localization measures in phase space*, Phys. Rev. E **103**, 052214 (2021).

6. Saúl Pilatowsky-Cameo, David Villaseñor, Miguel A. Bastarrachea-Magnani, Sergio Lerma-Hernández, Lea F. Santos, and Jorge G. Hirsch, *Identification of quantum scars via phase-space localization measures*, Quantum **6**, 644 (2022).

- **Related Publications**

1. Saúl Pilatowsky-Cameo, David Villaseñor, Miguel A. Bastarrachea-Magnani, Sergio Lerma-Hernández, and Jorge G. Hirsch, *Effective dimensions of infinite-dimensional Hilbert spaces: a phase-space approach*, arXiv:2111.09891 (2021).

Contents

List of Figures

List of Tables

Chapter 1

Introduction

Quantum systems have had a huge impact in recent years due to the development of the so-called quantum technologies. The terms quantum information and quantum computing are now terms away from science fiction. In this regard, scientific societies and industries around the world are joining efforts to make possible the near feature: *The Quantum World*. A wide wave of promising technologies is knocking at the door to change our world, among them, quantum cryptography, quantum computing, quantum communication, quantum networks, quantum metrology, and many others. Several communities have already realized the relevance of quantum technologies in our daily lives and the repercussions that they will have in society and development of humanity. Moreover, they have realized the urgent need to create professions related with the quantum knowledge in a pragmatic way. Thus, universities and research centers around the world are creating education programs based in quantum mechanics and its applications, as quantum engineering or photonic engineering, such that, the future professionals can make the scenarios outlined by the theory a reality. Nevertheless, the understanding and control of atomic-scale systems is still far from being reached in its whole. Thereby, the fundamental and exhaustive study of quantum phenomena will enable this goal to be achieved.

One of the most important quantum systems in light of quantum technologies is that where light and matter interact, because of quantum devices are based in this principle of interaction. The last type of quantum systems constitutes on its own an independent branch within quantum mechanics, known as quantum optics, which is studied under the formalism of the quantum electrodynamics. Many fundamental models to describe these physical systems have been proposed through the years, which have been represented mainly with sets of atoms interacting with electromagnetic fields inside optical cavities, a branch known as cavity quantum electrodynamics. One of the simplest models, which belongs to this branch, was proposed by the American astronomer and physicist Robert Henry Dicke in 1954 [1]. The well-known Dicke model defines in a simple way the light-matter collective interaction between a set of two-level atoms and a single mode of radiation of an electromagnetic field within an optical cavity. Despite the mathematical simplicity of the Dicke model, it brought with it a plethora of associated physical phenomena, as superradiance, phase transitions, chaos, scarring, localization, entanglement, equilibration and thermalization, among others [2–19].

In recent years, equilibration and thermalization of isolated quantum systems in chaotic regimes have become in featured topics, since the experimental advances in implementations of such systems have led to longer coherence times [20–23]. Equilibration is reached when a given observable only shows smalls fluctuations around an asymptotic value after a long time and these fluctuations decrease with system size. Thermalization implies that this asymptotic value (infinite-time average of the given observable) is very close to the predictions from statistical mechanics, and the difference between both approaches also decreases with system size. On the other hand, coherence time is a very important parameter to quantum technologies as quantum computing, quantum communication, and quantum metrology. In quantum computing, the coherence time directly limits the maximum number of quantum operations that can be performed sequentially by quantum computers. Furthermore, a long coherence time is a prerequisite for the realization of high fidelity

quantum operations. In this way, the theoretical and experimental analysis of long-time quantum dynamics is a key step to understand the above phenomenology.

An important question raised in the last scheme is how long it takes for isolated quantum systems to reach equilibrium. Many studies about time scales where equilibration occurs in these systems have been developed; however, there is no consensus on the time-scale dependence with system conditions as system size, range of interactions, observables, and initial states [24–30]. The behaviors of the quantum dynamics of observables prior to equilibrium, where the discreteness of the energy spectrum is already resolved, are determined by the properties of the eigenvalues. For some observables, effects of correlations between eigenvalues can be observed in the dynamics, as the correlation hole [31]. The correlation hole appears as a decay below the saturation value of the dynamics caused by such correlations. Correlations arise due to level repulsion between eigenvalues, which is a distinguishing feature of energy spectra of chaotic systems, where the conventional static indicators of chaos (spectral tests with no time evolution involved) are defined under the formalism of the random matrix theory. Thus, this correlation hole plays the role of an unconventional dynamical indicator of quantum chaos, what makes it attractive and useful when the spectral information of certain systems is not accessible.

There are many more open questions concerning equilibration for isolated quantum systems with classical limit. Classically, the mixing properties of chaotic dynamics have provided a fundamental mechanism to explain equilibration and the ergodic properties of physical systems. Under the quantum approach, this paradigm changes, since isolated quantum systems are described by linear equations; nevertheless, the idea of equilibration remains in the sense of saturation of the dynamics for some observables, where an asymptotic value is reached after long times showing small fluctuations that decrease with system size, as was exposed previously. Since the passage from the classical to the quantum domain entails the appearance of purely quantum phenomena, such as superpositions, interferences, the effects of universal spectral correlations, scarring, among others,

the analysis of the correspondence between both classical and quantum dynamics is a useful tool to understand further the equilibration process.

Quantum scarring has caused a new wave of fascination with the detection of the so-called quantum many-body scars, observed experimentally as long-lived oscillations in chains of Rydberg atoms [32–36]. The interest in quantum many-body scars lies in their potential as resources to manipulate and store quantum information. The origin of quantum scars can be traced back to the repercussions that measure-zero structures of the classical phase space can have in the quantum domain, which was a striking feature of the quantum-classical correspondence not recognized in the early days of the quantum theory. In the classical domain, typical trajectories of chaotic systems fill completely the available phase space. Nevertheless, sets of unstable periodic orbits of measure zero can be present in phase space at the same time. When a parameter of the classical system is varied and it transits from a regular to a chaotic regime, periodic orbits change from stable to unstable. In the quantum domain, these classical unstable periodic orbits can get imprinted in the quantum states as concentrated regions of high probability known as quantum scars [37–39]. On the other hand, quantum scarring has important repercussions in phase space of chaotic systems, since it prevents the uniform distribution of the eigenstates. For many years it was thought that the eigenstates of quantum systems which are fully chaotic in the classical limit will be completely delocalized in phase space, where the classical trajectories fill the phase space densely. This thought was changed with the discovery of quantum scars, which restrict the delocalization degree of the eigenstates concentrating them along the regions occupied by unstable periodic orbits in phase space.

Quantum localization is an interesting topic whose origin comes from the quantum limitation of classical diffusion [40]. Effects of quantum localization appear in many quantum systems, being one of the most notable types of localization the celebrated Anderson localization, which is an interference effect yielding a drastic reduction of diffusion in the presence of strong disorder [41–44]. Recent studies in disordered systems of interacting

quantum particles have shown that localization can persist in presence of weak interactions, resulting in the formation of a new phase of matter, the many-body localized phase [22,45–48]. This phase shows unconventional properties that can have potential applications in quantum technologies, as perfect zero conductivity at finite temperatures and the prevention of the system from reaching thermal equilibrium, that is, the failure to thermalize in spite of interactions. The effects caused by this many-body localized phase can appear in several experimental setups, as nuclear spin dynamics, charge transport in amorphous materials, cold atoms, spin-glasses, and quantum computers.

The exposed phenomena, as well as many others showed by the Dicke model, have associated experimental quantum applications, which will contribute to build the coming quantum world. Thus, the main objective of this Thesis is to provide to the reader a theoretical and technical framework, which contain all the tools to understand how these quantum phenomena behave and can be interpreted in one of the simplest interacting spin-boson systems, the Dicke model.

Organization of the Thesis

The Thesis is organized in 6 fundamental Parts:

1. In Part I is presented the theoretical background. In Chapter 2 is exposed the formulation of the Dicke model, its integrable limits, its classical limit, and its experimental realizations. In Chapter 3 is exposed the chaos theory in its both approaches, as classical and quantum chaos. In Chapter 4 are exposed the correlation functions and their relation with the survival probability, a dynamical quantity able to capture spectral correlations. Finally, in Chapter 5 is exposed the representation of quantum states in phase space, introducing the coherent states and the quasiprobability distributions.

2. In Part II are presented relevant results concerning chaos in the Dicke model. In Chapter 6 is exposed a review on previously found results on classical and quantum chaos in the

Dicke model. Furthermore, the results obtained with the correlation hole as dynamical indicator of quantum chaos in the Dicke model are also exposed. In Chapter 7 is exposed a detailed analysis on the classical-quantum dynamics of coherent states, where can be identified dynamical effects of purely quantum nature related with chaos or scarring.

3. In Part III are presented relevant results concerning scarring in the Dicke model. In Chapter 8 is exposed the historical background on quantum scarring, as well as the results on ubiquitous scarring identified in the Dicke model. In Chapter 9 is exposed a detailed explanation on the fundamental families of periodic orbits emanating from stationary points, which cause the ubiquitous scarring in the Dicke model.

4. In Part IV are presented relevant results concerning localization in the Dicke model. In Chapter 10 is exposed the historical background on quantum localization, as well as its relation with other forms of localization. Furthermore, the results on localization measures of quantum states in phase space of the Dicke model are also exposed. In Chapter 11 is exposed the utility to use localization measures in phase space to detect unstable periodic orbits that cause the phenomenon of scarring.

5. In Part V are presented the conclusions of the Thesis. Chapter 12 is devoted only to gather the conclusions of the results on chaos, scarring and localization in the Dicke model.

6. Finally, in Part VI is presented supplementary material. In Appendixes A-R are exposed explicit derivations and complementary information necessary to fully understand each Chapter.

Part I

Background

Chapter 2

The Dicke Model

In this Chapter is exposed the formulation of the Dicke model under conventional approximations and is introduced the Dicke Hamiltonian, as well as a generalized version of it, which gathers in a single expression particular cases as the Tavis-Cummings, Rabi, and Jaynes-Cummings models. The integrable limits of the Dicke Hamiltonian regarding the system parameters are also shown, which provide the available diagonalization bases to solve numerically the Hamiltonian. Furthermore, the classical limit of the model is exposed under a mean-field semiclassical approximation with coherent states generating the classical Dicke Hamiltonian, as well as important expressions derived from it, as the classical ground-state energy and the semiclassical density of states. Finally, a revision of different experimental setups of the Dicke model through the years is shown.

2.1 Formulation of the Model

Quantum optics is a branch of physics that studies the interaction between light and matter. On the one hand, light can be understood as an electromagnetic wave; however, it can be understood also as a stream of particles (quanta of light) called photons. Photons are relevant, since many counter-intuitive predic-

tions of quantum mechanics can be tested using them, as quantum entanglement and teleportation. On the other hand, matter refers to physical particles as atoms and molecules. In this way, the fundamental study of this kind of systems, which are studied under the formalism of Quantum Electrodynamics (QED), is a key step to understand the emerging quantum technologies, among them, the quantum computing and quantum communication. Thereby, the model presented here tries to describe in a simple way the system resulting from the interaction between these two physical entities, particles (atoms) and electromagnetic waves (light, photons). Typically, the system consists of a set of $\mathcal{N}$ two-level atoms transiting from the ground state to an excited state with an atomic transition frequency given by the parameter ω_0. These atoms are contained within an optical cavity and interact with a single-mode electromagnetic field with a radiation frequency given by the parameter ω. The atom-field interaction within the system is modulated by a coupling strength represented by the parameter γ. A model with the latter characteristics was first proposed by the American astronomer and physicist Robert Henry Dicke (see Fig. 2.1) in 1954 [1], and it is known as *The Dicke Model* in his honor.

The formulation of the Dicke model is based on a series of conventional approximations [49]:

1. All atoms are contained within a volume that is smaller than the wave length of the single-mode of electromagnetic radiation; that is, all atoms interact with the same electromagnetic field, and as a result, the coupling strength parameter is the same for all of them.

2. All atoms are immobile and far enough apart from each other, and in this way, the interactions between them are neglected.

3. An additional simplification can be taken in the model, where the atom-field interaction is described under the Rotating Wave Approximation (RWA) [50, 51]. This refers to eliminate the Hamiltonian terms that oscillate very fast in time, such that, their temporal average goes to zero.

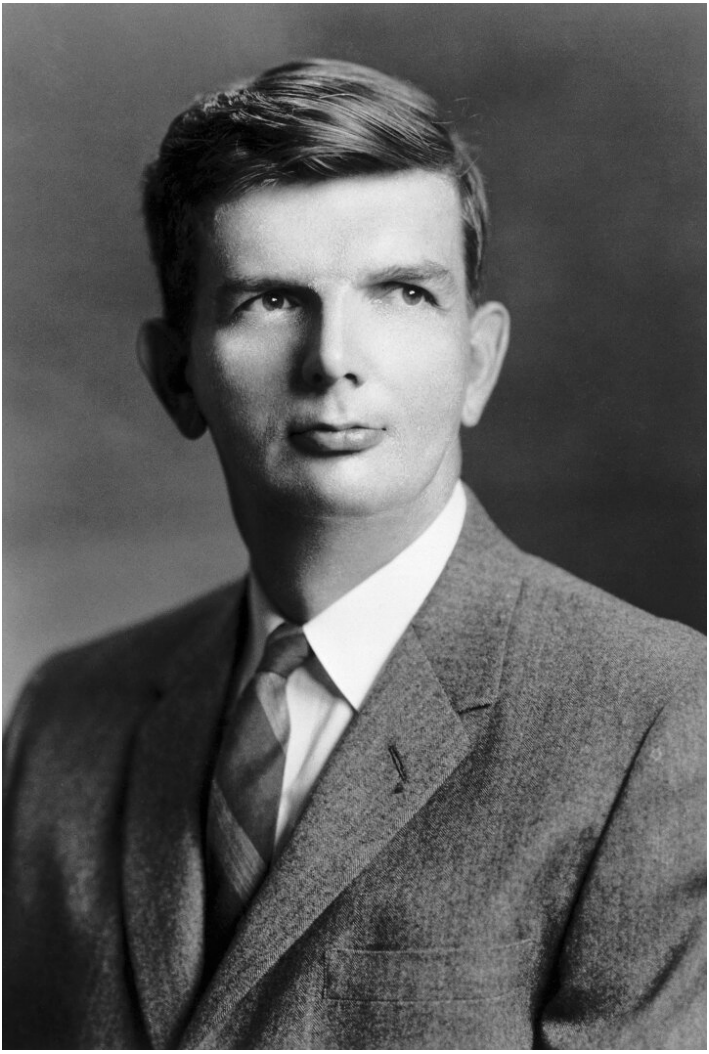

Figure 2.1: American astronomer and physicist Robert Henry Dicke born in 1916 in St. Louis, Missouri, United States of America. He made important contributions to the fields of astrophysics, atomic physics, cosmology and gravity.

The Hamiltonian of the system, which represents the energy contained within the optical cavity, is composed of three main terms: the first term represents the field energy $\hat{H}_{\mathrm{F}}$, the second one represents the atomic energy $\hat{H}_{\mathrm{A}}$, and the third one represents the atom-field interaction energy $\hat{H}_{\mathrm{I}}$. Therefore, with the previous approximations, the Dicke Hamiltonian takes the simple form

$$\hat{H}_{\mathrm{D}} = \hat{H}_{\mathrm{F}} + \hat{H}_{\mathrm{A}} + \hat{H}_{\mathrm{I}}. \tag{2.1}$$

Each of the last terms has an explicit representation through quantum operators of field (photons) and angular momentum (atoms). In Appendix A is presented a complete derivation of the following terms

$$\hat{H}_{\mathrm{F}} = \hbar\omega\hat{a}^{\dagger}\hat{a}, \tag{2.2}$$

$$\hat{H}_{\mathrm{A}} = \hbar\omega_0\hat{J}_z, \tag{2.3}$$

$$\hat{H}_{\mathrm{I}} = \frac{\hbar\gamma}{\sqrt{\mathcal{N}}}(\hat{a}^{\dagger} + \hat{a})(\hat{J}_+ + \hat{J}_-), \tag{2.4}$$

where $\hat{a}^{\dagger}$ and $\hat{a}$ are the creation-annihilation operators that satisfy the H(1) algebra (Heisenberg-Weyl algebra) of the bosonic operators. The atomic operators $\hat{J}_{x,y,z} = \frac{1}{2}\sum_{n=1}^{\mathcal{N}} \hat{\sigma}_{x,y,z}^{(n)}$ are collective pseudo-spin operators that satisfy the same SU(2) algebra of the spin-$\frac{1}{2}$ operators given by the Pauli matrices $\hat{\sigma}_{x,y,z}$, and the raising-lowering collective pseudo-spin operators $\hat{J}_{\pm} = \sum_{n=1}^{\mathcal{N}} \hat{\sigma}_{\pm}^{(n)}$ are defined as $\hat{J}_{\pm} = \hat{J}_x \pm i\hat{J}_y$.

Taking the above energy terms, and setting $\hbar = 1$ through the text without loss of generality, the Dicke Hamiltonian can be written as

$$\hat{H}_{\mathrm{D}} = \omega\hat{a}^{\dagger}\hat{a} + \omega_0\hat{J}_z + \frac{\gamma}{\sqrt{\mathcal{N}}}(\hat{a}^{\dagger} + \hat{a})(\hat{J}_+ + \hat{J}_-). \tag{2.5}$$

2.1.1 Generalized Dicke Hamiltonian

A useful way to write a generalized version of the Dicke Hamiltonian is as follows

$$\hat{H}_{\mathrm{D}}^{\delta} = \omega\hat{a}^{\dagger}\hat{a} + \omega_0\hat{J}_z + \frac{\gamma}{\sqrt{\mathcal{N}}}[\hat{a}^{\dagger}\hat{J}_- + \hat{a}\hat{J}_+ + \delta(\hat{a}^{\dagger}\hat{J}_+ + \hat{a}\hat{J}_-)], \tag{2.6}$$

where the case $\delta = 1$ defines the standard Dicke Hamiltonian $\hat{H}_{\mathrm{D}}^{\delta=1} = \hat{H}_{\mathrm{D}}$; while the case $\delta = 0$ defines its integrable limit known as the Tavis-Cummings Hamiltonian $\hat{H}_{\mathrm{D}}^{\delta=0} = \hat{H}_{\mathrm{TC}}$ [52], and given explicitly by

$$\hat{H}_{\mathrm{TC}} = \omega \hat{a}^\dagger \hat{a} + \omega_0 \hat{J}_z + \frac{\gamma}{\sqrt{\mathcal{N}}}(\hat{a}^\dagger \hat{J}_- + \hat{a}\hat{J}_+). \tag{2.7}$$

This Hamiltonian can be obtained formally when it is applied the RWA to the Dicke Hamiltonian. In that case, the counter-rotating terms (terms that oscillate very fast in time) $\hat{a}^\dagger \hat{J}_+$ and $\hat{a}\hat{J}_-$ are neglected. The Tavis-Cummings Hamiltonian possesses a conserved quantity $\hat{\Lambda} = \hat{a}^\dagger \hat{a} + \hat{J}_z + j\hat{1}$, which designates the number of excitations, and whose eigenvalues $\Lambda = n + m + j$ define the average number of photons n and excited atoms $m + j$ within the system. The parameter j defines the pseudo-spin value associated to the eigenvalue $j(j+1)$ of the squared collective pseudo-spin operator $\hat{\mathbf{J}}^2 = \hat{J}_x^2 + \hat{J}_y^2 + \hat{J}_z^2$.

Other particular case of the Dicke Hamiltonian and quite popular is the Rabi Hamiltonian, where only a single two-level atom is considered in the system ($\mathcal{N} = 1$). First proposed by I. I. Rabi in 1936 [53, 54], the explicit Hamiltonian takes the form

$$\hat{H}_{\mathrm{R}} = \omega \hat{a}^\dagger \hat{a} + \frac{\omega_0}{2}\hat{\sigma}_z + \gamma(\hat{a}^\dagger + \hat{a})(\hat{\sigma}_+ + \hat{\sigma}_-). \tag{2.8}$$

Analogously, when the RWA is applied to the Rabi Hamiltonian, another well-known Hamiltonian is obtained, called Jaynes-Cummings Hamiltonian [55], and given by

$$\hat{H}_{\mathrm{JC}} = \omega \hat{a}^\dagger \hat{a} + \frac{\omega_0}{2}\hat{\sigma}_z + \gamma(\hat{a}^\dagger \hat{\sigma}_- + \hat{a}\hat{\sigma}_+), \tag{2.9}$$

which has also a conserved quantity $\hat{\lambda} = \hat{a}^\dagger \hat{a} + \frac{1}{2}(\hat{\sigma}_z + \hat{1})$.

2.2 Integrable Limits

The notion of integrability of a quantum system can be extended from classical integrability [56]. A classical conservative system

with I degrees of freedom is called integrable if there exist I independent integrals of motion

$$O_i(q_1, \ldots, q_I; p_1, \ldots, p_I) = C_i, \tag{2.10}$$

for $i = 1, \ldots, I$, where C_i are constants and (q_i, p_i) are canonical position-momentum variables. The later statement can be put in another form, where the system is called integrable if there exist I independent globally functions $O_i(q_1, \ldots, q_I; p_1, \ldots, p_I)$ for $i = 1, \ldots, I$, whose mutual Poisson brackets vanish

$$\{O_i, O_{i'}\} = 0, \tag{2.11}$$

for $i, i' = 1, \ldots, I$. Following this definition, a quantum system with I degrees of freedom is called integrable if there exist I globally operators $\hat{O}_i(\hat{q}_1, \ldots, \hat{q}_I; \hat{p}_1, \ldots, \hat{p}_I)$ for $i = 1, \ldots, I$, whose mutual commutators vanish

$$[\hat{O}_i, \hat{O}_{i'}] = \hat{0}, \tag{2.12}$$

for $i, i' = 1, \ldots, I$.

The Dicke Hamiltonian (2.5) depends explicitly on the parameters $(\omega, \omega_0, \gamma)$ for a fixed number of atoms $\mathcal{N}$. Its integrable limits provide the available bases on which it can be diagonalized.

2.2.1 Null Coupling-Strength Limit

An exact solution of the Dicke Hamiltonian can be obtained when the null coupling-strength limit $\gamma \to 0$ is taken. In that case, the Hamiltonian (2.5) becomes in

$$\begin{aligned} \hat{H}_{\mathrm{D}}(\omega, \omega_0) &= \lim_{\gamma \to 0} \hat{H}_{\mathrm{D}}(\omega, \omega_0, \gamma) \\ &= \omega \hat{a}^\dagger \hat{a} + \omega_0 \hat{J}_z. \end{aligned} \tag{2.13}$$

A solution basis for this Hamiltonian is the tensor product between Fock states $|n\rangle$ associated to the field and angular momentum states $|j, m_z\rangle$ associated to the atoms

$$|n\rangle \otimes |j, m_z\rangle \equiv |n; j, m_z\rangle, \tag{2.14}$$

which satisfies the relations

$$\hat{a}^\dagger \hat{a}|n; j, m_z\rangle = n|n; j, m_z\rangle, \tag{2.15}$$

$$\hat{\mathbf{J}}^2|n; j, m_z\rangle = j(j+1)|n; j, m_z\rangle, \tag{2.16}$$

$$\hat{J}_z|n; j, m_z\rangle = m_z|n; j, m_z\rangle, \tag{2.17}$$

where $\hat{\mathbf{J}}^2 = \hat{J}_x^2 + \hat{J}_y^2 + \hat{J}_z^2$ is the squared collective pseudo-spin operator.

Thus, the Hamiltonian (2.13) is integrable, since it commutes with both operators $\hat{a}^\dagger\hat{a}$ and $\hat{J}_z$, and has the same number of conserved quantities as degrees of freedom. Therefore, its associated eigenbasis is given by Eq. (2.14) and is known as the Fock basis.

2.2.2 Null Atomic-Transition Limit

Other exact solution of the Dicke Hamiltonian is obtained for the null atomic-transition limit $\omega_0 \to 0$. However, some previous steps are needed to make it possible. First, a displacement is taken over the creation-annihilation operators $\hat{a}^\dagger$ and $\hat{a}$, given by

$$\hat{A} = \hat{a} + G\hat{J}_x, \tag{2.18}$$

where $G = 2\gamma/(\omega\sqrt{\mathcal{N}})$. Next, a $-\pi/2$ rotation around the y axis of the collective pseudo-spin operators is taken as

$$(\hat{J}_x, \hat{J}_y, \hat{J}_z) \to (\hat{J}'_z, \hat{J}'_y, -\hat{J}'_x). \tag{2.19}$$

Now, taking the limit $\omega_0 \to 0$ with the previous transformations, the Hamiltonian (2.5) becomes in

$$\begin{aligned}\hat{H}_{\mathrm{D}}(\omega, \gamma) &= \lim_{\omega_0 \to 0} \hat{H}_{\mathrm{D}}(\omega, \omega_0, \gamma) \\ &= \omega(\hat{A}^\dagger\hat{A} - G^2\hat{J}'^2_z),\end{aligned} \tag{2.20}$$

and the solution basis for the above Hamiltonian is the tensor product between states $|N\rangle$ (eigenstates of the operator $\hat{A}^\dagger\hat{A}$) associated to the modified field and rotated angular momentum states $|j, m'_z\rangle$ associated to the atoms

$$|N\rangle \otimes |j, m'_z\rangle \equiv |N; j, m'_z\rangle, \tag{2.21}$$

which satisfy the relations

$$\hat{A}^\dagger \hat{A}|N; j, m'_z\rangle = N|N; j, m'_z\rangle, \tag{2.22}$$

$$\hat{\mathbf{J}}'^2|N; j, m'_z\rangle = j(j+1)|N; j, m'_z\rangle, \tag{2.23}$$

$$\hat{J}'_z|N; j, m'_z\rangle = m'_z|N; j, m'_z\rangle, \tag{2.24}$$

where $\hat{\mathbf{J}}'^2 = \hat{J}'^2_x + \hat{J}'^2_y + \hat{J}'^2_z$ is the collective pseudo-spin operator in the rotated basis. It is important to emphasise that the rotated collective pseudo-spin operator $\hat{J}'_z = \hat{J}_x$, such that $|N; j, m'_z\rangle = |N; j, m_x\rangle$.

Again, the Hamiltonian (2.20) is integrable, since it commutes with both operators $\hat{A}^\dagger \hat{A}$ and $\hat{J}'_z$, and its associated eigenbasis is is given by Eq. (2.21). When the vacuum state ($N = 0$) of the operator $\hat{A}$ is defined with the equation $\hat{A}|0; j, m'_z\rangle = 0$, it is found

$$\hat{a}|0; j, m'_z\rangle = -Gm'_z|0; j, m'_z\rangle, \tag{2.25}$$

that is, it is an eigenstate of the annihilation operator $\hat{a}$ with eigenvalue $\alpha_{m'_z} = -Gm'_z$, or in other words, it is a coherent state in the Fock basis. Due to the last result, the basis (2.21) is known as the coherent basis.

2.2.3 Solutions of the Dicke Hamiltonian

The time-independent Schrödinger equation for the Dicke Hamiltonian is given by

$$\hat{H}_{\mathrm{D}}|E_k\rangle = E_k|E_k\rangle, \tag{2.26}$$

where E_k and $|E_k\rangle$ define the eigenvalues and the eigenvectors of the Hamiltonian, respectively. This equation can be solved numerically by diagonalizing the Hamiltonian; however, a matrix representation of the Hamiltonian in a given basis is needed.

As was seen in the previous sections, a solution is given by the Fock basis (2.14), a tensor product of Fock states $|n\rangle$ representing the bosonic subspace and angular momentum states $|j, m_z\rangle$ representing the atomic subspace. Nevertheless, as the bosonic subspace is infinite-dimensional, the resulting matrix also will have an infinite dimension. To solve this issue, a dimension truncation is proposed by choosing a truncation value of the number

of photons $n_{\max}$ (eigenvalue of the number operator $\hat{n} = \hat{a}^\dagger \hat{a}$). The latter procedure produces matrices with finite dimension $\mathcal{D}_{\mathrm{F}}^2$, where $\mathcal{D}_{\mathrm{F}} = (2j+1)(n_{\max}+1)$ is the dimension of the truncated Hilbert space.

On the other hand, convergence problems of the wave function appear for some eigenstates, when a truncation value is chosen. For instance, the truncation value that ensures convergence of the ground-state wave function depends on the number of atoms $\mathcal{N}$. For that reason, when the number of atoms increases the truncation value also increases, and as a result, the matrix dimension. As a consequence, the latter scenario demands more computational resources and processing time. Previous studies done on the Dicke model revealed that the Fock basis (2.14) is inefficient for a complete study of the Hamiltonian ($\mathcal{N} > 40$), and that the coherent basis (2.21) is a better option [57–60]. In Appendix B is presented a complete description of the numerical solutions of the Dicke Hamiltonian using the coherent basis as diagonalization basis.

2.3 Classical Limit

The operators of the Dicke Hamiltonian (2.5) obey an algebra or set of commutation relations. The set of bosonic operators $\{\hat{a}^\dagger, \hat{a}, \hat{1}\}$ obey the H(1) algebra (Heisenberg-Weyl algebra), while the set of collective pseudo-spin operators $\{\hat{J}_\pm, \hat{J}_z\}$ obey the SU(2) algebra of spin-$\frac{1}{2}$ operators. For this reason, the Dicke Hamiltonian can be considered as an algebraic Hamiltonian. Moreover, the Dicke Hamiltonian commutes with the squared collective pseudo-spin operator $\hat{\mathbf{J}}^2 = \hat{J}_x^2 + \hat{J}_y^2 + \hat{J}_z^2$, $[\hat{H}_{\mathrm{D}}, \hat{\mathbf{J}}^2] = \hat{0}$, and for that reason it does not mix its different eigenvalues $j(j+1)$. The maximum pseudo-spin value is given by $j = \mathcal{N}/2$, which defines the set of $2j+1 = \mathcal{N}+1$ symmetric states of the Hamiltonian including the ground state. The latter choice is known as the symmetric representation and it is the most commonly used, since the other representations with $0 < j < \mathcal{N}$ show a degeneracy [61].

2.3.1 Semiclassical Approximation

The algebraic nature of some Hamiltonians allows to define a semiclassical approximation, that is, a mean-field approximation that uses a variational wave function. The basic assumption is that starting from an initial state, the dynamics will remain around it as time passes [62]. Thus, a usual procedure consists of taking the expectation value of the quantum Hamiltonian under coherent states, which minimize the Heisenberg's uncertainty principle and can be considered in some sense as the most classically accessible quantum states [63].

Thus, the classical Dicke Hamiltonian can be obtained using a tensor product between Glauber coherent states $|\alpha\rangle$ associated to the bosonic subspace and Bloch coherent states associated to the atomic subspace $|z\rangle$

$$|\alpha\rangle = e^{-|\alpha|^2/2} e^{\alpha \hat{a}^\dagger} |0\rangle, \tag{2.27}$$

$$|z\rangle = \frac{1}{(1+|z|^2)^j} e^{z\hat{J}_+} |j,-j\rangle, \tag{2.28}$$

where $|0\rangle$ is the vacuum state of the field and $|j,-j\rangle$ the state with all atoms in their ground state. The parameters $\alpha, z \in \mathbb{C}$ of each coherent state can be defined as

$$\alpha = \sqrt{\frac{j}{2}}(q+ip), \tag{2.29}$$

$$z = \frac{Q+iP}{\sqrt{4-Q^2-P^2}}, \tag{2.30}$$

and are associated with canonical variables of phase space, say, $\mathbf{x} = (q,p;Q,P)$. The bosonic variables are given by (q,p) and the atomic ones by (Q,P), which satisfy the Poisson brackets

$$\{q,p\} = 1, \tag{2.31}$$

$$\{Q,P\} = 1. \tag{2.32}$$

In this way, a Glauber-Bloch coherent state can be defined as the tensor product

$$\begin{aligned} |\mathbf{x}\rangle &= |\alpha\rangle \otimes |z\rangle \\ &= |q,p\rangle \otimes |Q,P\rangle. \end{aligned} \tag{2.33}$$

Taking the expectation value of the Dicke Hamiltonian under Glauber-Bloch coherent states, three terms are found

$$\begin{aligned} h_{\mathrm{D}}(\mathbf{x}) &= \frac{1}{j}\langle \mathbf{x}|\hat{H}_{\mathrm{D}}|\mathbf{x}\rangle \\ &= \frac{1}{j}[\langle \mathbf{x}|\hat{H}_{\mathrm{F}}|\mathbf{x}\rangle + \langle \mathbf{x}|\hat{H}_{\mathrm{A}}|\mathbf{x}\rangle + \langle \mathbf{x}|\hat{H}_{\mathrm{I}}|\mathbf{x}\rangle] \\ &= h_{\mathrm{F}}(\mathbf{x}) + h_{\mathrm{A}}(\mathbf{x}) + h_{\mathrm{I}}(\mathbf{x}), \end{aligned} \tag{2.34}$$

which represent the classical field, atomic, and atom-field interaction energy of the system, respectively. The scaling j of the Hamiltonian produces a classical dynamics independent of the system size and defines an effective Planck constant $\hbar_{\mathrm{eff}} = j^{-1}$ [64]. Thus, the four-dimensional phase space in the coordinates $\mathbf{x} = (q, p; Q, P)$ associated to the latter classical Hamiltonian is denoted by $\mathcal{M}$. In Appendix C.1 is presented a complete derivation for the Dicke Hamiltonian (2.5) (setting $\hbar = 1$) of the following terms

$$h_{\mathrm{F}}(\mathbf{x}) = \frac{\omega}{2}(q^2 + p^2), \tag{2.35}$$

$$h_{\mathrm{A}}(\mathbf{x}) = \frac{\omega_0}{2}(Q^2 + P^2) - \omega_0, \tag{2.36}$$

$$h_{\mathrm{I}}(\mathbf{x}) = 2\gamma q Q\sqrt{1 - \frac{Q^2 + P^2}{4}}, \tag{2.37}$$

where the classical field $h_{\mathrm{F}}(\mathbf{x})$ and atomic $h_{\mathrm{A}}(\mathbf{x})$ Hamiltonians represent the energy of two classical harmonic oscillators, while the classical atom-field interaction Hamiltonian $h_{\mathrm{I}}(\mathbf{x})$ represents the classical coupling energy between them.

Adding the above terms, the classical Dicke Hamiltonian can be written in a complete expression as

$$\begin{aligned} h_{\mathrm{D}}(\mathbf{x}) =& \frac{\omega}{2}(q^2 + p^2) + \frac{\omega_0}{2}(Q^2 + P^2) - \omega_0 + \\ &+ 2\gamma q Q\sqrt{1 - \frac{Q^2 + P^2}{4}}, \end{aligned} \tag{2.38}$$

where the scaling j of the Hamiltonian associates a rescaled classical energy or classical energy shell given by the parameter $\epsilon = E/j$.

2.3.2 Quantum Phase Transition and Classical Ground-State Energy

In 1973 several authors pointed out a quantum phase transition for the ground state of the Dicke Hamiltonian [65–68], which was recently confirmed [69, 70]. This quantum phase transition occurs in the thermodynamic limit ($\mathcal{N} \to \infty$) at zero temperature. When the coupling strength reaches a critical value given by $\gamma_c = \sqrt{\omega\omega_0}/2$, the system goes from a normal phase ($\gamma < \gamma_c$, with zero photons and excited atoms on average), to a superradiant phase ($\gamma > \gamma_c$, with a number of photons and excited atoms of the same order of magnitude as the total number of atoms in the system). In the latter phase, the average photon emission is a non-zero collective emission, known as superradiance [71].

The quantum phase transition can be understood in the classical domain (thermodynamic limit $\mathcal{N} \to \infty$), by finding the ground-state energy of the classical Dicke Hamiltonian, which is given by (see Appendix C.2 for details on this derivation)

$$\epsilon_{gs} = -\omega_0 \begin{cases} 1 & \text{if } \gamma < \gamma_c \\ \frac{1}{2}\left[\left(\frac{\gamma}{\gamma_c}\right)^2 + \left(\frac{\gamma_c}{\gamma}\right)^2\right] & \text{if } \gamma > \gamma_c \end{cases}, \tag{2.39}$$

for each normal and superradiant phase. In Fig. 2.2 is shown the behavior of the ground-state energy as a function of the coupling-strength parameter. In addition, in the same Fig. 2.2 is shown the quantum phase transition, which is a second order phase transition, as a discontinuity in the second derivative of the ground-state energy.

On the other hand, the whole energy surface of the classical Dicke Hamiltonian (2.38) can be studied using the Hamilton's equations of motion to write the Hamiltonian as an exclusive function of the atomic variables (Q, P) (see Appendix C.2 for details about the Hamilton's equations of motion)

$$h_D(Q,P) = \omega_0 \left[\frac{Q^2+P^2}{2} - 1 - \frac{1}{2}\left(\frac{\gamma}{\gamma_c}\right)^2 Q^2 \left(1 - \frac{Q^2+P^2}{4}\right)\right]. \tag{2.40}$$

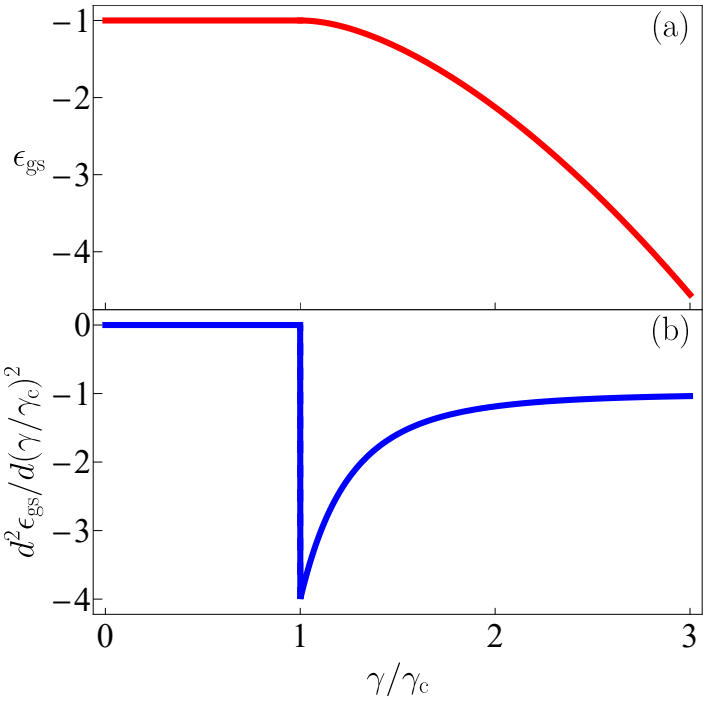

Figure 2.2: Classical ground-state energy (2.39) (a) and its second derivative (b) as a function of the scaled coupling-strength parameter $\gamma/\gamma_{\rm c}$. The atomic transition frequency was taken as $\omega_0 = 1$. In panel (b) the discontinuity in $\gamma/\gamma_{\rm c} = 1$ represents the quantum phase transition for the ground-state in the thermodynamic limit $\mathcal{N} \to \infty$.

The above equation can be plotted as contour lines for different classical energy shells. In Fig. 2.3 are shown three cases for different values of the coupling-strength parameter, where the quantum phase transition of the ground state can be seen as the change from a stable point (normal phase, $\gamma < \gamma_c$) to a unstable point (superradiant phase, $\gamma > \gamma_c$), where two global minimums appear.

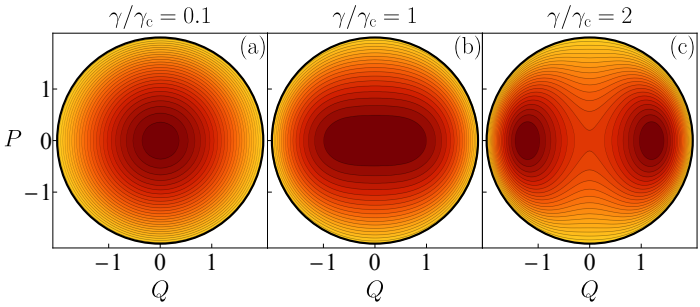

Figure 2.3: Contour lines of the classical energy surface (2.40) for different values of the scaled coupling-strength parameter: $\gamma/\gamma_c = 0.1$ (a), $\gamma/\gamma_c = 1$ (b), and $\gamma/\gamma_c = 2$ (c). The atomic transition frequency was taken as $\omega_0 = 1$. Darker colors define low energy values. The quantum phase transition can be seen as the change from a stable point (normal phase, $\gamma < \gamma_c$) in panel (a) to a unstable point (superradiant phase, $\gamma > \gamma_c$) in panel (c), where two global minimums appear.

2.3.3 Semiclassical Approximation to the Density of States

A semiclassical approximation to the density of states of a quantum system can be obtained using a particular case of the well-known Gutzwiller trace formula [2, 72]. Computing the phase-space volume at a classical energy shell $\epsilon = E/j$ and using the classical Dicke Hamiltonian (2.38), the explicit expression

is given by (see Appendix C.3 for a complete derivation)

$$\nu(\epsilon) = \frac{2j^2}{\omega} \begin{cases} \frac{1}{\pi}\int_{\xi_\epsilon^-}^{\xi_\epsilon^+} d\xi\, f_\epsilon(\xi) & \text{if } \epsilon_0 \leq \epsilon < -\omega_0 \\ \frac{1+\epsilon/\omega_0}{2} + \frac{1}{\pi}\int_{\epsilon/\omega_0}^{\xi_\epsilon^+} d\xi\, f_\epsilon(\xi) & \text{if } |\epsilon| \leq \omega_0 \\ 1 & \text{if } \epsilon > \omega_0 \end{cases}, \tag{2.41}$$

where

$$f_\epsilon(\xi) = \cos^{-1}\left(\frac{\gamma_c}{\gamma}\sqrt{\frac{2(\xi - \frac{\epsilon}{\omega_0})}{1-\xi^2}}\right), \tag{2.42}$$

$$\xi_\epsilon^\pm = -\frac{\gamma_c}{\gamma}\left(\frac{\gamma_c}{\gamma} \mp \sqrt{\frac{2(\epsilon-\epsilon_0)}{\omega_0}}\right), \tag{2.43}$$

and $\epsilon_0 = \epsilon_{gs}$ is the ground-state energy in the superradiant phase ($\gamma > \gamma_c$) (see Eq. (2.39)).

In Fig. 2.4 is shown a typical case for the superradiant phase ($\gamma > \gamma_c$), where the correspondence between the semiclassical density of states (2.41) and the density of sates computed numerically can be seen.

2.4 Experimental Realizations

An important characteristic of the Dicke model is that it is experimentally accessible. Early setups were proposed concerning superradiance with pumped gases [73]. Through the years, different setups have been proposed to represent the Dicke model, which have been improved and have become more sophisticated with the development of the technology. Among the contemporary experimental proposals can be mentioned setups with ultracold atoms [74–79], trapped ions [80–82], cavity-assisted Raman transitions [83,84], superconducting circuits [85,86], and others. In Appendix D is shown an experimental setup realized with a Bose-Einstein condensate, which was one of most important setups proposed in recent years, since it was able to detect experimentally the quantum phase transition predicted theoretically

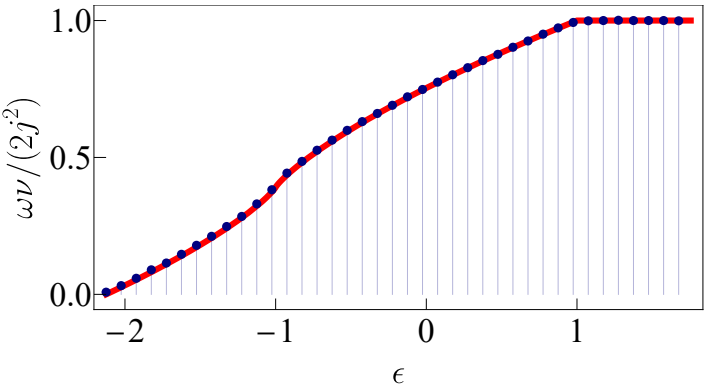

Figure 2.4: Semiclassical density of states (2.41) (red solid curve). Histogram of the numerical energy levels (blue dots). Hamiltonian parameters: $\omega = \omega_0 = 1$, $\gamma = 2\gamma_c = 1$, and $j = 100$. The truncation value of the modified bosonic subspace was taken as $N_{\max} = 390$, obtaining a Hilbert space dimension $\mathcal{D}_C = 39296$ with 24453 converged energy levels in the coherent basis with positive parity.

by the model. A very detailed reference about the engineering involved with Bose-Einstein condensation and cavity QED is shown in Ref. [87]. Furthermore, some setups have been proposed to represent the classical limit of the Dicke model using resonant circuits [88].

On the other hand, implementations with Bose-Einstein condensates were proposed for the Dicke model under the RWA [89], that is, the well-known Tavis-Cummings model (see Eq. (2.7)). A useful revision of this model and its experimental setups is shown in Ref. [90]. Furthermore, complete revisions about different experimental implementations in cavity QED are presented in Refs. [91, 92].

Chapter 3

Chaos Theory

In this Chapter is exposed the phenomenon of chaos in its both classical and quantum approaches. On the one hand, the classical approach is explained as loss integrability for Hamiltonian systems and sensitive dependence on initial conditions. Moreover, the conventional indicators of classical chaos are introduced, which due to their nature can be classified as qualitative or quantitative tests. An introduction to the theory of periodic orbits is also exposed, which is of fundamental interest for the phenomenon of quantum scarring explained in Chapter 8. On the other hand, the quantum approach is motivated with the origin of chaos in classical systems and it is studied under the formalism of the random matrix theory, which is the traditional method to treat quantum chaos through statistical tests of spectral fluctuations. In this regard, two main groups of indicators of quantum chaos are introduced, static (conventional) and dynamical (unconventional) indicators.

3.1 Classical Chaos

The chaotic behavior arises in nonlinear dynamical systems and is characterized by a strong sensitivity to small changes in initial conditions, such that, despite the deterministic nature of the

dynamical systems, the solutions cannot be predicted at long times [93–95]. The phenomenon of chaos is associated with loss of integrability, since the solutions for regular systems can be found from integrable equations. In this way, the chaotic behavior lies between regular behavior characterized by deterministic equations of motion and a state of unpredictable stochastic behavior characterized by complete randomness [96].

3.1.1 Integrability of Hamiltonian Systems

For conservative Hamiltonian systems with I degrees of freedom there is a Hamiltonian function $H(q_1, \ldots, q_I; p_1, \ldots, p_I)$ independent of time, where (q_i, p_i) are the canonical position-momentum variables which satisfy the Hamilton's equations of motion [56, 97]

$$\dot{q}_i = \frac{\partial H}{\partial p_i}, \tag{3.1}$$

$$\dot{p}_i = -\frac{\partial H}{\partial q_i}, \tag{3.2}$$

for $i = 1, \ldots, I$. The integrability is defined by the existence of I integrals of motion given by Eq. (2.10), whose Poisson brackets vanish (see Eq. (2.11)). If the last conditions are achieved by the Hamiltonian system, then it can be reduced to quadrature and it is called integrable, since its solutions (trajectories) can be found in closed form by integrating the equations of motion. The integrability implies that the trajectories are constrained to remain in an I-dimensional manifold in phase space, whose geometry is equivalent to an invariant I-dimensional torus. The torus geometry allows to exactly transform the integrable system in terms of action-angle variables, where the actions are invariants of motion. The last feature has important repercussions, since the geometric constraints and uniqueness of solutions of the equations of motion ensure that two near initial conditions will continue asymptotically close to each other during their time evolution, that is, an ensemble of initial conditions located in a small region of phase space cannot explore the whole phase space [97].

Kolmogorov-Arnold-Moser Theorem

The loss of integrability of a perturbed Hamiltonian system is explained with the famous Kolmogorov-Arnold-Moser (KAM) theorem [56, 93, 96, 98]. The method of proof for this theorem was proposed by A. N. Kolmogorov in 1954 [99]; however, the rigorous proofs were made independently by J. Moser and V. I. Arnold some years later [100–102].

The KAM theorem takes into account a generic Hamiltonian system with I degrees of freedom, which can be written in terms of action-angle variables (J_i, θ_i) as follows [56, 93, 96]

$$H(J_1, \ldots, J_I; \theta_1, \ldots, \theta_I) = H_0(J_1, \ldots, J_I) + \\ + \varepsilon V(J_1, \ldots, J_I; \theta_1, \ldots, \theta_I), \quad (3.3)$$

where H_0 is integrable, V is a perturbing potential that breaks the integrability of the system, and the strength of the perturbation is controlled by the parameter ε. Basically, the KAM theorem states that the motion of the perturbed system will remain confined to an I-dimensional torus when the perturbation of the system is sufficiently small $\varepsilon \ll 1$ and the normal frequencies of the integrable system H_0 are incommensurable (irrational numbers). The last can be stated in other words, as the strength of the perturbation increases, the integrability of the system is gradually lost, such that, the invariant torus is gradually deformed and destroyed. As a result, the whole phase space becomes connected and filled with chaotic trajectories when all the invariant tori are destroyed [97].

3.1.2 Qualitative and Quantitative Indicators of Chaos

Two basic tests are widely used to determine if Hamiltonian systems are chaotic or not. Qualitative tests are used to visualize the loss of integrability in phase space, while quantitative tests are used to measure the sensitive dependence on initial conditions, which is a singular characteristic of chaotic systems [93, 96]. While the nature of the tests can vary from one to another, the essence is to determine specific characteristics that only arise in

the chaotic motion. Thus, the last tests are widely recognized as conventional indicators of chaos in Hamiltonian systems.

Poincaré Section

The Poincaré section, named after French mathematician and physicist J. H. Poincaré, is a useful tool to identify visually in phase space chaotic behavior of Hamiltonian systems [56, 72, 93, 94, 96, 97]. The Poincaré section is a global indicator of chaos, since involves a complete scheme of the dynamics in phase space [97]. The construction method is based by viewing the phase space stroboscopically, such that, the motion is observed periodically. The idea is to reduce the I-dimensional phase space of a given Hamiltonian system by intersecting some trajectory of the system with a plane (surface of section), obtaining as a result an $(I-1)$-dimensional map where the motion is caught by points distributed in accord to some pattern. If the point distribution resembles a well organized pattern, it is said that the system is integrable and the motion is regular. On the other hand, if the point distribution is spread over the map with any identified pattern, then that translates into loss of integrability of the system and the motion is chaotic. In Fig. 3.1 is shown a schematic representation of a Poincaré section which shows the intersections of a given trajectory with a selected plane.

Lyapunov Exponent

The Lyapunov exponent, named after Russian mathematician and physicist A. M. Lyapunov, is a measure of the divergence degree in phase space between two near initial conditions under the action of the Hamiltonian evolution [56, 93, 94, 96, 97]. The Lyapunov exponent is a local indicator of chaos which depends on each point of phase space, contrary to the Poincaré section which is a global indicator of chaos [97]. Early studies using the Lyapunov exponent in dynamical systems were performed by V. I. Oseledts in 1968 [103].

The Hamiltonian evolution of two initial conditions $\mathbf{x}_1(0)$ and $\mathbf{x}_2(0)$ yield the trajectories $\mathbf{x}_1(t)$ and $\mathbf{x}_2(t)$ at an arbitrary time t,

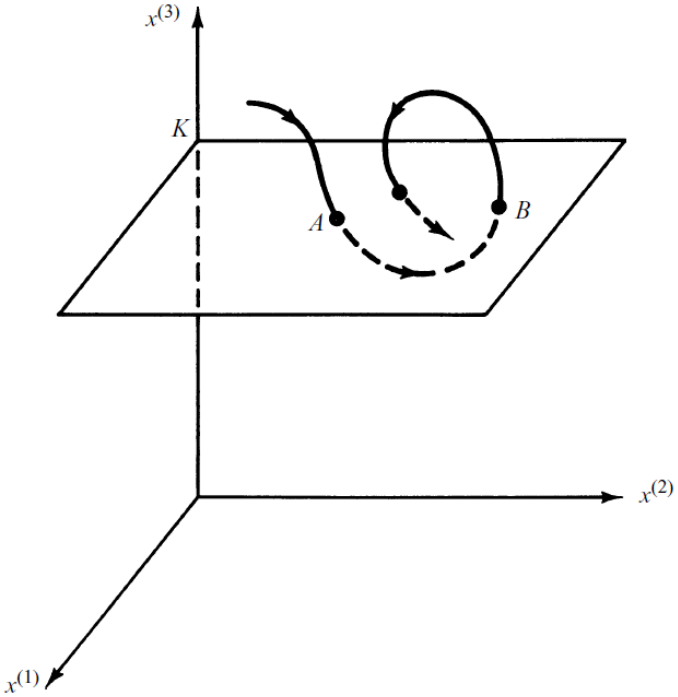

Figure 3.1: Schematic representation of a Poincaré section for a given trajectory (black solid line). A three-dimensional phase space is considered for a hypothetical Hamiltonian system, which is reduced to a two-dimensional map (Poincaré section) when it is intersected with the plane K, where the crossings of the trajectory (black dots) can be seen at different times as a dot distribution. Figure taken from Ref. [93].

where the separation between them at the same time is given by $\Delta(t) = \mathbf{x}_2(t) - \mathbf{x}_1(t)$. For a Hamiltonian system with I degrees of freedom the norm of the separation between two near trajectories provides a measure of their divergence

$$||\Delta(t)|| = \sqrt{\sum_{i=1}^{I} \delta x_i^2(t)}, \tag{3.4}$$

where δx_i is the variation to first order with respect to a given reference trajectory [97,104]. The sensitive dependence on initial conditions is attained if the divergence between both trajectories grows exponentially

$$||\Delta(t)|| \sim e^{\lambda t}||\Delta(0)||, \tag{3.5}$$

where $\lambda > 0$ identifies the Lyapunov exponent. In Fig. 3.2 is shown a schematic representation of the divergence between two near trajectories when time grows.

From the last relation can be defined the Lyapunov exponent, taking a double limit, in the following way

$$\lambda = \lim_{t \to +\infty} \lim_{||\Delta(0)|| \to 0} \frac{1}{t} \ln \left(\frac{||\Delta(t)||}{||\Delta(0)||} \right). \tag{3.6}$$

Nevertheless, there are $2I$ orthogonal directions for a Hamiltonian system with I degrees of freedom yielding a set of $2I$ Lyapunov exponents $\{\lambda_1, \ldots, \lambda_{2I}\}$ corresponding to each direction, which satisfy the symmetry constraint $\lambda_i = -\lambda_{2I-i+1}$ for $i = 1, \ldots, 2I$.

For regular motion, all Lyapunov exponents are zero, since the divergence only grows linearly. Thus, a value $\lambda = 0$ implies regular motion for systems that preserve the phase space volume, while a value $\lambda > 0$ indicates that the motion is chaotic [56, 97, 104]. The positive Lyapunov exponent must be found everywhere in phase space to link it with chaotic motion, since isolated unstable points also show positive Lyapunov exponent. The methods to calculate all the Lyapunov exponents of Hamiltonian systems numerically could be quite complicated and challenging. A detail explanation on how to calculate Lyapunov exponents is given in Refs. [105,106].

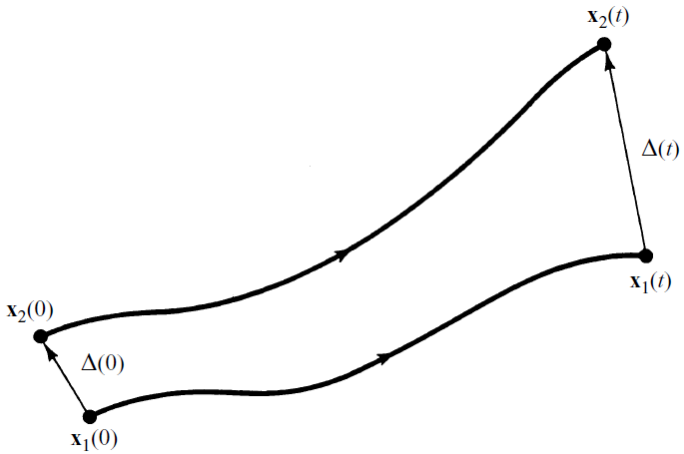

Figure 3.2: Schematic representation of the divergence between two near trajectories $\mathbf{x}_1(t)$ and $\mathbf{x}_2(t)$. The Hamiltonian evolution of two initial conditions $\mathbf{x}_1(0)$ and $\mathbf{x}_2(0)$ yield the latter trajectories which separate exponentially as time grows. Figure taken from Ref. [93].

KS Entropy

Another quantitative measure of chaos related with the Lyapunov exponent is the Krylov-Kolmogorov-Sinai (KS) entropy, which is a measure of the hyperbolic instability in the relative motion of trajectories in phase space [56, 107]. The last measure was first used by N. S. Krylov in studies of statistical properties of mechanical systems, later was introduced in the ergodic theory by A. N. Kolmogorov, and finally it was connected with local instability of motion by Ya. G. Sinai [107]. If the KS entropy for a flow of trajectories in a given region of phase space is positive, that implies chaotic motion. On the other hand, the KS entropy of a single connected stochastic region is equal to the sum of the positive Lyapunov exponents. The last relation was established by Ya. B. Pesin in 1977 [108].

For a Hamiltonian system with I degrees of freedom the KS

entropy can be is defined in the following way [56, 109]

$$S_{\mathrm{KS}}(E) = \int_{\Gamma_E} dv_E \, s(\mathbf{q}), \tag{3.7}$$

where Γ_E is a compact surface of constant energy, dv_E is an invariant volume element of the energy surface and

$$s(\mathbf{x}) = \sum_{i=1}^{I-1} \lambda_i(\mathbf{q}) \tag{3.8}$$

is the KS-entropy density, where $\lambda_i(\mathbf{q})$ are the Lyapunov exponents defined in a region of phase space on the energy surface.

3.1.3 Theory of Periodic Orbits

Periodic orbits are solutions of the equations of motion for a dynamical system that return to their initial conditions after a finite time called period. J. H. Poincaré was the first to suggest that the study of periodic orbits would clarify the overall behavior of mechanical systems, since they are densely distributed among all possible classical trajectories [72]. With the birth of quantum mechanics the study of periodic orbits became a fundamental topic for the understanding of the classical-quantum correspondence or how the classical limit emerges from the quantum domain as $\hbar \to 0$ [72, 97]. Among the popular proposals to link both domains is the Bohr-Sommerfeld quantization condition used to obtain eigenvalues from integrable classical systems. Another proposal is the Einstein-Brillouin-Keller (EBK) quantization condition, which is an improvement of the Bohr-Sommerfeld quantization condition and also provides an estimate of the eingevalues from integrable classical systems [110]. For a system with I degrees of freedom with position-momentum variables (q_i, p_i), the EBK quantization condition consists in compute the path integrals of p_i over the periodic orbits of q_i and is given by

$$\oint dq_i p_i = 2\pi\hbar \left(n_i + \frac{\mu_i}{4}\right), \tag{3.9}$$

for $i = 1, \ldots, I$, where n_i is an integer quantum number and μ_i is a Maslov index which represents the number of classical turning points in the trajectory of q_i.

Gutzwiller Trace Formula

The idea of describing non-integrable systems was suggested by A. Einstein in 1917 [111]. Nevertheless, the formal periodic orbit theory was developed many years later by M. C. Gutzwiller to treat chaotic systems [72,112–116]. The treatment to reconstruct the energy spectra of a given quantum system using only parameters of the classical system was achieved with the Gutzwiller trace formula. This formula connects the density of states of the quantum system with classical parameters of the periodic orbits, as the stability exponent and the classical action. The explicit formula comes from taking the trace of the classical approximation to the Green's function $G(\mathbf{q}, \mathbf{q}', E)$, where $\mathbf{q}$ and $\mathbf{q}'$ is a starting and an end position, respectively. The trace of the Green's function contains explicit information about the eigenvalues of a quantum system and can define its density of states. Moreover, the trace is taken in the same starting and end point $\mathbf{q} = \mathbf{q}'$ over all phase space and it is evaluated under the stationary phase approximation, which provides the condition $\mathbf{p} = \mathbf{p}'$ for the starting and end momentum. The last condition implies that the trajectory is closed and it is a periodic orbit [72,116]. In Appendix E is shown the derivation of the trace of the Green's function. The classical approximation of the Green's function $\widetilde{G}(\mathbf{q}, \mathbf{q}', E)$ can be written as a sum of periodic orbits and its trace defines approximately the density of states of the quantum system [72,115,116]

$$\begin{aligned} \nu(E) &\approx \mathrm{Tr}[\widetilde{G}(\mathbf{q}, \mathbf{q}, E)] \\ &\approx \int d^I\mathbf{q}\, \widetilde{G}(\mathbf{q}, \mathbf{q}, E) \\ &\approx \sum_o A_o e^{i[S_o(E)/\hbar - \pi\mu_o/2]}, \end{aligned} \tag{3.10}$$

where I are the degrees of freedom of the classical system and

$$A_o = \frac{T_0}{2i\hbar}\left[\frac{1}{\sinh(\chi/2)}, \frac{1}{\cosh(\chi/2)}\right] \tag{3.11}$$

is a coefficient that depends on the primitive period of the periodic orbit T_0 and the stability exponent χ (the first coefficient defines an hyperbolic periodic orbit and the second one an inverse hyperbolic periodic orbit). The classical action $S_o(E) = \int_{\mathbf{q}}^{\mathbf{q}'} d\mathbf{q} \cdot \mathbf{p}$ is taken over each periodic orbit and μ_o counts the conjugate points at constant energy between $\mathbf{q}$ and $\mathbf{q}'$.

Although the Gutzwiller trace formula seems simple at first sight, it is quite complicated and challenging to perform the sums in chaotic systems, since the knowledge of the classical trajectories is too poor. Nevertheless, it is expected that this formula provides an approximate spectrum for the energy eigenvalues of these chaotic system [72, 116]. Later studies based in the idea of recovering quantum information from classical information have proposed schemes to reconstruct chaotic eigenfunctions using only few sets of periodic orbits [117].

3.2 Quantum Chaos

The concept of quantum chaos comes from its classical counterpart, that is, the necessity to characterize the chaotic behavior which arises in quantum systems, with respect to the chaotic behavior in classical systems [72, 93, 95, 118, 119]. Nevertheless, the quantum mechanical formalism implies a different treatment of chaos in such systems. On the one hand, the fundamental equation of quantum mechanics, the Schrödinger equation, is a linear equation. This fact is contrary to the classical counterpart, where the core feature is the nonlinearities of the classical equations of motion which originate the chaotic behavior [56, 95, 119]. In addition, the concepts of trajectory and phase space are not well defined in quantum mechanics, since the Heisenberg's uncertainty principle says that it is impossible to know simultaneously position and momentum of a quantum particle [56, 118, 120]. Although a key step is to use quasiprobability distributions, which

possess certain similarity with classical phase-space distribution functions, in the way of expressing the quantum averages with respect to the classical ones [120]. Thus, the concept of phase space in quantum mechanics can be defined acceptably. On the other hand, the correspondence principle demands that in the classical limit, when the de Broglie's wavelength is smaller than the characteristic lengths of the system, quantum mechanics should become classical mechanics [93, 119].

As a result, the chaotic behavior present in quantum systems must be studied in a different way, to such an extent that some authors have proposed to use the term quantum chaology instead of quantum chaos [121, 122]. For quantum systems with discrete energy spectra, the dynamics is characterized by quasiperiodicities or recurrences, instead of trajectories as occurs in the classical dynamics. This allows to define a criterion which can identify chaotic from regular behavior and it is based on energy spectra or in the evolution of some observables of the quantum system [123].

3.2.1 Random Matrix Theory

Originally, the Random Matrix Theory (RMT) was developed by E. P. Wigner to characterize the statistical properties of energy spectra of complex quantum many-body systems [95, 119, 123–131]. Thus, the system Hamiltonians were replaced by ensembles of Hamiltonians with random components, where the assumption was the ability to describe generic properties [129, 131]. In this way, the RTM was widely used to describe the properties of spectral fluctuations of atomic nuclei, complex atoms, and complex molecules [131–133]. Under this formalism, the basic idea is to generate the Hamiltonian matrix components randomly. Thus, E. P. Wigner and F. J. Dyson using some tools from group theory, showed that these Hamiltonian matrices are classified in three generic ensembles, defined by the symmetry properties of the Hamiltonian [124–126, 134]:

1. For time-reversal invariant systems with rotational symmetry, the Hamiltonian matrix is real and symmetric $H_{ii'} =$

$H_{i'i} = H^*_{ii'}$. Time-reversal invariant systems with integer spin and broken rotational symmetry also belong to this ensemble.

2. For systems where the time-reversal invariance is broken, the Hamiltonian matrix is Hermitian $H_{ii'} = (\hat{H}^\dagger)_{ii'}$.

3. For time-reversal invariant systems with half-integer spin and broken rotational symmetry, the Hamiltonian matrix can be written in terms of quaternions or the Pauli matrices σ_n with $n = 1, 2, 3$, that is, $H^{(0)}_{ii'} 1_2 - i \sum_{n=1}^{3} H^{(n)}_{ii'} \sigma_n$, where $H^{(0)}_{ii'}$ is real and symmetric, while $H^{(n)}_{ii'}$ are real and asymmetric.

For each of the above cases a probability distribution is defined with Gaussian shape

$$P_{N,\beta}(\hat{H}) \propto e^{-\frac{\beta N}{\lambda^2} \mathrm{Tr}(\hat{H}^2)}, \tag{3.12}$$

where N is the dimension of the Hamiltonian matrix, λ is a dimension-independent constant which ensures that the ensemble spectrum stay bounded in the limit $N \to \infty$. Moreover, the value of the constant β ($\beta = 1, 2, 4$) defines the three possible cases with real, complex, and quaternion elements, respectively. In this way, the symmetry properties of the Hamiltonian matrices and the probability distributions $P_{N,\beta}(\hat{H})$ in each case, stay invariant under orthogonal, unitary, and symplectic transformations. With the latter properties in mind, the characteristic ensembles of random matrices are classified in three main groups called by F. J. Dyson: Gaussian Orthogonal Ensemble (GOE), Gaussian Unitary Ensemble (GUE), and Gaussian Symplectic Ensemble (GSE), respectively [124–126, 129].

3.2.2 Static Indicators of Chaos

In 1984 O. Bohigas, M. J. Giannoni, and C. Schmidt showed that the spectral fluctuations of quantum systems whose classical limit is chaotic coincide with those of the GOE from RMT,

conjecturing that these fluctuations are universal [135]. The latter is known as the Bohigas-Giannoni-Schmit conjecture. Under this framework, the traditional study of quantum chaos is performed through the statistical analysis of quantum spectral fluctuations. Basically, there are two conventional spectral tests which study short and long range spectral correlations. These tests from RMT play the role of indicators of chaos in quantum systems. Both short and long range spectral tests have been widely explored in different quantum systems [136–143]. Furthermore, in Appendix F is shown the unfolding procedure, which is an essential tool applied to the energy spectra before performing the spectral tests.

Nearest-Neighbor Spacing Distribution

The Nearest-Neighbor Spacing (NNS) distribution identifies the probability distribution for the energy spectra of quantum systems [95, 119, 123–126, 129, 131]. It is the standard test to study short-range spectral correlations, since few spacings between energy levels are involved on average. In this way, a spacing between adjacent (nearest-neighbor) energy levels is given by $S = E_{n+1} - E_n$, such that, the dimensionless variable $s = S/D$ can be defined, where $D = \langle S \rangle$ is the mean level spacing. Thus, $P(s)$ identifies the level-spacing probability density function, which along with its first moment satisfy the normalization condition

$$\int_0^{+\infty} ds\, P(s) = 1, \tag{3.13}$$

$$\int_0^{+\infty} ds\, sP(s) = 1. \tag{3.14}$$

Additionally, a useful tool to verify the agreement between the analytical function $P(s)$ and experimental or numerical data is the level-spacing cumulative distribution function

$$F(s) = \int_0^s ds' P(s'), \tag{3.15}$$

which is independent of spacing effects.

Typically, for integrable quantum systems whose classical limit is regular, the NNS distribution is a Poisson distribution

$$P_{\mathrm{P}}(s) = e^{-s}. \tag{3.16}$$

On the other hand, for a great quantity of non-integrable quantum systems whose Hamiltonian satisfy the time-reversal invariance and whose classical limit is chaotic, the NNS distribution shows an agreement with the GOE predictions from RMT. That is, the typical NNS distribution is the Wigner-Dyson surmise

$$P_{\mathrm{WD}}(s) = \frac{\pi}{2} s\, e^{-\frac{\pi}{4}s^2}. \tag{3.17}$$

This distribution was proposed by E. P. Wigner as an approximation when the experimental evidence did not agree with theory [129, 131]. Mathematically, the most general expression of this surmise takes into account the three Gaussian ensembles (GOE, GUE, GSE)

$$P_\beta(s) = a_\beta s^\beta e^{-b_\beta s^2}, \tag{3.18}$$

where

$$a_\beta = 2\frac{\Gamma^{\beta+1}\left(\frac{\beta+2}{2}\right)}{\Gamma^{\beta+2}\left(\frac{\beta+1}{2}\right)}, \tag{3.19}$$

$$b_\beta = \frac{\Gamma^{2}\left(\frac{\beta+2}{2}\right)}{\Gamma^{2}\left(\frac{\beta+1}{2}\right)}, \tag{3.20}$$

and

$$\Gamma(z) = \int_0^{+\infty} dx\, e^{-x} x^{z-1} \tag{3.21}$$

is the gamma function with $\Re[z] > 0$. The parameter $\beta = 1, 2, 4$ identifies the respective Gaussian ensembles (GOE, GUE, GSE), whose explicit coefficients are given by

$$[(a_1, a_2, a_4), (b_1, b_2, b_4)] = \left[\left(\frac{\pi}{2}, \frac{32}{\pi^2}, \frac{2^{18}}{3^6\pi^3}\right), \left(\frac{\pi}{4}, \frac{4}{\pi}, \frac{64}{9\pi}\right)\right]. \tag{3.22}$$

In Fig. 3.3 is shown the Poisson distribution (3.16), as well as the generalized Wigner-Dyson distribution (3.18) for the three Gaussian ensembles (GOE, GUE, GSE).

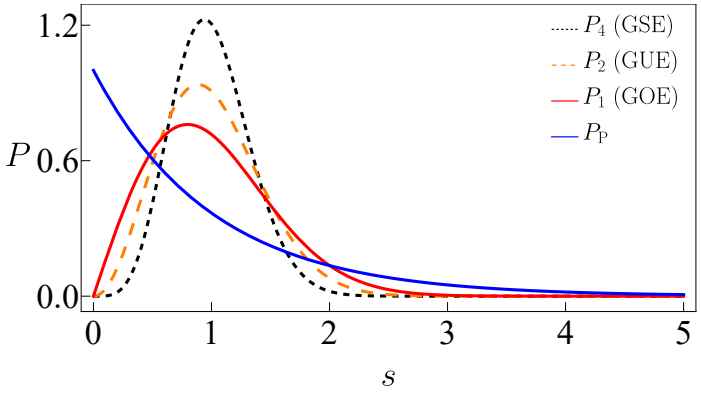

Figure 3.3: Poisson distribution (3.16) and generalized Wigner-Dyson distribution (3.18) for the Gaussian ensembles (GOE, GUE, GSE).

Another well-known distribution, which interpolates between the Poisson and Wigner-Dyson distributions, was proposed by T. A. Brody in 1973 and is known as the Brody distribution [130, 144]

$$P_\upsilon(s) = A(\upsilon) s^\upsilon e^{-\alpha(\upsilon) s^{\upsilon+1}}, \tag{3.23}$$

where

$$A(\upsilon) = (\upsilon+1)\alpha(\upsilon), \tag{3.24}$$

$$\alpha(\upsilon) = \Gamma^{\upsilon+1}\left(\frac{\upsilon+2}{\upsilon+1}\right), \tag{3.25}$$

and the parameter υ quantifies the level-repulsion degree and it is found by a least squares data fitting method. Therefore, the boundary case $\upsilon = 0$ ($\upsilon = 1$) defines the Poisson (Wigner-Dyson) distribution. Although the Brody distribution is able to characterize the NNS distribution of an energy spectrum between Poisson and Wigner-Dyson by varying the parameter υ, some

authors have argued that it is just an empirical expression and that the parameter υ has no definite physical meaning [119,145].

Level Number Variance and Spectral Rigidity

The long-range spectral correlations are typically studied using the level number variance [95,119,123,127,131,146], given by

$$\Sigma^2(L) = \langle \eta^2(L, E_\mathrm{s}) \rangle - \langle \eta(L, E_\mathrm{s}) \rangle^2, \tag{3.26}$$

where the function $\eta(L, E_\mathrm{s})$ counts the number of levels contained within the energy interval $[E_\mathrm{s}, E_\mathrm{s} + L]$, and $\langle \bullet \rangle$ denotes the average over the initial point E_s.

For the Poisson distribution is found

$$\Sigma^2_\mathrm{P}(L) = L, \tag{3.27}$$

while the Gaussian ensembles (GOE, GUE, GSE) with $\beta = 1, 2, 4$ have the following approximations valid until order L^{-1}

$$\Sigma^2_1(L) = \frac{2}{\pi^2}\left[\ln(2\pi L) + \gamma + 1 - \frac{\pi^2}{8}\right] + \mathcal{O}(L^{-1}), \tag{3.28}$$

$$\Sigma^2_2(L) = \frac{1}{\pi^2}\left[\ln(2\pi L) + \gamma + 1\right] + \mathcal{O}(L^{-1}), \tag{3.29}$$

$$\Sigma^2_4(L) = \frac{1}{2\pi^2}\left[\ln(4\pi L) + \gamma + 1 + \frac{\pi^2}{8}\right] + \mathcal{O}(L^{-1}), \tag{3.30}$$

where

$$\gamma = \lim_{n \to +\infty} \left[\sum_{k=1}^{n} \frac{1}{k} - \ln(n)\right] \approx 0.5772 \tag{3.31}$$

is the Euler-Mascheroni constant.

Another known test to study long-range spectral correlations, which is closely related with the level number variance, is the spectral rigidity, first introduced by F. J. Dyson and M. L. Mehta [95,119,127,131,146]. The spectral rigidity is defined as the least squares deviation of the function $y = \eta(E)$ to the best fit to a straight line $y = AE + B$

$$\Delta_3(L) = \min_{A,B} \left\langle \frac{1}{L} \int_{E_\mathrm{s}}^{E_\mathrm{s}+L} dE \left[\eta(E) - AE - B\right]^2 \right\rangle, \tag{3.32}$$

where $\langle \bullet \rangle$ denotes the average over the initial point E_s.

For the Poisson distribution is found

$$\Delta_{3,\mathrm{P}}(L) = \frac{L}{15}, \tag{3.33}$$

while the Gaussian ensembles (GOE, GUE, GSE) with $\beta = 1, 2, 4$, analogously to the level number variance, have the following approximations valid until order L^{-1}.

$$\Delta_{3,1}(L) = \frac{1}{\pi^2}\left[\ln(2\pi L) + \gamma - \frac{5}{4} - \frac{\pi^2}{8}\right] + \mathcal{O}(L^{-1}), \tag{3.34}$$

$$\Delta_{3,2}(L) = \frac{1}{2\pi^2}\left[\ln(2\pi L) + \gamma - \frac{5}{4}\right] + \mathcal{O}(L^{-1}), \tag{3.35}$$

$$\Delta_{3,4}(L) = \frac{1}{4\pi^2}\left[\ln(4\pi L) + \gamma - \frac{5}{4} + \frac{\pi^2}{8}\right] + \mathcal{O}(L^{-1}), \tag{3.36}$$

where the Euler-Mascheroni constant γ is given by Eq. (3.31).

In Fig. 3.4 is shown the level number variance for the Poisson distribution (3.27), as well as the approximations (3.28)-(3.30) for the Gaussian ensembles (GOE, GUE, GSE). Likewise, in Fig. 3.4 are shown the spectral rigidity for the Poisson distribution (3.33) and the approximations (3.34)-(3.36) for the Gaussian ensembles (GOE, GUE, GSE).

3.2.3 Dynamical Indicators of Chaos

The conventional tests of quantum chaos study the energy spectra of quantum systems. Basically, with the available data a spectral function is constructed and subsequently the short and long-range spectral tests (NNS distribution, level number variance, and spectral rigidity) are applied. However, all these chaos indicators are static, since any time evolution is involved. In this regard, it has been proposed to study quantum chaos through transformations which relate energy and time, generating this way unconventional dynamical indicators of quantum chaos based on spectral correlations. The observation of avoided crossings between energy levels or level repulsion is due basically to correlations between these levels [95, 119, 123, 131]. Level repulsion

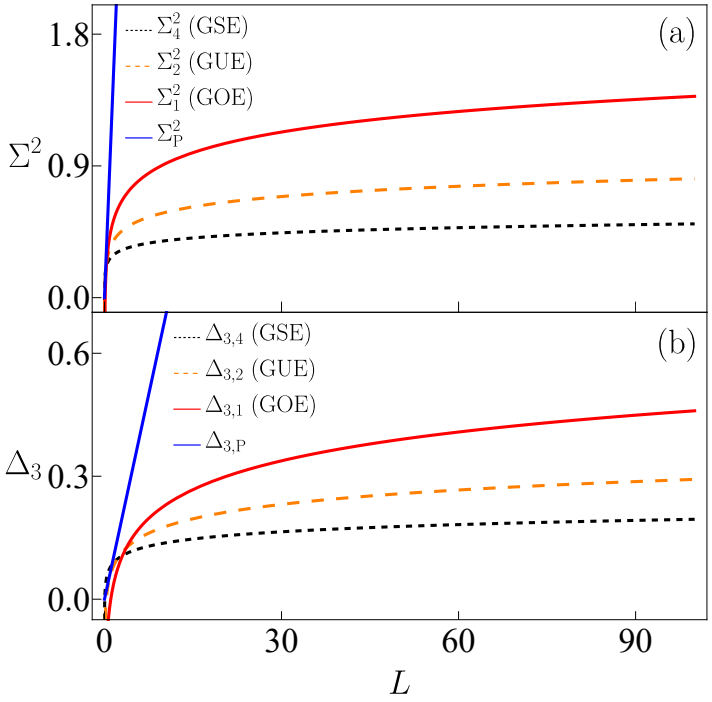

Figure 3.4: Level number variance (3.26) (a) and spectral rigidity (3.32) (b) for the Poisson distribution and approximations of order L^{-1} for the Gaussian ensembles (GOE, GUE, GSE). In panel (a) see Eqs. (3.27)-(3.30). In panel (b) see Eqs. (3.33)-(3.36).

was verified in a study made by E. P. Wigner where statistical properties of nuclear spectra were analyzed [132]. Thus, there are some quantum quantities capable of capturing effects of spectral correlations and manifest them in its dynamics. On the other hand, in recent years have been proposed quantifiers of quantum chaos, that is, in a rough way has been proposed a quantum analog of a classical Lyapunov exponent.

Correlation Hole

In 1986 L. Leviandier et al. proposed an alternative procedure to study chaos in quantum systems [31]. The method was based in using the Fourier transform of the available spectral data and to generate a time-dependent function, say $f(t)$. This procedure was proposed arguing that the conventional spectral analysis can be questionable, since there could be a great number of levels lost in the noise or in unresolved mixtures. The latter affects directly the NNS test by reducing the number of small spacings, which is the most important difference between the Poisson (random decoupled levels) and Wigner-Dyson (strongly coupled levels) distributions [31, 131].

Thereby, the interpretation of experimental spectral data using the Fourier transform method implies a series of steps. Typically, is calculated the average $\langle |f(t)|^2 \rangle$ for a spectral ensemble. The average $\langle \bullet \rangle$ is based in the fact that the function $|f(t)|^2$ comes from the Fourier transform of a simple spectrum and exhibits a lot of fluctuations. Thus, to recover the useful information, these fluctuations need to be reduced by some kind of ensemble average (several level sequences considered as equivalent) or time average as well [31, 131]. Generally, the quantity $\langle |f(t)|^2 \rangle$ has two components, a "fast" component related with the envelope of the energy spectrum, and a "slow" component related with the system saturation. All the previous features characterize globally the time evolution of the function $\langle |f(t)|^2 \rangle$; however, it can capture effects related with spectral correlations at intermediate times. Specifically, the presence of these energy level correlations arises as a hole in the time evolution, which is called correlation hole and works as a dynamical indicator of

chaos in quantum systems [31]. This indicator has been widely studied in several quantum systems, among them, random matrices, quantum billiards, molecules, spin and dispersion systems, and others [31, 147–166].

Quantum Lyapunov Exponent

A controversial quantum indicator of chaos, which was very popular when it was proposed, is the Out-of-Time-Ordered Correlator (OTOC) [11, 167–172]. The popularity of the OTOC was based in the fact that it had been identified as a "quantum Lyapunov exponent", since in the semiclassical limit $\hbar \to 0$ its exponential growth ratio resembles that of a classical Lyapunov exponent. Nevertheless, some authors have shown that the short-time exponential growth of the OTOC is not a universal signature of chaos, since it can emerge also near critical points [13, 173–176]. The OTOC measures the degree of non-commutativity in time between two quantum operators

$$C(t) = -\langle [\hat{W}(t), \hat{V}(0)]^2 \rangle, \tag{3.37}$$

where $\hat{W}(t) = e^{i\hat{H}t}\hat{W}e^{-i\hat{H}t}$ and $\hat{V}(t) = e^{i\hat{H}t}\hat{V}e^{-i\hat{H}t}$ are time evolved operators in the Heisenberg picture, and $\langle \bullet \rangle$ is a thermal average. A particular case of the OTOC is given by

$$\begin{aligned} C_F(t) &= \langle \hat{W}(t)^\dagger \hat{V}^\dagger \hat{W}(t) \hat{V} \rangle \\ &\propto \sigma_O^2(t), \end{aligned} \tag{3.38}$$

where $\hat{W} = e^{i\delta\phi\hat{O}}$ with $\delta\phi \ll 1$, $\hat{O}$ is an Hermitian operator with variance $\sigma_O^2(t) = \langle \hat{O}^2(t) \rangle - \langle \hat{O}(t) \rangle^2$, and $\hat{V} = |\Psi(0)\rangle\langle\Psi(0)|$ is the projector of an arbitrary initial state $|\Psi(0)\rangle$. An OTOC with the latter properties is known as Fidelity Out-of-Time Ordered Correlator (FOTOC) [13, 177].

Chapter 4

Spectral Correlations

In this Chapter are exposed the correlation functions and their relation with the two-level form factor, which determines the behavior of the correlation hole exposed in Chapter 3 as an unconventional dynamical indicator of quantum chaos. Furthermore, the survival probability is introduced as a quantum observable able to detect spectral correlations in its time evolution, where the correlation hole appears. The definition and properties of this dynamical quantity are exposed, as well as its explicit relation with the two-level form factor through an analytical expression.

4.1 Correlation Functions

A spectral ensemble is defined with a probability distribution $P_N(x_1, \ldots, x_N)$, where each spectrum has N energy levels x_n for $n = 1, \ldots, N$. For the Gaussian ensembles (GOE, GUE, GSE) with $\beta = 1, 2, 4$, the explicit probability distribution is given by [131, 146] (see Appendix G.1 for the GOE)

$$P_{N,\beta}(x_1, \ldots, x_N) = C_{N,\beta} e^{-\frac{\beta}{2}\sum_{n=1}^{N} x_n^2} \prod_{n<m} |x_n - x_m|^\beta, \quad (4.1)$$

where

$$C_{N,\beta} = \frac{\beta^{N/2+\beta N(N-1)/4}\Gamma^N\left(1+\frac{\beta}{2}\right)}{(2\pi)^{N/2}\prod_{n=1}^{N}\Gamma\left(1+\frac{\beta n}{2}\right)}, \tag{4.2}$$

is a normalization constant, such that

$$\int_{-\infty}^{+\infty}\dots\int_{-\infty}^{+\infty} dx_1\dots dx_N P_{N,\beta}(x_1,\dots,x_N) = 1, \tag{4.3}$$

and Γ is the Gamma function given by Eq. (3.21).

The correlation functions describe correlations between energy levels. An n-level correlation function is defined as [124–126, 131, 146]

$$R_n(x_1,\dots,x_n) = \frac{N!}{(N-n)!}P_n(x_1,\dots,x_n), \tag{4.4}$$

which is normalized to the factor $N!/(N-n)!$, and where

$$P_n(x_1,\dots,x_n) = \int_{-\infty}^{+\infty}\dots\int_{-\infty}^{+\infty} dx_{n+1}\dots dx_N P_N(x_1,\dots,x_N). \tag{4.5}$$

The n-level correlation function is interpreted as the probability density to find an energy level around each of the positions $\{x_1,\dots,x_n\}$, when the positions of the remaining levels are not observed. The case $n = 1$ gives the generalized level density $R_1(x_1)$; however, when $n > 1$, each function $R_n(x_1,\dots,x_n)$ contains mixed terms, which describe the grouping of n levels into several subgroups or clusters. For this reason, it is useful to define a cumulative n-level correlation function or n-level cluster function given by

$$T_n(x_1,\dots,x_n) = \sum_{m=G}(-1)^{n-m}(m-1)!\prod_{k=1}^{m}R_{G_k}(x_i), \tag{4.6}$$

where i is contained in G_k, and G represents any division of the indices $\{1,\dots,n\}$ in m subgroups $\{G_1,\dots,G_m\}$. That is

$$T_1(x_1) = R_1(x_1), \tag{4.7}$$

$$T_2(x_1,x_2) = -R_2(x_1,x_2) + R_1(x_1)R_1(x_2), \tag{4.8}$$

and so on. Thus, the n-level correlation function (4.4) can be written as

$$R_n(x_1,\ldots,x_n) = \sum_{m=G} (-1)^{n-m} \prod_{k=1}^{m} T_{G_k}(x_i), \tag{4.9}$$

with i contained in G_k.

The cluster functions are the best option for experimental verifications [146]. In such cases, it is required to measure energy in units of mean level spacing D, and the scaled variables $y_i = x_i/D$ can be defined when the limit $N \to \infty$ is taken. These scaled variables conform a statistical model for an infinite series of energy levels whose mean level spacing is unity $D = 1$. Thus, the latter scaling defines the scaled n-level cluster function

$$Y_n(y_1,\ldots,y_n) = \lim_{N\to+\infty} D^n T_n(x_1,\ldots,x_n). \tag{4.10}$$

On the other hand, an n-level form factor can be defined as the Fourier transform of the scaled n-level cluster function

$$b_n(k_1,\ldots,k_n) = \frac{\widetilde{Y}_n(k_1,\ldots,k_n)}{\delta(k_1+\ldots+k_n)}, \tag{4.11}$$

where δ is the Dirac delta function given by Eq. (C.14), and

$$\widetilde{Y}_n(k_1,\ldots,k_n) = \int_{-\infty}^{+\infty} \ldots \int_{-\infty}^{+\infty} dy_1 \ldots dy_n Y_n(y_1,\ldots,y_n) \times \\ \times\, e^{2\pi i \sum_{i=1}^{n} k_i y_i}. \tag{4.12}$$

The term $Y_n(y_1,\ldots,y_n)$ depends only on the differences between the variables y_i, that is, $r_{ii'} = |y_i - y_{i'}|$.

4.1.1 Two-Level Form Factor

The two-level form factor plays an important role, since some properties of the distributions of energy levels, as mean squared values, depend explicitly on it [146]. Furthermore, for quantum

systems which exhibit chaos using the correlation hole as dynamical indicator, the analytical behavior of the correlation hole is governed approximately by the function

$$c_2(t) = 1 - b_2(t), \tag{4.13}$$

where $b_2(t)$ is the two-level form factor of the GOE from RMT.

The two-level form factor is given by the Fourier transform of the scaled two-level cluster function $Y_2(r)$

$$b_2(t) = \int_{-\infty}^{+\infty} dr\, Y_2(r) e^{2\pi i r t}, \tag{4.14}$$

where $r = |y_1 - y_2|$. For the Poisson distribution

$$b_{2,\mathrm{P}}(t) = 0, \tag{4.15}$$

and for the Gaussian ensembles (GOE, GUE, GSE) with $\beta = 1, 2, 4$, it is found (see Appendix G.2 for the GOE)

$$b_{2,1}(t) = \begin{cases} 1 - 2|t| + |t| \ln(2|t| + 1) & \text{if } |t| \leq 1 \\ -1 + |t| \ln\left(\frac{2|t|+1}{2|t|-1}\right) & \text{if } |t| > 1 \end{cases}, \tag{4.16}$$

$$b_{2,2}(t) = \begin{cases} 1 - |t| & \text{if } |t| \leq 1 \\ 0 & \text{if } |t| > 1 \end{cases}, \tag{4.17}$$

$$b_{2,4}(t) = \begin{cases} 1 - \frac{1}{2}|t| + \frac{1}{4}|t| \ln\left(|(|t| - 1)|\right) & \text{if } |t| \leq 2 \\ 0 & \text{if } |t| > 2 \end{cases}. \tag{4.18}$$

In addition, the scaled two-level cluster function $Y_2(r)$ defines the two-level correlation function as

$$R_2(r) = 1 - Y_2(r), \tag{4.19}$$

where $r = |y_1 - y_2|$. For the Poisson distribution the scaled two-level cluster function is given by

$$Y_{2,\mathrm{P}}(r) = 0, \tag{4.20}$$

while for the Gaussian ensembles (GOE, GUE, GSE) with $\beta =$

$1, 2, 4$, is given by the following expressions

$$Y_{2,1}(r) = s^2(r) + \frac{ds(r)}{dr}\int_r^{+\infty} dr' s(r'), \tag{4.21}$$

$$Y_{2,2}(r) = s^2(r), \tag{4.22}$$

$$Y_{2,4}(r) = s^2(2r) - \frac{ds(2r)}{dr}\int_0^{r} dr' s(2r'), \tag{4.23}$$

where $s(r) = \sin(\pi r)/(\pi r)$ is the sinc function.

In Fig. 4.1 is shown the correlation-hole function (4.13) and the two-level correlation function(4.19) for the Gaussian ensembles (GOE, GUE, GSE).

4.2 Survival Probability

Observables of quantum systems which evolve in time are known as dynamical quantities. Some of these quantities can capture signals of quantum chaos and identify the time scales where this happens. A well-known dynamical quantity is the survival probability, first studied in the context of the decay theory of quasistationary states [178]. The survival probability is also known as fidelity or Loschmidt echo [179–185], and has been experimentally verified [186–189], where the time measurement scales are about $\sim 10^{-6}$ s (1 μs, microsecond) [186, 187]. The survival probability is directly related with energy spectra and can be seen as the Fourier transform of these spectra. This feature allows it manifests spectral correlations in its time evolution, and as a result, the correlation hole can be determined.

The survival probability is defined as the probability to find a quantum system in its initial state at a later time. The initial state $|\Psi\rangle = |\Psi(0)\rangle$ can be expanded in terms of the eigenbasis $\{|\phi_n\rangle\}$ with dimension N of a given Hamiltonian $\hat{H}$

$$|\Psi(0)\rangle = \sum_{n=1}^{N} c_n |\phi_n\rangle, \tag{4.24}$$

such that, the eigenvalue equation $\hat{H}|\phi_n\rangle = E_n|\phi_n\rangle$ is satisfied and the coefficients are given by $c_n = \langle\phi_n|\Psi(0)\rangle$. Moreover,

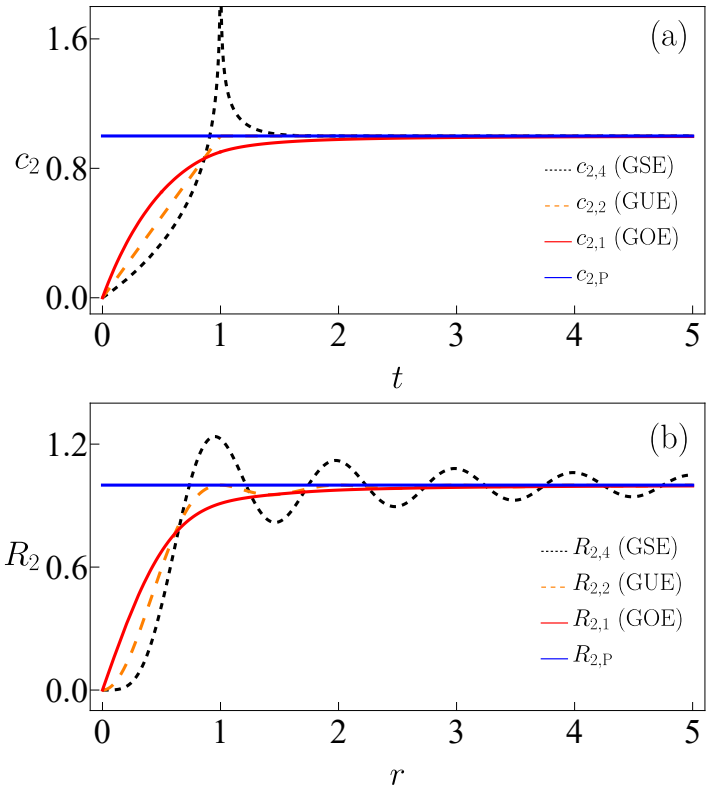

Figure 4.1: Correlation-hole function (4.13) (a) and two-level correlation function (4.19) (b) for the Gaussian ensembles (GOE, GUE, GSE).

the time evolution of the initial state can be found from the expression

$$\begin{aligned} |\Psi(t)\rangle &= \hat{U}(t)|\Psi(0)\rangle \\ &= e^{-i\hat{H}t}|\Psi(0)\rangle, \end{aligned} \tag{4.25}$$

where $\hat{U}(t) = e^{-i\hat{H}t}$ (setting $\hbar = 1$) defines the unitary time evolution operator. Thus, the survival probability can be expressed as

$$\begin{aligned} S_P(t) &= |\langle\Psi(0)|\Psi(t)\rangle|^2 \\ &= |\langle\Psi(0)|e^{-i\hat{H}t}|\Psi(0)\rangle|^2 \\ &= |C_0(t)|^2, \end{aligned} \tag{4.26}$$

where its amplitude is given by

$$\begin{aligned} C_0(t) &= \sum_{n=1}^{N} |c_n|^2 e^{-iE_n t} \\ &= \mathfrak{F}\{\rho_0(E)\} \\ &= \int_{-\infty}^{+\infty} dE\, \rho_0(E) e^{-iEt}, \end{aligned} \tag{4.27}$$

and from them, is recognized the function

$$\rho_0(E) = \sum_{n=1}^{N} |c_n|^2 \delta(E - E_n), \tag{4.28}$$

known as the Local Density of States (LDoS) or strength function, which is the energy distribution weighted by the squared absolute value of the coefficients $|c_n|^2$. The term δ is the Dirac delta function given by Eq. (C.14). Thus, the survival probability is interpreted as the squared norm of the Fourier transform of the LDoS, or in other words, the Fourier transform of a spectral function. The LDoS structure affects the dynamics of the survival probability at different time scales [163, 166, 190, 191], and for that reason, a smoothed version of the LDoS helps to reveal

such effects. A typical procedure consists of defining a smoothed LDoS through a finite time resolution function given by

$$\rho_T(E) = \frac{T}{\pi} \sum_{n=1}^{N} |c_n|^2 \mathrm{sinc}[T(E - E_n)], \tag{4.29}$$

where $\mathrm{sinc}(x) = \sin(x)/x$ is the sinc function and the time resolution $T = \pi/\Delta$ reflects LDoS aspects of order Δ in energy.

An alternative way to write the survival probability is separating the diagonal from the non-diagonal terms, as follows

$$S_P(t) = \sum_{n \neq n'=1}^{N} |c_n|^2 |c_{n'}|^2 e^{-i(E_n - E_{n'})t} + \sum_{n=1}^{N} |c_n|^4, \tag{4.30}$$

where the inverse of the last term, taking $|\Psi\rangle = |\Psi(0)\rangle$, defines the generalized expression

$$P_R = \left(\sum_{n=1}^{N} |\langle \phi_n | \Psi \rangle|^4 \right)^{-1} \in [1, N], \tag{4.31}$$

known as participation ratio. This quantity is a localization measure of an arbitrary quantum state $|\Psi\rangle$ in a given orthonormal basis $\{|\phi_n\rangle\}$ with dimension N, which can be an eigenbasis or any arbitrary orthonormal basis. The term $|\langle \phi_n | \Psi \rangle|^2$ defines the probability to find the arbitrary state $|\Psi\rangle$ in the basis state $|\phi_n\rangle$. The limit value $P_R = 1$ implies that the arbitrary state is identical to a single basis state $|\Psi\rangle = |\phi_n\rangle$ and defines a maximally localized state in the orthonormal basis, while the other one $P_R = N$ implies that the arbitrary state is equally spread in all basis states $|\langle \phi_n | \Psi \rangle| = 1/\sqrt{N}$ and defines a maximally delocalized or spread state in the orthonormal basis.

The survival probability shows characteristic behaviors in its dynamics at different time scales. At very short times $t \ll \sigma_0^{-1}$, is found a universal quadratic behavior [187] given by

$$S_P(t \ll \sigma_0^{-1}) \approx 1 - \sigma_0^2 t^2, \tag{4.32}$$

where σ_0 is the standard deviation of the Hamiltonian $\hat{H}$ under the initial state $|\Psi(0)\rangle$ (see Appendix H.1 for a full derivation of the last expression).

At short times, the survival probability shows an initial decay, which is determined by the LDoS envelope, say $\rho(E)$ [192–194]. Thus, taking the approximation $\rho_0(E) \approx \rho(E)$ in Eq. (4.26), is found

$$S_P^{\mathrm{st}}(t) = |C(t)|^2, \tag{4.33}$$

where the amplitude is given by

$$\begin{aligned} C(t) &= \mathfrak{F}\{\rho(E)\} \\ &= \int_{-\infty}^{+\infty} dE\, \rho(E) e^{-iEt}. \end{aligned} \tag{4.34}$$

After the initial decay, the survival probability can develop a power law decay, which is associated to border effects of the LDoS envelope [190, 191].

At long times, the survival probability saturates to an asymptotic value, given by its infinite time average

$$S_P^{\infty} = \lim_{t\to+\infty} \frac{1}{t} \int_0^t dt' S_P(t'), \tag{4.35}$$

which equals the inverse of the participation ratio, $S_P^{\infty} = P_R^{-1}$, when there are no degeneracies in the energy spectrum.

4.2.1 Correlation Hole

Generally, the correlation hole arises in the time evolution of the survival probability at intermediate times. Its analytical behavior is well described by Eq. (4.13), which incorporates the two-level form factor of the GOE from RMT. The explicit relation between the GOE and the survival probability implies universal behaviors coming from RMT, which will develop from intermediate times to long times in its time evolution. On the other hand, at short times the time evolution shows specific behaviors, since the initial decay depends on the choice of the initial state.

In Appendix H.2 is shown a complete derivation of the survival probability which incorporate the two-level form factor of the GOE, and which is valid in the whole time scale. The explicit

expression is given by

$$\langle S_P(t)\rangle = \frac{1-\left\langle \frac{1}{P_R}\right\rangle}{\eta-1}\left[\eta S_P^{\mathrm{st}}(t) - b_2\left(\frac{Dt}{2\pi}\right)\right] + \left\langle \frac{1}{P_R}\right\rangle, \quad (4.36)$$

where $\langle\bullet\rangle$ defines an ensemble average, η is an effective dimension that depends on the ensemble of initial states, the two-level form factor of the GOE is given by Eq. (4.16) and was renamed as b_2, D is the mean level spacing, the PR and survival probability at short times are given by Eqs. (4.31) and (4.33), respectively.

Chapter 5

Phase Space Representation

In this Chapter is exposed the use of coherent states to create a connection between classical and quantum mechanics, being these the states that minimize the Heisenberg's uncertainty principle. The definitions and properties of the Glauber (field) coherent states and their extension, the Bloch (spin) coherent states, are reviewed. On the other hand, the phase space representation of quantum states is exposed through the quasiprobability distributions based in the overcomplete basis of coherent states. Three main quasiprobability distributions are exposed, the Glauber-Sudarshan, Wigner, and Husimi functions, as well as their representation using characteristic functions.

5.1 Coherent States

The coherent states were first introduced by E. Schrödinger in 1926 [63,195,196] without a defined name, while he was searching solutions that satisfy the Heisenberg's uncertainty principle. In 1963, these states were studied by R. J. Glauber and E. C. G. Sudarshan [196–201], and later popularized by R. J. Glauber as coherent states. Because of this, they are commonly known

as Glauber coherent states or field coherent states, since they are states of the quantum harmonic oscillator whose dynamics resembles the behavior of the classical harmonic oscillator. In this sense, the coherent states were thought as a special kind of quantum states that can create connections between classical and quantum mechanics.

5.1.1 Glauber Coherent States

The Glauber coherent states can be defined as normalized eigenstates of the annihilation operator

$$\hat{a}|\alpha\rangle = \alpha|\alpha\rangle, \tag{5.1}$$

where $\alpha \in \mathbb{C}$ is the coherent state parameter. Thus, the expectation values of the creation-annihilation operators under these coherent states can be easily obtained as

$$\langle\alpha|\hat{a}^\dagger|\alpha\rangle = \alpha^*, \tag{5.2}$$

$$\langle\alpha|\hat{a}|\alpha\rangle = \alpha. \tag{5.3}$$

In addition, these coherent states has an explicit representation in the Fock basis $\{|n\rangle\}$ as

$$|\alpha\rangle = e^{-|\alpha|^2/2} \sum_{n=0}^{\infty} \frac{\alpha^n}{\sqrt{n!}} |n\rangle. \tag{5.4}$$

The last feature suggests that the Glauber coherent states can be considered as generating functions of Fock sates

$$|n\rangle = \frac{1}{\sqrt{n!}} \left. \frac{d^n (e^{|\alpha|^2/2}|\alpha\rangle)}{d\alpha^n} \right|_{\alpha=0}. \tag{5.5}$$

Another way to define the Glauber coherent states is through a displacement operator

$$|\alpha\rangle = \hat{D}(\alpha)|0\rangle, \tag{5.6}$$

where $|0\rangle$ is the vacuum of the field and

$$\hat{D}(\alpha) = e^{\alpha\hat{a}^\dagger - \alpha^*\hat{a}} \tag{5.7}$$

is the displacement operator with $\hat{D}^{-1}(\alpha) = \hat{D}^{\dagger}(\alpha) = \hat{D}(-\alpha)$.

The Glauber coherent states form a basis in the space of Fock states given by the closure relation

$$\frac{1}{\pi}\int\int d^2\alpha|\alpha\rangle\langle\alpha| = \sum_{n=0}^{\infty}|n\rangle\langle n| = \hat{1}, \tag{5.8}$$

where $d^2\alpha = d[\Re(\alpha)]d[\Im(\alpha)]$ and the integration is computed over the complex plane, which is the analogous space of the phase space of the field. In addition, the basis spanned by these coherent states is an overcomplete basis

$$\begin{aligned}|\alpha\rangle &= \frac{1}{\pi}\int\int d^2\alpha'|\alpha'\rangle\langle\alpha'|\alpha\rangle \\ &= \frac{1}{\pi}\int\int d^2\alpha'|\alpha'\rangle e^{-|\alpha'|^2/2-|\alpha|^2/2+(\alpha')^*\alpha}.\end{aligned} \tag{5.9}$$

The Glauber coherent states are normalized states, but they are non-orthogonal, such that, their overlap is a Gaussian function

$$\langle\alpha|\alpha'\rangle = e^{-|\alpha|^2/2-|\alpha'|^2/2+\alpha^*\alpha'}, \tag{5.10}$$

with probability

$$|\langle\alpha|\alpha'\rangle|^2 = e^{-|\alpha-\alpha'|^2}. \tag{5.11}$$

The most important feature of the Glauber coherent states is that they minimize the Heisenberg's uncertainty principle and can be considered as the quantum states most classically available [49]. In Appendix I.1 is shown the demonstration of this property for Glauber coherent states.

5.1.2 Bloch Coherent States

The atomic or spin coherent states are an extension of the Glauber coherent states [196,201–204]. They are commonly known as the Bloch coherent states and can be defined through a rotation operator

$$|\tau\rangle = \hat{\Omega}(\tau)|j,-j\rangle, \tag{5.12}$$

where $\tau \in \mathbb{C}$ is the coherent state parameter, $|j,-j\rangle$ is the extreme eigenstate of the collective pseudo-spin operator $\hat{J}_z$, and

$$\begin{aligned}\hat{\Omega}(\tau) &= e^{-i\theta[\sin(\phi)\hat{J}_x - \cos(\phi)\hat{J}_y]} \\ &= e^{\tau\hat{J}_+ - \tau^*\hat{J}_-}\end{aligned} \tag{5.13}$$

is the rotation operator with $\hat{\Omega}^{-1}(\tau) = \hat{\Omega}^{\dagger}(\tau) = \hat{\Omega}(-\tau)$ and the explicit parameter $\tau = (\theta/2)e^{-i\phi}$. The angular variables (ϕ, θ) are the azimuthal and zenith angles of the spherical coordinates, measuring the θ angle from the negative z axis. The rotation operator takes the form of a displacement operator and using the Baker-Campbell-Hausdorff formula can be written as

$$\hat{\Omega}(z) = e^{z\hat{J}_+} e^{\ln(1+|z|^2)\hat{J}_z} e^{-z^*\hat{J}_-}, \tag{5.14}$$

where the new parameter $z = \tan(\theta/2)\, e^{-i\phi}$ is related with τ through a stereographic projection of the Bloch sphere [203]. In this way, the Bloch coherent state can be written using the new parameter as

$$|z\rangle = \hat{\Omega}(z)|j,-j\rangle. \tag{5.15}$$

The Bloch coherent states can be expressed using the basis of angular momentum states $\{|j,m_z\rangle\}$ (also known as Dicke basis) as

$$|z\rangle = \frac{1}{(1+|z|^2)^j} \sum_{m_z=-j}^{j} \sqrt{\binom{2j}{j+m_z}} z^{j+m_z} |j,m_z\rangle, \tag{5.16}$$

which form an overcomplete basis in the space of Dicke states using a specific normalization condition [202], given by the closure relation

$$\frac{2j+1}{\pi} \int\int d^2z \frac{|z\rangle\langle z|}{(1+|z|^2)^2} = \sum_{m_z=-j}^{j} |j,m_z\rangle\langle j,m_z| = \hat{1}, \tag{5.17}$$

where $d^2z = d[\Re(z)]d[\Im(z)]$.

The Bloch coherent states are normalized states and non-orthogonal

$$\langle z|z'\rangle = \frac{(1+z^*z')^{2j}}{(1+|z|^2)^j(1+|z'|^2)^j}, \tag{5.18}$$

where their overlap has probability

$$|\langle z|z'\rangle|^2 = \left[1 - \frac{|z - z'|^2}{(1 + |z|^2)(1 + |z'|^2)}\right]^{2j}. \tag{5.19}$$

The Bloch coherent states are not eigenstates of the collective pseudo-spin operators and for that reason their expectation values under such coherent states must be developed. In Appendix I.2 is shown the complete derivation of the expectation values of the collective pseudo-spin operators under Bloch coherent states.

5.2 Quasiprobability Distributions

The way to represent an arbitrary mixed quantum state composed of a set of pure states $\{|\Psi_1\rangle, \ldots, |\Psi_N\rangle\}$ (ensemble of states) with dimension N is using the density matrix given by [205]

$$\hat{\rho} = \sum_{n=1}^{N} p_n |\Psi_n\rangle\langle\Psi_n|, \tag{5.20}$$

where the weights p_n represent the probability to find the system in the member $|\Psi_n\rangle$ of the ensemble and satisfy the relation

$$\mathrm{Tr}(\hat{\rho}) = \sum_{n=1}^{N} p_n = 1. \tag{5.21}$$

The density matrix for pure states $|\Psi\rangle$ is given simply by the projector $\hat{\rho} = |\Psi\rangle\langle\Psi|$.

The representation of an arbitrary quantum state in phase space can be achieved through the use of coherent states (states of minimum uncertainty, see Appendix I.1), which can create a connection between classical and quantum mechanics. Early studies that investigated the representation of quantum states in phase space were made by J. R. Klauder in 1963 [206, 207]. Thereby, the common way to represent a quantum state in phase space is through the use of quasiprobability distributions defined

in the overcomplete basis of coherent states [120, 208–214]. As the name indicates, these functions are not probability distributions properly, since some of them can show negative values for certain regions of phase space, which results in nonclassical quantum states [205]. Formally, the properties that a probability distribution must satisfy are [209]:

1. It must be bilinear.
2. It must be real.
3. It must be nonnegative.
4. It must be complete and orthonormal.
5. Its marginal distributions must be satisfied correctly.

5.2.1 Glauber-Sudarshan Function

One of the well-known quasiprobability distributions that allows to represent a quantum state in phase space is the Glauber-Sudarshan function, proposed independently by R. J. Glauber and E. C. G. Sudarshan in 1963 [198, 200]. The explicit representation of the quantum state in phase space is given by

$$\hat{\rho} = \int\int d^2\alpha \, \mathcal{P}(\alpha) |\alpha\rangle\langle\alpha|, \tag{5.22}$$

where

$$\mathcal{P}(\alpha) = \frac{e^{|\alpha|^2}}{\pi^2} \int\int d^2\alpha' e^{|\alpha'|^2} \langle -\alpha'|\hat{\rho}|\alpha'\rangle e^{\alpha(\alpha')^* - \alpha^*\alpha'} \tag{5.23}$$

is the Glauber-Sudarshan function, which can take negative values for some states and satisfies the normalization condition

$$\mathrm{Tr}(\hat{\rho}) = \int\int d^2\alpha \, \mathcal{P}(\alpha) = 1. \tag{5.24}$$

5.2.2 Wigner Function

The first known quasiprobability distribution was the Wigner function, proposed by E. Wigner in 1932 [215]. The standard representation of the Wigner function is expressed in position-momentum coordinates (q, p) of the phase space

$$\mathcal{W}(q,p) = \frac{1}{2\pi\hbar}\int_{-\infty}^{+\infty} dq' \langle (q+q'/2)|\hat{\rho}|(q-q'/2)\rangle e^{ipq'/\hbar}. \quad (5.25)$$

However, it can be defined from the Glauber-Sudarshan function $\mathcal{P}(\alpha)$ in the following way

$$\mathcal{W}(\alpha) = \frac{2}{\pi}\int\int d^2\alpha' \mathcal{P}(\alpha') e^{-2|\alpha-\alpha'|^2}. \quad (5.26)$$

Moreover, the Wigner function satisfies the normalization condition

$$\mathrm{Tr}(\hat{\rho}) = \int\int d^2\alpha\, \mathcal{W}(\alpha) = 1, \quad (5.27)$$

and can take negative values for some states. As a particular case, in Appendix J.1 is shown the Wigner function for Glauber and Bloch coherent states.

5.2.3 Husimi Function

Other well-known quasiprobability distribution is the Husimi function, proposed by K. Husimi in 1940 [216]. This function can be defined as the expectation value of a quantum state under coherent states

$$\begin{aligned}\mathcal{Q}(\alpha) &= \frac{1}{\pi}\langle\alpha|\hat{\rho}|\alpha\rangle \\ &= \frac{1}{\pi}\int\int d^2\alpha' \mathcal{P}(\alpha') e^{-|\alpha-\alpha'|^2} \\ &= \frac{2}{\pi}\int\int d^2\alpha' \mathcal{W}(\alpha') e^{-2|\alpha-\alpha'|^2}, \end{aligned} \quad (5.28)$$

and can be further defined from the Glauber-Sudarshan $\mathcal{P}(\alpha)$ and Wigner $\mathcal{W}(\alpha)$ function, respectively. The Husimi function

satisfies the normalization condition

$$\mathrm{Tr}(\hat{\rho}) = \int\int d^2\alpha\, \mathcal{Q}(\alpha) = 1. \tag{5.29}$$

The singularity of the Husimi function is that never takes negative values, which makes it a better candidate to be considered as a probability distribution. Nevertheless, their marginal distributions are not satisfied correctly, which is one of the necessary properties to be considered as a probability distribution. As a particular case, in Appendix J.2 is shown the Husimi function for Glauber and Bloch coherent states.

5.2.4 Characteristic Functions

A useful way to represent the quasiprobability distributions is using the concept of characteristic functions. Given a probability distribution $P(\alpha) \geq 0$ which satisfies the relations

$$\int d\alpha\, P(\alpha) = 1, \tag{5.30}$$

$$\int d\alpha\, \alpha^k P(\alpha) = \langle \alpha^k \rangle, \tag{5.31}$$

a characteristic function can be defined as the Fourier transform of the given probability distribution [205]

$$\begin{aligned} C(\alpha) &= \mathfrak{F}\{P(\alpha')\} \\ &= \int d\alpha' P(\alpha') e^{i\alpha\alpha'} \\ &= \langle e^{i\alpha\alpha'} \rangle \\ &= \sum_{k=0}^{\infty} \frac{(i\alpha)^k}{k!} \langle (\alpha')^k \rangle. \end{aligned} \tag{5.32}$$

If all the moments $\langle (\alpha')^k \rangle$ are known the characteristic function is completely determined. From Eq. (5.32) is clearly seen that the probability distribution is given by the inverse Fourier transform

of the characteristic function

$$\begin{aligned} P(\alpha) &= \mathfrak{F}^{-1}\{C(\alpha')\} \\ &= \frac{1}{2\pi}\int d\alpha' C(\alpha') e^{-i\alpha\alpha'}. \end{aligned} \tag{5.33}$$

On the other hand, given a characteristic function the moments can be found using the expression

$$\langle (\alpha')^k \rangle = \frac{1}{i^k}\left.\frac{d^k C(\alpha)}{d\alpha^k}\right|_{\alpha=0}. \tag{5.34}$$

For the three exposed quasiprobability distributions a characteristic function can be defined based in the order of creation-annihilation operators as normal order (Glauber-Sudarshan function), symmetric order (Wigner function), and antinormal order (Husimi function) [205]. The explicit expressions are given by

$$\begin{aligned} C_{\mathcal{P}}(\alpha) &= \mathrm{Tr}(\hat{\rho} e^{\alpha\hat{a}^\dagger} e^{-\alpha^*\hat{a}}) \\ &= \int\int d^2\alpha' \mathcal{P}(\alpha') \langle \alpha' | e^{\alpha\hat{a}^\dagger} e^{-\alpha^*\hat{a}} | \alpha' \rangle \\ &= \int\int d^2\alpha' \mathcal{P}(\alpha') e^{\alpha(\alpha')^* - \alpha^*\alpha'}, \end{aligned} \tag{5.35}$$

$$\begin{aligned} C_{\mathcal{W}}(\alpha) &= \mathrm{Tr}(\hat{\rho} e^{\alpha\hat{a}^\dagger - \alpha^*\hat{a}}) \\ &= \frac{1}{\pi}\int\int d^2\alpha' \langle \alpha' | \hat{\rho} e^{\alpha\hat{a}^\dagger - \alpha^*\hat{a}} | \alpha' \rangle \\ &= \int\int d^2\alpha' \mathcal{W}(\alpha') e^{\alpha(\alpha')^* - \alpha^*\alpha'}, \end{aligned} \tag{5.36}$$

$$\begin{aligned} C_{\mathcal{Q}}(\alpha) &= \mathrm{Tr}(\hat{\rho} e^{-\alpha^*\hat{a}} e^{\alpha\hat{a}^\dagger}) \\ &= \frac{1}{\pi}\int\int d^2\alpha' \langle \alpha' | e^{\alpha\hat{a}^\dagger} \hat{\rho} e^{-\alpha^*\hat{a}} | \alpha' \rangle \\ &= \int\int d^2\alpha' \mathcal{Q}(\alpha') e^{\alpha(\alpha')^* - \alpha^*\alpha'}. \end{aligned} \tag{5.37}$$

Moreover, using the Baker-Campbell-Hausdorff formula all the characteristic functions can be related through the expression

$$C_{\mathcal{P}}(\alpha) = C_{\mathcal{W}}(\alpha) e^{|\alpha|^2/2} = C_{\mathcal{Q}}(\alpha) e^{|\alpha|^2}. \tag{5.38}$$

Now, as was exposed initially, the probability distribution can be found as the inverse Fourier transform of the given characteristic function. For the considered characteristic functions the corresponding quasiprobability distributions are found as follows

$$\mathcal{P}(\alpha) = \frac{1}{\pi^2} \int \int d^2\alpha' C_{\mathcal{P}}(\alpha') e^{\alpha(\alpha')^* - \alpha^*\alpha'}, \tag{5.39}$$

$$\mathcal{W}(\alpha) = \frac{1}{\pi^2} \int \int d^2\alpha' C_{\mathcal{W}}(\alpha') e^{\alpha(\alpha')^* - \alpha^*\alpha'}, \tag{5.40}$$

$$\mathcal{Q}(\alpha) = \frac{1}{\pi^2} \int \int d^2\alpha' C_{\mathcal{Q}}(\alpha') e^{\alpha(\alpha')^* - \alpha^*\alpha'}. \tag{5.41}$$

Part II

Chaos in the Dicke Model

Chapter 6

Signs of Classical and Quantum Chaos

In this Chapter is exposed a complete revision of results on classical and quantum chaos previously found in the Dicke model. Furthermore, results obtained with the correlation hole as unconventional dynamical indicator of quantum chaos in the Dicke model are presented. Particularly, results on the correlation hole detected in the time evolution of the survival probability taking random states as initial states are shown, as well as a revision on time scales derived from the quantum dynamics.

6.1 Previously Found Results of Classical and Quantum Chaos

The Dicke model shows chaotic behavior in both classical and quantum counterparts. On the one hand, for the classical model have been applied the qualitative and quantitative conventional tests, that is, the study of Poincaré sections and Lyapunov exponents of the classical trajectories. The computation of the Lyapunov exponent for a set of trajectories in phase space allows to generate a map of percentage of chaos as a function of

the classical energy shell and the Hamiltonian parameters, which can serve as a guide to study the quantum model in the parameter region where classical chaos is sure to be found. The main idea is to choose a set of initial conditions in phase space for a given classical energy shell and fixed Hamiltonian parameters. These initial conditions are evolved in time and later are selected those with Lyapunov exponent different from zero. The fraction of chaotic trajectories to the total number of initial trajectories gives a chaos percentage value. This procedure is computed for different values of energy shells and Hamiltonian parameters. The result is a map of percentage of chaos in the parameter space of the classical Dicke model.

On the other hand, for the quantum model have been applied the conventional tests of energy spectrum fluctuations, that is, the NNS distribution and its verification via the Anderson-Darling parameter. The Anderson-Darling parameter quantifies the deviation degree of a data set from a given probability distribution [217]. Furthermore, another less popular test known as the Peres lattice has been applied to the Dicke model. A Peres lattice represents the expectation value of a given operator under the eigenstates of a quantum system and can be interpreted as the quantum analog of a Poincaré section, in the sense that the loss of integrability of the quantum system is captured by it visually [218]. Additionally, recent studies with other quantum indicators have been applied in the same way to the model. In particular, the study of the correlation hole as a dynamical indicator of chaos in the time evolution of the survival probability and the study of the OTOC considered recently as the quantum analog of the Lyapunov exponent.

A series of studies performed in the Dicke model with the previous described classical and quantum indicators are shown in detail in Refs. [3–13]. In Fig. 6.1 are shown some of these classical and quantum indicators confirming the chaotic behavior of the Dicke model.

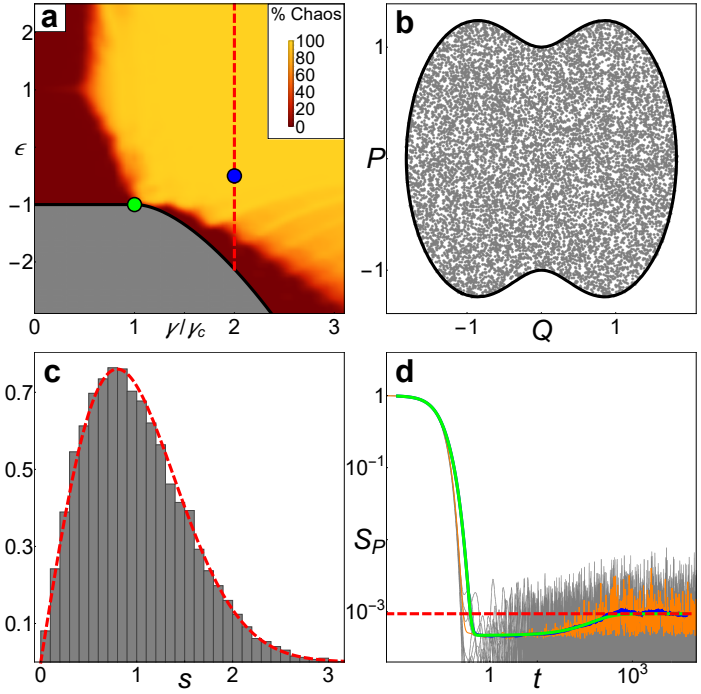

Figure 6.1: **Panel a:** Map of percentage of chaos as a function of the classical energy shell ϵ and the scaled coupling-strength parameter γ/γ_c. **Panel b:** Poincaré section in atomic plane $Q-P$ ($p=0$) for a chaotic classical energy shell. **Panel c:** NNS distribution (gray bars) for 22458 energy levels contained in the energy interval $\epsilon_k \in [-1, 1.755]$ and Wigner-Dyson surmise (3.17) (red dashed line). **Panel d:** Survival probability (4.26) (gray solid curves) for an ensemble of 500 initial random states centered at $E_c = j\epsilon$, its ensemble average (orange solid curve), its time average (blue solid curve), and analytical survival probability (4.36) (green solid curve), where the correlation hole is detected. Classical energy shell: $\epsilon = -0.5$ (chaotic). Hamiltonian parameters: $\omega = \omega_0 = 1$, $\gamma = 2\gamma_c = 1$. The system size for panels c and d is $j = 100$. Figure taken from the supplementary information of Ref. [15].

6.2 Correlation Hole

The chaotic behavior of the Dicke model is well known for certain parameter regions of the Hamiltonian [3]. As different indicators confirm this phenomenon in both classical and quantum realms, an initial goal in this Thesis was to study the unconventional dynamical indicators of quantum chaos. In particular, the first objective was to detect the correlation hole in the time evolution of the survival probability for some kind of initial states. Since the survival probability is defined around an arbitrary quantum state, some initial states are able to detect spectral correlations better than some others. The latter gives some freedom in choosing the initial states.

6.2.1 Random States as Initial States

A special quantum state is a state randomly constructed, that is, the components of its wave function are randomly sampled in an interval of the energy spectrum. Particularly, these random states are able to detect spectral correlations between the energy levels contained in the selected energy interval. In Appendix K.1 is presented the construction method for this kind of states. An advantage of the latter method is that the LDoS envelope associated to the random state can be arbitrarily imposed, that is, explicit mathematical functions can be chosen as LDoS envelopes.

As a case study, three known mathematical functions were selected as LDoS envelopes, a rectangular, bounded Gaussian, and Gaussian function, respectively [12]

$$\rho_{\mathrm{R}}(E) = \begin{cases} \frac{1}{2\sigma_{\mathrm{R}}} & \text{if } E_{\mathrm{c}} - \sigma_{\mathrm{R}} \leq E \leq E_{\mathrm{c}} + \sigma_{\mathrm{R}} \\ 0 & \text{otherwise} \end{cases}, \tag{6.1}$$

$$\rho_{\mathrm{BG}}(E) = \begin{cases} \frac{e^{-(E-E_{\mathrm{c}})^2/(2\sigma_{\mathrm{BG}}^2)}}{\mathcal{C}\sqrt{2\pi}\sigma_{\mathrm{BG}}} & \text{if } E_{\min} \leq E \leq E_{\max} \\ 0 & \text{otherwise} \end{cases}, \tag{6.2}$$

$$\rho_{\mathrm{G}}(E) = \frac{e^{-(E-E_{\mathrm{c}})^2/(2\sigma_{\mathrm{G}}^2)}}{\sqrt{2\pi}\sigma_{\mathrm{G}}}, \tag{6.3}$$

where

$$\mathcal{C} = \frac{1}{2}\left[\mathrm{erf}\left(\frac{E_c - E_{\min}}{\sqrt{2}\sigma_{BG}}\right) - \mathrm{erf}\left(\frac{E_c - E_{\max}}{\sqrt{2}\sigma_{BG}}\right)\right], \tag{6.4}$$

and

$$\mathrm{erf}(z) = \frac{2}{\sqrt{\pi}}\int_0^z dx\, e^{-x^2} \tag{6.5}$$

is the error function. Thus, an ensemble of initial random states was constructed generating their coefficients c_k from a real number uniform distribution through the weights $r_k \in [0,1]$, whose moments are given by $\langle r_k^n \rangle = (n+1)^{-1}$. In Fig. 6.2 is shown the average LDoS envelope for this ensemble of initial random states considering the three later LDoS envelope cases for a chaotic energy regime.

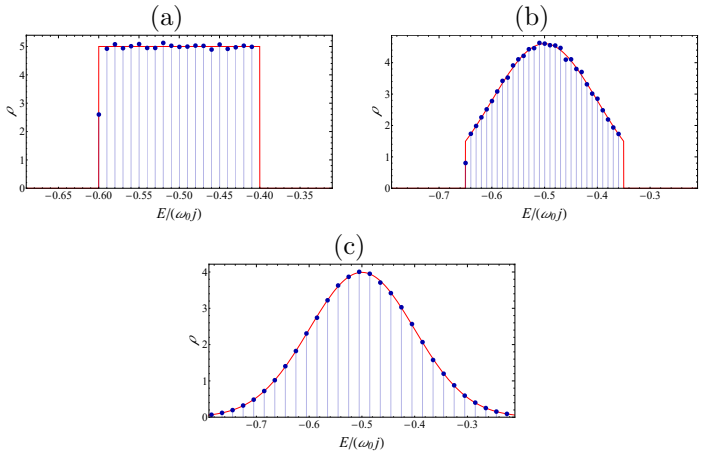

Figure 6.2: Average LDoS envelope (blue dots) for an ensemble of 500 initial random states and analytical LDoS envelopes (6.1)-(6.3) (red solid curves) for each LDoS envelope case: rectangular (a), bounded Gaussian (b), and Gaussian (c). Classical energy shell: $\epsilon = -0.5$ (chaotic). Parameters: $E_c = j\epsilon$, $\sigma_R = \sigma_{BG} = \sigma_G = 0.1j$, $E_{\min,\max} = E_c \mp 1.5\sigma_{BG}$. Hamiltonian parameters: $\omega = \omega_0 = 1$, $\gamma = 2\gamma_c = 1$. The system size is $j = 100$. Figure taken from Ref. [12].

The Fourier transform of the analytical LDoS envelope describes the behavior of the survival probability at short times (see

Eq. (4.33)). For the three later LDoS envelope cases is found [12]

$$\begin{aligned} S^{\mathrm{st}}_{P,\mathrm{R}}(t) &= |\mathfrak{F}\{\rho_{\mathrm{R}}(E)\}|^2 \\ &= \frac{\sin^2(\sigma_{\mathrm{R}} t)}{\sigma_{\mathrm{R}}^2 t^2}, \end{aligned} \tag{6.6}$$

$$\begin{aligned} S^{\mathrm{st}}_{P,\mathrm{BG}}(t) &= |\mathfrak{F}\{\rho_{\mathrm{BG}}(E)\}|^2 \\ &= \frac{e^{-\sigma_{\mathrm{BG}}^2 t^2}}{4\mathcal{C}^2}\mathcal{F}(t), \end{aligned} \tag{6.7}$$

$$\begin{aligned} S^{\mathrm{st}}_{P,\mathrm{G}}(t) &= |\mathfrak{F}\{\rho_{\mathrm{G}}(E)\}|^2 \\ &= e^{-\sigma_{\mathrm{G}}^2 t^2}, \end{aligned} \tag{6.8}$$

where

$$\mathcal{F}(t) = \left| \mathrm{erf}\left[\frac{1}{\sqrt{2}\sigma_{\mathrm{BG}}} f_{E_{\min}}(t)\right] - \mathrm{erf}\left[\frac{1}{\sqrt{2}\sigma_{\mathrm{BG}}} f_{E_{\max}}(t)\right] \right|^2, \tag{6.9}$$

and $f_E(t) = E_{\mathrm{c}} - E - i\sigma_{\mathrm{BG}}^2 t$. Nevertheless, to study the survival probability completely an analysis at long times is needed. In this way, for each element of the corresponding ensemble the survival probability can be constructed numerically using Eq. (4.26), and it can be compared with the analytical expression (4.36) using the relations $\eta = (4/3)\langle P_R^{-1}\rangle^{-1}$, $D \approx \nu_{\mathrm{c}}^{-1}$, and $\nu_{\mathrm{c}} = \nu(E_{\mathrm{c}})/2$. In Appendix K.2 is shown the derivation of the ensemble effective dimension η.

In Fig. 6.3 is shown the comparison between the numerical survival probability (4.26) and the analytical expression (4.36) for the three LDoS envelope cases. As can be seen, the analytical expression is able to describe accurately the numerical survival probability at all times for the three cases. At short times, for the rectangular and bounded Gaussian LDoS envelope cases arises a power-law decay related with border effects (discontinuities at the ends) in the LDoS envelope. At intermediate times, the correlation hole is detected for the three cases, which confirms the presence of spectral correlations between the energy levels contained within the chosen intervals of the energy spectrum. At long times, the saturation of the system fluctuates indefinitely around its asymptotic value. Also, in the same Fig. 6.3 is shown

a time average for both numerical and analytical survival probabilities for the three LDoS envelope cases. The utility of the latter time average is that it can erase remaining strong fluctuations present in the dynamics obtaining smoothed curves, which show the agreement between curves more clearly.

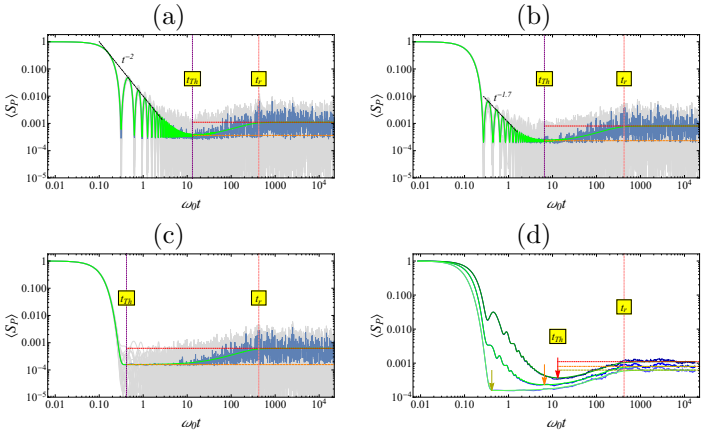

Figure 6.3: **Panels (a)-(c):** Survival probability (4.26) (gray solid curves) numerically constructed for each element of an ensemble of 500 initial random states, ensemble average (blue solid curve) over the latter 500 initial random states, and analytical survival probability (4.36) (green solid curve) for each LDoS envelope case: rectangular (a), bounded Gaussian (b), and Gaussian (c). The horizontal lines represent the asymptotic value (red dotted line) and the minimum value (orange dashed line) of the survival probability, respectively. The vertical lines represent the Thouless time (purple dotted line) and the relaxation time (pink dashed line), respectively. The black dotted-dashed lines represent the power-law decay for the bounded cases (a) and (b). **Panel (d):** Time average over the ensemble average (blue solid curve) and analytical (green solid curve) survival probabilities for each LDoS envelope case (a)-(c). The time average was generated taking time intervals that grow according to an exponential rule. Hamiltonian parameters: $\omega = \omega_0 = 1$, $\gamma = 2\gamma_c = 1$. The system size is $j = 100$. Figure taken from Ref. [12].

6.2.2 Time Scales

Time scales of some time-evolved observables provide information about the regimes where occur changes in the dynamics of quantum systems. Thus, the time scale where the correspondence between the classical and quantum dynamics breaks down is known as the Ehrenfest time, say t_{E}. The latter name arises because, according to the Ehrenfest theorem [219], the time evolution of a quantum wave packet at short times is well described by classical equations of motion [220–222]. For systems with chaotic dynamics it has been found that the Ehrenfest time is given by $t_{\mathrm{E}} \propto (1/\lambda)\ln(S/\hbar)$, where λ is the classical Lyapunov exponent given by Eq. (3.6) and S is a characteristic action [223,224]. Another time scale due to dynamical localization, where the quantum diffusion ends and the classical and quantum dynamics are equivalent, has an explicit relation with the Ehrenfest time given by $t_{\mathrm{d}} \propto \hbar^{-2} > t_{\mathrm{E}}$ [221,222]. On the other hand, the time scale where the quantum fluctuations remain in the dynamics around an asymptotic value is known as the Heisenberg time, say t_{H}. The Ehrenfest and Heisenberg times are the most popular time scales studied in time-evolved observables, however, the are others less popular time scales which determine specific dynamical behaviors in some systems.

Particularly, two time scales have been found in the time evolution of the survival probability. The first time scale is the Thouless time, say t_{Th}, which is the time where the survival probability attains its minimum value and defines the depth of the correlation hole [166]. Before this time, the behavior of the survival probability is governed by the selected initial state, that is, it is a specific behavior. After this time, the behavior of the survival probability is universal, that is, generalized behaviors independent of the initial state govern the dynamics until the system saturation. The second time scale is known as the relaxation time, say t_{r}, which is just the time where the system saturates fluctuating indefinitely around its asymptotic value [166]. In Ref. [12] is shown a complete derivation of the Thouless and relaxation times for the survival probability of random states in the Dicke model, where was found that both time scales are di-

rectly proportional to the system size. The later time scales are shown in Fig. 6.3 for the three LDoS envelope cases previously exposed.

6.3 Conclusions of Chapter 5

The detection of the correlation hole in the time evolution of the survival probability was successfully achieved for initial random states located in a chaotic energy regime. The spectral correlations related with the correlation hole are associated with the GOE, since the two-level form factor that reproduces the behavior of the correlation hole was derived from such ensemble. In this way, the detection of the correlation hole in the time evolution of the survival probability confirms its validity as a dynamical indicator of quantum chaos in the Dicke model.

On the other hand, it was found that, at short times, the time evolution of the survival probability is governed by the selection of the initial state showing particular behaviors. On the other hand, at long times, the dynamics is governed by universal behaviors, where the spectral GOE correlations manifest themselves until saturation. Two time scales were identified in the time evolution of the survival probability, the Thouless time that defines the depth of the correlation hole, and the relaxation time where the dynamics saturates. It was found that both time scales are directly proportional to the system size.

The results exposed in this Chapter are shown in more detail in Ref. [12].

Chapter 7

Classical and Quantum Dynamic Effects

In this Chapter is exposed a comparison between the classical and quantum dynamics of coherent states in the Dicke model. Results on the classical-quantum correspondence for these coherent states are shown, which determine dynamical effects of purely quantum nature that can be associated with chaos or scarring. The classical dynamics is generated defining the classical limit of the survival probability. The method to generate this classical limit is shown, as well as the criterion to select initial coherent states.

7.1 Coherent States as Initial States

Glauber-Bloch coherent states have been previously studied in the Dicke model [9, 10]. They allow to obtain the classical limit of the Dicke model and are considered as the most classically accessible quantum states. Since these states can create a link between the classical and quantum realms, they are good candi-

dates to further explore the quantum-classical correspondence in the Dicke model. In this way, a second goal in this Thesis was to compare the classical and quantum dynamics of Glauber-Bloch coherent states identifying generic behaviors in each counterpart, as those who only appear in the quantum domain and can be caused by chaotic behavior.

7.1.1 Classical Limit of the Survival Probability for Coherent States

The classical limit of the survival probability can be obtained by employing a method known as the Truncated Wigner Approximation (TWA) [225–229]. This method takes into account the time evolution of the Wigner function and can establish a link between both classical and quantum realms. In Appendix L is shown the complete derivation of the classical limit of the survival probability, which can be defined as follows [14]

$$\mathfrak{S}_P(t) = \left(\frac{2\pi}{j}\right)^2 \int_{\mathcal{M}} d\mathbf{x}\, \mathcal{W}_\Psi(\mathbf{x}) \mathcal{W}_\Psi[\varphi^{-t}(\mathbf{x})], \tag{7.1}$$

where $\mathcal{W}_\Psi(\mathbf{x})$ is the Wigner function of an arbitrary state $|\Psi\rangle$ defined in the overcomplete basis of Glauber-Bloch coherent states $\{|\mathbf{x}\rangle\}$. The Wigner function defined in the latter basis is the product of the Wigner functions of the same state associated to each Glauber $\{|\alpha\rangle\}$ and Bloch $\{|z\rangle\}$ coherent state basis

$$\begin{aligned} \mathcal{W}_\Psi(\mathbf{x}) &= \mathcal{W}_\Psi(\alpha)\mathcal{W}_\Psi(z) \\ &= \mathcal{W}_\Psi(q,p)\mathcal{W}_\Psi(Q,P), \end{aligned} \tag{7.2}$$

where $\mathbf{x} = (q, p; Q, P)$ are the coordinates of the four-dimensional phase space $\mathcal{M}$ of the Dicke model.

The asymptotic value of the classical limit of the survival probability $\mathfrak{S}_P^\infty$ can be obtained with Eq. (4.35), analogously to the quantum case. For initial Glauber-Bloch coherent states $|\Psi\rangle = |\mathbf{x}_0\rangle$ the explicit Wigner function is given by Eq. (J.5).

7.1.2 Selection Criterion of Coherent States

Glauber-Bloch coherent states were selected as initial states to study their survival probability as in the case of random states. The selection criterion was based initially in Poincaré sections of the classical trajectories to identify visually regular regions from chaotic ones. The Poincaré sections have a correspondence with the participation ratio of coherent states, since a map of participation ratio can be generated for a set of initial coherent states located in phase space. On the one hand, for regular energy shells (low energy surfaces) the states located far from a separatrix have a correspondence with low participation ratio, while the states located near a separatrix have a correspondence with high participation ratio. On the other hand, for chaotic energy shells (high energy surfaces) all trajectories fill densely the phase space. For that reason, the map of participation ratio is a useful tool in the selection of coherent states located in the chaotic energy regime, since it shows specific structures which are missing in the Poincaré section [14].

Thus, as a case study based in the last criterion were selected initial Glauber-Bloch coherent states in both regular and chaotic energy regimes. Specifically, two coherent states were selected in the regular energy regime, one located far from a separatrix (stable center) (identified as state I) and another one located close to a separatrix (identified as state II). For the chaotic energy regime were selected also two coherent states based in their participation ratio, one with low participation ratio (identified as state III) and another one with high participation ratio (identified as state IV). The Glauber-Bloch coherent states can be expanded in the energy eigenbasis of the Dicke Hamiltonian having an explicit representation (see Appendix M for a complete description of this representation using the coherent basis), and for that reason, their LDoS is completely determined showing approximately a Gaussian LDoS envelope for all energy regimes and sets of coordinates in phase space (see Eq. (6.3)). The last feature of the LDoS envelope determines the survival probability at short times, which is also a Gaussian function (see Eq. (6.8)). The explicit parameters for the initial

coherent states in phase space are given by the initial conditions $\mathbf{x}_0 = (q_+(\epsilon_{\mathrm{R,C}}), 0; Q_0, P_0)$, where q_+ is the positive root of the second-degree equation $h_{\mathrm{D}}(\mathbf{x}) - \epsilon_{\mathrm{R,C}} = 0$, and $\epsilon_{\mathrm{R,C}}$ identifies the classical energy shell of each regular and chaotic regime, respectively. In Fig. 7.1 are shown the Poincaré section and the map of participation ratio for both regular and chaotic energy regimes, as well as the initial coherent states selected in each case.

Coherent States Located Far and Close to a Separatrix

The initial step for study the selected initial coherent states located in the regular energy regime was to know their LDoS. As the LDoS structure affects the dynamics of the survival probability at different time scales, the smoothed LDoS (4.29) was considered for study these coherent states. In Fig. 7.2 is shown the smoothed LDoS at finite time resolution for states I and II, as well as the LDoS at infinite time resolution. As can be seen, both states I and II show a Gaussian LDoS envelope clearly defined at finite time resolution. At infinite time resolution, state I has only few energy components well described by a Gaussian LDoS envelope, while state II has more energy components and shows a contribution of multiple Gaussian LDoS envelopes.

The survival probability and its classical limit can be numerically constructed for states I and II using Eqs. (4.26) and (7.1), respectively. For the regular energy regime there is an explicit analytical expression of the survival probability, which is able to reproduce its behavior at all times and is given by (the complete derivation of the following expression is shown in Ref. [10])

$$S_P(t) \approx \frac{\omega_1}{2\sigma_0\sqrt{\pi}}\Theta_3[x(t), y(t)], \tag{7.3}$$

where

$$\Theta_3(x, y) = 1 + 2\sum_n y^{n^2}\cos(2nx) \tag{7.4}$$

is the Jacobi theta function with arguments

$$x(t) = \frac{\omega_1 t}{2}, \tag{7.5}$$

$$y(t) = e^{-(1/4)(\omega_1/\sigma_0)^2 - (t/t_{\mathrm{D}})^2}, \tag{7.6}$$

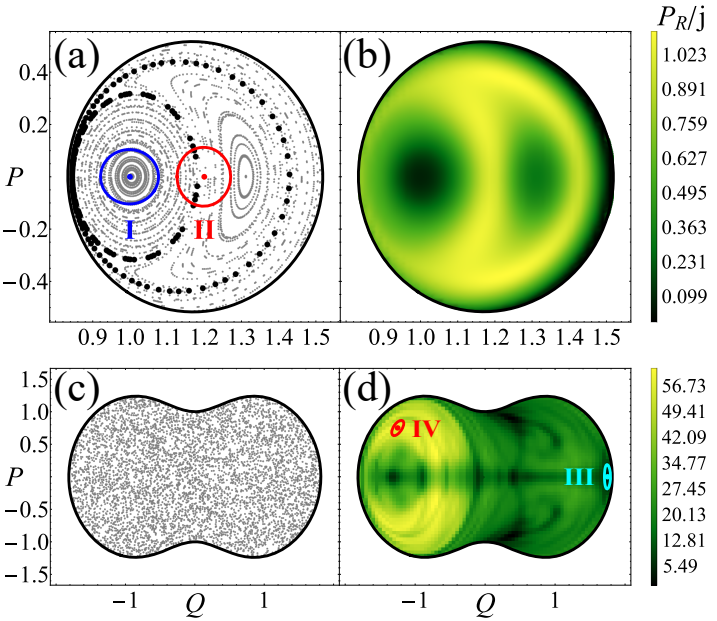

Figure 7.1: **Panels (a) and (c):** Poincaré section for regular (a) and chaotic (c) energy regimes. The black dots in panel (a) represent a separatrix. **Panels (b) and (d):** Map of participation ratio of coherent states for the same regular (b) and chaotic (d) energy regimes. In panel (a) are shown the selected initial coherent states for the regular energy regime: state I far from a separatrix (stable center, blue dot) and state II close to a separatrix (red dot). In panel (d) are shown the selected initial coherent states for the chaotic energy regime: state III (low participation ratio, $P_R = 1066$, cyan dot) and state IV (high participation ratio, $P_R = 5743$, red dot). Classical energy shells: $\epsilon_{\mathrm{R}} = -1.8$ (regular) and $\epsilon_{\mathrm{C}} = -0.5$ (chaotic). Initial conditions: $(Q_0, P_0) = (1, 0)$ (state I), $(Q_0, P_0) = (1.2, 0)$ (state II), $(Q_0, P_0) = (1.75, 0)$ (state III), $(Q_0, P_0) = (-1.25, 0.75)$ (state IV). Hamiltonian parameters: $\omega = \omega_0 = 1$, $\gamma = 2\gamma_c = 1$. The system size for panels (b) and (d) is $j = 100$. Figure taken from Ref. [14].

and n is the index that determines the distance between two adjacent energies $\omega_k^{(n)} = E_{k+n} - E_k$. Moreover, $t_{\rm D} = \omega_1/(\sigma_0|e_2|)$ is a decay time, $\omega_1 \approx E_{k_{\rm max}+1} - E_{k_{\rm max}}$ is the fundamental frequency restricted to the energy interval $(E_{k_{\rm max}} < E_0 < E_{k_{\rm max}+1})$, and $e_2 = \frac{1}{2}(E_{k_{\rm max}+1} + E_{k_{\rm max}-1}) - E_{k_{\rm max}}$ is known as the anharmonicity, which measures the deviation of an energy spectrum whose energies are equally spaced [10]. The energy center E_0 and energy width σ_0 come from a Gaussian approximation to the coefficient distribution

$$|c_k|^2 \approx \frac{\Delta E_1}{\sqrt{2\pi}\sigma_0} e^{-(E_k - E_0)^2/(2\sigma_0^2)}, \tag{7.7}$$

where $\Delta E_1 = \langle E_{k+1} - E_k \rangle$ is the mean spacing between the energies that conform the Gaussian function.

In Figs. 7.3 and 7.4 are shown the survival probability (4.26) and its classical limit (7.1) for both initial states I and II, respectively. The comparison between the numerical survival probability (4.26) and the analytical expression (7.3) is shown for state I only. For state II is shown a time average for the survival probability and its classical limit. On the other hand, in the same Figs. 7.3 and 7.4 is shown the time evolved Wigner function projected in the atomic $Q-P$ and bosonic $q-p$ planes for both states I and II, respectively. The time evolution of the Wigner function in phase space can help in understanding some features of the classical survival probability. As can be seen, for state I there is a complete agreement between the numerical survival probability and the analytical expression until a decay time, where the quantum fluctuations remain in the dynamics and the analytical expression is unable to reproduce them. Additionally, periodic revivals arise for state I related with a regular dynamics. At short times, the validity of the TWA is clearly seen for both states I and II, since the survival probability and its classical limit match each other. The values near to zero of the survival probability and its classical limit can be explained with the time evolved Wigner function. The Wigner function is localized in an initial region of phase space, when this function evolves there is a time interval where the distribution never crosses the initial region where was localized. The latter implies that the classical

survival probability is identically zero. Moreover, the correlation hole is not detected at intermediate times implying that the energy levels are uncorrelated as is expected for the regular energy regime.

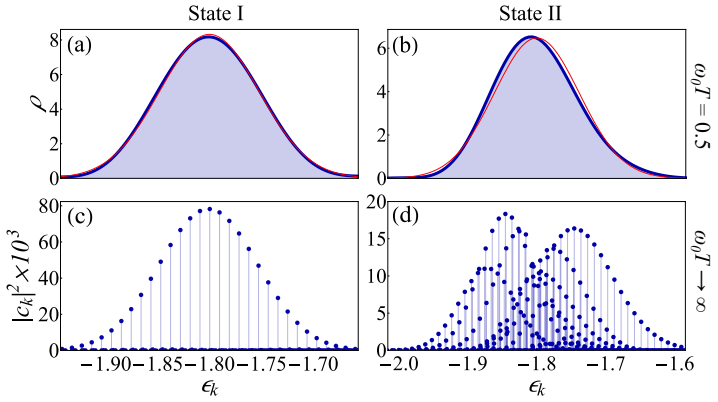

Figure 7.2: **Panels (a)-(b):** Smoothed LDoS (4.29) (blue solid curve) of states I (a) and II (b) at finite time resolution, and Gaussian LDoS envelope (6.3) (red thin curve) for the regular energy regime. **Panels (c)-(d):** LDoS (blue dots) of the same states I (c) and II (d) at infinite time resolution. The states I and II are shown in Fig. 7.1 (a). Classical energy shell: $\epsilon_{\mathrm{R}} = -1.8$ (regular). Parameters: $E_{\mathrm{c}} = j\epsilon_{\mathrm{R}}$, $\sigma_{\mathrm{G}} = 0.048j$ (state I), $\sigma_{\mathrm{G}} = 0.062j$ (state II). Hamiltonian parameters: $\omega = \omega_0 = 1$, $\gamma = 2\gamma_{\mathrm{c}} = 1$. The system size is $j = 100$. Figure taken from Ref. [14].

Coherent States with Low and High Participation Ratio

For coherent states located in the chaotic energy regime with high participation ratio, it was found that the correct ensemble of random states which can reproduce the behavior of their survival probability until saturation is an ensemble of initial random states whose weights r_k are generated within an exponential distribution $P(r_k) = \upsilon e^{-\upsilon r_k}$ and whose moments are given by $\langle r_k^n \rangle = n!/\upsilon^n$. The wave function of the coherent states in the energy eigenbasis of the Dicke Hamiltonian has a defined shape, that is, the sampling of the coefficients occurs in a structured way. In this way, the main finding is that random states whose

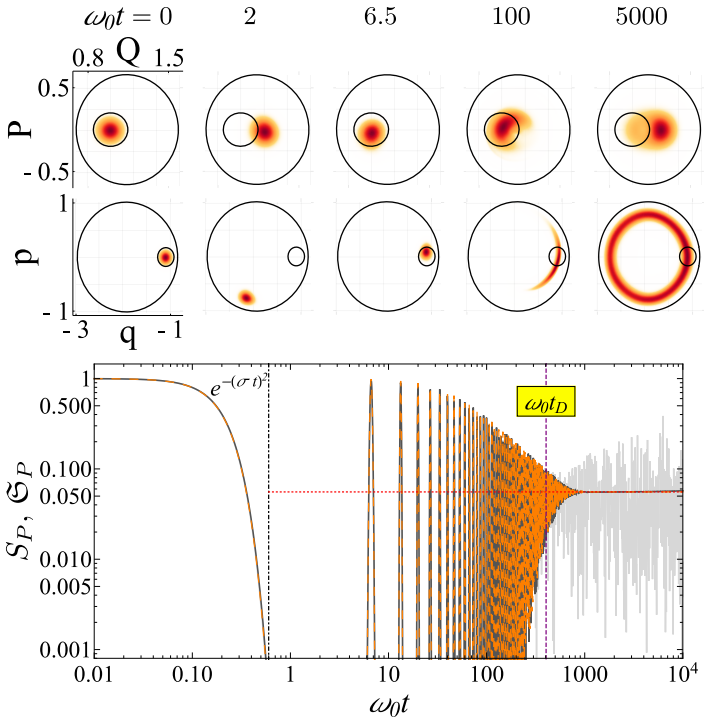

Figure 7.3: **Top panels:** Time evolved Wigner function of state I for different finite times. The projection in phase space is shown in each atomic $Q-P$ and bosonic $q-p$ plane. The inner small circle represents the initial volume occupied by the Wigner function, while the outer big circle represents the available phase space. **Bottom panel:** Survival probability (4.26) (light gray solid curve) and its classical limit (7.1) (dark gray solid curve) numerically constructed for state I. Analytical survival probability (7.3) (orange dashed curve) for the regular energy regime. The horizontal red dotted line represents the asymptotic value of the survival probability and its classical limit. The vertical purple dashed line represents the decay time. Classical energy shell: $\epsilon_{\rm R} = -1.8$ (regular). Parameters: $E_0 = j\epsilon_{\rm R}$, $\sigma_0 = 4.79$, $\omega_1 = 0.94$, $e_2 = -4.88 \times 10^{-4}$. Hamiltonian parameters: $\omega = \omega_0 = 1$, $\gamma = 2\gamma_{\rm c} = 1$. The system size is $j = 100$. Figure taken from Ref. [14].

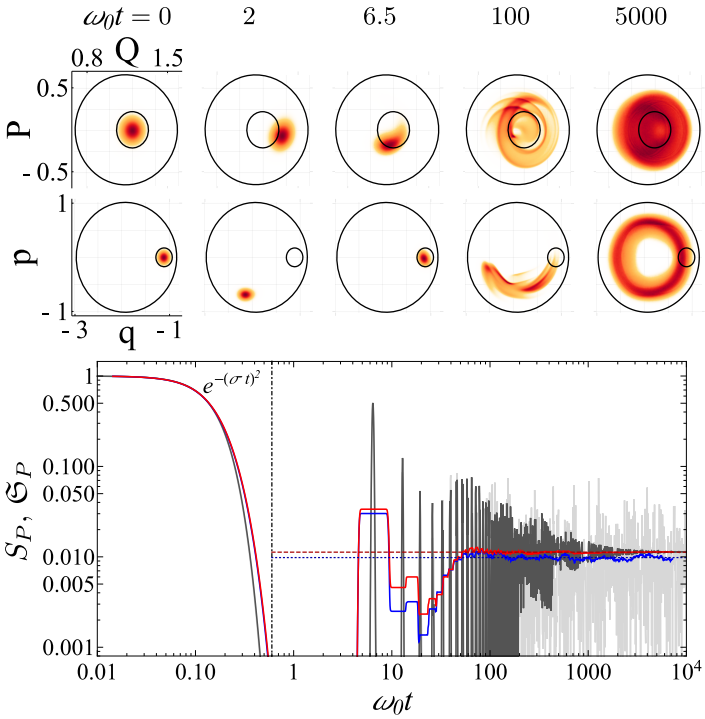

Figure 7.4: **Top panels:** Time evolved Wigner function of state II for different finite times. The projection in phase space is shown in each atomic $Q - P$ and bosonic $q - p$ plane. The inner small circle represents the initial volume occupied by the Wigner function, while the outer big circle represents the available phase space. **Bottom panel:** Survival probability (4.26) (light gray solid curve) and its classical limit (7.1) (dark gray solid curve) numerically constructed for state II. A time average over the survival probability (light blue solid curve) and its classical limit (light red solid curve) is shown, which was generated with exponential time intervals. The horizontal lines represent the asymptotic value of the survival probability (dark blue dotted line) and its classical limit (dark red dashed line), respectively. Classical energy shell: $\epsilon_{\mathrm{R}} = -1.8$ (regular). Hamiltonian parameters: $\omega = \omega_0 = 1$, $\gamma = 2\gamma_{\mathrm{c}} = 1$. The system size is $j = 100$. Figure taken from Ref. [14].

coefficients c_k come from an exponential distribution through the weights r_k resemble the dynamics of coherent states with high participation ratio in the chaotic energy regime [14].

For the selected initial coherent states located in the chaotic energy regime the same procedure as in the regular energy regime was applied. In Fig. 7.5 is shown the smoothed LDoS for different finite time resolutions for states III and IV, as well as the LDoS at infinite time resolution. Additionally, to understand the connection between coherent states and random states whose coefficients come from an exponential distribution, an initial random state was constructed as described by Eqs. (K.1) and (K.2). As can be seen, state III shows a finite time resolution where the Gaussian LDoS envelope breaks down. At infinite time resolution the energy components are bunched around specific energy levels resembling a periodicity in energy. State IV has the Gaussian LDoS envelope for all finite time resolutions, while at infinite time resolution contribute the most energy components. The Gaussian LDoS envelope of the random state at finite time resolution breaks down earlier and at infinite time resolution the LDoS resembles that of the state IV.

For states III and IV the survival probability and its classical limit can be also constructed using Eqs. (4.26) and (7.1), respectively. For the chaotic energy regime are considered some changes in the analytical expression (4.36) due to the nature of coherent states. Since the ensemble fluctuations for random states are due to the random sampling method in an energy interval, the ensemble average $\langle \bullet \rangle$ is not needed to study the survival probability of coherent states, which have a structured LDoS. For this kind of states the following relations are considered in Eq. (4.36) $\eta = 2P_R$, $D \approx 2/\nu_c$, and $\nu_c = \nu(E_c)$. Following Appendix K.2 the effective dimension for an ensemble of random states can be found for this case as $\eta = 2\langle P_R^{-1} \rangle^{-1}$.

In Figs. 7.6 and 7.7 are shown the survival probability (4.26) and its classical limit (7.1) for both initial states III and IV, respectively. For state IV is shown the comparison between the numerical survival probability (4.26) and the analytical expression (4.36). For both states III and IV is shown a time average for the survival probability and its classical limit. Moreover, in

the same Figs. 7.6 and 7.7 is shown the time evolved Wigner function projected in the atomic $Q-P$ and bosonic $q-p$ planes for states III and IV, respectively. As can be seen, the analytical expression describes accurately almost all the time interval of the numerical survival probability for state IV, except for the zone where the survival probability goes to zero at short times. Again, the validity of the TWA is confirmed for both states III and IV at short times, where the survival probability and its classical limit match each other. The zone where the survival probability goes to zero is newly understood by the time evolved Wigner function. At intermediate times, the correlation hole is detected only for state IV, confirming the presence of spectral correlations of the GOE as is expected for the chaotic energy regime. The correlation hole is nonexistent in the classical survival probability, confirming that it is a quantum feature. Moreover, for state IV can be obtained a relaxation time as described in Refs. [12,166]. For state III is detected an unusual behavior at short times where arise periodic revivals, which resembles a regular dynamics. The last effect is associated with quantum scarring, where unstable periodic orbits of the classical realm affect the dynamics of the quantum realm [14]. The phenomenon of quantum scarring is exposed in Chapter 8.

A useful quantity to detect coherent states that show dynamical effects as quantum scarring or spectral correlations is based in the ratio between their quantum and classical asymptotic values, given by the factor [14]

$$R = 2\frac{\mathfrak{S}_P^{\infty}}{S_P^{\infty}} \in [0,1], \tag{7.8}$$

where a value $R = 0$ defines a coherent state whose dynamics is affected mainly by quantum scarring, while a value $R = 1$ defines a coherent state where spectral correlations (correlation hole) of the GOE arise in its dynamics. In Fig. 7.8 is shown a map of factor R for a set of initial coherent states located in phase space for a chaotic energy regime.

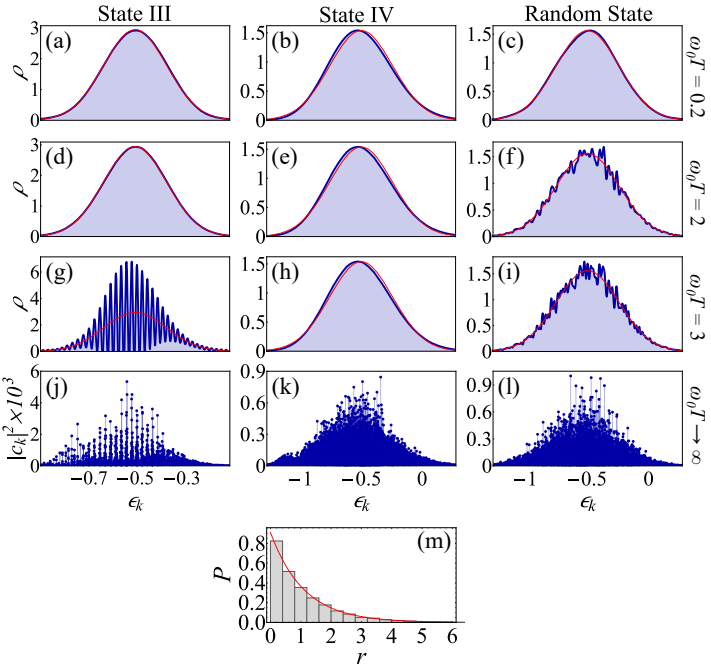

Figure 7.5: **Panels (a)-(i):** Smoothed LDoS (4.29) (blue solid curve) of states III (a), (d), (g) and IV (b), (e), (h), and random state (c), (f), (i) for different finite time resolutions, and Gaussian LDoS envelope (6.3) (red thin curve) for the chaotic energy regime. **Panels (j)-(l):** LDoS (blue dots) of the same states III (j) and IV (k), and random state (l) at infinite time resolution. The states III and IV are shown in Fig. 7.1 (d). **Panel (m):** Histogram (gray bars) of the weights r_k, which constitutes the coefficients of the state IV. The red dashed curve represents an analytical fit to an exponential distribution $P(r_k) = \upsilon e^{-\upsilon r_k}$. Classical energy shell: $\epsilon_C = -0.5$ (chaotic). Parameters: $E_c = j\epsilon_C$, $\sigma_G = 0.136j$ (state III), $\sigma_G = 0.259j$ (state IV and random state), $\upsilon = 0.91$. Hamiltonian parameters: $\omega = \omega_0 = 1$, $\gamma = 2\gamma_c = 1$. The system size is $j = 100$. Figure taken from Ref. [14].

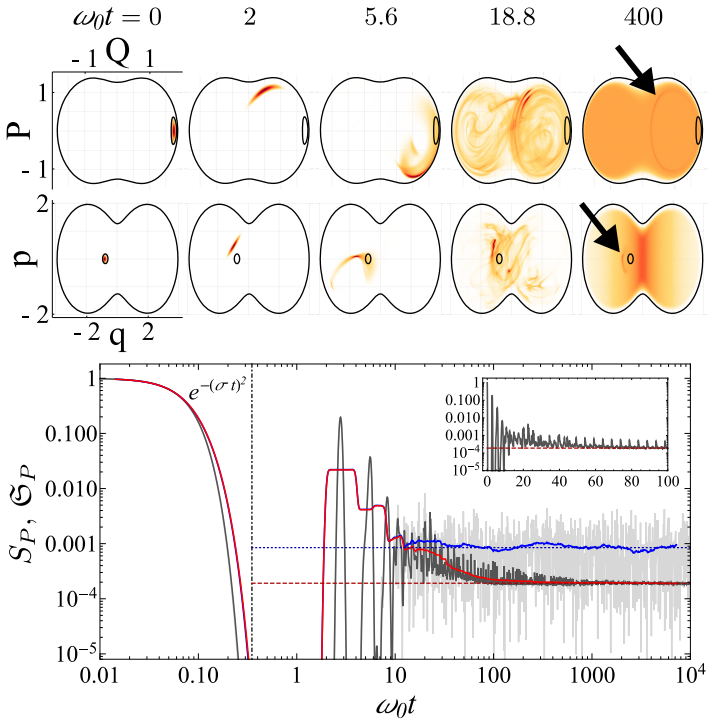

Figure 7.6: **Top panels:** Time evolved Wigner function of state III for different finite times. The projection in phase space is shown in each atomic $Q - P$ and bosonic $q - p$ plane. The inner small circle represents the initial volume occupied by the Wigner function, while the outer big circle represents the available phase space. The black arrow at the last time indicates the presence of an unstable periodic orbit. **Bottom panel:** Survival probability (4.26) (light gray solid curve) and its classical limit (7.1) (dark gray solid curve) numerically constructed for state III. A time average over the survival probability (light blue solid curve) and its classical limit (light red solid curve) is shown, which was generated with exponential time intervals. The horizontal lines represent the asymptotic value of the survival probability (dark blue dotted line) and its classical limit (dark red dashed line), respectively. The inset shows the classical limit of the survival probability in a linear time scale where the periodicities can be seen better. Classical energy shell: $\epsilon_C = -0.5$ (chaotic). Hamiltonian parameters: $\omega = \omega_0 = 1$, $\gamma = 2\gamma_c = 1$. The system size is $j = 100$. Figure taken from Ref. [14].

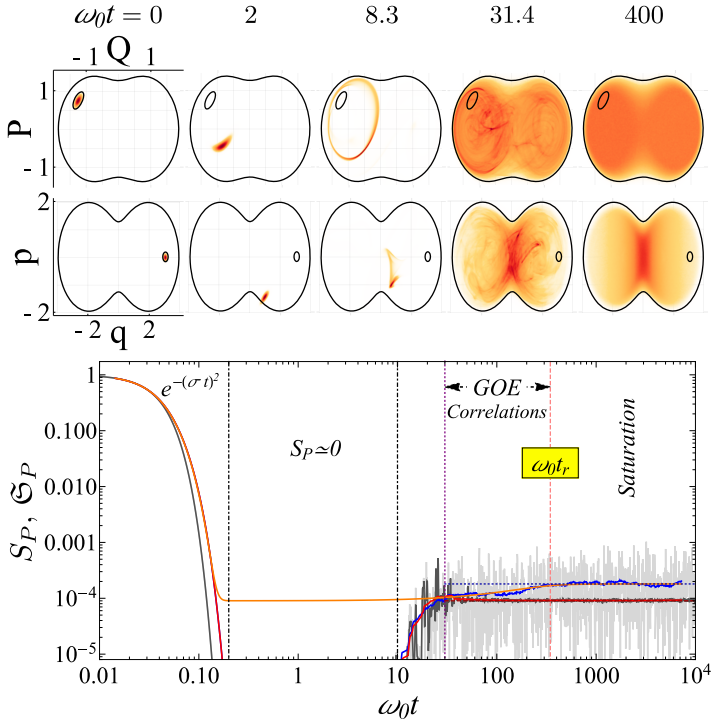

Figure 7.7: **Top panels:** Time evolved Wigner function of state IV for different finite times. The projection in phase space is shown in each atomic $Q - P$ and bosonic $q - p$ plane. The inner small circle represents the initial volume occupied by the Wigner function, while the outer big circle represents the available phase space. **Bottom panel:** Survival probability (4.26) (light gray solid curve) and its classical limit (7.1) (dark gray solid curve) numerically constructed for state IV. Analytical survival probability (4.36) (orange solid curve) for the chaotic energy regime, where the ensemble average $\langle \bullet \rangle$ was not considered. A time average over the survival probability (light blue solid curve) and its classical limit (light red solid curve) is shown, which was generated with exponential time intervals. The horizontal lines represent the asymptotic value of the survival probability (dark blue dotted line) and its classical limit (dark red dashed line), respectively. The vertical pink dashed line represents the relaxation time. Classical energy shell: $\epsilon_C = -0.5$ (chaotic). Hamiltonian parameters: $\omega = \omega_0 = 1$, $\gamma = 2\gamma_c = 1$. The system size is $j = 100$. Figure taken from Ref. [14].

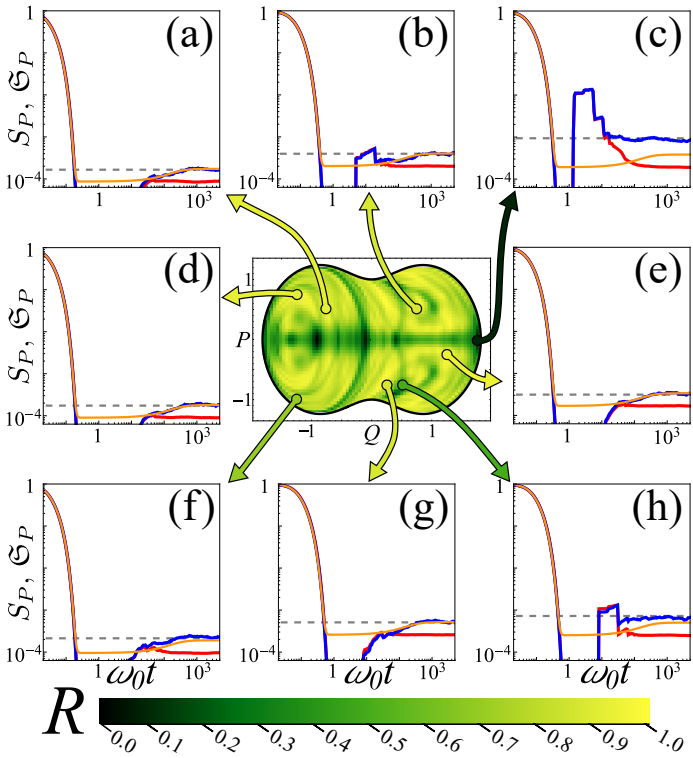

Figure 7.8: **Central panel**: Map of factor R (7.8) of coherent states for the chaotic energy regime. **Panels (a)-(h):** Survival probability (4.26) (blue solid line) and its classical limit (7.1) (red solid line) averaged in time for a set of initial coherent states. Analytical survival probability (4.36) (orange solid curve) for the chaotic energy regime. The horizontal gray dashed line represents the asymptotic value of the survival probability. Classical energy shell: $\epsilon_C = -0.5$ (chaotic). Initial conditions: $(Q_0, P_0) = (-0.75, 0.5)$ (a), $(Q_0, P_0) = (0.75, 0.5)$ (b), $(Q_0, P_0) = (1.75, 0)$ (c), $(Q_0, P_0) = (-1.25, 0.75)$ (d), $(Q_0, P_0) = (1.25, -0.25)$ (e), $(Q_0, P_0) = (-1.25, -1)$ (f), $(Q_0, P_0) = (0.25, -0.75)$ (g), $(Q_0, P_0) = (0.5, -0.75)$ (h). Hamiltonian parameters: $\omega = \omega_0 = 1$, $\gamma = 2\gamma_c = 1$. The system size is $j = 100$. Figure taken from Ref. [14].

7.2 Conclusions of Chapter 6

Generic behaviors in each classical and quantum counterpart were identified in the dynamics of the cases presented. On the one hand, for coherent states located in the regular energy regime are found two generic behaviors: 1) If the initial state is located far from a separatrix in phase space, the survival probability and its classical limit match each other until saturation, where the classical dynamics saturates to an asymptotic value, while the quantum dynamics fluctuates around it due to the discreteness of the energy spectrum. 2) If the initial state is located close to a separatrix in phase space, the survival probability and its classical limit match each other until a time where arise tunnelling effects between classically disconnected phase-space regions (stable centers) affecting the quantum dynamics only. The latter causes that the quantum and classical asymptotic values do not match each other, being the quantum asymptotic value slightly lower than the classical one.

On the other hand. for coherent states located in the chaotic energy regime are found two generic behaviors: 1) If the initial state has low participation ratio, the survival probability and its classical limit match each other until a time where the quantum dynamics saturates faster than the classical one. As the number of eigenstates which participate in the quantum evolution is small, the phase space available for the quantum evolution shrinks and the saturation occurs faster. 2) If the initial state has high participation ratio, the survival probability and its classical limit match each other until a time where arise spectral correlations and the quantum dynamics saturates slower than the classical one. For a state highly delocalized in the energy eigenbasis the correlation hole is detected affecting the quantum dynamics only. The saturation occurs after the correlation hole appears and is slower. In both cases, the quantum and classical asymptotic values do not match each other, being the quantum asymptotic value higher than the classical one. Summarizing, the spectral correlations, scarring and tunneling are considered as purely quantum effects, manifesting themselves in the dynam-

ics in particular ways.

The results exposed in this Chapter are shown in more detail in Ref. [14].

Part III

Scarring in the Dicke Model

Chapter 8

Quantum Scarring and Unstable Periodic Orbits

In this Chapter is exposed a historical review on the phenomenon of quantum scarring. The origin, first studies and theoretical explanations of this singular phenomenon are also exposed, as well as the revision of the systems where it appears and the motivation to study it in recent years. Furthermore, results on the ubiquitous quantum scarring found in the Dicke model are shown. The projection method of the Husimi function to identify visually the quantum scars is explained, as well as the relation between scarring and localization, introducing a localization measure defined in the phase space of the Dicke model. The concept of dynamical scarring is also exposed and its relation with a proposed definition of quantum ergodicity.

8.1 Quantum Scarring

In 1983 M. V. Berry formulated the semiclassical eigenfunction hypothesis, which says that semiclassical states are associated

with minimal generic classical invariant sets [230,231]. A special case of the last hypothesis is formulated for quantum eigenstates in the semiclassical limit $\hbar \to 0$. In this case, when the orbits of a classical system are chaotic, it is conjectured that quantum eigenstates are associated with the whole energy shell explored ergodically by the classical orbits [231]. In phase space, the last statement implies that the phase-space distribution function of the eigenstate is a Dirac delta function centered at the shell with the same energy as the energy of the eigenstate. The last is supported by the well-known Shnirelman theorem [232], which says that the quantum expectation value of a smooth operator equals the classical microcanonical average for almost all states. Surprisingly, thanks to the computational work and theoretical explanations of several authors, it was found that eigenstates are not only influenced by the energy surface, but by individual unstable periodic orbits, which are invariant sets of measure zero in phase space. The imprints left by the unstable periodic orbits in the quantum realm could affect many states and could survive in the classical limit [231]. These imprints manifest themselves as enhanced regions of high probability around the unstable periodic orbits and were denominated as quantum scars by E. J. Heller in 1984 [37–39]. Although the term was coined later, the first evidence of quantum scars was found by S. W. McDonald in the Bunimovich stadium billiard [233]. Early numerical studies performed in the same system concerning quantum stochasticity were determinant to reach the discovery of quantum scars [234]. Subsequent numerical studies also confirmed the phenomenon [235,236].

Common studies about quantum scarring have focused mainly in one-body systems [237–249]. Early studies in the Dicke model were also performed [250–252]. Recent studies have considered two-dimensional harmonic oscillators [253,254], as well as time-dependent systems [255,256], where the dynamical scarring takes place. Furthermore, the recent experimental observation of long-lived oscillations in chains of Rydberg atoms [32], associated with what is now called quantum many-body scars, has caused a new wave of fascination with this singular phenomenon [33–36].

8.2 Ubiquitous Quantum Scarring

As was seen in Chapter 7, unusual behaviors arise in the quantum dynamics for states that are affected by the phenomenon of quantum scarring. This phenomenon emerges in regimes where the chaotic behavior proliferates classically. In this way, a third goal in this Thesis was to detect the onset of quantum scarring in the Dicke model, the sources that originate it, and the connections with the sets of unstable periodic orbits which causes this singular phenomenon.

8.2.1 Scarring and Husimi Function

The unnormalized Husimi function of an arbitrary state $\hat{\rho}$ (see Eq. (5.20)) pure or mixed (for a pure state $|\Psi\rangle$ the density matrix is given by the projector $\hat{\rho} = |\Psi\rangle\langle\Psi|$) in the overcomplete Glauber-Bloch coherent state basis $\{|\mathbf{x}\rangle\}$ is the product of the Husimi functions of the same state associated to each Glauber $\{|\alpha\rangle\}$ and Bloch $\{|z\rangle\}$ coherent state basis

$$\begin{aligned} \mathcal{Q}_{\hat{\rho}}(\mathbf{x}) &= \langle \mathbf{x}|\hat{\rho}|\mathbf{x}\rangle \\ &= \mathcal{Q}_{\hat{\rho}}(\alpha)\mathcal{Q}_{\hat{\rho}}(z) \\ &= \mathcal{Q}_{\hat{\rho}}(q,p)\mathcal{Q}_{\hat{\rho}}(Q,P), \end{aligned} \tag{8.1}$$

where $\mathbf{x} = (q, p; Q, P)$ are the coordinates of the four-dimensional phase space $\mathcal{M}$ of the Dicke model. As quantum scars are concentrated around unstable periodic orbits in phase space, a way to visualize them is through a projection of the Husimi function. Specifically, the projection over the atomic plane $Q - P$ at a given classical energy shell allows to visualize clearly the quantum scars in the phase space of the Dicke model. In this way, the projected Husimi function at a classical energy shell $\epsilon = E/j$ is defined as [15]

$$\widetilde{\mathcal{Q}}_{\epsilon,\hat{\rho}}(Q,P) = \int\int dq\, dp\, \delta[h_{\mathrm{D}}(\mathbf{x}) - \epsilon]\mathcal{Q}_{\hat{\rho}}(\mathbf{x}). \tag{8.2}$$

where δ is the Dirac delta function given by Eq. (C.14) and $h_{\mathrm{D}}(\mathbf{x})$ is the classical Dicke Hamiltonian (2.38).

The identification of unstable periodic orbits, which scar the eigenstates of a quantum system, is a challenging task, since they are a set of measure zero in phase space. Thus, only two fundamental families of periodic orbits can be identified in the Dicke model [15, 16]. The last families arise in the superradiant phase ($\gamma > \gamma_c$) and emanate from the two normal modes around a stable stationary point at the ground-state energy. These families are called family $\mathcal{A}$ (with the shortest period) and family $\mathcal{B}$, respectively, and are exposed in Chapter 9. Because of the invariance of the classical Dicke Hamiltonian (2.38) under the transformation $(q, p; Q, P) \to (-q, p; -Q, P)$ they have complementary families $\widetilde{\mathcal{A}}$ and $\widetilde{\mathcal{B}}$, which causes that every periodic orbit has a mirrored image.

The first step to identify quantum scarring in the Dicke model was to study the projected Husimi function of some eigenstates and in the same way to detect the unstable periodic orbits which scar them. In Appendix N.1 is shown the numerical procedure to construct the Husimi function of eigenstates of the Dicke model. In the same way, the numerical procedure to compute the Husimi function projected in the atomic phase space is explained in Appendix N.2.

In Fig. 8.1 is shown the projected Husimi function (8.2) for some eigenstates of the Dicke model and their correspondence with periodic orbits of families $\mathcal{A}$ and $\mathcal{B}$. The eigenstates sample the energy spectrum from regular (where the periodic orbits are stable) to chaotic (where the periodic orbits become unstable) energy regimes. As can be seen, the confirmation of quantum scarring in the Dicke model is clearly visible in all projections, since the eigenstates are highly concentrated around these periodic orbits of each family $\mathcal{A}$ and $\mathcal{B}$. Nevertheless, some eigenstates show unusual behaviors where the concentration region is not confined exclusively to the periodic orbits. The last behavior is attributed to the scarring caused by some other unidentified periodic orbits, such that, each eigenstate can have different scarring degree [15]. The latter has important repercussions in phase space, since scarring can be seen as a source of localization of quantum states in phase space.

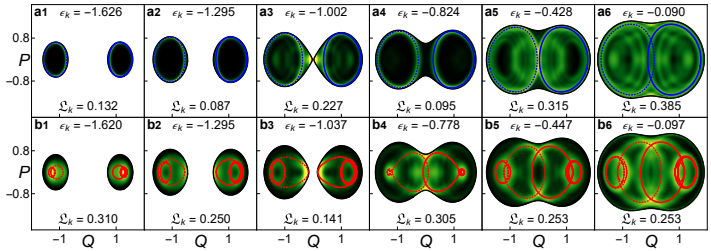

Figure 8.1: Projected Husimi function (8.2) for selected eigenstates which cover the energy spectrum from regular to chaotic ($\epsilon > -0.8$) energy regimes. Lighter colors indicate higher concentrations, while black corresponds to zero. Periodic orbits from family $\mathcal{A}$ (blue solid curve) (a1-a6) and family $\mathcal{B}$ (red solid curve) (b1-b6), and their corresponding mirrored images from family $\widetilde{\mathcal{A}}$ (blue dashed curve) (a1-a6) and family $\widetilde{\mathcal{B}}$ (red dashed curve) (b1-b6). The values of the classical energy shell ϵ_k and the phase-space localization measure (8.3) for each eigenstate are indicated in each panel. Hamiltonian parameters: $\omega = \omega_0 = 1$, $\gamma = 2\gamma_c = 1$. The system size is $j = 30$. Figure taken from Ref. [15].

8.2.2 Scarring and Localization in Phase Space

Typically, localization (delocalization) of a quantum state defines the region where the state is concentrated (spread) in a given orthonormal basis. The well-known measure that quantifies this is the participation ratio (4.31). However, the concept can be extended to continuous spaces, such that, quantum localization in phase space can be established through the use of the overcomplete coherent-state basis. The phenomenon of quantum localization is exposed in Chapter 10. The basic idea is to replace the probability to find an arbitrary state in a basis state with a quasiprobability distribution in phase space (Wigner or Husimi function). Thus, a simple localization measure of a state $\hat{\rho}$ in the phase space $\mathcal{M}$ of the Dicke model can be defined for a single classical energy shell $\epsilon = E/j$. The proposed measure takes the explicit form [15]

$$\mathfrak{L}_{\epsilon,\hat{\rho}} = \frac{C_\epsilon^2}{\mathcal{V}_\epsilon}\left[\int_{\mathcal{M}_\epsilon} d\mathbf{s}\, \mathcal{Q}_{\hat{\rho}}^2(\mathbf{x})\right]^{-1} \in (0,1], \tag{8.3}$$

where $\mathbf{x} = (q, p; Q, P)$ are the coordinates of the four-dimensional phase space $\mathcal{M}$ of the Dicke model, $d\mathbf{s} = \delta[h_{\mathrm{D}}(\mathbf{x}) - \epsilon]d\mathbf{x}$ is a surface element, the constant

$$C_\epsilon = \int_{\mathcal{M}_\epsilon} d\mathbf{s}\, \mathcal{Q}_{\hat{\rho}}(\mathbf{x}) \tag{8.4}$$

ensures normalization of the Husimi function, and

$$\mathcal{M}_\epsilon = \{\mathbf{x} = (q, p; Q, P) | h_{\mathrm{D}}(\mathbf{x}) = \epsilon\} \tag{8.5}$$

defines the subspace associated to the classical energy shell. The scaling by the phase-space volume of the classical energy shell

$$\begin{aligned} \mathcal{V}_\epsilon &= \int_{\mathcal{M}_\epsilon} d\mathbf{s} \\ &= \int_{\mathcal{M}} d\mathbf{x}\, \delta[h_{\mathrm{D}}(\mathbf{x}) - \epsilon] \\ &= (2\pi\hbar_{\mathrm{eff}})^2 \nu(\epsilon), \end{aligned} \tag{8.6}$$

where $\hbar_{\mathrm{eff}} = j^{-1}$ and the term $\nu(\epsilon)$ is the semiclassical density of states (2.41), which allows to obtain a measure bounded to the interval $(0, 1]$. The limit value $\mathfrak{L} \to 0$ defines a state maximally localized in phase space, while the other one $\mathfrak{L} = 1$ defines a state maximally delocalized or spread in the whole classical energy shell. In this way, the phase-space localization measure (8.3) can be considered as the analog of the participation ratio (4.31) for a continuous basis.

To understand the relation between scarring and localization, the phase-space localization measure (8.3) was computed for the eigenstates shown in Fig. 8.1. This measure can be numerically constructed with the same method exposed in Appendix N.2, where the integral over the remaining atomic variables (Q, P) is computed with an standard Riemann sum. The value for each eigenstate is shown in the same Fig. 8.1. As can be seen, all eigenstates show different localization degree in phase space, which has an intrinsic relation with quantum scarring. Thus, the best way to understand this relation is by further studying both phenomena for the eigenstates of the Dicke model.

In Fig. 8.2 is shown a Peres lattice of the phase-space localization measure (8.3) for all eigenstates of the Dicke model, which go from the ground-state energy to a chaotic energy regime. In Fig. 8.2 is shown also the projected Husimi function (8.2) for some eigenstates located exclusively in the chaotic energy regime ($\epsilon > -0.8$) and their comparison with pure random states (K.1) centered at a chaotic classical energy shell. In the same Fig. 8.2 is shown the probability distribution of the phase-space localization measure for an ensemble of random states centered at a chaotic classical energy shell and for the eigenstates contained in the chaotic energy regime for different system sizes. As can be seen, all eigenstates of the Dicke model in the chaotic energy regime are scarred by unstable periodic orbits, since all projected Husimi functions show structures that resemble closed periodic orbits. The same is not true for random states, whose projected Husimi functions show a granular pattern. The eigenstates of the Dicke model show different degrees of localization in phase space. At low energies (regular energy regime) the lattice is organized along lines associated to quasi-integrals of motion related to classical periodic orbits [15]. However, at high energies (chaotic energy regime) the lattice becomes dense and losses order grouping the eigenstates around a mean value $\mathfrak{L} \sim 1/2$. The last result is associated with an upper limit on the spreading of any pure state at chaotic energy regimes [15]. Furthermore, the probability distribution of the phase-space localization measure of random states is centered at this upper limit and becomes thinner when the system size increases. On the other hand, for eigenstates in the chaotic energy regime the probability distribution is skewed and broader, where there is always a fraction of eigenstates highly localized when the system size increases, while the fraction of eigenstates highly delocalized decreases.

8.2.3 Dynamical Scarring and Quantum Ergodicity

The concept of quantum ergodicity can be extended from classical ergodicity, where the trajectories of an ergodic system cover its phase space homogeneously. In this way, quantum ergodicity

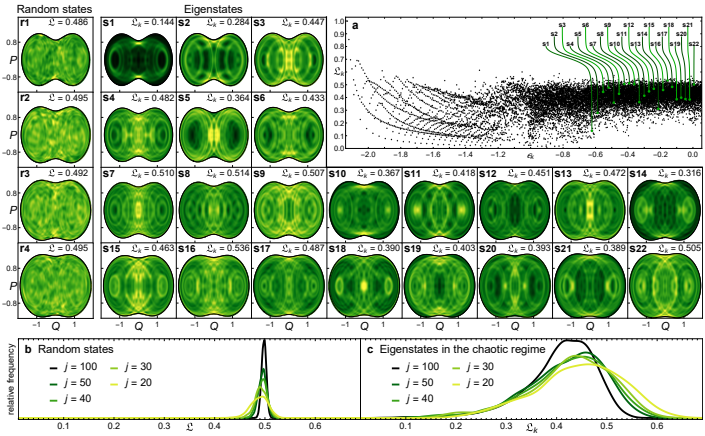

Figure 8.2: **Panel a:** Peres lattice (black dots) of phase-space localization measure (8.3) for selected eigenstates contained in the energy interval $\epsilon_k \in [\epsilon_{\rm gs} = -2.125, 0.1]$. **Panels s1-s22:** Projected Husimi function (8.2) for different selected eigenstates which cover the energy spectrum in the chaotic regime. Lighter colors define higher concentrations, while black corresponds to zero. **Panels r1-r4:** Projected Husimi function for random states (K.1) centered at different classical energy shells $E_{\rm c} = j\epsilon$ with energy width $j\sigma$. **Panel b:** Probability distribution of phase-space localization measure for 20000 random states centered at $E_{\rm c} = j\epsilon$ with energy width $j\sigma$. **Panel c:** Probability distribution of phase-space localization measure for eigenstates contained in the chaotic energy interval $\epsilon_k \in [-0.8, 0]$. Parameters: $\epsilon = -0.6$ (r1), $\epsilon = -0.4$ (r2), $\epsilon = -0.2$ (r3), $\epsilon = -0.1$ (r4), $\epsilon = -0.5$ (b), $\sigma = 0.3$ (r1-r4 and b). Hamiltonian parameters: $\omega = \omega_0 = 1$, $\gamma = 2\gamma_c = 1$. The system size for panels a, s1-s22, and r1-r4 is $j = 100$. The system size for panels b and c is indicated in each panel. Figure taken from Ref. [15].

can be defined through the time-averaged ensemble [15, 257, 258]

$$\overline{\rho} = \lim_{t\to+\infty} \frac{1}{t} \int_0^t dt' \hat{\rho}(t'), \tag{8.7}$$

where

$$\hat{\rho}(t) = e^{-i\hat{H}_{\mathrm{D}}t} \hat{\rho} e^{i\hat{H}_{\mathrm{D}}t} \tag{8.8}$$

is the time evolved density matrix. Thus, an arbitrary quantum state $\hat{\rho}$ is called ergodic if the phase-space localization measure (8.3) of its time-averaged ensemble (8.7) is unity, $\overline{\mathfrak{L}}_{\epsilon,\hat{\rho}} \equiv \mathfrak{L}_{\epsilon,\overline{\rho}} = 1$, which implies that the whole classical energy shell is homogeneously visited by the state. A projected Husimi function for some time-averaged ensembles can show structures resembling periodic orbits as occurs with single eigenstates. In this case, the scarring phenomenon is identified as dynamical scarring of the time-averaged ensemble [15].

An upper limit of spreading was found for chaotic energy regimes, which means that any pure state can only cover a half of the available phase space. The latter result implies that any pure state is a non-ergodic state, since they never cover the classical energy shell completely. To understand what kind of states can reach ergodicity in the quantum sense, some time-averaged ensembles of states are considered.

In Fig. 8.3 is shown the LDoS of initial coherent states located in the chaotic energy regime, whose explicit parameters in phase space are given by the initial conditions $\mathbf{x}_0 = (q_+(\epsilon), 0; Q_0, P_0)$, where q_+ is the positive root of the second-degree equation $h_{\mathrm{D}}(\mathbf{x}) - \epsilon = 0$. Moreover, is shown the LDoS of a random state (K.1) centered at the same chaotic classical energy shell as the initial coherent states. In addition, in Fig. 8.3 are shown the survival probability (4.26) and its time average for the last states, as well as the projected Husimi function (8.2) for the time-average ensemble (8.7) of the same states. In the same Fig. 8.2 is shown the probability distribution of the phase-space localization measure (8.3) of the time-averaged ensemble for coherent states and random states located in a chaotic energy regime for different system sizes. As can be seen, the LDoS of coherent states shows generic behaviors, those states with low participation ratio show

an LDoS with the energy components bunched around specific energy levels, while those with high participation ratio show an LDoS more similar to that of the random state, where the most energy components participate. The survival probability confirms these generic behaviors, where states with low participation ratio (states strongly scarred) show periodicities before saturation, while those with high participation ratio (states with different scarring degrees) show the correlation hole before saturation as occurs with the random state. The projected Husimi functions show the dynamical scarring for the time-average ensembles of coherent states, since clear structures resembling periodic orbits can be seen, while the random state does not show these structures. On the other hand, the phase-space localization measure of the time-averaged ensembles for the last states show also generic behaviors in light of quantum ergodicity. The random state shows a phase-space localization measure $\mathfrak{L} \sim 1$, which implies that this state can be considered as an ergodic state, while coherent states show a direct relation between the phase-space localization measure and the participation ratio. When the participation ratio grows, the phase-space localization measure also grows, but it never reaches unity as the random state. This is shown in the probability distribution of the phase-space localization measure for both type of states. On the one hand, for coherent states the broad distribution becomes thinner when the system size increases, but the fraction of states with phase-space localization measure near unity is small. On the other hand, for random states the distribution becomes thinner and better centered at unity when the system size increases, ensuring their ergodic behavior.

8.3 Conclusions of Chapter 7

The ubiquitous quantum scarring of the Dicke model was confirmed for all eigenstates in the chaotic energy regime. This feature of the Dicke model was a counter intuitive result, since for many years it was thought that the eigenstates of quantum systems affected by scarring were a few ones with specific char-

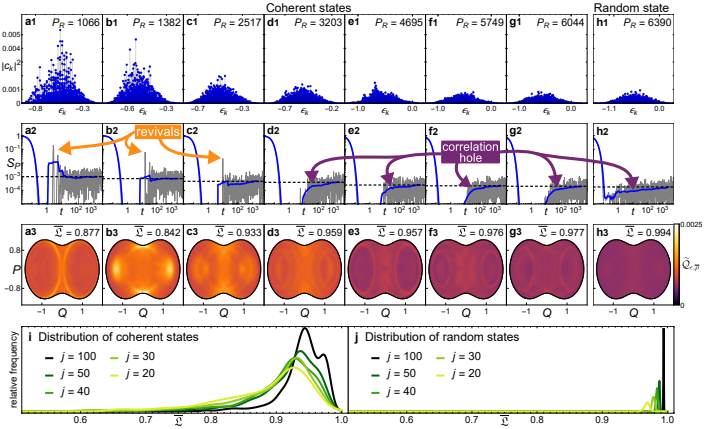

Figure 8.3: **Panels a1-g1:** LDoS of coherent states centered at the classical energy shell ϵ. The selected states a1-g1 are shown in Fig. 7.8: a1 (c), b1 (h), c1 (b), d1 (e), e1 (f), f1 (d), g1 (a). **Panel h1:** LDoS of random state (K.1) centered at $E_c = j\epsilon$ with energy width $j\sigma$. The participation ratio of each state a1-h2 is indicated in each panel. **Panels a2-h2:** Survival probability (4.26) (gray solid curve) numerically constructed, its time average (blue solid curve) with exponential time intervals, and its asymptotic value (horizontal black dashed line) for states a1-h1. **Panels a3-h3:** Projected Husimi function (8.2) of time-averaged ensemble (8.7) for states a1-h1. Lighter colors define higher concentrations. The value of the phase-space localization measure (8.3) for each state a1-h2 is indicated in each panel. **Panel i:** Probability distribution of phase-space localization measure of time-averaged ensemble (8.7) for 1551 coherent states distributed equally in the atomic plane $Q - P$. **Panel j:** Probability distribution of phase-space localization measure of time-averaged ensemble for 500 random states centered at $E_c = j\epsilon$ with energy width $j\sigma$. Parameters: $\epsilon = -0.5$ (h1 and j), $\sigma = 0.3$ (h1 and j). Hamiltonian parameters: $\omega = \omega_0 = 1$, $\gamma = 2\gamma_c = 1$. The system size for panels a1-h1, a2-h2, and a3-h3 is $j = 100$. The system size for panels i and j is indicated in each panel. Figure taken from Ref. [15].

acteristics. The eigenstates show different scarring degree and at the same time different localization degree in phase space. An eigenstate strongly scarred is also highly localized in phase space; however, an eigenstate can be scarred by different unstable periodic orbits and reach values of delocalization comparable to a random state. The initial coherent states strongly scarred by unstable periodic orbits cause the breaking of ergodicity arising the periodic revivals in their survival probability.

On the other hand, any pure state (scarred or unscarred) is localized in phase space, since an upper limit of spreading was found. This limit is related with quantum interferences of the wave function and not with quantum scarring, and the only way to achieve quantum ergodicity is through time averages, that is, quantum ergodicity is an ensemble property. Thus, the three main concepts investigated, scarring, localization, and lack of ergodicity are related to each other, but they do not mean the same. In this way, the ubiquitous quantum scarring displayed by the Dicke model does not mean directly breaking of quantum ergodicity. Any pure state, including eigenstates, coherent states and random states, is a non-ergodic state, since it never reaches complete delocalization in phase space. The only type of states considered as ergodic states are non-stationary states as time-averaged ensembles of random states and some time-averaged ensembles of coherent states which reach values of delocalization near to those of random states.

The results exposed in this Chapter are shown in more detail in Ref. [15].

Chapter 9

Fundamental Families of Periodic Orbits

In this Chapter are exposed the fundamental families of periodic orbits emanating from a stationary point in the Dicke model, which cause the ubiquitous quantum scarring detected in the model. Results on the identification of these families of periodic orbits are shown, as well as the perturbing method to find well-converged periodic orbits. Furthermore, a scarring measure is introduced to quantify the scarring degree of quantum states caused by such families of periodic orbits. An analysis of dynamical scarring for coherent states is also shown.

9.1 Families of Periodic Orbits that Emanate from Stationary Points

In Chapter 8 were introduced two fundamental families of periodic orbits in the Dicke model that emanate from a stationary point. At low energies these periodic orbits are stable, but when energy increases reaching high energy regions where classical chaos appears, these periodic orbits become unstable and cause the scarring of the eigenstates. In this way, a fourth goal

in this Thesis was to detect these families of periodic orbits, identifying the generic effects over the eigenstates they produce.

9.1.1 Perturbation of Stationary Points

A periodic orbit is a subset of phase space and can be defined as

$$\mathcal{O}_\epsilon = \{\mathbf{x}(t)|t \in [0,T]\}, \tag{9.1}$$

where ϵ is the energy of the periodic orbit and T defines its normal period, which satisfies the condition $\mathbf{x}(0) = \mathbf{x}(T)$, and $\mathbf{x} = (q,p;Q,P)$ are the coordinates of the four-dimensional phase space $\mathcal{M}$ of the Dicke model. The simplest periodic orbit comes from a single stationary point $\mathbf{x}_{\rm sp}$, such that, $\mathbf{x}_{\rm sp}(0) = \mathbf{x}_{\rm sp}(t)$ for all times. For the superradiant phase ($\gamma > \gamma_{\rm c}$) of the Dicke model, the stationary point $\mathbf{x}_{\rm gs}$ associated with the ground-state energy $\epsilon_{\rm gs}$ can be found by minimizing the classical Dicke Hamiltonian (2.38), and is given by Eq. (C.12). There is another stationary point $\widetilde{\mathbf{x}}_{\rm gs}$ where the variables q and Q have opposite sign to those of $\mathbf{x}_{\rm gs}$. By considering small displacements around the stationary point $\mathbf{x}_{\rm gs}$ its normal modes can be obtained. That is, two normal angular frequencies can be obtained [16]

$$\Omega^{\rm A,B}_{\epsilon_{\rm gs}} = \frac{1}{\omega}\sqrt{\frac{1}{2}\left(\omega^4 + 16\gamma^4 \pm \sqrt{(\omega^4 - 16\gamma^4)^2 + 4\omega^6\omega_0^2}\right)}, \tag{9.2}$$

as well as their normal periods $T^{\rm A,B}_{\epsilon_{\rm gs}} = 2\pi/\Omega^{\rm A,B}_{\epsilon_{\rm gs}}$. Thus, for the latter periods their fundamental periodic orbits are given by $\mathcal{O}^{\rm A,B}_{\epsilon_{\rm gs}} = \{\mathbf{x}_{\rm gs}\}$. Using a method known as monodromy method to guarantee convergence [251, 259–261], these periodic orbits can be perturbed to find new periodic orbits $\mathcal{O}^{\rm A,B}_{\epsilon'}$ with energy $\epsilon' = \epsilon_{\rm gs} + \delta\epsilon$ and period $T^{\rm A,B}_{\epsilon'} = T^{\rm A,B}_{\rm gs} + \delta T$. This process can be done iteratively for increasing energies until the chaotic regime $\epsilon > -0.8$, where the periodic orbits become unstable. In Appendix O.1 is shown the monodromy method to find periodic orbits in the phase space of the Dicke model. Two fundamental families of periodic orbits are found in the Dicke model and are

given by [16]

$$\mathcal{A} = \{\mathcal{O}_\epsilon^{\mathrm{A}} | \epsilon_{\mathrm{gs}} \leq \epsilon\}, \tag{9.3}$$

$$\mathcal{B} = \{\mathcal{O}_\epsilon^{\mathrm{B}} | \epsilon_{\mathrm{gs}} \leq \epsilon\}. \tag{9.4}$$

The parity conservation of the Dicke Hamiltonian (2.5) is manifested in the classical Dicke Hamiltonian (2.38) as invariance under the transformation $(q, p; Q, P) \to (-q, p; -Q, P)$. The last feature allows to find mirrored images of each periodic orbit as $\mathcal{O}_\epsilon \to \widetilde{\mathcal{O}}_\epsilon$, which have the same energy and period than the original ones. Thus, the complementary families of periodic orbits that emanate from the stationary point $\widetilde{\mathbf{x}}_{\mathrm{gs}}$ can be defined as

$$\widetilde{\mathcal{A}} = \{\widetilde{\mathcal{O}}_\epsilon^{\mathrm{A}} | \mathcal{O}_\epsilon^{\mathrm{A}} \in \mathcal{A}\}, \tag{9.5}$$

$$\widetilde{\mathcal{B}} = \{\widetilde{\mathcal{O}}_\epsilon^{\mathrm{B}} | \mathcal{O}_\epsilon^{\mathrm{B}} \in \mathcal{B}\}. \tag{9.6}$$

Analyzing the properties of the fundamental families of periodic orbits $\mathcal{A}$ and $\mathcal{B}$ can help to understand the way they cause the ubiquitous scarring for the eigenstates of the Dicke model. The study of the period and maximum Lyapunov exponent as a function of the energy can give some insight on how these periodic orbits, stable at low energies, become unstable at high energies. In Appendix O.2 is shown the numerical procedure to compute the Lyapunov exponent for periodic orbits.

In Fig. 9.1 is shown a set of periodic orbits from family $\mathcal{A}$ and family $\mathcal{B}$ projected in both bosonic $q - p$ and atomic $Q - P$ planes. The period an the maximum Lyapunov exponent of the orbits for both families as a function of the energy is also shown. The stationary point from where emanate both families of periodic orbits is marked with blue (family $\mathcal{A}$) and red (family $\mathcal{B}$) arrows in each plane. As can be seen, the period of family $\mathcal{A}$ grows linearly and softly, while the period of family $\mathcal{B}$ shows a maximum near the energy value $\epsilon \sim 1$, where an exited-state quantum phase transition appears in the model. On the other hand, the Lyapunov exponent of family $\mathcal{A}$ shows clearly the energy where orbits become unstable ($\epsilon \sim -0.8$) taking positive values. Nevertheless, for family $\mathcal{B}$ appears a characteristic behavior, since there is a region at high energies where the orbits can be stable near the energy value $\epsilon \sim -0.1$.

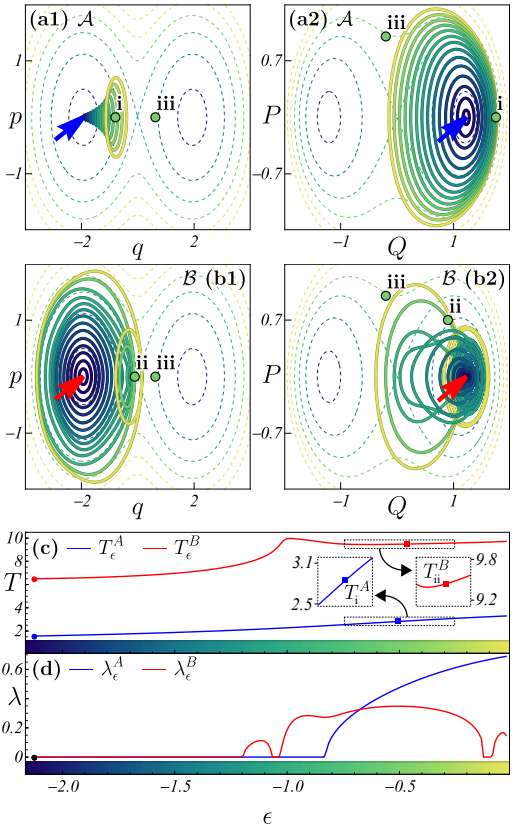

Figure 9.1: **Panels (a1)-(b2):** Periodic orbits (solid curves) from family $\mathcal{A}$ and $\mathcal{B}$ projected in the bosonic $q-p$ [(a1) and (b1)] and atomic $Q-P$ [(a2) and (b2)] plane, respectively. The dashed curves represent the available phase space for different classical energy shells. Darker colors define low energy values. The blue and red arrows define the stationary point $\mathbf{x}_{\rm gs}$ at the ground-state energy. **Panels (c)-(d):** Period (c) and maximum Lyapunov exponent (d) of the periodic orbits from family $\mathcal{A}$ (blue solid curve) and family $\mathcal{B}$ (red solid curve) as a function of the energy. In panels (a1)-(b2) are shown the selected initial coherent states for the chaotic energy regime: state i (near family $\mathcal{A}$), state ii (near family $\mathcal{B}$), and state iii (far from families $\mathcal{A}$ and $\mathcal{B}$). Classical energy shell: $\epsilon = -0.5$ (chaotic). Initial conditions: $(Q_0, P_0) = (1.75, 0)$ (state i), $(Q_0, P_0) = (0.9, 0.7)$ (state ii), $(Q_0, P_0) = (-0.2, 1)$ (state iii). Hamiltonian parameters: $\omega = \omega_0 = 1$, $\gamma = 2\gamma_c = 1$. The system size is $j = 30$. Figure taken from Ref. [16].

9.1.2 Scarring of Periodic Orbits

To quantify how much an arbitrary state $\hat{\rho}$ is scarred by a given periodic orbit $\mathcal{O}_\epsilon$ with energy ϵ and period T, a scarring measure can be defined as [16]

$$\mathcal{P}(\mathcal{O}_\epsilon, \hat{\rho}) = \frac{\mathrm{Tr}(\hat{\rho}\hat{\rho}_{\mathcal{O}_\epsilon})}{\mathrm{Tr}(\hat{\rho}_\epsilon \hat{\rho}_{\mathcal{O}_\epsilon})}, \tag{9.7}$$

where $\hat{\rho}_{\mathcal{O}_\epsilon}$ represents a tubular Gaussian distribution around the periodic orbit $\mathcal{O}_\epsilon$ and $\hat{\rho}_\epsilon$ represents a state composed of all coherent states within the classical energy shell $\epsilon = h_{\mathrm{D}}(\mathcal{O}_\epsilon)$, which is completely delocalized. In appendix O.3 is shown the complete derivation of the proposed scarring measure. In this way, a scarring measure of an arbitrary state $\hat{\rho}$ caused by the fundamental families $\mathcal{A}$ and $\mathcal{B}$, as well as the complementary families $\widetilde{\mathcal{A}}$ and $\widetilde{\mathcal{B}}$, is defined as

$$\mathcal{P}^{\mathrm{A}}(\epsilon, \hat{\rho}) = \mathcal{P}(\mathcal{O}^{\mathrm{A}}_\epsilon, \hat{\rho}) + \mathcal{P}(\widetilde{\mathcal{O}}^{\mathrm{A}}_\epsilon, \hat{\rho}), \tag{9.8}$$

$$\mathcal{P}^{\mathrm{B}}(\epsilon, \hat{\rho}) = \mathcal{P}(\mathcal{O}^{\mathrm{B}}_\epsilon, \hat{\rho}) + \mathcal{P}(\widetilde{\mathcal{O}}^{\mathrm{B}}_\epsilon, \hat{\rho}), \tag{9.9}$$

where a value $\mathcal{P} = 1$ indicates that the overlap between the state $\hat{\rho}$ and the periodic orbit $\mathcal{O}_\epsilon$ is the same of a completely delocalized state $\hat{\rho}_\epsilon$. Values $\mathcal{P} > 1$ indicate a state $\hat{\rho}$ scarred by the periodic orbit $\mathcal{O}_\epsilon$, while values $\mathcal{P} < 1$ indicate a state $\hat{\rho}$ is less likely to be found near the periodic orbit $\mathcal{O}_\epsilon$ than a completely delocalized state $\hat{\rho}_\epsilon$.

A graphic way to condensate the effects caused by the families $\mathcal{A}$ and $\mathcal{B}$ over the eigenstates is through a Peres lattice of a given operator. A known an previously studied operator is the angular momentum operator $\hat{J}_z$, whose scaled expectation value can be represented classically using an average over periodic orbits of the classical variable $j_z = (Q^2 + P^2)/2 - 1$ [16]

$$\langle j_z \rangle_{\mathcal{O}^{\mathrm{A,B}}_\epsilon} = \frac{1}{T^{\mathrm{A,B}}_\epsilon} \int_0^{T^{\mathrm{A,B}}_\epsilon} dt\, j_z[\mathbf{x}(t)], \tag{9.10}$$

where $T^{\mathrm{A,B}}_\epsilon$ are the normal periods of families $\mathcal{A}$ and $\mathcal{B}$, which can be obtained from the normal frequencies (9.2). Moreover,

using the Bohr-Sommerfeld quantization condition, the energies of the families $\mathcal{A}$ and $\mathcal{B}$ can be semiclassically quantized as [16]

$$\int_{\varepsilon_{i-1}^{\mathrm{A,B}}}^{\varepsilon_{i}^{\mathrm{A,B}}} d\epsilon\, T_{\epsilon}^{\mathrm{A,B}} = 2\pi\hbar_{\mathrm{eff}}, \tag{9.11}$$

where $\hbar_{\mathrm{eff}} = j^{-1}$, and both families begin from the ground-state energy $\varepsilon_0^{\mathrm{A}} = \varepsilon_0^{\mathrm{B}} = \epsilon_{\mathrm{gs}}$. The last procedure allows to visualize the exact energies which conform each fundamental family of periodic orbits.

In Fig. 9.2 is shown a Peres lattice of operator $\hat{J}_z/j$ for all eigenstates of the Dicke model, which go from the ground-state energy to a chaotic energy regime. For all eigenstates was computed the scarring measure of family $\mathcal{A}$ (9.8) and family $\mathcal{B}$ (9.9), and is represented as the intensity of color of each eigenstate. Moreover, the classical expectation value (9.10) and the semiclassically quantized energies given by Eq. (9.11) are also shown for both families. In the same Fig. 9.2 is shown the projected Husimi function (8.2) for the same eigenstates of the Dicke model presented in Fig. 8.1 and their correspondence with periodic orbits of families $\mathcal{A}$ and $\mathcal{B}$. The eigenstates sample the energy spectrum from regular (where the periodic orbits are stable) to chaotic (where the periodic orbits become unstable) energy regimes. The scarring measure for family $\mathcal{A}$ (9.8) and family $\mathcal{B}$ (9.9) was computed for these eigenstates. The value for each eigenstate is shown in the same Fig. 9.2, confirming that the selected eigenstates are effectively scarred by each fundamental family $\mathcal{A}$ and $\mathcal{B}$. As can be seen, all eigenstates show different scarring degree caused by each family $\mathcal{A}$ and $\mathcal{B}$ in accord with the color bars. At low energies, the strongly scarred eigenstates are ordered in a lattice-like shape and coincide perfectly with the semiclassical quantized energies for each family. However, as energy increases the order losses and the strongly scarred states are bunched around the semiclassical quantized energies forming cluster-like shapes. For both families, the classical expectation value (9.10) for each family $\mathcal{A}$ and $\mathcal{B}$ shows an agreement with the Peres lattice of the quantum operator $\hat{J}_z/j$, since the eigenstates scarred by each family are grouping around it.

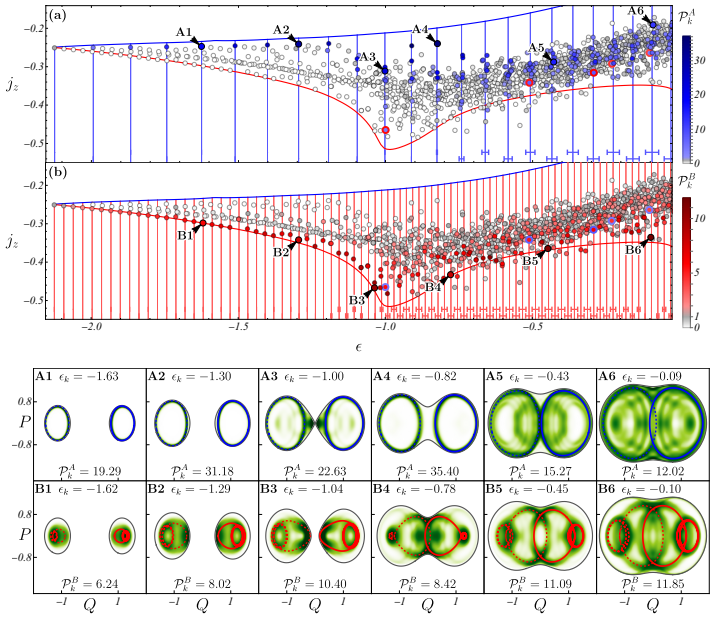

Figure 9.2: **Panels (a)-(b):** Peres lattice (circles) of operator $\hat{J}_z/j$ for eigenstates contained in the energy interval $\epsilon_k \in [\epsilon_{\rm gs} = -2.125, 0]$. The intensity of color for each circle represents the scarring measure of family $\mathcal{A}$ (9.8) (blue) (a) and family $\mathcal{B}$ (9.9) (red) (b) indicated with the right bar. The vertical lines represent the Bohr-Sommerfeld quantization condition (9.11) for energies of family $\mathcal{A}$ (blue thin lines) (a) and family $\mathcal{B}$ (red thin lines) (b). The black arrows represent the selected eigenstates presented in panels A1-B6. **Panels A1-B6:** Projected Husimi function (8.2) for selected eigenstates which cover the energy spectrum from regular to chaotic ($\epsilon > -0.8$) energy regimes. Darker colors indicate higher concentrations, while white corresponds to zero. Periodic orbits from family $\mathcal{A}$ (blue solid curve) (A1-A6) and family $\mathcal{B}$ (red solid curve) (B1-B6), and their corresponding mirrored images from family $\widetilde{\mathcal{A}}$ (blue dashed curve) (A1-A6) and family $\widetilde{\mathcal{B}}$ (red dashed curve) (B1-B6). The values of the classical energy shell ϵ_k and the scarring measure of family $\mathcal{A}$ and family $\mathcal{B}$ for each eigenstate are indicated in each panel. Hamiltonian parameters: $\omega = \omega_0 = 1$, $\gamma = 2\gamma_c = 1$. The system size is $j = 30$. Figure taken from Ref. [16].

9.1.3 Dynamical Scarring of Periodic Orbits

Two fundamental families of periodic orbits that emanate from a stationary point cause the ubiquitous quantum scarring of the eigenstates of the Dicke model at high energies were identified. A next step was to study how these families of periodic orbits affect the dynamics of non-stationary states. In particular, initial Glauber-Bloch coherent states located in a chaotic energy regime were selected to study the survival probability and the connections with the last families of periodic orbits. Three coherent states were selected, one located in a point of a periodic orbit of family $\mathcal{A}$ (identified as state i), another one located in a point of a periodic orbit of family $\mathcal{B}$ (identified as state ii), and the last one located far from both families $\mathcal{A}$ and $\mathcal{B}$, as well as from the complementary families $\widetilde{\mathcal{A}}$ and $\widetilde{\mathcal{B}}$. The explicit parameters of the initial coherent states in phase space are given by the initial conditions $\mathbf{x}_0 = (q_+(\epsilon), 0; Q_0, P_0)$, where q_+ is the positive root of the second-degree equation $h_{\mathrm{D}}(\mathbf{x}) - \epsilon = 0$. These initial coherent states are shown in Fig. 9.1.

The selected Glauber-Bloch coherent states can be numerically constructed in the eigenbasis of the Dicke Hamiltonian (see Appendix M). To understand the connection between eigenstates scarred by each family of periodic orbits and the latter states, the LDoS needs to be analysed. In Fig. 9.3 is shown the LDoS of states i, ii, and iii, where each eigenstate is colored with the scarring measure for family $\mathcal{A}$ (9.8) and family $\mathcal{B}$ (9.9). Moreover, the semiclassically quantized energies given by Eq. (9.11) are also shown for both families. In the same Fig. 9.3 is shown a Peres lattice of operator $\hat{J}_z/j$ for states i, ii, and iii, where the contribution to the LDoS of each eigenstate is represented by the intensity of color. As can be seen, state i is strongly scarred by family $\mathcal{A}$, since the energy components which contribute to the LDoS have large values of the scarring measure of family $\mathcal{A}$. The eigenstates with the highest contribution to the LDoS are identified as i1-i6. The same scenario occurs for state ii with family $\mathcal{B}$, where the eigenstates with the highest contribution to the LDoS are identified as ii1-ii6. For state iii the scenario is different, since any family scar the eigenstates significantly.

For this sate the eigenstates with the highest contribution to the LDoS are identified as iii1-iii6. The last results are confirmed with the corresponding Peres lattice for states i, ii, and iii. For state i, the eigenstates with high contribution to the LDoS tend to be located near the classical expectation value of family $\mathcal{A}$, while the same occurs for state ii with family $\mathcal{B}$. For state iii is unclear which family has a dominant effect on the eigenstates.

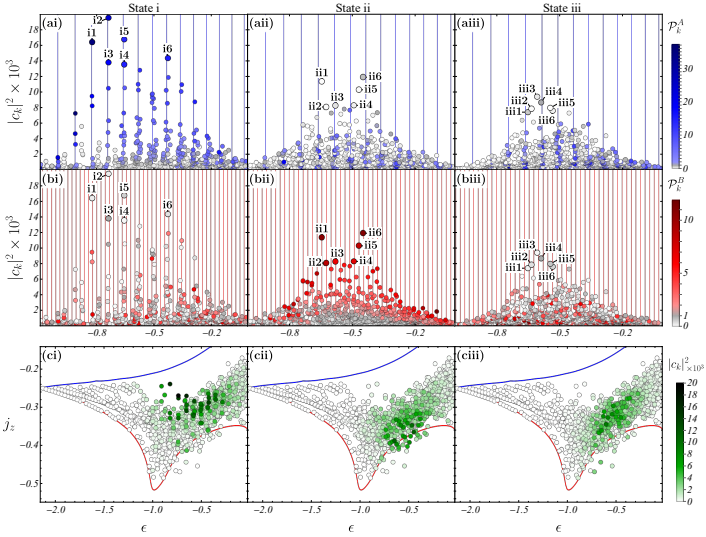

Figure 9.3: **Panels (ai)-(biii):** LDoS (circles) of states i, ii, and iii. The intensity of color for each circle represents the scarring measure of family $\mathcal{A}$ (9.8) (blue) (ai)-(aiii) and family $\mathcal{B}$ (9.9) (red) (bi)-(biii) indicated with the right bar. The vertical lines represent the Bohr-Sommerfeld quantization condition (9.11) for energies of family $\mathcal{A}$ (blue thin lines) (ai)-(aiii) and family $\mathcal{B}$ (red thin lines) (bi)-(biii). Selected eigenstates with the highest contribution to the LDoS of state i (i1-i6), state ii (ii1-ii6), and state iii (iii1-iii6). **Panels (ci)-(ciii):** Peres lattice (circles) of operator $\hat{J}_z$ for eigenstates contained in the energy interval $\epsilon_k \in [\epsilon_{\rm gs} = -2.125, 0]$. The intensity of color for each circle represents the participation degree of the eigenstates (green) in the LDoS of each state i, ii, and iii indicated with the right bar. The states i, ii, and iii are shown in Fig. 9.1 (a1)-(b2). Classical energy shell: $\epsilon = -0.5$ (chaotic). Hamiltonian parameters: $\omega = \omega_0 = 1$, $\gamma = 2\gamma_c = 1$. The system size is $j = 30$. Figure taken from Ref. [16].

To confirm the quantum scarring due to families $\mathcal{A}$ and $\mathcal{B}$ present in states i, ii, and iii, the projected Husimi function was computed for the eigenstates with the highest contribution to the LDoS. In Fig. 9.4 is shown the projected Husimi function (8.2) for each set of states i1-i6, ii1-ii6, and iii1-iii6. In the same Fig. 9.4 is shown a projected Husimi function computed over all available classical energy shells. In Appendix N.3 is shown the explicit expression for this kind of projection. As can be seen, both sets of eigenstates i1-i6 and ii1-ii6 show clearly the concentration of probability around regions which resemble both sets of families of periodic orbits from family $\mathcal{A}$ and family $\mathcal{B}$. For the set of eigenstates iii1-iii6 there is no agreement with the known families, but the projections seem to suggest that a third unidentified family of periodic orbits cause their scarring. On the other hand, the projections computed over all available classical energy shells allow to identify also the known families of periodic orbits, however they erase some finite structures captured by the projections at a single classical energy shell.

In order to study the dynamical effects associated with the fundamental families $\mathcal{A}$ and $\mathcal{B}$, an analysis of frequencies was done for the states i, ii, and iii. The survival probability can be defined as the Fourier transform of a spectral autocorrelation function (see Eq. (H.6)). In this way, the inverse Fourier transform of the survival probability allows to obtain such spectral function as [16]

$$\begin{aligned} S(E) &= \mathfrak{F}^{-1}\{S_P(t)\} \\ &= \frac{1}{2\pi\hbar_{\text{eff}}} \int_0^{+\infty} dt\, S_P(t) e^{iEt}, \end{aligned} \tag{9.12}$$

where $\hbar_{\text{eff}} = j^{-1}$. This function allows to study the time effects of the survival probability in the energy domain.

In Fig. 9.5 are shown the survival probability (4.26) and its time average for states i, ii, and iii. For state iii is shown the comparison with the analytical survival probability (4.36). Moreover, the normal periods of families $\mathcal{A}$ and $\mathcal{B}$ obtained with Eq. (9.2) are superposed for states i and ii, while for state iii is shown the time region where the correlation hole appears until satura-

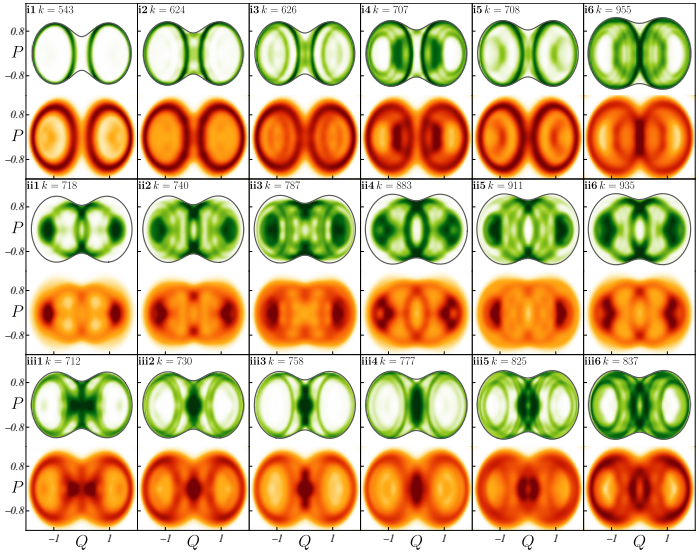

Figure 9.4: Projected Husimi function (8.2) (green color scale) for selected eigenstates with the highest contribution to the LDoS of state i (i1-i6), state ii (ii1-ii6), and state iii (iii1-iii6). Darker colors indicate higher concentrations, while white corresponds to zero. The selected eigenstates (i1-iii6) are shown in Fig. 9.1 (ai)-(biii). Projected Husimi function (N.4) (orange color scale) for the same selected eigenstates, whose projection takes all the classical energy shells. The value of the spectrum label k for each eigenstate is indicated in each panel. Hamiltonian parameters: $\omega = \omega_0 = 1$, $\gamma = 2\gamma_c = 1$. The system size is $j = 30$. Figure taken from Ref. [16].

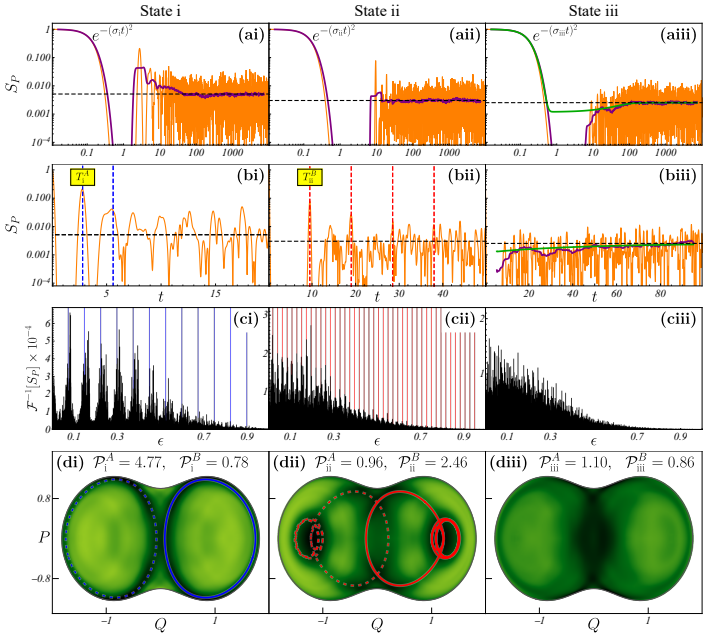

Figure 9.5: **Panels (ai)-(aiii):** Survival probability (4.26) (orange solid curve) and its time average (purple solid curve) with exponential time intervals numerically constructed for states i, ii, and iii. The horizontal black dashed line represents the asymptotic value of the survival probability. In panel (aiii) is shown the analytical survival probability (4.36) (green solid curve). **Panels (bi)-(biii):** Survival probability of the same states i, ii, and iii in a linear time scale. The vertical lines represent the periods of family $\mathcal{A}$ (blue dashed line) (bi) and family $\mathcal{B}$ (red dashed line) (bii) for states i and ii. In panel (biii) is shown the time average of the survival probability (purple solid curve) and the analytical survival probability (green solid curve), where the correlation hole appears for state iii. **Panels (ci)-(ciii):** Analysis of angular frequencies (black thin bars) for states i, ii, and iii. The vertical lines represent the periodic angular frequencies of family $\mathcal{A}$ (blue solid lines) (ci) and family $\mathcal{B}$ (red solid lines) (cii). **Panels (di)-(diii):** Projected Husimi function (8.2) of time-averaged ensemble (8.7) for states i, ii, and iii. Darker colors define higher concentrations. Periodic orbits from family $\mathcal{A}$ (blue solid curve) (di) and family $\mathcal{B}$ (red solid curve) (dii), and their corresponding mirrored images from family $\widetilde{\mathcal{A}}$ (blue dashed curve) (di) and family $\widetilde{\mathcal{B}}$ (red dashed curve) (dii). The value of the scarring measure of family $\mathcal{A}$ (9.8) and family $\mathcal{B}$ (9.9) for each state i, ii, and iii is indicated in each panel. Classical energy shell: $\epsilon=-0.5$ (chaotic). Hamiltonian parameters: $\omega=\omega_0=1$, $\gamma=2\gamma_c=1$. The system size is $j=30$. Figure taken from Ref. [16].

tion. Furthermore, the analysis of angular frequencies given by Eq. (9.12) is presented for states i, ii, and iii. In the same Fig. 9.5 is shown the projected Husimi function (8.2) for the time-average ensemble (8.7) of the same states and the scarring measure for family $\mathcal{A}$ (9.8) and family $\mathcal{B}$ (9.9). The correspondence with periodic orbits of families $\mathcal{A}$ and $\mathcal{B}$ is shown only for states i and ii. As can be seen, the survival probability of states i and ii shows clear revivals associated with quantum scarring, while for state iii shows the correlation hole, typical of an ergodic state which captures the spectral correlations of the GOE. Moreover, the periods of each family $\mathcal{A}$ and $\mathcal{B}$ describe accurately the revivals in the survival probability of states i and ii. The analysis of the angular frequencies for states i and ii show clear periodic structures around the periods of families $\mathcal{A}$ and $\mathcal{B}$, while for state iii there is no clear identified pattern. Furthermore, the projected Husimi functions for the latter states show an agreement with periodic orbits from families $\mathcal{A}$ and $\mathcal{B}$ for states i and ii, and that is corroborated with the scarring measure of each family. For state iii, the scarring measure of each family indicates that this state is unscarred by them; nevertheless, it shows a concentration region, which can be associated with an unknown periodic orbit from an unidentified family of periodic orbits.

9.2 Conclusions of Chapter 8

Two fundamental families of periodic orbits were identified in the Dicke model for the supperradiant phase ($\gamma > \gamma_c$), which emanate from a stationary point at the ground-state energy and which scar the eigenstates of the Dicke model. The proposed scarring measure of arbitrary states caused by these families of periodic orbits allows to identify the sets of eigenstates scarred by each family of periodic orbits. The analysis of the periods and Lyapunov exponents of the periodic orbits from both families allows to characterize the distribution of eigenstates scarred by each family. The semiclassical quantization of the energies using the Bohr-Sommerfeld quantization condition for the normal periods of each family of periodic orbits identify the eigen-

states scarred by such families, since they are exactly distributed around the corresponding semiclassical quantized energies. At low energies the eigenstates are ordered in lattice-like shapes, while at high energies they lose such order and form cluster-like shapes. The width of these clusters is associated with the Lyapunov exponent of the corresponding periodic orbits.

Three general behaviors about dynamical scarring are found for initial coherent states located in a chaotic energy regime: 1) If the initial state is located near a periodic orbit of family $\mathcal{A}$, it is strongly scarred by this family and its survival probability shows clear revivals associated with eigenstates scarred by this family. 2) If the initial state is located near a periodic orbit of family $\mathcal{B}$, the same behavior described for the previous case occurs. 3) If the initial state is far enough from both families of periodic orbits $\mathcal{A}$ and $\mathcal{B}$, it is unscarred by such families and show any revivals in the survival probability. In this case, the survival probability shows the correlation hole as occurs with a random state. The last behavior does not mean that the state is unscarred at all, since it can be scarred by unknown periodic orbits from unidentified families of periodic orbits.

The results exposed in this Chapter are shown in more detail in Ref. [16].

Part IV

Localization in the Dicke Model

Chapter 10

Localization Measures in Phase Space

In this Chapter is exposed a historical review on the phenomenon of quantum localization. The origin, first studies and its relation with other types of localization are reviewed and is exposed the revision of the common systems where this phenomenon is detected. Furthermore, results on localization of quantum states in the unbounded phase space of the Dicke model are shown. Generalized localization measures defined in continuous spaces and based in the generalized Rényi entropy are introduced. When the continuous space is unbounded the selection of a bounded subspace is needed. Thus, two bounded subspaces of the Dicke model are studied in detail and the implications they have.

10.1 Quantum Localization

Quantum localization has its origin in dynamical localization, a term coined to denote the quantum limitation of classical diffusion in the chaotic regime [40, 142]. Dynamical localization has been related to the well-known Anderson localization, which refers to the suppression of the classical diffusion of particles in real space due to quantum interferences and is present in one-

dimensional disordered systems [41–44]. The first systems where dynamical localization was observed were periodically kicked rotors [40, 42, 142], later it was also found in different systems, as the hydrogen atom in a monochromatic field and Rydberg atoms [262–264]. The phenomenon was also observed in conservative systems, such as the bandrandom-matrix model and quantum billiards [265–271]. The most recent studies have focused its onset on quantum many-body systems because of the increasing interest in the many-body localized phase, which is a state of matter that prevents thermalization [22, 45–48]. Other studies cover the dynamical many-body localization [272–275].

Quantum scarring and quantum localization are not synonyms, but both carry the idea of confined eigenstates [15]. The mathematical way to measure delocalization is through the exponential of an entropy [276]. Under different names this measure is widely used throughout many areas of science. In ecology, the diversity indices are used to count the number of species in a population [277]. In information science and linguistics, the perplexity quantifies how well a probabilistic model fits some data [278, 279]. In physics, delocalization is defined with respect to a given space. In finite spaces, the degree of delocalization of a quantum state is based on how much it spreads on a chosen finite basis representation, as quantified by the participation ratio and the Rényi entropy [142, 280–282]. The concept of delocalization can be extended to continuous spaces; however, in unbounded continuous spaces, the measures can reach arbitrarily large values. To investigate maximally delocalized states in this kind of unbounded spaces, a finite region must be selected as a reference volume to define the measures appropriately.

Using the phase space, a connection between the structures of classical dynamics and those of the quantum realm can be outlined [283]. The exponential of the generalized Rényi-Wehrl entropy can be used to measure the localization of quantum states in phase space [284, 285]. Quantum states may be represented in the phase space through quasiprobability distributions [120, 209].

10.2 Localization in Phase Space

In Chapter 8 was introduced a localization measure in phase space to explain the connection with the ubiquitous quantum scarring of the Dicke model. This measure can be considered as the analog of the participation ratio for a continuous basis. Nevertheless, the concept of localization in continuous basis can lead to misinterpretations when the continuous space is unbounded. The last has important repercussions, since there is no unique way to define localization measures in such spaces. In this way, a fifth goal in this Thesis was to propose a general scheme to define localization measures of quantum states in the phase space of the Dicke model.

10.2.1 Rényi Occupation

A generalized localization measure in continuous spaces can be defined as [17]

$$\mathfrak{L}_{\alpha,1}(\mathfrak{N},\Phi)=\frac{\mathcal{V}_{\alpha,1}(\mathfrak{N},\Phi)}{\mathcal{V}_{\mathfrak{N}}}\in(0,1], \tag{10.1}$$

where $\mathfrak{N}$ defines the continuous space with volume $\mathcal{V}_{\mathfrak{N}}$ and $\Phi(\upsilon)$ defines a probability distribution which depends on a parameter υ defined in the latter space $\upsilon\in\mathfrak{N}$. The last measure is called Rényi occupation of order α. The name comes from the well-known generalized Rényi entropy which allows to define the Rényi volume $\mathcal{V}_{\alpha,1}(\mathfrak{N},\Phi)$. In Appendix P is shown the procedure to define the Rényi occupation of order α, its relation with the generalized Rényi entropy, and the derivation of the Rényi volume.

To establish a connection with the phase space $\mathcal{M}$ of the Dicke model the over complete coherent-state basis $\{|\mathbf{x}\rangle\}$ is used, where $\mathbf{x}=(q,p;Q,P)$ are the coordinates of the four-dimensional phase space. The phase space of the Dicke model is an unbounded space with volume $\mathcal{V}_{\mathcal{M}}=\int_{\mathcal{M}}d\mathcal{V}(\mathbf{x})=\infty$. The last issue causes that the probability distribution $\Phi(\mathbf{x})$ is arbitrarily delocalized and the Rényi occupation (10.1) is not well defined.

A way to fix this issue is to define the Rényi occupation as follows

$$\mathfrak{L}_{\alpha,1}(\mathcal{S},\Phi)=\frac{\mathcal{V}_{\alpha,1}(\mathcal{S},\Phi)}{\mathcal{V}_{\mathcal{S}}}\in(0,1], \tag{10.2}$$

where $\mathcal{S}\subset\mathcal{M}$ is a bounded subspace with finite volume $\mathcal{V}_{\mathcal{S}}<\mathcal{V}_{\mathcal{M}}$ (see Appendix P). The selection of this kind of bounded subspaces is not universal and different choices can lead to different interpretations about localization of quantum states in phase space.

10.2.2 Rényi Occupation in Bounded Subspaces

As was explained previously, the phase space $\mathcal{M}$ of the Dicke model is unbounded and the Rényi occupation must be defined within bounded subspaces. The selection of this bounded subspaces is arbitrary in principle. For this reason, to understand the way localization of quantum states in phase space must be interpreted, two subspaces are studied in the Dicke model.

The phase space $\mathcal{M}$ of the Dicke model is conformed by a bounded atomic subspace and an unbounded bosonic subspace. Thus, the natural choice of a bounded subspace is given by the atomic subspace, such that, the following Rényi occupations of order α can be defined as follows [17, 286]

$$\mathfrak{L}_{\alpha}(\mathcal{A},\hat{\rho})=\frac{C_{\mathrm{A}}^{\alpha/(\alpha-1)}}{\mathcal{V}_{\mathcal{A}}}\left[\int_{\mathcal{A}}dQ\,dP\,\widetilde{\mathcal{Q}}_{\hat{\rho}}^{\alpha}(Q,P)\right]^{1/(1-\alpha)}, \tag{10.3}$$

$$\mathfrak{L}_{1}(\mathcal{A},\hat{\rho})=\frac{C_{\mathrm{A}}}{\mathcal{V}_{\mathcal{A}}}e^{-(1/C_{\mathrm{A}})\int_{\mathcal{A}}dQ\,dP\,\widetilde{\mathcal{Q}}_{\hat{\rho}}(Q,P)\ln[\widetilde{\mathcal{Q}}_{\hat{\rho}}(Q,P)]}, \tag{10.4}$$

where

$$\mathcal{A}=\{(Q,P)|Q^2+P^2\leq 4\} \tag{10.5}$$

represents the bounded atomic subspace of the Dicke model with phase-space volume $\mathcal{V}_{\mathcal{A}}$ and the constant C_{A} ensures the normalization of the projected Husimi function (N.4). In Appendix Q.1 is shown the complete derivation of the Rényi occupation of order α defined in the atomic subspace $\mathcal{A}$ of the Dicke model.

On the other hand, the second selected subspace corresponds to that of a classical energy shell $\mathcal{M}_{\epsilon}$ given by Eq. (8.5) with

phase-space volume $\mathcal{V}_\epsilon$, such that, can be defined the following Rényi occupations [17]

$$\mathfrak{L}_\alpha(\epsilon,\hat{\rho}) = \frac{C_\epsilon^{\alpha/(\alpha-1)}}{\mathcal{V}_\epsilon}\left[\int_{\mathcal{M}_\epsilon} d\mathbf{s}\, \mathcal{Q}_{\hat{\rho}}^{\alpha}(\mathbf{x})\right]^{1/(1-\alpha)}, \tag{10.6}$$

$$\mathfrak{L}_1(\epsilon,\hat{\rho}) = \frac{C_\epsilon}{\mathcal{V}_\epsilon} e^{-(1/C_\epsilon)\int_{\mathcal{M}_\epsilon} d\mathbf{s}\, \mathcal{Q}_{\hat{\rho}}(\mathbf{x})\ln[\mathcal{Q}_{\hat{\rho}}(\mathbf{x})]}, \tag{10.7}$$

where $\mathbf{x} = (q, p; Q, P)$ are the coordinates of the four-dimensional phase space $\mathcal{M}$ of the Dicke model, the constant C_ϵ ensures the normalization of the Husimi function within the phase space of the classical energy shell, and $d\mathbf{s} = \delta[h_{\mathrm{D}}(\mathbf{x}) - \epsilon]d\mathbf{x}$ is a surface element. In Appendix Q.2 is shown the derivation of the Rényi occupation of order α defined at a classical energy shell.

To compare the latter Rényi occupations an order α must be selected. The order selected as a case study is $\alpha = 2$, since it corresponds with the order of the well-known participation ratio (4.31) coming from the generalized participation ratios of order α (see Appendix P). Moreover, the Rényi occupation of order $\alpha = 2$ defined at a classical energy shell was previously introduced in Chapter 8 to understand the relation with quantum scarring and was considered as the analog of the participation ratio for a continuous basis. The explicit expression is given by Eq. (8.3), where can be seen that it is a particular case of Eq. (10.6) for $\alpha = 2$. Some inconveniences can arise when comparing both Rényi occupations, since the Rényi occupation defined in the atomic subspace does not depend explicitly on energy, while the Rényi occupation at a classical energy shell does. However, a peculiarity of the latter Rényi occupation is that it remains almost constant around energies close to the classical energy shell. The last is proved for selected eigenstates of the Dicke model. In Fig. 10.1 are shown the energy profile of the Husimi function (8.4) and the Rényi occupation at a classical energy shell (10.6) ($\alpha = 2$) for such eigenstates. The first eigenstate is located in the mixed energy regime where regularity and chaos coexist, while the remaining ones are located in a chaotic energy regime ($\epsilon > -0.8$). As can be seen, the profiles of the Husimi function are well described by Gaussian functions, while

the Rényi occupations remain almost constant around the corresponding classical energy shells. The last implies that the Rényi occupation at a classical energy shell is well defined even when energy changes.

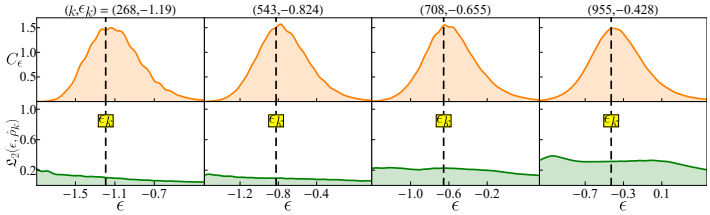

Figure 10.1: **Top panels:** Energy profile of the Husimi function (8.4) (orange solid curve) for selected eigenstates located in the chaotic energy interval $\epsilon_k \in [-1.2, -0.43]$. The vertical dashed line represents the eigenenergy of each eigenstate. The values of the spectrum label k and the eigenenergy ϵ_k for each eigenstate are indicated on top of each panel. **Bottom panels:** Energy distribution of the Rényi occupation at a classical energy shell (10.6) (green solid curve) (order $\alpha = 2$) for the same selected eigenstates. Hamiltonian parameters: $\omega = \omega_0 = 1$, $\gamma = 2\gamma_c = 1$. The system size is $j = 30$. Figure taken from Ref. [17].

Localization of Eigenstates

In order to understand further the latter Rényi occupations, the phase-space localization of eigenstates was first studied. Both Rényi occupations (10.3) and (10.6) ($\alpha = 2$) were computed for a set of eigenstates located in the chaotic energy regime.

In Fig. 10.2 is shown the probability distribution of each Rényi occupation (10.3) and (10.6) ($\alpha = 2$) for eigenstates located in the chaotic energy regime ($\epsilon > -0.8$). As can be seen, two different interpretations arise with each Rényi occupation. On the one hand, the mean value of Rényi occupation in the atomic subspace is located near unity $\mathfrak{L}_2 \sim 0.9$, which implies that the most eigenstates are completely delocalized in the atomic Bloch sphere. On the other hand, the mean value of the Rényi occupation at a classical energy shell is given by $\mathfrak{L}_2 \sim 0.4$, whose interpretation is that the most eigensates occupy less than

half of the phase space of the classical energy shell.

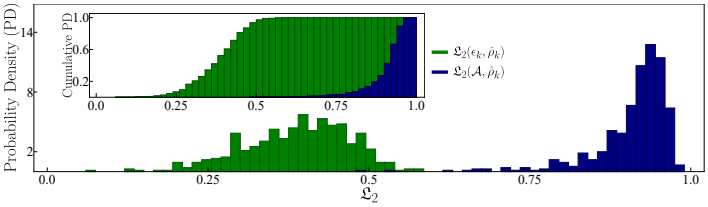

Figure 10.2: Probability distribution of the Rényi occupation at classical energy shell (10.6) (green bars) and in the atomic subspace (10.3) (blue bars) (order $\alpha = 2$) for eigenstates contained in the chaotic energy interval $\epsilon_k \in (1, 1.274)$. The inset shows the cumulative probability distribution of each probability distribution. Hamiltonian parameters: $\omega = \omega_0 = 1$, $\gamma = 2\gamma_c = 1$. The system size is $j = 30$. Figure taken from Ref. [17].

In order to elucidate the latter discrepancies between both Rényi occupations other kind of states are considered. In particular, time evolved Glauber-Bloch coherent states are considered, as well as initial Glauber-Bloch coherent states mixed in phase space.

Localization of Time Evolved Coherent States

The initial Glauber-Bloch coherent states can be evolved in time using Eq. (8.8), whose parameters are given by the initial conditions $\mathbf{x}_0 = (q_+(\epsilon), 0; Q_0, P_0)$, where q_+ is the positive root of the second-degree equation $h_{\mathrm{D}}(\mathbf{x}) - \epsilon = 0$. Moreover, a time-averaged ensemble for these coherent states can be defined as [17]

$$\overline{\rho}_{\mathbf{x}} = \frac{1}{T} \int_0^T dt\, \hat{\rho}_{\mathbf{x}}(t), \tag{10.8}$$

where $\hat{\rho}_{\mathbf{x}}(t)$ is the time evolved Glauber-Bloch coherent state.

In Fig. 10.3 are shown the Rényi occupations (10.3) and (10.6) ($\alpha = 2$) for a time evolved coherent state located in the chaotic energy regime ($\epsilon > -0.8$) and for the time-average ensemble (10.8) of the same state. In the same Fig. 10.3 is shown the time evolved Husimi function of the selected coherent state projected in each atomic (N.4) and bosonic (N.3) plane. As can be seen, the Rényi

occupation in the atomic subspace for the time evolved coherent state saturates immediately to unity, indicating that the coherent state is completely delocalized over the phase space of the Bloch sphere. Furthermore, the Rényi occupation at the classical energy shell saturates to the limit value $\mathfrak{L} \sim 1/2$, indicating that the coherent state never occupies more than half of the available phase space of the classical energy shell. This limit was previously found in Chapter 8 and is fulfilled for any pure state, since quantum interferences of the wave function prevent the complete delocalization of these kind of states over the classical energy shell. On the other hand, the Rényi occupation in the atomic subspace of the time-averaged ensemble for coherent states has a similar behavior like the instantaneous occupation reaching unity. However, the Rényi occupation at a classical energy shell for the same time-averaged ensemble of coherent states shows a characteristic behavior, since it also reaches unity manifesting that quantum ergodicity is only achievable as an ensemble property when temporal averages are performed. By inspecting the time evolved Husimi functions of the time-average ensemble of coherent states can be identified the dynamical scarring at long times.

Localization of Coherent States Mixed in Phase Space

Another test to understand the differences between the exposed Rényi occupations takes into account Glauber-Bloch coherent states mixed in phase space. Two types of mixed states are considered. The first type is a mixed state composed of two Glauber-Bloch coherent states, such that, one state is fixed in phase space, while the second one is separated from it gradually in the atomic or bosonic plane. The second type is a mixed state composed of a set of Glauber-Bloch coherent states which are added gradually until saturate completely the atomic plane.

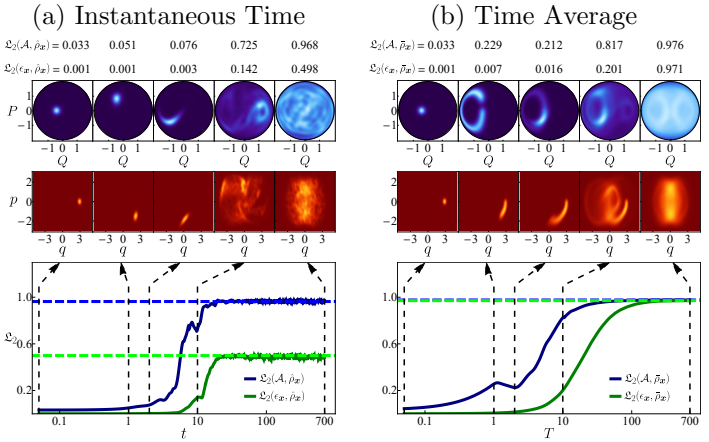

Figure 10.3: **Top panels:** Time evolved Husimi function of a coherent state (a) and a time-averaged ensemble of coherent states (b) for different finite times. The projection in phase space is shown in each atomic $Q-P$ and bosonic $q-p$ plane. **Bottom panel:** Rényi occupation at a classical energy shell (10.6) (dark green solid curve) and in the atomic subspace (10.3) (dark blue solid curve) (order $\alpha = 2$) for a time evolved coherent state (a) and a time-averaged ensemble of coherent states (10.8) (b). The horizontal lines represent the asymptotic value of the Rényi occupation for a classical energy shell (light green dashed line) and the atomic subspace (light blue dashed line). The vertical lines represent the time values where the projections are shown. The values of each Rényi occupation for each time are indicated on top of the squared panels. Classical energy shell: $\epsilon = 1$ (chaotic). Initial condition: $(Q_0, P_0) = (-0.4, 0)$. Hamiltonian parameters: $\omega = \omega_0 = 1$, $\gamma = 2\gamma_c = 1$. The system size is $j = 30$. Figure taken from Ref. [17].

The last mixed coherent states are given by [17]

$$\hat{\rho}_{\mathrm{M}}(D_{\mathcal{M}}) = \frac{1}{2}(\hat{\rho}_{\mathbf{x}_0} + \hat{\rho}_{\mathbf{x}}), \tag{10.9}$$

$$\hat{\rho}_{\mathrm{M}}(n) = \frac{1}{n}\sum_{i=1}^{n} \hat{\rho}_{\mathbf{x}_i}, \tag{10.10}$$

where $D_{\mathcal{M}}$ is the phase-space separation given by Eq. (J.6) and n designs the number of added coherent states in the atomic plane.

In Fig. 10.4 are shown the Rényi occupations (10.3) and (10.6) ($\alpha = 2$) for a mixed coherent state gradually separated in the atomic $Q - P$ and the bosonic $q - p$ planes and located in the chaotic energy regime ($\epsilon > -0.8$). In the same Fig. 10.3 is shown the Husimi function of the mixed state at different phase-space separations projected in each atomic (N.4) and bosonic (N.3) plane. As can be seen, both Rényi occupations are sensible to changes in the atomic plane $Q - P$ increasing their initial value twice and saturating. Nevertheless, the situation is different for changes in the bosonic plane $q - p$, since only the Rényi occupation at a classical energy shell behaves as before increasing its initial value twice and saturating. The Rényi occupation in the atomic subspace is unable to detect changes in the bosonic plane because of the projection of the probability distribution (Q.2), where the integration over the bosonic variables (q, p) erase information about delocalization in the bosonic plane.

In Fig. 10.5 are shown the Rényi occupations (10.3) and (10.6) ($\alpha = 2$) for a mixed coherent state composed of n added coherent states which saturate gradually the atomic $Q - P$ plane. This mixed state is located in the chaotic energy regime ($\epsilon > -0.8$). In the same Fig. 10.3 is shown the Husimi function of the mixed state at different number of added coherent states projected in each atomic (N.4) and bosonic (N.3) plane. As can be seen, the Rényi occupation in the atomic subspace linearly grows until reach unity as the number of added coherent states increases, indicating that the mixed state is completely delocalized over the available phase space of the Bloch sphere, filling it uniformly. On the other hand, the Rényi occupation at a classical energy

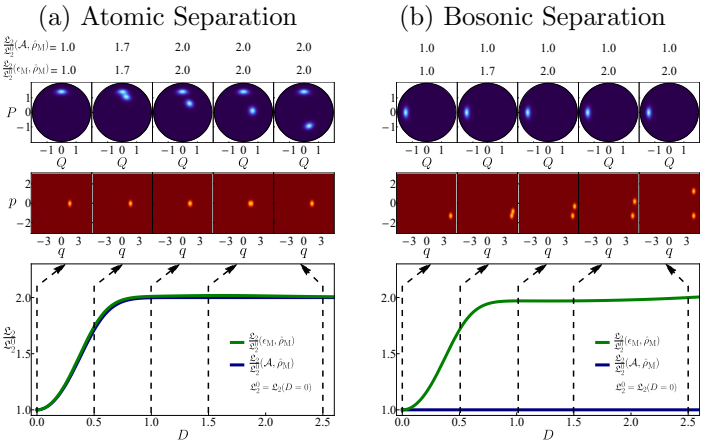

Figure 10.4: **Top panels:** Husimi function of a mixed coherent state for different finite phase-space separations in the atomic $Q-P$ (a) and bosonic $q-p$ (b) plane. The projection in phase space is shown in each atomic $Q-P$ and bosonic $q-p$ plane. **Bottom panel:** Rényi occupation at a classical energy shell (10.6) (dark green solid curve) and in the atomic subspace (10.3) (dark blue solid curve) (order $\alpha = 2$) scaled to their initial value at $D_{\mathcal{M}} = 0$ for a mixed coherent state (10.9) gradually separated in the atomic $Q-P$ (a) and bosonic $q-p$ (b) plane. The vertical lines represent the values of the phase-space separation where the projections are shown. The values of each Rényi occupation for each time are indicated on top of the squared panels. Classical energy shell: $\epsilon = 1$ (chaotic). Hamiltonian parameters: $\omega = \omega_0 = 1$, $\gamma = 2\gamma_c = 1$. The system size is $j = 30$. Figure taken from Ref. [17].

shell only covers a fraction $\mathfrak{L}_2 \sim 0.1$ of the available phase space of the classical energy shell. The last is clearly visible in the Husimi projections over the bosonic plane $q-p$, since the mixed state never covers completely the bosonic phase space as occurs with the atomic one.

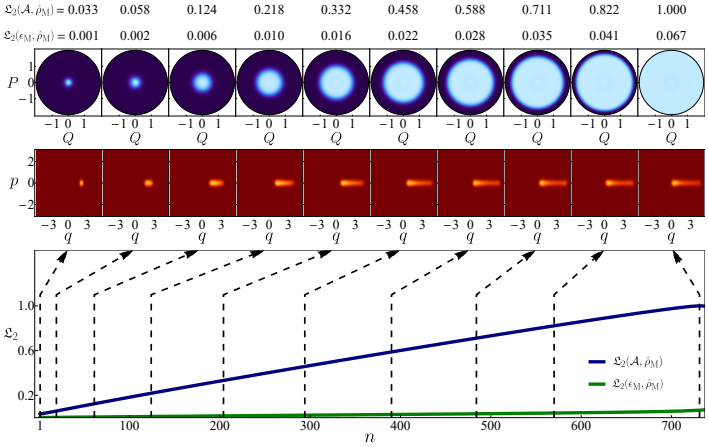

Figure 10.5: **Top panels:** Husimi function of a mixed coherent state for different number of added coherent states, which saturate the atomic plane $Q-P$. The projection in phase space is shown in each atomic $Q-P$ and bosonic $q-p$ plane. **Bottom panel:** Rényi occupation at a classical energy shell (10.6) (dark green solid curve) and in the atomic subspace (10.3) (dark blue solid curve) (order $\alpha = 2$) for a mixed coherent state (10.10) composed of n added coherent states which saturate the atomic plane $Q-P$. The vertical lines represent the values of the phase-space separation where the projections are shown. The values of each Rényi occupation for each time are indicated on top of the squared panels. Classical energy shell: $\epsilon = 1$ (chaotic). Hamiltonian parameters: $\omega = \omega_0 = 1$, $\gamma = 2\gamma_c = 1$. The system size is $j = 30$. Figure taken from Ref. [17].

10.3 Conclusions of Chapter 9

A general framework to define localization measures defined over continuous spaces was presented. It was shown that these localization measures are not well defined for unbounded continuous

spaces and the selection of bounded subspaces must be done. The selection criterion for these bounded subspaces is not universal and different choices could lead to different interpretations about localization of quantum states in phase space.

The localization measure presented was called Rényi occupation of order α because of their similarity with the generalized Rényi entropy of order α. Two particular bounded subspaces were selected to study localization of quantum states in the phase space of the Dicke model. One that is defined in the bounded atomic subspace and other one defined at a classical energy shell. It was shown that the Rényi occupation in the atomic subspace can miss information about localization in the bosonic plane and the Rényi occupation at a classical energy shell is more appropriate for states well localized in energy as eigenstates or coherent states. The selected order of the Rényi occupation was $\alpha = 2$ because of their connection with the well-known participation ratio. Nevertheless, other orders can reveal different aspects about localization of quantum states that the selected order cannot.

The results exposed in this Chapter are shown in more detail in Ref. [17].

Chapter 11

Localization in Phase Space and Quantum Scarring

In this Chapter is exposed one of the localization measures in phase space introduced in Chapter 10 as a tool to identify unstable periodic orbits based on the order of the measure. The selected localization measure is the Rényi occupation defined at a classical energy shell of the Dicke model. Moreover, a new localization measure is introduced, which is a scaling of the usual Rényi occupation by the Rényi occupation of maximally delocalized sates. The identification of unstable periodic orbits is achieved qualitatively with the projections for different moments of the Husimi function and quantitatively using the perturbing method introduced in Chapter 9. An analysis of the dynamics of the detected periodic orbits that can clarify some behaviors of quantum localization is also exposed.

11.1 Rényi Occupation and Quantum Scars

In Chapter 10 was introduced the Rényi occupation of order α to measure localization of quantum states in continuous spaces. It was shown that when the continuous space is unbounded, to take bounded subspaces is needed in order to define the Rényi occupation correctly. Thus, to study localization in the phase space of the Dicke model two bounded subspaces were selected. The first one defined in the bounded atomic subspace and the second one defined at a classical energy shell. The order of the Rényi occupation was selected as $\alpha = 2$. It was found that the first Rényi occupation losses information about quantum localization in the bosonic subspace, such that, the second Rényi occupation is more adequate for states well localized in energy. Nevertheless, the last results have a functionality with the selected order of the Rényi occupation and different aspects related to quantum scarring can be revealed when different orders are studied. In this way, a sixth goal in this Thesis was to understand the connection between different orders of the Rényi occupation defined at a classical energy shell and the ubiquitous quantum scarring presented by the Dicke model, such that, the Rényi occupation can serve as a tool to identify unstable periodic orbits which causes such scarring.

11.1.1 Maximally Delocalized States

An alternative localization measure in phase space can be defined taking into account the value of the Rényi occupation of maximally delocalized states as are the random states. Contrary to the Rényi occupation which formally measures delocalization, the following expression measures localization properly [18]

$$\Lambda_{\alpha,1}(\epsilon,\hat{\rho}) = \frac{\mathfrak{L}^{\max}_{\alpha,1}}{\mathfrak{L}_{\alpha,1}(\epsilon,\hat{\rho})} \in [1,\infty), \tag{11.1}$$

where the limit value $\Lambda_{\alpha,1} = 1$ defines a state delocalized as a random state, while a finite value $\Lambda_{\alpha,1} = L$ defines a state L

times more localized as a random state. The Rényi occupation for maximally delocalized states is given by [18]

$$\mathfrak{L}_{\alpha}^{\max} = \Gamma^{1/(1-\alpha)}(\alpha+1), \tag{11.2}$$

$$\begin{aligned}\mathfrak{L}_{1}^{\max} &= \lim_{\alpha\to 1} \mathfrak{L}_{\alpha}^{\max} \\ &= e^{\gamma-1}, \end{aligned} \tag{11.3}$$

where γ is the Euler-Mascheroni constant given by Eq. (3.31). The last expressions are formally developed for systems with finite dimension of the Hilbert space; however, they can be extrapolated to systems with infinite-dimensional Hilbert space as the Dicke model. The bounded phase space of the classical energy shells induces a finite effective dimension which allows to use the Rényi occupation for states maximally delocalized in Hilbert spaces with finite dimension as a benchmark to compare the delocalization degree of generic states [18, 19]. In Appendix R is shown the derivation of the Rényi occupation for maximally delocalized states in Hilbert spaces with finite dimension.

In order to reveal some features about the order α of the Rényi occupation in light of quantum scarring, the localization measure (11.1) was computed for eigenstates of the Dicke model for different orders. In Fig. 11.1 is shown the localization measure (A.17) as a function of the order α for eigenstates of the Dicke model located in a chaotic energy regime. As can be seen, different behaviors arise with the different orders. Most eigenstates cluster around a value $\Lambda \sim 1$, indicating they behave as random states for all orders. Nevertheless, some eigestates reach high localization values for high orders. The relation is not clear, since some eigenstates which have the highest localization at the highest order show lower localization at lower orders, such that, multiple crossings appear between these eigenstates. The high localization of such eigenstates is due to strong quantum scarring [18]. In this way, the further analysis of different orders can reveal important aspects in this regard.

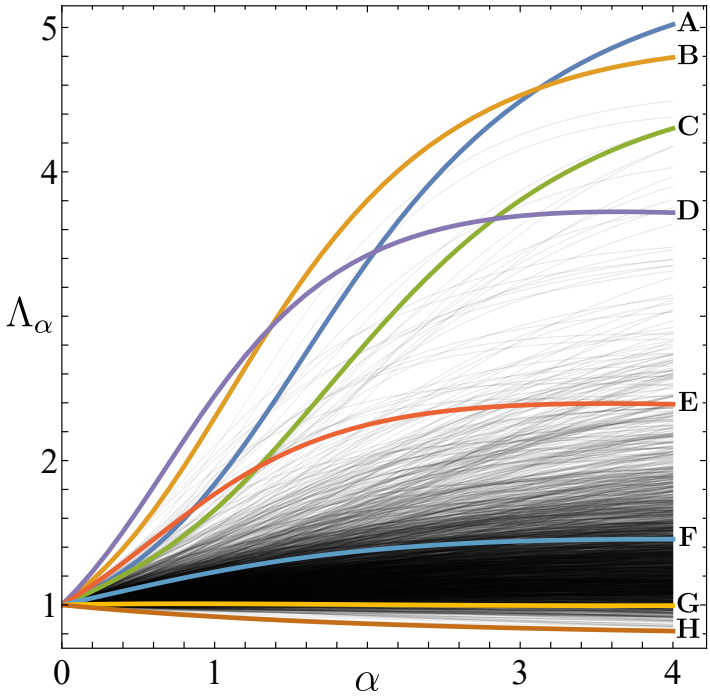

Figure 11.1: Localization measure (11.1) as a function of the order α (gray thin lines) for eigenstates contained in the chaotic energy interval $\epsilon_k \in [-0.6, -0.4]$. The colored curves represent the selected eigenstates A-H. Hamiltonian parameters: $\omega = \omega_0 = 1$, $\gamma = 2\gamma_c = 1$. The system size is $j = 100$. Figure taken from Ref. [18].

11.1.2 Identification of Unstable Periodic Orbits

The order α of Rényi occupation at a classical energy shell (10.6) defines the moments or powers of the unnormalized Husimi function of a state $\hat{\rho}$ as follows [18]

$$\mathcal{Q}^{\alpha}_{\hat{\rho}}(\mathbf{x}) = \langle \mathbf{x}|\hat{\rho}|\mathbf{x}\rangle^{\alpha}. \tag{11.4}$$

The study of the moments of the Husimi function are a useful tool to reveal unstable periodic orbits that scar strongly some eigenstates of the Dicke model. In general, low moments $\alpha < 1$ tend to homogenize the projection of the Husimi function looking blurrier, while high moments $\alpha > 1$ tend to erase small contributions in the projection of the Husimi function and enhance the high concentration regions where the periodic orbits lie. The last feature allows to determine regions with high concentration which can be used as initial conditions to find unstable periodic orbits with the monodromy method exposed in Appendix O.1.

In Fig. 11.2 is shown the projected Husimi function (N.2) at different moments α for selected eigenstates A-H highly localized and for random states centered at a chaotic classical energy shell. As can be seen, all projections of the eigenstates show structures resembling periodic orbits in contrast with those of random states, which show granular structures. The projected Husimi functions look more homogeneous for low moments $\alpha < 1$ and for high moments $\alpha > 1$ they delimit better the high concentration regions where the unstable periodic orbits lie. The last correspondence can be seen for some eigenstates whose corresponding unstable periodic orbits were identified taking as initial conditions the high concentration regions of the Husimi function for the highest moment, and whose trajectories were found explicitly with the monodromy method (see Appendix O.1). The last periodic orbits do not correspond to the fundamental families of periodic orbits $\mathcal{A}$ and $\mathcal{B}$ that emanate from a stationary point, since those orbits are well known and can be traced back. Thus, the identified periodic orbits through the high moments of the Husimi function can belong to other unidentified families of periodic orbits [18]. Moreover, the scarring measure (9.7) can be

used to confirm the scarring degree of the eigenstates caused by these identified unstable periodic orbits. On the other hand, examining all projections of the Husimi function for high moments is clearly understood why grows the localization value with the order α for eigenstates strongly scarred, since the regions with high concentration decrease in the available phase space indicating high localization degree.

11.1.3 Dynamics of Unstable Periodic Orbits

The dynamics of the unstable periodic orbits can be used to clarify the localization effects saw in the projections of the Husimi function at high moments for eigenstates strongly scarred. The last is achieved by considering a tubular state $\hat{\rho}_{\mathcal{O}_\epsilon}$ which resembles the corresponding classical unstable periodic orbit $\mathcal{O}_\epsilon$ with energy ϵ and period T. The tubular state is composed of coherent states $|\mathbf{x}\rangle$ centered at $\mathbf{x}(t) \in \mathcal{O}_\epsilon$, it was introduced in Chapter 9 to define the scarring measure of periodic orbits (9.7) and is given by Eq. (O.16). Its Husimi function given by Eq. (O.17) can be projected using Eq. (N.2) at the classical energy shell $\epsilon = h_{\mathrm{D}}(\mathcal{O}_\epsilon)$, such that, their classical dynamics can be studied.

In Fig. 11.3 is shown the projected Husimi function (8.2) for tubular states which represent the corresponding unstable periodic orbits that scar strongly eigenstates A-D. In the same Fig. 11.3 is shown the three-dimensional representation of these unstable periodic orbits. As can be seen, all projections of the Husimi function for tubular states show an agreement with those of eigenstates the unstable periodic orbits scar. Regions where the dynamics is slow are associated with regions of high concentration of the Husimi function, while regions where the dynamics is fast are associated with regions of low concentration of the Husimi function. The last is confirmed when the high moments of the Husimi function for the eigenstates are analyzed in Fig 11.2. On the one hand, the high concentrations regions of the Husimi function remain in regions with slow dynamics. On the other hand, the low concentration regions of the Husimi function tend to disappear in regions with fast dynamics. Furthermore, an analysis of the three-dimensional representations shows that

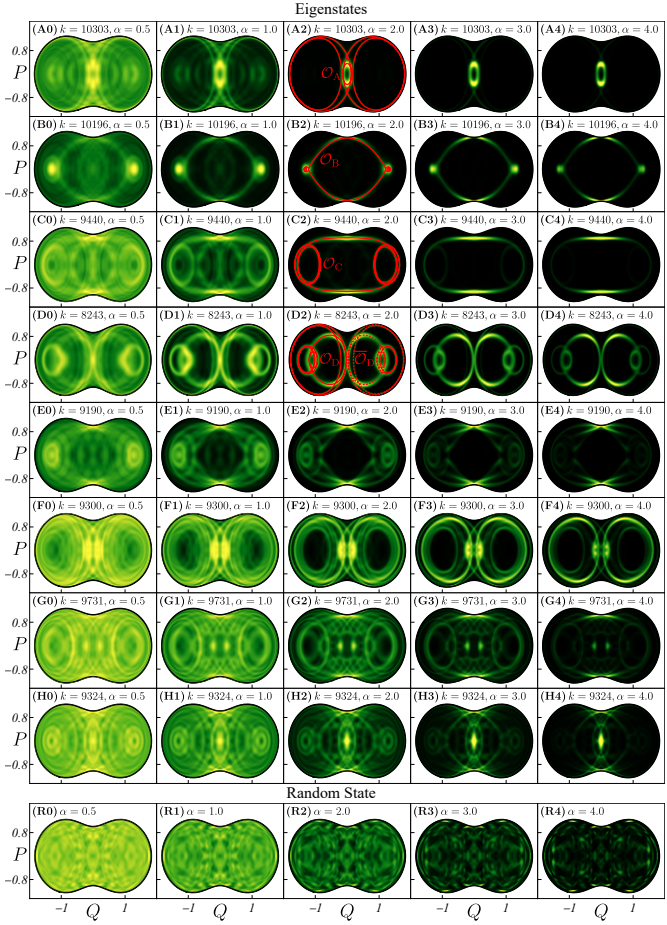

Figure 11.2: **Panels (A0)-(H4):** Projected Husimi function (N.2) for selected eigenstates located in a chaotic energy regime ($\epsilon > -0.8$). The projections are show for different moments α of the Husimi function. Lighter colors indicate higher concentrations, while black corresponds to zero. Unstable periodic orbits (red solid curve) (A2),(B2),(C2),(D2). In panel (D2) is shown the mirrored image (red dashed curve) of the periodic orbit. The selected eigenstates A-H are shown in Fig. 11.1. The values of the spectrum label k and the moment α of the Husimi function for each eigenstate are indicated in each panel. **Panels (R0)-(R4):** Projected Husimi function for random states centered at a chaotic energy shell. Classical energy shell: -0.5 (chaotic). Hamiltonian parameters: $\omega = \omega_0 = 1$, $\gamma = 2\gamma_c = 1$. The system size is $j = 100$. Figure taken from Ref. [18].

the unstable periodic orbits are quite complex in phase space.

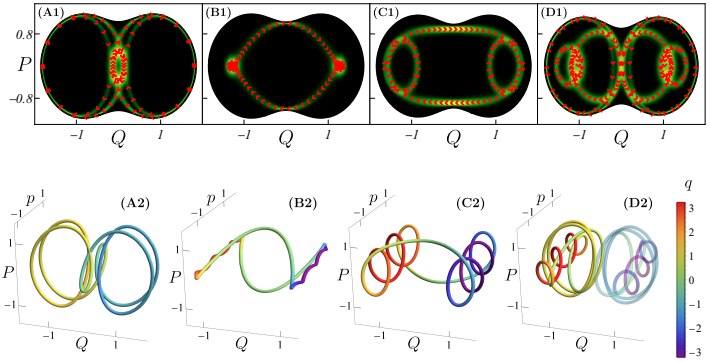

Figure 11.3: **Panels (A1)-(D1):** Projected Husimi function (8.2) for tubular states (O.16) centered at a chaotic energy shell. The projections are show for different moments α of the Husimi function. Lighter colors indicate higher concentrations, while black corresponds to zero. The red arrows represent the dynamics of the unstable periodic orbits and are placed at constant time intervals. **Panels (A2)-(D2):** Three-dimensional unstable periodic orbits. The intensity of color represents the value of the coordinate q indicated with the right bar. Classical energy shell: -0.5 (chaotic). Hamiltonian parameters: $\omega = \omega_0 = 1$, $\gamma = 2\gamma_c = 1$. The system size is $j = 100$. Figure taken from Ref. [18].

11.2 Conclusions of Chapter 10

The Rényi occupation of order α for maximally delocalized states (random states) in Hilbert spaces with finite dimension is an exclusive function of that order. The last result can be extrapolated to systems with infinite-dimensional Hilbert space as the Dicke model. When the Rényi occupation is defined at a classical energy shell, the bounded phase space of the classical energy shell induces a finite effective dimension and the Rényi occupation for maximally delocalized states in this subspace has the same functional form. The last result can be used as a benchmark to characterize the delocalization degree of generic states,

such that, an alternative localization measure in phase space can be defined. It was found that generally the localization degree grows with the order of the latter measure for strongly scarred eigenstates of the Dicke model.

The moments of the Husimi function are determined by the order α of the Rényi occupation defined at a classical energy shell. It was shown that the analysis of the moments of the Husimi function are a useful tool to identify visually unstable periodic orbits which scar strongly some eigenstates of the Dicke model. Furthermore, the explicit trajectories can be found using the monodromy method for periodic orbits. It was found that the identified orbits do not correspond with the well-known fundamental families of periodic orbits that emanate from a stationary point introduced in Chapter 8 and widely exposed in Chapter 9. It is conjectured that these periodic orbits belong to unidentified families of periodic orbits which scar the eigenstates of the Dicke model.

The results exposed in this Chapter are shown in more detail in Refs. [18, 19].

Part V

Conclusions

Chapter 12

Conclusions of the Thesis

The results exposed in this Thesis show the relevance and versatility of the Dicke model as a paradigmatic model in quantum mechanics, specifically in the field of quantum optics. This fundamental interacting radiation-matter system allows to analyze a plethora of interesting phenomenology. The main topics investigated in this work, chaos, scarring and localization, seemed to be disconnected at first sight; nevertheless, a close bond unites them indicating that nature cannot be described under an absolute theory or point of view. The intricate behavior of nature forces us to use all available tools to try to understand it and predict it.

The study of quantum chaos in the Dicke model with the correlation hole showed that spectral correlations can be successfully identified in the time evolution of a quantum observable, which makes it attractive in the experimental field when spectral information is not accessible. The spectral correlations were identified as GOE correlations from RMT with the derivation of an analytical expression developed from this ensemble, which verified the numerical studies. GOE correlations arise typically in quantum systems whose classical limit is chaotic and support the validity

of the correlation hole as dynamical indicator of quantum chaos. Moreover, the study of the classical and quantum dynamics of coherent states allowed to identify quantum dynamical effects which have their origin in chaos or scarring. Thus, states influenced by chaotic behavior capture spectral GOE correlations and show the correlation hole in their dynamics. On the other hand, states affected by scarring show typically no correlation hole and instead show clearly revivals associated with unstable periodic orbits. In this way, the absence of the correlation hole can be used as a tool to identify scarred states in chaotic regimes.

Scarring is a peculiar phenomenon were structures of the classical domain affect the quantum one. The discovery of an omnipresent scarring in all eigenstates of the Dicke model changed the landscape about this phenomenon, originally attributed to some sets of particular states. The scarring can be seen as a source of localization, and for that reason, it was thought initially that states strongly scarred were highly localized. This pictured changed when the ubiquitous scarring saw the light, since some scarred states can be as delocalized as maximally delocalized states. Nevertheless, an upper bound of the spreading of quantum sates was found when studying quantum localization in phase space, implying that quantum pure states are localized in some extent. The last result lead us to propose a definition of quantum ergodicity as an ensemble property, where the complete distribution of states in phase space is only achievable when time averages are performed. The intrinsic relation between scarring and localization is far from being understood completely and constitutes a topic for further study.

Localization in phase space was formulated mathematically as the exponential of the generalized Rényi entropy. A general scheme to define localization measures in continuous spaces was proposed, which produced peculiarities for unbounded spaces where these measures cannot be defined appropriately. This issue was resolved by selecting bounded subspaces, implying that there is no absolute way to define localization in such spaces. Furthermore, the applicability of these measures was based in their potential ability to detect unstable periodic orbits.

Thereby, it can be seen that the latter phenomenology is

correlated and the particularity of this this work is that it can be studied with one simple and interesting model, the ever reliable Dicke model.

The initial motivation of this Thesis was exposed as the necessity to provide a general theoretical framework to understand and develop quantum technologies, which are revolutionizing our daily world. Nevertheless, another personal motivation is based in the simple pleasure to understand nature and its implications. Future studies that can be outlined following this line of research are to extend the developed analyses to open quantum systems, where the dissipative effects make them more realistic. I hope this Thesis serves as a guide for future scientists interested in this kind of phenomenology.

Part VI

Appendices

Appendix A

Derivation of the Dicke Hamiltonian

In this Appendix is exposed the complete derivation of the Dicke Hamiltonian, obtaining explicitly each one of the energy terms that compose it under a set of conventional approximations.

A.1 Quantization of the Electromagnetic Field

The classical energy or Hamiltonian H of an electromagnetic field, in SI units, is given by

$$H_{\mathrm{F}}(t) = \frac{1}{2}\int dV \left[\varepsilon_0 |\mathbf{E}(\mathbf{q},t)|^2 + \frac{1}{\mu_0}|\mathbf{B}(\mathbf{q},t)|^2\right], \tag{A.1}$$

where $\mathbf{E}$ and $\mathbf{B}$ represent the electric and magnetic fields, respectively, $\mathbf{q}$ and t are variables of position and time, ε_0 and μ_0 are the permittivity and permeability of free space, and V identifies an effective or reference volume.

Without loss of generality, a simple scenario can be considered, where an electromagnetic field is confined within an optical

cavity of volume V, the electric field $\mathbf{E}(\mathbf{q},t) = E_x(z,t)\mathbf{i}$ propagates only in the z direction and is polarized in the x direction, the cavity has perfect conducting walls at the ends $z = 0$ and $z = L$, and there are no charges, currents or dielectric media inside the cavity [205]. The latter system is represented in Fig. A.1.

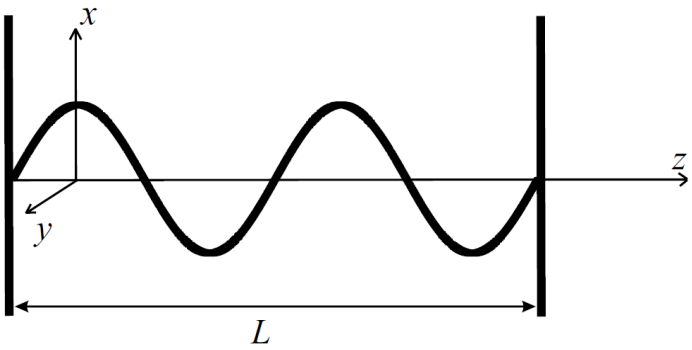

Figure A.1: Optical cavity of volume V with perfect conducting walls at the ends $z = 0$ and $z = L$. The electric field propagates only in the z direction and is polarized in the x direction. Figure taken from Ref. [205].

The Maxwell equations for electromagnetic fields in vacuum, in SI units, which represent the system described within the cavity are given by

$$\nabla \times \mathbf{E}(\mathbf{q},t) = -\frac{\partial \mathbf{B}(\mathbf{q},t)}{\partial t}, \tag{A.2}$$

$$\nabla \times \mathbf{B}(\mathbf{q},t) = \mu_0 \varepsilon_0 \frac{\partial \mathbf{E}(\mathbf{q},t)}{\partial t}, \tag{A.3}$$

$$\nabla \cdot \mathbf{E}(\mathbf{q},t) = 0, \tag{A.4}$$

$$\nabla \cdot \mathbf{B}(\mathbf{q},t) = 0. \tag{A.5}$$

From these equations and the boundary conditions $E_x(0,t) = E_x(L,t) = 0$, it is possible to find a solution for the electric field

$$E_x(z,t) = \sqrt{\frac{2\omega^2}{V\varepsilon_0}} q(t) \sin(kz), \tag{A.6}$$

where the boundary condition $z = L$ gives the allowed radiation frequencies $\omega_n = c(n\pi/L)$, which are function of an integer $n = 1, 2, \ldots$ and $c = 1/\sqrt{\varepsilon_0 \mu_0}$ is the speed of light. In this case, only one radiation frequency (single mode) is considered and denoted by the parameter ω. The parameter k identifies the wave number associated with the frequency through the expression $k = \omega/c$. The term $q(t)$ is a function of time only and has length dimensions.

On the other hand, a solution for the magnetic field can be obtained also from Maxwell equations, such that $\mathbf{B}(\mathbf{q}, t) = B_y(z, t)\mathbf{j}$ with

$$B_y(z, t) = \frac{\mu_0 \varepsilon_0}{k} \sqrt{\frac{2\omega^2}{V \varepsilon_0}} \dot{q}(t) \cos(kz), \tag{A.7}$$

where $\dot{q}(t)$ is a function of time too. If the function $q(t)$ is considered as a canonical position variable, then its corresponding canonical momentum variable can be obtained as $p(t) = \dot{q}(t)$. Using the previous results (A.6) and (A.7) in Eq. (A.1), it is found

$$H_{\mathrm{F}}(t) = \frac{1}{2}[p^2(t) + \omega^2 q^2(t)], \tag{A.8}$$

that is, the classical energy of a single-mode electromagnetic field is equivalent to the energy of a harmonic oscillator with unitary mass.

Now, to obtain a quantum analog of Eq. (A.8), we apply the quantization procedure proposed by P. A. M. Dirac in 1927 [287]. Basically, the procedure consists of substituting the conjugate canonical variables (q, p) of the classical system by the equivalent operators $\hat{q}$ and $\hat{p}$ of the quantum system, which satisfy the commutation relation $[\hat{q}, \hat{p}] = i\hbar\hat{1}$. In this way, the Hamiltonian can be written as an operator $\hat{H}_{\mathrm{F}}$, and in a similar way the electric and magnetic fields $\hat{\mathbf{E}}$ and $\hat{\mathbf{B}}$. Nevertheless, it is useful to introduce the non-Hermitian creation-annihilation operators $\hat{a}^\dagger$ and $\hat{a}$, which are defined by the expression

$$\hat{a} = \frac{1}{\sqrt{2\hbar\omega}}(\omega\hat{q} + i\hat{p}). \tag{A.9}$$

Thus, the set of bosonic operators $\{\hat{a}^\dagger, \hat{a}, \hat{1}\}$ satisfy the H(1) algebra (Heisenberg-Weyl algebra), which is defined by the com-

mutation relations

$$[\hat{a}, \hat{a}^\dagger] = \hat{1}, \tag{A.10}$$

$$[\hat{a}, \hat{1}] = [\hat{a}^\dagger, \hat{1}] = \hat{0}. \tag{A.11}$$

Taking into account the latter considerations, the electric and magnetic fields can be written as the operators

$$\hat{E}_x(z,t) = \mathcal{E}_0 \sin(kz)[\hat{a}^\dagger(t) + \hat{a}(t)], \tag{A.12}$$

$$\hat{B}_y(z,t) = i\mathcal{B}_0 \cos(kz)[\hat{a}^\dagger(t) - \hat{a}(t)], \tag{A.13}$$

where $\mathcal{E}_0 = \sqrt{\hbar\omega/(V\varepsilon_0)}$ and $\mathcal{B}_0 = (\mu_0/k)\sqrt{\varepsilon_0\hbar\omega^3/V}$. Finally, the quantum Hamiltonian of the electromagnetic field is given by

$$\begin{aligned}\hat{H}_{\mathrm{F}}(t) &= \frac{1}{2}[\hat{p}^2(t) + \omega^2\hat{q}^2(t)] \\ &= \hbar\omega\left[\hat{a}^\dagger(t)\hat{a}(t) + \frac{1}{2}\hat{1}\right].\end{aligned} \tag{A.14}$$

A.2 Atom-Field Interaction

The classical interaction energy between an atom ($\mathcal{N} = 1$) with a single interacting electron and an external electromagnetic field is described with the minimal-coupling Hamiltonian [51]

$$H_{\text{a-f}}(\mathbf{q},t) = \frac{1}{2m}[\mathbf{p} - e\mathbf{A}(\mathbf{q},t)]^2 + eU(\mathbf{q},t) + V(q), \tag{A.15}$$

where e and m are the charge and mass of the electron, $\mathbf{p}$ is the canonical momentum, $\mathbf{A}(\mathbf{q},t)$ and $U(\mathbf{q},t)$ are the vector and scalar potentials of the external field, respectively, and $V(q)$ is an electrostatic potential that binds the electron to the atomic nucleus.

On the other hand, the motion of a free electron ($V(q) = 0$) can be described by the time-dependent Schrödinger equation

$$i\hbar\frac{\partial\psi(\mathbf{q},t)}{\partial t} = -\frac{\hbar^2}{2m}\nabla^2\psi(\mathbf{q},t), \tag{A.16}$$

where $\psi(\mathbf{q},t)$ is the wave function of the electron and $\rho(\mathbf{q},t) = |\psi(\mathbf{q},t)|^2$ represents the probability density to find it at the position $\mathbf{q}$ and time t. Now, if a solution $\psi(\mathbf{q},t) \to \psi(\mathbf{q},t)e^{i\chi}$ is considered, where χ defines a constant phase, then $\rho(\mathbf{q},t)$ remains unchanged, since two wave functions differing by only a constant phase represent the same physical state. Nevertheless, if this phase varies locally, that is, it is a function of position an time $\chi(\mathbf{q},t)$, then

$$\psi(\mathbf{q},t) \to \psi(\mathbf{q},t)e^{i\chi(\mathbf{q},t)}, \tag{A.17}$$

and $\rho(\mathbf{q},t)$ remains unchanged again, but in order to satisfy local gauge (phase) invariance, the time-dependent Schrödinger equation must become in

$$i\hbar\frac{\partial\psi(\mathbf{q},t)}{\partial t} = \left[-\frac{\hbar^2}{2m}\left[\nabla - i\frac{e}{\hbar}\mathbf{A}(\mathbf{q},t)\right]^2 + eU(\mathbf{q},t)\right]\psi(\mathbf{q},t), \tag{A.18}$$

where the potentials $\mathbf{A}(\mathbf{q},t)$ and $U(\mathbf{q},t)$ are given by

$$\mathbf{A}(\mathbf{q},t) \to \mathbf{A}(\mathbf{q},t) + \frac{\hbar}{e}\nabla\chi(\mathbf{q},t), \tag{A.19}$$

$$U(\mathbf{q},t) \to U(\mathbf{q},t) - \frac{\hbar}{e}\frac{\partial\chi(\mathbf{q},t)}{\partial t}, \tag{A.20}$$

to make possible the transformation (A.17). Moreover, it is important to emphasise that these potentials $\mathbf{A}(\mathbf{q},t)$ and $U(\mathbf{q},t)$ are gauge-dependent; however, at the same time they define the gauge-independent electric and magnetic fields

$$\mathbf{E}(\mathbf{q},t) = -\nabla U(\mathbf{q},t) - \frac{\partial\mathbf{A}(\mathbf{q},t)}{\partial t}, \tag{A.21}$$

$$\mathbf{B}(\mathbf{q},t) = \nabla\times\mathbf{A}(\mathbf{q},t). \tag{A.22}$$

With the previous development, the natural extension of the minimal-coupling Hamiltonian (A.15) to its quantum analog is given by

$$\hat{H}_{\text{a-f}}(\mathbf{q},t) = \frac{1}{2m}[\hat{\mathbf{p}} - e\hat{\mathbf{A}}(\mathbf{q},t)]^2 + e\hat{U}(\mathbf{q},t) + \hat{V}(q), \tag{A.23}$$

where $\hat{\mathbf{p}} = -i\hbar\nabla$ is the momentum operator.

A.2.1 Dipole Approximation

A typical simplification of the Hamiltonian (A.23) consists in apply the dipole approximation [51]. To do that, an electron bound by an electrostatic potential $V(q)$ to a nucleus located at $\mathbf{q}_0$ is considered. The atom is immersed in an electromagnetic plane wave described by a vector potential $\mathbf{A}(\mathbf{q}_0+\mathbf{q},t) = \mathbf{A}(t)e^{i\mathbf{k}\cdot(\mathbf{q}_0+\mathbf{q})}$, which can be written in the dipole approximation $(\mathbf{k}\cdot\mathbf{q} \ll 1)$ as

$$\begin{aligned}\mathbf{A}(\mathbf{q}_0+\mathbf{q},t) &= \mathbf{A}(t)e^{i\mathbf{k}\cdot\mathbf{q}_0}(1+i\mathbf{k}\cdot\mathbf{q}+\ldots)\\ &\simeq \mathbf{A}(t)e^{i\mathbf{k}\cdot\mathbf{q}_0}.\end{aligned} \tag{A.24}$$

Taking this approximation, the time-dependent Schrödinger equation with the condition $\mathbf{A}(\mathbf{q},t) \equiv \mathbf{A}(\mathbf{q}_0,t)$, can be written as

$$i\hbar\frac{\partial\psi(\mathbf{q},t)}{\partial t} = \left[-\frac{\hbar^2}{2m}\left[\nabla - i\frac{e}{\hbar}\mathbf{A}(\mathbf{q}_0,t)\right]^2 + V(q)\right]\psi(\mathbf{q},t), \tag{A.25}$$

where the radiation gauge was considered

$$U(\mathbf{q},t) = 0, \tag{A.26}$$

$$\nabla\cdot\mathbf{A}(\mathbf{q},t) = 0. \tag{A.27}$$

Now, using the transformation (A.17) with the local phase given by $\chi(\mathbf{q},t) = (e/\hbar)\mathbf{q}\cdot\mathbf{A}(\mathbf{q}_0,t)$, the time-dependent Schrödinger equation takes the form

$$i\hbar\frac{\partial\psi(\mathbf{q},t)}{\partial t} = \left[-\frac{\hbar^2}{2m}\nabla^2 + V(q) - e\mathbf{q}\cdot\mathbf{E}(\mathbf{q}_0,t)\right]\psi(\mathbf{q},t), \tag{A.28}$$

where the relation $\mathbf{E}(\mathbf{q},t) = -\partial\mathbf{A}(\mathbf{q},t)/\partial t$ was used.

At this point, the atom-field Hamiltonian $\hat{H}_{\text{a-f}}$ can be written as a sum of two contributions, one that represents the atomic energy $\hat{H}_{\text{a}}$, and other one that represents the atom-field interaction energy $\hat{H}_{\text{i}}$

$$\hat{H}_{\text{a-f}}(\mathbf{q},t) = \hat{H}_{\text{a}}(\mathbf{q}) + \hat{H}_{\text{i}}(\mathbf{q},t), \tag{A.29}$$

$$\hat{H}_{\text{a}}(\mathbf{q}) = \frac{\hat{\mathbf{p}}^2}{2m} + \hat{V}(q), \tag{A.30}$$

$$\hat{H}_{\text{i}}(\mathbf{q},t) = -e\hat{\mathbf{q}}\cdot\hat{\mathbf{E}}(\mathbf{q}_0,t). \tag{A.31}$$

The last Hamiltonians can be represented in terms of the atomic transition operators given by $\hat{\sigma}_{nn'} = |n\rangle\langle n'|$. The basis $\{|n\rangle\}$ represents a complete set of atomic energy eigenstates with closure relation $\sum_n |n\rangle\langle n| = \hat{1}$. From the eigenvalue equation $\hat{H}_\mathrm{a}|n\rangle = E_n|n\rangle$, the representation of the atomic Hamiltonian $\hat{H}_\mathrm{a}$ can be found directly. However, for the interaction Hamiltonian $\hat{H}_\mathrm{i}$, some steps need to be developed. The interaction term can be found as $e\hat{\mathbf{q}} = e\sum_{n,n'}|n\rangle\langle n|\hat{\mathbf{q}}|n'\rangle\langle n'| = \sum_{n,n'}\wp_{nn'}\hat{\sigma}_{nn'}$, where $\wp_{nn'} = e\langle n|\hat{\mathbf{q}}|n'\rangle$ is the matrix element of the electric dipole transition. The electric field operator (A.12) is evaluated in the dipole approximation placing the atom just at the center of the cavity $\mathbf{q}_0 = (0, 0, L/2)$, and from the allowed radiation frequency relation it is found that $\sin(kL/2) = 1$, such that $\hat{\mathbf{E}}(L/2, t) = \mathcal{E}_0[\hat{a}^\dagger(t) + \hat{a}(t)]\mathbf{i}$ with $\mathcal{E}_0 = \sqrt{\hbar\omega/(V\varepsilon_0)}$. Following all the previous steps, the explicit Hamiltonians take the position-independent form

$$\hat{H}_\mathrm{a} = \sum_n E_n|n\rangle\langle n| = \sum_n E_n\hat{\sigma}_{nn}, \tag{A.32}$$

$$\hat{H}_\mathrm{i}(t) = \hbar[\hat{a}^\dagger(t) + \hat{a}(t)]\sum_{n,n'} g_{nn'}\hat{\sigma}_{nn'}, \tag{A.33}$$

where $g_{nn'} = -\wp_{nn'}\cdot\mathcal{E}_0\mathbf{i}/\hbar$ defines a coupling parameter, and the term $\wp_{nn'}$ is taken as a real quantity without loss of generality.

A.2.2 Two-Level Atom Approximation

Another typical simplification taken in the model is the two-level atom approximation [50,51]. The basic idea is to consider atoms that transit from the ground state to an excited state only. For this case, the coupling parameter is $g = g_{01} = g_{10}$ because of $\wp = \wp_{01} = \wp_{10} = e\langle 0|\hat{\mathbf{q}}|1\rangle = e\langle 1|\hat{\mathbf{q}}|0\rangle$. Thus, the atomic and interaction Hamiltonians can be written as

$$\begin{aligned}\hat{H}_\mathrm{a} &= E_0\hat{\sigma}_{00} + E_1\hat{\sigma}_{11} \\ &= \frac{\hbar\omega_0}{2}(\hat{\sigma}_{11} - \hat{\sigma}_{00}) + \frac{E_0 + E_1}{2}\hat{1},\end{aligned} \tag{A.34}$$

$$\hat{H}_\mathrm{i}(t) = \hbar g[\hat{a}^\dagger(t) + \hat{a}(t)](\hat{\sigma}_{01} + \hat{\sigma}_{10}), \tag{A.35}$$

where $\hbar\omega_0 = E_1 - E_0$ and $\hat{\sigma}_{00} + \hat{\sigma}_{11} = \hat{1}$. Moreover, when the atomic transition operators $\hat{\sigma}_{nn'}$ are written in the atomic energy eigenbasis

$$\hat{\sigma}_x = \hat{\sigma}_{01} + \hat{\sigma}_{10} = |0\rangle\langle 1| + |1\rangle\langle 0|, \tag{A.36}$$
$$\hat{\sigma}_y = i\,(\hat{\sigma}_{01} - \hat{\sigma}_{10}) = i(|0\rangle\langle 1| - |1\rangle\langle 0|), \tag{A.37}$$
$$\hat{\sigma}_z = \hat{\sigma}_{11} - \hat{\sigma}_{00} = |1\rangle\langle 1| - |0\rangle\langle 0|, \tag{A.38}$$

are identified the Pauli matrices

$$\sigma_{x,y,z} = \left[\begin{pmatrix} 0 & 1 \\ 1 & 0 \end{pmatrix}, \begin{pmatrix} 0 & -i \\ i & 0 \end{pmatrix}, \begin{pmatrix} 1 & 0 \\ 0 & -1 \end{pmatrix}\right]. \tag{A.39}$$

Similarly, the raising-lowering spin operators $\hat{\sigma}_\pm = \frac{1}{2}(\hat{\sigma}_x \pm i\hat{\sigma}_y)$

$$\hat{\sigma}_+ = \hat{\sigma}_{10} = |1\rangle\langle 0|, \tag{A.40}$$
$$\hat{\sigma}_- = \hat{\sigma}_{01} = |0\rangle\langle 1|, \tag{A.41}$$

with the matrices

$$\sigma_\pm = \left[\begin{pmatrix} 0 & 1 \\ 0 & 0 \end{pmatrix}, \begin{pmatrix} 0 & 0 \\ 1 & 0 \end{pmatrix}\right]. \tag{A.42}$$

Now, from the identity $[\hat{\sigma}_{nn'}, \hat{\sigma}_{mm'}] = \hat{\sigma}_{nm'}\delta_{n'm} - \hat{\sigma}_{mn'}\delta_{nm'}$ it follows that the set of spin-$\frac{1}{2}$ operators $\{\hat{\sigma}_\pm, \hat{\sigma}_z\}$ satisfy the SU(2) algebra, defined by the commutation relations

$$[\hat{\sigma}_+, \hat{\sigma}_-] = \hat{\sigma}_z, \tag{A.43}$$
$$[\hat{\sigma}_z, \hat{\sigma}_\pm] = \pm 2\hat{\sigma}_\pm. \tag{A.44}$$

Taking into account all the previous developments, the atomic and interaction Hamiltonians for a single atom are given by

$$\hat{H}_\mathrm{a} = \frac{\hbar\omega_0}{2}\hat{\sigma}_z, \tag{A.45}$$
$$\hat{H}_\mathrm{i}(t) = \hbar g[\hat{a}^\dagger(t) + \hat{a}(t)](\hat{\sigma}_+ + \hat{\sigma}_-), \tag{A.46}$$

where the constant energy term $\frac{1}{2}(E_0 + E_1)$ can be neglected, since it is only a displacement term in the whole Hamiltonian.

A.3 Dicke Hamiltonian

Equations (A.45) and (A.46) represent the atomic and interaction terms of the Dicke Hamiltonian (2.5) for a single atom. However, as the Dicke Hamiltonian describes a set of $\mathcal{N}$ two-level atoms, a superposition of all atomic contributions is considered explicitly in the atom-field term $\hat{H}_{\text{A-F}} = \sum_{n=1}^{\mathcal{N}} \hat{H}_{\text{a-f}}^{(n)}$. Using the atomic density $\rho = \mathcal{N}/V$, the coupling parameter g can be written as $g = \gamma/\sqrt{\mathcal{N}}$, where the new coupling parameter is given by $\gamma = -\wp \cdot \sqrt{\omega\rho/(\hbar\varepsilon_0)}\mathbf{i}$. Thus, all the terms that compose the Dicke Hamiltonian are given by the expressions

$$\hat{H}_{\text{F}} = \hbar\omega \hat{a}^{\dagger}\hat{a}, \tag{A.47}$$

$$\hat{H}_{\text{A}} = \sum_{n=1}^{\mathcal{N}} \hat{H}_{\text{a}}^{(n)} = \frac{\hbar\omega_0}{2} \sum_{n=1}^{\mathcal{N}} \hat{\sigma}_z^{(n)}, \tag{A.48}$$

$$\hat{H}_{\text{I}} = \sum_{n=1}^{\mathcal{N}} \hat{H}_{\text{i}}^{(n)} = \frac{\hbar\gamma}{\sqrt{\mathcal{N}}}(\hat{a}^{\dagger} + \hat{a}) \sum_{n=1}^{\mathcal{N}} \left[\hat{\sigma}_{+}^{(n)} + \hat{\sigma}_{-}^{(n)}\right], \tag{A.49}$$

where the constant energy displacement $\hbar\omega/2$ of the field Hamiltonian (A.14) was neglected, and we moved to the Schrödinger picture, such that, the explicit time dependence of the creation-annihilation operators $\hat{a}^{\dagger}$ and $\hat{a}$ is removed.

An additional consideration in the terms $\hat{H}_{\text{A}}$ and $\hat{H}_{\text{I}}$ is taken into account, where the superposition of all atomic contributions is represented as collective pseudo-spin operators of the form

$$\hat{J}_{x,y,z} = \frac{1}{2} \sum_{n=1}^{\mathcal{N}} \hat{\sigma}_{x,y,z}^{(n)}, \tag{A.50}$$

$$\hat{J}_{\pm} = \sum_{n=1}^{\mathcal{N}} \hat{\sigma}_{\pm}^{(n)}, \tag{A.51}$$

where the raising-lowering collective pseudo-spin operators are defined as $\hat{J}_{\pm} = \hat{J}_x \pm i\hat{J}_y$. With these definitions it follows that the set of collective pseudo-spin operators $\{\hat{J}_{\pm}, \hat{J}_z\}$ satisfy the

same SU(2) algebra of spin-$\frac{1}{2}$ operators

$$[\hat{J}_+, \hat{J}_-] = 2\hat{J}_z, \tag{A.52}$$

$$[\hat{J}_z, \hat{J}_\pm] = \pm\hat{J}_\pm. \tag{A.53}$$

Using the collective pseudo-spin operators explicitly in the terms $\hat{H}_\mathrm{A}$ and $\hat{H}_\mathrm{I}$, the Dicke Hamiltonian can be written as in Eq. (2.5).

Appendix B

Numerical Solutions of the Dicke Hamiltonian

In this Appendix is exposed the coherent basis as a diagonalization basis of the Dicke Hamiltonian, as well as its alternate representation when the parity symmetry of the Hamiltonian is taken into account.

B.1 Coherent Basis

In 2008, Q.-H. Chen et al. [288] proposed an alternate numerical solution of the Dicke Hamiltonian using the coherent basis (2.21). Applying the transformations (2.18) and (2.19) to the Dicke Hamiltonian (2.5), it can be written as

$$\hat{H}_{\mathrm{D}} = \omega(\hat{A}^{\dagger}\hat{A} - G^2\hat{J}_z'^2) - \omega_0\hat{J}_x', \tag{B.1}$$

with $G = 2\gamma/(\omega\sqrt{\mathcal{N}})$. Using the coherent basis and the recalling that the operator $\hat{J}_z' = \hat{J}_x$, such that the rotated eigenvalue $m_z' = m_x$, the matrix elements of the above Hamiltonian are

given by

$$\begin{aligned}\langle N';j,m'_x|\hat{H}_{\rm D}|N;j,m_x\rangle =&\omega(N-G^2m_x^2)\delta_{N',N}\delta_{m'_x,m_x}+\\ &-\frac{\omega_0}{2}C_+(N',N;j,m'_x,m_x)\delta_{m'_x,m_x+1}+\\ &-\frac{\omega_0}{2}C_-(N',N;j,m'_x,m_x)\delta_{m'_x,m_x-1},\end{aligned} \tag{B.2}$$

where

$$\begin{aligned}C_\pm(N',N;j,m'_x,m_x) =&\sqrt{j(j+1)-m_x(m_x\pm1)}\times\\ &\times\langle N';j,m'_x|N;j,m_x\pm1\rangle\end{aligned} \tag{B.3}$$

contains the coherent basis overlap, which has explicit form

$$\langle N';j,m'_x|N;j,m_x\rangle=\begin{cases}(-1)^N D_{N',N} & \text{if } m_x>m'_x\\ (-1)^{N'}D_{N',N} & \text{if } m_x<m'_x\\ \delta_{N',N} & \text{if } m_x=m'_x\end{cases}, \tag{B.4}$$

where

$$D_{N',N}=e^{-G^2/2}\sum_{k=0}^{\min(N',N)}\frac{\sqrt{N'!N!}(-1)^{-k}G^{N'+N-2k}}{(N'-k)!(N-k)!k!}. \tag{B.5}$$

A truncation value can be defined in the coherent basis in a similar way as in the Fock basis, and is given by $N_{\rm max}$ (eigenvalue of the operator $\hat{N}=\hat{A}^\dagger\hat{A}$). Thus, the resulting matrices will have finite dimension $\mathcal{D}_{\rm C}^2$, where $\mathcal{D}_{\rm C}=(2j+1)(N_{\rm max}+1)$ is the dimension of the truncated modified Hilbert space.

B.2 Coherent Basis with Well-Defined Parity

The Dicke Hamiltonian (2.5) has a well-defined parity, that is, it commutes with the parity operator defined by $\hat{\Pi}=e^{i\pi\hat{\Lambda}}$, $[\hat{H}_{\rm D},\hat{\Pi}]=\hat{0}$, where $\hat{\Lambda}=\hat{a}^\dagger\hat{a}+\hat{J}_z+j\hat{1}$. In some cases it is

useful to separate the parity sectors (eigenvalues and eigenvectors) of the numerical diagonalization. To do that, the action of the parity operator is calculated over the coherent basis states given by

$$\begin{aligned} |N; j, m_x\rangle &= \frac{(\hat{A}^\dagger)^N}{\sqrt{N!}}|0; j, m_x\rangle \\ &= \frac{(\hat{a}^\dagger - \alpha_{m_x})^N}{\sqrt{N!}}|\alpha_{m_x}; j, m_x\rangle, \end{aligned} \tag{B.6}$$

where $\alpha_{m_x} = -Gm_x$. The result is given by

$$\hat{\Pi}|N; j, m_x\rangle = (-1)^N|N; j, -m_x\rangle, \tag{B.7}$$

where the parity operator $\hat{\Pi}$ can be represented in the subspace $\{|N; j, m_x\rangle, |N; j, -m_x\rangle\}$

$$\hat{\Pi} = (-1)^N \begin{pmatrix} 0 & 1 \\ 1 & 0 \end{pmatrix}, \tag{B.8}$$

and by diagonalizing it, its eigenvectors can be found as

$$|N; j, m_x; p\rangle = \frac{|N; j, m_x\rangle + p(-1)^N|N; j, -m_x\rangle}{\sqrt{2(1+\delta_{m_x,0})}}, \tag{B.9}$$

where $p = \pm 1$ defines its eigenvalues, such that the eigenvalue equation $\hat{\Pi}|N; j, m_x; p\rangle = p|N; j, m_x; p\rangle$ is satisfied. The basis (B.9) is called coherent basis with well-defined parity.

Appendix C

Classical Expressions of the Dicke Model

In this Appendix is exposed the complete derivation of the classical Dicke Hamiltonian, as well as useful classical expressions derived from it, as the classical ground-state energy and the semiclassical density of states.

C.1 Classical Dicke Hamiltonian

Taking the expectation value of the Dicke Hamiltonian (2.5) under Glauber-Bloch coherent states $|\mathbf{x}\rangle = |\alpha\rangle \otimes |z\rangle$ (see Eq. (2.33)), and scaling it by j, it is found

$$\begin{aligned} h_{\mathrm{D}}(\mathbf{x}) &= \frac{1}{j}\langle \mathbf{x}|\hat{H}_{\mathrm{D}}|\mathbf{x}\rangle \\ &= \frac{1}{j}\left[\omega|\alpha|^2 - j\omega_0 \frac{1-|z|^2}{1+|z|^2} + \gamma\sqrt{2j}\,\frac{z+z^*}{1+|z|^2}\,(\alpha+\alpha^*)\right], \end{aligned} \tag{C.1}$$

where $\mathbf{x} = (q, p; Q, P)$ are the coordinates of the four-dimensional phase space $\mathcal{M}$ of the Dicke model, and the parameters of each coherent state α and z and have an specific representation in

phase space through bosonic (q, p) and atomic (Q, P) variables (see Eqs. (2.29) and (2.30)).

At this point, the mapping given by Eqs. (2.29) and (2.30) gives directly the classical Dicke Hamiltonian (2.38). Nevertheless, the natural way to reach that mapping needs to be explained. It is known that the bosonic parameter is associated with the position-momentum canonical variables of the classical harmonic oscillator $\alpha \to \alpha(q, p)$, but the same thing is not clear for the atomic parameter $z \to z(Q, P)$. The natural connection between the atomic parameter and some kind of canonical variables comes from the Bloch sphere. The classical angular momentum vector represented in the Bloch sphere is given by

$$\begin{aligned}\vec{j} &= j(j_{x,y,z}) \\ &= j[\cos(\phi)\sin(\theta), \sin(\phi)\sin(\theta), -\cos(\theta)],\end{aligned} \tag{C.2}$$

whose magnitude is given by $|\vec{j}| = j$, and the angular variables (ϕ, θ) correspond to the azimuthal and zenith angles of the spherical coordinates, respectively, measuring the θ angle from the negative z axis. In addition, through a stereographic projection of the Bloch sphere, the atomic parameter can be written as

$$\begin{aligned}z &= \tan\left(\frac{\theta}{2}\right) e^{-i\phi} \\ &= \sqrt{\frac{1+j_z}{1-j_z}} e^{-i\phi},\end{aligned} \tag{C.3}$$

where was used its squared absolute value

$$\begin{aligned}|z|^2 &= \tan^2\left(\frac{\theta}{2}\right) \\ &= \frac{1-\cos(\theta)}{1+\cos(\theta)},\end{aligned} \tag{C.4}$$

and from where are identified the action-angle canonical variables

$$(\phi, j_z) = \left[\tan^{-1}\left(\frac{j_y}{j_x}\right), -\cos(\theta)\right], \tag{C.5}$$

which satisfy the Poisson bracket $\{\phi, j_z\} = 1$. Now, defining a canonical transformation of the form

$$(Q, P) = \sqrt{2(1 + j_z)}[\cos(\phi), -\sin(\phi)], \tag{C.6}$$

whose Poisson bracket satisfies $\{Q, P\} = 1$, the atomic parameter can be transformed and the mapping (2.30) is reached. In this way, the classical Dicke Hamiltonian (2.38) can be found as before.

C.2 Classical Ground-State Energy

The Hamilton's equations of motion for the classical Dicke Hamiltonian (2.38) are given by the expressions

$$\frac{\partial h_{\mathrm{D}}(\mathbf{x})}{\partial p} = \dot{q} = \omega p, \tag{C.7}$$

$$-\frac{\partial h_{\mathrm{D}}(\mathbf{x})}{\partial q} = \dot{p} = -\omega q - 2\gamma Q F(Q, P), \tag{C.8}$$

$$\frac{\partial h_{\mathrm{D}}(\mathbf{x})}{\partial P} = \dot{Q} = \omega_0 P - \frac{\gamma}{2}\frac{qQP}{F(Q, P)}, \tag{C.9}$$

$$-\frac{\partial h_{\mathrm{D}}(\mathbf{x})}{\partial Q} = \dot{P} = -\omega_0 Q - 2\gamma q F(Q, P) + \frac{\gamma}{2}\frac{qQ^2}{F(Q, P)}, \tag{C.10}$$

where $F(Q, P) = \sqrt{1 - (Q^2 + P^2)/4}$.

By minimizing the classical energy surface $h_{\mathrm{D}}(\mathbf{x}) = \epsilon = E/j$ can be found the set of coordinates $\mathbf{x}_{\mathrm{gs}} = (q_{\mathrm{gs}}, p_{\mathrm{gs}}; Q_{\mathrm{gs}}, P_{\mathrm{gs}})$, for which this surface takes the minimum value and represents the classical ground-state energy ϵ_{gs}

$$h_{\mathrm{D}}(\mathbf{x}_{\mathrm{gs}}) = \epsilon_{\mathrm{gs}}. \tag{C.11}$$

The minimization procedure consists in setting equal to zero the Hamilton's equations of motion and determine the coordinates

$\mathbf{x}_{\rm gs}$. Two solutions are found

$$\mathbf{x}_{\rm gs} = \begin{cases} (0,0;0,0) & \text{if } \gamma < \gamma_{\rm c} \\ \left(-\frac{2\gamma}{\omega}\sqrt{1-\left(\frac{\gamma_{\rm c}}{\gamma}\right)^4}, 0; \sqrt{2\left[1-\left(\frac{\gamma_{\rm c}}{\gamma}\right)^2\right]}, 0\right) & \text{if } \gamma > \gamma_{\rm c} \end{cases}, \tag{C.12}$$

which represent the classical separation between phases.

By substituting the coordinates $\mathbf{x}_{\rm gs}$ in the classical Dicke Hamiltonian Eq. (2.38), the classical ground-state energy (2.39) can be found for both normal and superradiant phases.

C.3 Semiclassical Density of States

Following a particular case of the Gutzwiller trace formula [2,72], the density of states of a quantum system can be approximated classically by computing the available phase-space volume at a given classical energy shell $\epsilon = E/j$

$$\nu(\epsilon) \approx \frac{1}{(2\pi\hbar_{\rm eff})^2}\int_{\mathcal{M}} d\mathbf{x}\, \delta[h_{\rm D}(\mathbf{x}) - \epsilon], \tag{C.13}$$

where

$$\delta(z - z_0) = \frac{1}{2\pi}\int_{-\infty}^{+\infty} dx\, e^{ix(z-z_0)} \tag{C.14}$$

is the Dirac delta function, $\hbar_{\rm eff} = j^{-1}$, and $h_{\rm D}(\mathbf{x})$ is the classical Dicke Hamiltonian (2.38) with four-dimensional phase space $\mathcal{M}$ in the coordinates $\mathbf{x} = (q, p; Q, P)$.

The Dirac delta function can be written as

$$\delta\left[h_{\rm D}(\mathbf{x}) - \epsilon\right] = \frac{\delta(q-q_+)}{\left|\frac{\partial h_{\rm D}(\mathbf{x})}{\partial q}\right|_{q_+}} + \frac{\delta(q-q_-)}{\left|\frac{\partial h_{\rm D}(\mathbf{x})}{\partial q}\right|_{q_-}}, \tag{C.15}$$

where $q_\pm$ are the two solutions of the second degree equation $h_{\rm D}(\mathbf{x}) - \epsilon = 0$, given by

$$q_\pm = -\frac{2\gamma}{\omega}QF(Q,P) \pm \frac{1}{\omega}\sqrt{\Delta_\epsilon(p,Q,P)}, \tag{C.16}$$

where

$$\Delta_\epsilon(p,Q,P) = A_\epsilon(Q,P) - \omega^2 p^2, \tag{C.17}$$

and

$$A_\epsilon(Q,P) = 4\gamma^2 Q^2 F^2(Q,P) + 2\omega\left[\epsilon + \omega_0\left(1 - \frac{Q^2+P^2}{2}\right)\right], \tag{C.18}$$

with $F(Q,P) = \sqrt{1-(Q^2+P^2)/4}$.

On the other hand, using Eq. (C.8), the following term can be obtained

$$\left|\frac{\partial h_{\mathrm{D}}(\mathbf{x})}{\partial q}\right|_{q_\pm} = \sqrt{\Delta_\epsilon(p,Q,P)}, \tag{C.19}$$

and the integral over q can be computed, such that

$$\nu(\epsilon) = 2\left(\frac{j}{2\pi}\right)^2 \int\int\int dp\, dQ\, dP \frac{1}{\sqrt{\Delta_\epsilon(p,Q,P)}}. \tag{C.20}$$

Now, from the second degree equation $\Delta_\epsilon(p,Q,P) = 0$, two solutions $p_\pm = \pm\sqrt{A_\epsilon(Q,P)}/\omega$ are found, such that it can be written as $\Delta_\epsilon(p,Q,P) = \omega^2(p_+ - p)(p - p_-)$. Through a change of variable given by $u = [p - (p_+ + p_-)/2]/[(p_+ - p_-)/2]$, the integral over p can be evaluated

$$\int_{p_-}^{p_+} dp \frac{1}{\sqrt{\Delta_\epsilon(p,Q,P)}} = \frac{\pi}{\omega}, \tag{C.21}$$

and the inequality $4\omega^2 A_\epsilon(Q,P) \geq 0$ must be satisfied, in order to ensure that the solutions $p_\pm$ are real.

At this point, the better option to compute the remaining integral over the atomic variables (Q,P), is by transforming them to the action-angle variables, $(Q,P) \to (\phi, j_z)$. Using the canonical transformation given by Eq. (C.6), it can be found the Jacobian of the transformation $dQ\, dP = J(\phi, j_z) d\phi\, dj_z$ (in this case $J(\phi.j_z) = 1$), such that, the integral takes the form

$$\begin{aligned}\nu(\epsilon) &= \frac{j^2}{2\pi\omega}\int\int dQ\, dP \\ &= \frac{j^2}{2\pi\omega}\int\int d\phi\, dj_z.\end{aligned} \tag{C.22}$$

Now, from the relation $4\omega^2 A_\epsilon(\phi, j_z) \geq 0$, is found the condition

$$\cos^2(\phi) \geq 2\left(\frac{\gamma_c}{\gamma}\right)^2 \frac{j_z - \epsilon/\omega_0}{1 - j_z^2}, \tag{C.23}$$

which restricts the values of the variables (ϕ, j_z) in the following way

$$\phi_\pm = \cos^{-1}\left(\pm\frac{\gamma_c}{\gamma}\sqrt{\frac{2(j_z - \epsilon/\omega_0)}{1 - j_z^2}}\right), \tag{C.24}$$

$$j_z^\pm = -\frac{\gamma_c}{\gamma}\left(\frac{\gamma_c}{\gamma} \mp \sqrt{\frac{2(\epsilon - \epsilon_0)}{\omega_0}}\right), \tag{C.25}$$

where $\epsilon_0 = \epsilon_{gs}$ of the superradiant phase ($\gamma > \gamma_c$) (see Eq. (2.39)). Three main energy regions are identified

1. If $\epsilon_0 \leq \epsilon < -\omega_0$, then $j_z \in [j_z^-, j_z^+]$ and $\phi = 0, \pi$. This energy region only appears in the superradiant phase.

2. If $|\epsilon| \leq \omega_0$, then $j_z \in [-1, j_z^+]$, but appears the restriction over ϕ. On the one hand, if $j_z \in [-1, \epsilon]$, then $\phi \in [0, 2\pi)$. On the other hand, if $j_z \in [\epsilon, j_z^+]$, then $\phi = 0, \pi$.

3. If $\epsilon > \omega_0$, then $j_z \in [-1, 1]$ and $\phi \in [0, 2\pi)$.

By computing the integral (C.22) over each energy region, the Eq. (2.41) can be recovered.

Appendix D

Experimental Setups of the Dicke Model

In this Appendix is exposed one of the most relevant contemporary experimental setups of the Dicke model, which allowed to verify experimentally the quantum phase transition predicted by the theoretical model.

D.1 Experimental Setup with a Bose-Einstein Condensate

In 2010 K. Baumann et al. implemented the Dicke model with a Bose-Einstein condensate within an optical cavity [74]. The proposed setup was successful in reproducing experimentally the quantum phase transition predicted theoretically by the Dicke model for the superradiant phase. The basic procedure consist of trapping a Bose-Einstein condensate of rubidium atoms ^{87}Rb within an optical cavity, which is driven through a pumped laser. The laser can be modulated and this modifies the effective coupling strength within the system. When the laser exceeds a critical pump power given by the parameter P_{c}, an atomic self-organization takes place within the cavity, where the rubidium

atoms take the odd or even places of a checkerboard pattern. The last collective effect manifest the appearance of the superradiant phase in the system and verifies the validity of the theoretical quantum phase transition. In Fig. D.1 is shown the theoretical concept of the latter experimental setup.

Although superradiance was verified many years before in the Dicke model [73], the proposed setup was able to show the agreement between the experimental realization and the theoretical model by a mapping of the corresponding parameters [75]. The explicit mapping between both approaches is given by the theoretical parameters defined as

$$\omega = -\Delta_{\mathrm{c}} + \frac{\mathcal{N}U_0}{2}, \tag{D.1}$$

$$\omega_0 = 2\omega_{\mathbf{r}}, \tag{D.2}$$

$$\gamma = \frac{\eta\sqrt{\mathcal{N}}}{2}, \tag{D.3}$$

where the experimental-setup parameters are given by

$$U_0 = \frac{g_0^2}{\Delta_{\mathrm{a}}}, \tag{D.4}$$

$$\omega_{\mathbf{r}} = \sqrt{\omega_x^2 + \omega_y^2 + \omega_z^2} = \frac{\hbar k^2}{2m}, \tag{D.5}$$

$$\eta = \frac{g_0\Omega_{\mathrm{p}}}{\Delta_{\mathrm{a}}}, \tag{D.6}$$

with $\Delta_{\mathrm{c}} = \omega_{\mathrm{p}} - \omega_{\mathrm{c}}$, $\Delta_{\mathrm{a}} = \omega_{\mathrm{p}} - \omega_{\mathrm{a}}$, and $\Omega_{\mathrm{p}} = \mu_{12}B_{\mathrm{mw}}/\hbar$. In the last expressions $\mathcal{N}$ represents the number of atoms within the system, U_0 is the light shift of a maximally coupled atom, $\omega_{\mathbf{r}}$ is the recoil frequency, η is the two-photon Rabi frequency, ω_{p} is the pump laser frequency, ω_{c} is the cavity resonance frequency, ω_{a} is the atomic transition frequency, g_0 is the atom-cavity coupling strength, k is the magnitude of the wave number vector, m is the mass of a rubidium atom, Ω_{p} is the maximum pump Rabi frequency, μ_{12} is the magnetic dipole matrix element between two

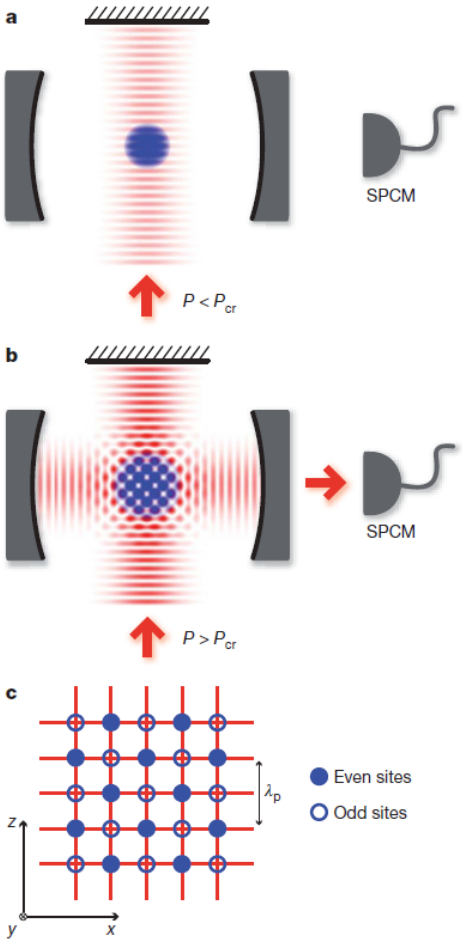

Figure D.1: Experimental setup of the Dicke model realized with a Bose-Einstein condensate of rubidium atoms ^{87}Rb driven with a pump laser within an optical cavity. **Panel a:** Case $P < P_c$, where the build-up of a coherent cavity field for a homogeneous atomic density distribution along the cavity axis is suppressed by the destructive interference effect between the individual scatterers. Single-Photon Counting Module (SPCM). **Panel b:** Case $P > P_c$, where the self-organization of the rubidium atoms is induced, maximizing the cooperative scattering and originating the appearance of the superradiant phase. **Panel c:** Checkerboard pattern where the rubidium atoms are self-organized on the odd or even places. Figure taken from Ref. [74].

coupled states, and B_{mw} is the magnetic field of the microwave radiation.

The theoretical parameters of the Dicke model can be estimated by mapping the experimental-setup parameters given in Refs. [74, 87], where the relation $\mathcal{N}U_0 = 6.5\kappa$ is considered with κ representing the cavity decay ratio. In Table D.1 is shown the corresponding mapping.

Experimental-Setup Parameters		
$\mathcal{N}$ (atoms)	Δ_{c} (MHz)	κ (MHz)
1.53×10^5	$-2\pi \times 14.92$	$2\pi \times 1.3$
ω_x (Hz)	ω_y (Hz)	ω_z (Hz)
$2\pi \times 252$	$2\pi \times 48$	$2\pi \times 238$
g_0 (MHz)	Δ_{a} (MHz)	μ_{12} (J/T)
$2\pi \times 10.4$	$\approx 2\pi \times (30 - 40)$	6.95×10^{-24}
B_{mw} (T)		
10^{-5}		
Estimated Theoretical Parameters		
ω (MHz)	ω_0 (Hz)	γ (MHz)
120.29	4397.4	38.31
γ_{c} (MHz)		
0.3636		

Table D.1: Experimental-setup parameters of the Dicke model realized with a Bose-Einstein condensate of rubidium atoms ^{87}Rb driven with a pump laser within an optical cavity [74, 87], and estimated theoretical parameters.

Appendix E

Trace of the Green's Function

In this Appendix is exposed the trace of the Green's function, which determines the density of states of a quantum system.

E.1 Green's Function and Density of States

The Green's function is a special solution of the inhomogeneous time-independent Schrödinger equation [39]

$$\left[E - \left[-\frac{\hbar^2}{2m}\nabla^2 + V(\mathbf{q}')\right]\right] G(\mathbf{q}, \mathbf{q}', E) = \delta(\mathbf{q}' - \mathbf{q}), \tag{E.1}$$

where $\mathbf{q}$ and $\mathbf{q}'$ define a starting and an end position, respectively, and δ is the Dirac delta function given by Eq. (C.14). The Green's function is given explicitly by

$$\begin{aligned} G(\mathbf{q}, \mathbf{q}', E) &= \frac{1}{i\hbar}\int_0^{+\infty} dt\, K(\mathbf{q}, \mathbf{q}', E) e^{iEt/\hbar} \\ &= \sum_{n=1}^{N} \frac{\phi_n(\mathbf{q}')\phi_n^*(\mathbf{q})}{E - E_n}, \end{aligned} \tag{E.2}$$

where

$$K(\mathbf{q},\mathbf{q}',E)=\sum_{n=1}^{N}\phi_n(\mathbf{q}')\phi_n^*(\mathbf{q})e^{-iE_nt/\hbar} \tag{E.3}$$

is the propagator and the eigenstates $\phi_n(\mathbf{q})$ satisfy the eigenvalue equation

$$\left[-\frac{\hbar^2}{2m}\nabla^2+V(\mathbf{q})\right]\phi_n(\mathbf{q})=E_n\phi_n(\mathbf{q}) \tag{E.4}$$

for a Hilbert space with dimension N. Taking the trace of the Green's function in the same starting and end point $\mathbf{q}=\mathbf{q}'$ is found the expression

$$\begin{aligned} g(E) &= \mathrm{Tr}[G(\mathbf{q},\mathbf{q},E)] \\ &= \int d^I\mathbf{q}\, G(\mathbf{q},\mathbf{q},E) \\ &= \sum_{n=1}^{N}\frac{1}{E-E_n}. \end{aligned} \tag{E.5}$$

where I defines the degrees of freedom of the classical system. The last expression contains the eigenvalues explicitly. In this way, the trace of the Green's function defines the density of states of a quantum system as follows

$$\begin{aligned} \nu(E) &= -\frac{1}{\pi}\lim_{\varepsilon\to 0}\Im[g(E+i\varepsilon)] \\ &= \frac{1}{\pi}\lim_{\varepsilon\to 0}\sum_{n=1}^{N}\frac{\varepsilon}{(E-E_n)^2+\varepsilon^2} \\ &= \sum_{n=1}^{N}\delta(E-E_n), \end{aligned} \tag{E.6}$$

where δ is the Dirac delta function given by Eq. (C.14).

Appendix F

Static Tests of Quantum Chaos

In this Appendix is exposed the unfolding procedure of the energy spectrum, which is a necessary step to develop before computing the short and long range spectral tests.

F.1 Unfolding Procedure

An important procedure to perform the short and long-range spectral tests consists of unfolding the energy spectrum [95, 123, 131]. The idea is to delete the global tendencies of the spectral fluctuations, which are specific to each system. Thereby, an ordered set of energy levels $\{E_1, \ldots, E_N\}$ of a given quantum system originate a spectral function, level density, or density of states $\nu(E)$ given by Eq. (E.6). However, a cumulative spectral function can be defined as

$$\begin{aligned} \eta(E) &= \int_{-\infty}^{E} dE' \nu(E') \\ &= \sum_{n=1}^{N} \Theta(E - E_n), \end{aligned} \tag{F.1}$$

where

$$\Theta(z) = \int_{-\infty}^{z} dx\, \delta(x) \tag{F.2}$$

is the Heaviside step function, which counts the number of levels with energy less than or equal to E, and it is known also as staircase function. In the last expression, δ is the Dirac delta function defined in Eq. (C.14). In general, the cumulative spectral function can be separated into two parts

$$\eta(E) = \xi(E) + \xi_{\mathrm{f}}(E), \tag{F.3}$$

that is, a smooth term $\xi(E)$ which determines the global tendencies of the system, and a fluctuating term $\xi_{\mathrm{f}}(E)$ which represents the local fluctuations [95, 131]. The relevant information is contained in local fluctuations only, for that reason, the unfolding procedure consists of mapping the set of energy levels $\{E_1, \ldots, E_N\}$ to another set $\{\xi_1, \ldots, \xi_N\}$ scaled by the smooth term $\xi_n = \xi(E_n)$ with $n = 1, \ldots, N$. As a result, the latter procedure allows the mean level density to remain constant over the whole energy spectrum

$$\langle \nu(\xi) \rangle = \frac{1}{\Delta\xi} \int_{\xi_1 - \Delta\xi/2}^{\xi_1 + \Delta\xi/2} d\xi\, \nu(\xi) \approx 1, \tag{F.4}$$

where $\nu(\xi) = \sum_{n=1}^{N} \delta(\xi - \xi_n)$.

Appendix G

Gaussian Orthogonal Ensemble

In this Appendix is exposed the complete derivation of the joint probability density function and the two-level form factor for the GOE.

G.1 Joint Probability Density Function

The most general form of the probability density function of the Gaussian ensembles is given by the expression [146]

$$P(\hat{H}) = e^{-a\mathrm{Tr}(\hat{H}^2)+b\mathrm{Tr}(\hat{H})+c}, \tag{G.1}$$

where $a, b, c \in \mathbb{R}$, and $a > 0$. For this function, the components of $\hat{H}$ can be expressed in terms of N eigenvalues θ_n, such that

$$\mathrm{Tr}(\hat{H}) = \sum_{n=1}^{N} \theta_n, \tag{G.2}$$

$$\mathrm{Tr}(\hat{H}^2) = \sum_{n=1}^{N} \theta_n^2, \tag{G.3}$$

and also in terms of p_l mutually independent variables, such that $\{\theta_n, p_l\}$ form a complete set. For the GOE, the matrix is real and symmetric with dimension N^2, and the number of parameters which determine the components H_{nm} is $\frac{1}{2}N(N+1)$, that is H_{nm} with $n \leq m$; so that, the number of extra parameters is $L = \frac{1}{2}N(N+1) - N = \frac{1}{2}N(N-1)$. Following this, the probability distribution can be written as

$$P_{N,L}(\theta_1, \ldots, \theta_N; p_1, \ldots, p_L) = J(\theta, p) e^{-a\sum_{n=1}^{N}\theta_n^2 + b\sum_{n=1}^{N}\theta_n + c}, \tag{G.4}$$

where

$$J(\theta, p) = \left| \frac{\partial(H_{11}, H_{12}, \ldots, H_{NN})}{\partial(\theta_1, \ldots, \theta_N; p_1, \ldots, p_L)} \right| \tag{G.5}$$

is the Jacobian. Moreover, an orthogonal real matrix $\hat{U}$ can diagonalize any symmetric real matrix $\hat{H}$ through the expressions

$$\hat{H} = \hat{U}\hat{\Theta}\hat{U}^{-1} = \hat{U}\hat{\Theta}\hat{U}^T, \tag{G.6}$$

$$1 = \hat{U}\hat{U}^T = \hat{U}^T\hat{U}, \tag{G.7}$$

where $\hat{\Theta}$ is a diagonal real matrix with elements $\{\theta_1, \ldots, \theta_N\}$. By differentiating the latter expressions with respect to p_l, are found the expressions

$$\frac{\partial \hat{H}}{\partial p_l} = \frac{\partial \hat{U}}{\partial p_l}\hat{\Theta}\hat{U}^T + \hat{U}\hat{\Theta}\frac{\partial \hat{U}^T}{\partial p_l}, \tag{G.8}$$

$$0 = \frac{\partial \hat{U}^T}{\partial p_l}\hat{U} + \hat{U}^T\frac{\partial \hat{U}}{\partial p_l}, \tag{G.9}$$

and the results

$$\hat{U}^T\frac{\partial \hat{U}}{\partial p_l} = -\frac{\partial \hat{U}^T}{\partial p_l}\hat{U} = \hat{S}^l, \tag{G.10}$$

$$\hat{U}^T\frac{\partial \hat{H}}{\partial p_l}\hat{U} = \hat{S}^l\hat{\Theta} - \hat{\Theta}\hat{S}^l, \tag{G.11}$$

such that

$$\sum_{n,m} \frac{\partial H_{nm}}{\partial p_l} U_{n\alpha} U_{m\beta} = S^l_{\alpha\beta}(\theta_\beta - \theta_\alpha), \tag{G.12}$$

$$\sum_{n,m} \frac{\partial H_{nm}}{\partial \theta_k} U_{n\alpha} U_{m\beta} = \frac{\partial \Theta_{\alpha\beta}}{\partial \theta_k} = \delta_{\alpha\beta}\delta_{\alpha k}, \tag{G.13}$$

where the last expression was found by differentiating with respect to θ_k. Using the latter relations, the Jacobian can be written in partitioned form as

$$[J(\theta, p)] = \begin{bmatrix} \frac{\partial H_{nn}}{\partial \theta_k} & \frac{\partial H_{nm}}{\partial \theta_k} \\ \frac{\partial H_{nn}}{\partial p_l} & \frac{\partial H_{nm}}{\partial p_l} \end{bmatrix}, \tag{G.14}$$

where $1 \leq n < m \leq N$, $k = 1, \ldots, N$, and $l = 1, \ldots, L$, respectively. Multiplying the Jacobian by the partitioned matrix $[V]$

$$[J(\theta, p)][V] = \begin{bmatrix} \delta_{\alpha\beta}\delta_{\alpha k} \\ S^l_{\alpha\beta}(\theta_\beta - \theta_\alpha) \end{bmatrix}, \tag{G.15}$$

where

$$[V] = \begin{bmatrix} U_{n\alpha} U_{n\beta} \\ 2U_{n\alpha} U_{m\beta} \end{bmatrix}, \tag{G.16}$$

and $1 \leq \alpha < \beta \leq N$. Thus, the determinant can be written as

$$J(\theta, p)|V| = \prod_{\alpha<\beta} (\theta_\beta - \theta_\alpha) \begin{vmatrix} \delta_{\alpha\beta}\delta_{\alpha k} \\ S^l_{\alpha\beta} \end{vmatrix}, \tag{G.17}$$

where

$$J(\theta, p) = \prod_{\alpha<\beta} |\theta_\beta - \theta_\alpha| f(p), \tag{G.18}$$

and $f(p)$ is an exclusively function of the variables p_l. Thus, the probability distribution takes the form

$$P_{N,L}(\theta_1, \ldots, \theta_N; p_1, \ldots, p_L) = e^{-a\sum_{n=1}^N \theta_n^2 + b\sum_{n=1}^N \theta_n + c} \times \\ \times \prod_{n<m} |\theta_m - \theta_n| f(p), \tag{G.19}$$

and integrating over the variables p_l is found

$$\begin{aligned} P_N(\theta_1,\ldots,\theta_N) = &\int_{-\infty}^{+\infty}\ldots\int_{-\infty}^{+\infty} dp_1\ldots dp_L \times \\ &\times P_{N,L}(\theta_1,\ldots,\theta_N;p_1,\ldots,p_L) \\ =&Ae^{-a\sum_{n=1}^{N}\theta_n^2+b\sum_{n=1}^{N}\theta_n+c}\prod_{n<m}|\theta_m-\theta_n|, \end{aligned} \tag{G.20}$$

where

$$A = \int_{-\infty}^{+\infty}\ldots\int_{-\infty}^{+\infty} dp_1\ldots dp_L\, f(p_1,\ldots,p_L) \tag{G.21}$$

is a constant. Now, by proposing the change of variable $\theta_n = x_n/\sqrt{2a}+b/(2a)$, is found the probability density function of the GOE

$$P_{N,1}(\theta_1,\ldots,\theta_N) = C_{N,1}e^{-\frac{1}{2}\sum_{n=1}^{N}x_n^2}\prod_{n<m}|x_n-x_m|, \tag{G.22}$$

where

$$\begin{aligned} C_{N,1} &= \frac{A}{\sqrt{2a}}e^{\frac{b^2}{4a}N+c} \\ &= \frac{1}{2^{3N/2}\prod_{n=1}^{N}\Gamma\left(1+\frac{n}{2}\right)}, \end{aligned} \tag{G.23}$$

which is Eq. (4.1) with $\beta = 1$.

G.2 Two-Level Form Factor

The two-level form factor is given by the Fourier transform of the two-level cluster function

$$b_2(t) = \mathfrak{F}\{Y_2(r)\}, \tag{G.24}$$

which for the GOE is given by Eq. (4.21) (the explicit derivation of this function is very extensive and will not be presented here,

however, it can be reviewed in Ref. [146]), and can be written as

$$Y_{2,1}(r) = s^2(r) + \frac{1}{2}\frac{ds(r)}{dr} - \frac{ds(r)}{dr}\int_0^r dr' s(r'). \tag{G.25}$$

The function $s(r)$, its first derivative $ds(r)/dr$, and its integral $\int_0^r dr' s(r')$, where $s(r) = \sin(\pi r)/(\pi r)$ is the sinc function, are defined for $r > 0$. For negative values, it is stated that these functions are even functions, and as a result, the Fourier transform of the function $s(r)$ can be expressed as the Fourier cosine transform [146]

$$\begin{aligned}\mathfrak{F}\{s(r)\} &= \int_{-\infty}^{+\infty} dr\, s(r) e^{2\pi i r t} \\ &= 2\int_0^{+\infty} dr\, s(r)\cos(2\pi|t|r).\end{aligned} \tag{G.26}$$

In this way, for the function $s^2(r)$ is found

$$\begin{aligned}\mathfrak{F}\left\{s^2(r)\right\} =& 2\int_0^{+\infty} dr \frac{\sin^2(\pi r)}{\pi^2 r^2}\cos(2\pi|t|r) \\ =& \int_0^{+\infty} dr \frac{1-\cos(2\pi r)}{\pi^2 r^2}\cos(2\pi|t|r) \\ =& \int_0^{+\infty} dr \frac{1}{2\pi^2 r^2}[2\cos(2\pi|t|r) + \\ & - \cos[2\pi(|t|+1)r] - \cos[2\pi(|t|-1)r)]],\end{aligned} \tag{G.27}$$

where were used the identities

$$\cos(2\theta) = 1 - 2\sin^2(\theta), \tag{G.28}$$

$$2\cos(\theta)\cos(\phi) = \cos(\theta-\phi) + \cos(\theta+\phi). \tag{G.29}$$

Now, considering the integral

$$\begin{aligned}\int_0^{+\infty} dx \frac{\cos(ax)-\cos(bx)}{x^2} &= \int_a^b d\xi \int_0^{+\infty} dx \frac{\sin(\xi x)}{x} \\ &= \frac{\pi}{2}(|b|-|a|),\end{aligned} \tag{G.30}$$

where was used the integral

$$\int_0^{+\infty} dx \frac{\sin(\xi x)}{x} = \frac{\pi}{2} \begin{cases} -1 & \text{if } \xi < 0 \\ 0 & \text{if } \xi = 0 \\ 1 & \text{if } \xi > 0 \end{cases}, \tag{G.31}$$

the Fourier cosine transform of the function $s^2(r)$ can be found as

$$\mathfrak{F}\left\{s^2(r)\right\} = \frac{1}{2}(1 - |t| + |(|t| - 1)|) = \begin{cases} 1 - |t| & \text{if } |t| \leq 1 \\ 0 & \text{if } |t| > 1 \end{cases}. \tag{G.32}$$

For the function $ds(r)/dr$ is found

$$\begin{aligned} \mathfrak{F}\left\{\frac{ds(r)}{dr}\right\} =& 2\int_0^{+\infty} dr \frac{d}{dr}\left[\frac{\sin(\pi r)}{\pi r}\right] \cos(2\pi|t|r) \\ =& 2\frac{\sin(\pi r)}{\pi r}\cos(2\pi|t|r)\Big|_0^{+\infty} + \\ &+ 4\pi|t| \int_0^{+\infty} dr \frac{\sin(\pi r)}{\pi r} \sin(2\pi|t|r) \\ =& -2 + 2|t| \int_0^{+\infty} dr \frac{1}{r}[\cos[\pi(2|t| - 1)r] + \\ &- \cos[\pi(2|t| + 1)r]], \end{aligned} \tag{G.33}$$

where were used the limits

$$\lim_{r \to +\infty} s(r)\cos(2\pi|t|r) = 0, \tag{G.34}$$

$$\lim_{r \to 0} s(r)\cos(2\pi|t|r) = 1, \tag{G.35}$$

and the identity

$$2\sin(\theta)\sin(\phi) = \cos(\theta - \phi) - \cos(\theta + \phi). \tag{G.36}$$

Now, considering the integral

$$\begin{aligned} \int_0^{+\infty} dx \frac{\cos(ax) - \cos(bx)}{x} &= \int_a^b d\xi \int_0^{+\infty} dx \sin(\xi x) \\ &= \ln\left(\frac{b}{a}\right), \end{aligned} \tag{G.37}$$

where were used the integrals

$$\int_0^{+\infty} dx\, e^{-\alpha r} \sin(\xi x) = \frac{\xi}{\alpha^2 + \xi^2}, \tag{G.38}$$

$$\begin{aligned} \int_0^{+\infty} dx\, \sin(\xi x) &= \lim_{\alpha \to 0} \int_0^{+\infty} dx\, e^{-\alpha r} \sin(\xi x) \\ &= \frac{1}{\xi}, \end{aligned} \tag{G.39}$$

the Fourier cosine transform of the function $ds(r)/dr$ can be found as

$$\mathfrak{F}\left\{\frac{ds(r)}{dr}\right\} = 2\left[-1 + |t| \ln\left(\frac{2|t|+1}{2|t|-1}\right)\right]. \tag{G.40}$$

For the function $f(r) = [ds(r)/dr] \int_0^r dr' s(r')$ is found

$$\begin{aligned} \mathfrak{F}\{f(r)\} =& 2\int_0^{+\infty} dr \frac{d}{dr}\left[\frac{\sin(\pi r)}{\pi r}\right]\left[\int_0^r dr' \frac{\sin(\pi r')}{\pi r'}\right] \times \\ & \times \cos(2\pi|t|r) \\ =& 2\frac{\sin(\pi r)}{\pi r}\left[\int_0^r dr' \frac{\sin(\pi r')}{\pi r'}\right]\cos(2\pi|t|r)\Big|_0^{+\infty} + \\ & - 2\int_0^{+\infty} dr \frac{\sin^2(\pi r)}{\pi^2 r^2}\cos(2\pi|t|r) + \\ & + 4\pi|t| \int_0^{+\infty} dr \frac{\sin(\pi r)}{\pi r}\left[\int_0^r dr' \frac{\sin(\pi r')}{\pi r'}\right]\sin(2\pi|t|r) \\ =& -\mathfrak{F}\{s^2(r)\} + 2|t| \int_0^{+\infty} dr \frac{1}{r}[\cos[\pi(2|t|-1)r] + \\ & - \cos[\pi(2|t|+1)r]]\left[\int_0^r dr' \frac{\sin(\pi r')}{\pi r'}\right], \end{aligned} \tag{G.41}$$

where were used the limits

$$\lim_{r \to +\infty} s(r)\left[\int_0^r dr' s(r')\right]\cos(2\pi|t|r) = 0, \tag{G.42}$$

$$\lim_{r \to 0} s(r)\left[\int_0^r dr' s(r')\right]\cos(2\pi|t|r) = 0, \tag{G.43}$$

and the identity (G.36). Now, considering the integral

$$\begin{aligned} I(a,b) &= \int_0^{+\infty} dx \frac{\cos(ax)-\cos(bx)}{x} \int_0^x dy \frac{\sin(\pi y)}{\pi y} \\ &= \int_a^b d\xi \int_0^{+\infty} dx \sin(\xi x) \int_0^x dy \frac{\sin(\pi y)}{\pi y} \\ &= -\int_a^b d\xi \frac{\cos(\xi x)}{\xi} \int_0^x dy \frac{\sin(\pi y)}{\pi y}\Bigg|_0^{+\infty} + \\ &\quad + \int_a^b d\xi \int_0^{+\infty} dx \frac{\sin(\pi x)}{\pi x} \frac{\cos(\xi x)}{\xi} \\ &= \int_a^b d\xi \frac{1}{2\pi\xi} \int_0^{+\infty} dx \frac{\sin((\pi+\xi)x)+\sin((\pi-\xi)x)}{x} \\ &= \begin{cases} -\frac{1}{2}\ln\left|\frac{a}{\pi}\right| & \text{if } |t| \le 1 \\ 0 & \text{if } |t| > 1 \end{cases}, \end{aligned} \tag{G.44}$$

where were used the limits

$$\lim_{x\to+\infty} \cos(\xi x) \int_0^x dy\, s(y) = 0, \tag{G.45}$$

$$\lim_{x\to 0} \cos(\xi x) \int_0^x dy\, s(y) = 0, \tag{G.46}$$

the values $\xi = a = \pi(2|t|-1)$ and $\xi = b = \pi(2|t|+1)$ for which $\lim_{x\to+\infty}\cos(\xi x) = 0$, the identity

$$2\sin(\theta)\cos(\phi) = \sin(\theta+\phi)+\sin(\theta-\phi), \tag{G.47}$$

and the integral

$$\int_0^{+\infty} dx \frac{\sin((\pi\pm\xi)x)}{x} = \frac{\pi}{2} \begin{cases} -1 & \text{if } \pm\xi < -\pi \\ 0 & \text{if } \xi = \mp\pi \\ 1 & \text{if } \pm\xi > -\pi \end{cases}, \tag{G.48}$$

the Fourier cosine transform of the function $[ds(r)/dr]\int_0^r dr' s(r')$ can be found as

$$\mathfrak{F}\left\{\frac{ds(r)}{dr}\int_0^r dr' s(r')\right\} = \begin{cases} -1+|t|-|t|\ln|2|t|-1| & \text{if } |t| \le 1 \\ 0 & \text{if } |t| > 1 \end{cases}. \tag{G.49}$$

In this way, using Eqs. (G.32), (G.40), and (G.49) is found the two-level form factor of the GOE given by Eq. (4.16).

Appendix H

Behavior of the Survival Probability

In this Appendix is exposed the universal behavior of the survival probability at short times, as well as the complete derivation of the analytical expression that reproduces the correlation hole.

H.1 Universal Quadratic Behavior

The survival probability shows a universal quadratic behavior at very short times [187], which can be derived analytically for a given Hamiltonian $\hat{H}$ with eigenvalue equation $\hat{H}|\phi_n\rangle = E_n|\phi_n\rangle$ and dimension N of the Hilbert space, using its expectation value E_0 and variance σ_0^2 under the initial state (4.24),

$$\begin{aligned} E_0 &= \langle\Psi(0)|\hat{H}|\Psi(0)\rangle \\ &= \sum_{n=1}^{N} |c_n|^2 E_n, \end{aligned} \tag{H.1}$$

$$\begin{aligned} \sigma_0^2 &= \langle\Psi(0)|\hat{H}^2|\Psi(0)\rangle - \langle\Psi(0)|\hat{H}|\Psi(0)\rangle^2 \\ &= \sum_{n=1}^{N} |c_n|^2 (E_n - E_0)^2. \end{aligned} \tag{H.2}$$

In this way, Eq. (4.26) can be written as

$$\begin{aligned} S_P(t) &= |\langle\Psi(0)|e^{-i\hat{H}t}|\Psi(0)\rangle|^2 \\ &= |e^{-iE_0t}\langle\Psi(0)|e^{-i(\hat{H}-E_0)t}|\Psi(0)\rangle|^2 \\ &= \left(1-\frac{\sigma_0^2}{2}t^2\right)^2+\dots \\ &= 1-\sigma_0^2t^2+\frac{\sigma_0^4}{4}t^4+\dots, \end{aligned} \tag{H.3}$$

where the term

$$e^{-i(\hat{H}-E_0)t} = 1-i(\hat{H}-E_0)t-\frac{1}{2!}(\hat{H}-E_0)^2t^2+\dots \tag{H.4}$$

was Taylor expanded, such that, by evaluating the survival probability at very short times $S_P(t \ll \sigma_0^{-1})$ is found the universal quadratic behavior given by Eq. (4.32).

H.2 Correlation Hole

The representation of the survival probability in diagonal and non-diagonal terms (see Eq. (4.30)) defines a spectral autocorrelation function [152, 161, 162, 166], given by

$$S(E) = \sum_{n\neq n'}|c_n|^2|c_{n'}|^2\delta[E-(E_n-E_{n'})]+\sum_n|c_n|^4\delta(E), \tag{H.5}$$

δ is the Dirac delta function given by Eq. (C.14). In this way, the survival probability can be expressed as the Fourier transform of this spectral autocorrelation function as

$$\begin{aligned} S_P(t) &= \mathfrak{F}\{S(E)\} \\ &= \int_{-\infty}^{+\infty} dE\, S(E)e^{-iEt}. \end{aligned} \tag{H.6}$$

Taking an ensemble average over the above equation is found

$$\begin{aligned}\langle S_P(t)\rangle &= \left\langle \int_{-\infty}^{+\infty} dE\, S(E) e^{-iEt} \right\rangle \\ &= \int_{-\infty}^{+\infty} dE \langle S(E)\rangle e^{-iEt}, \end{aligned} \tag{H.7}$$

where the ensemble average and the integral were interchanged. For the second term of Eq. (H.5) is found directly

$$\begin{aligned}\left\langle \sum_n |c_n|^4 \delta(E) \right\rangle &= \left\langle \sum_n |c_n|^4 \right\rangle \delta(E) \\ &= \left\langle \frac{1}{P_R} \right\rangle \delta(E), \end{aligned} \tag{H.8}$$

where P_R is given by Eq. (4.31). On the other hand, for the first term of Eq. (H.5), it is considered that the eigenenergies are statistically independent of the eigenstates, such that, the following factorization is possible

$$\begin{aligned}\left\langle \sum_{n\neq n'} |c_n|^2 |c_{n'}|^2 \delta[E-(E_n - E_{n'})] \right\rangle = \left\langle \sum_{n\neq n'} |c_n|^2 |c_{n'}|^2 \right\rangle \times \\ \times \langle \delta[E-(E_n - E_{n'})]\rangle. \end{aligned} \tag{H.9}$$

The first term of the product is given by

$$\begin{aligned}\left\langle \sum_{n\neq n'} |c_n|^2 |c_{n'}|^2 \right\rangle &= 1 - \left\langle \sum_n |c_n|^4 \right\rangle \\ &= 1 - \left\langle \frac{1}{P_R} \right\rangle, \end{aligned} \tag{H.10}$$

while the second one can be written as

$$\begin{aligned}\langle\delta[E-(E_n-E_{n'})]\rangle &= \int_{-\infty}^{+\infty}\dots\int_{-\infty}^{+\infty} dE_1\dots dE_\eta\times \\ &\quad\times\delta[E-(E_n-E_{n'})]P_\eta(E_1,\dots,E_\eta) \\ &= \int_{-\infty}^{+\infty}\int_{-\infty}^{+\infty} dE_n\, dE_{n'}\times \\ &\quad\times\delta[E-(E_n-E_{n'})]P_2(E_n,E_{n'}) \\ &= \frac{(\eta-2)!}{\eta!}\int_{-\infty}^{+\infty}\int_{-\infty}^{+\infty} dE_n\, dE_{n'}\times \\ &\quad\times\delta[E-(E_n-E_{n'})]R_2(E_n,E_{n'}),\end{aligned} \tag{H.11}$$

where E_n and $E_{n'}$ are two energy levels contained in the effective set of eigenenergies $\{E_1,\dots,E_\eta\}$, and $R_2(E_n,E_{n'})$ is the two-level correlation function, which can be expressed through the two-level cluster function $T_2(E_n,E_{n'})$ (see Eqs. (4.4) and (4.6) for 2 energy levels) as

$$\begin{aligned}R_2(E_n,E_{n'}) &= \frac{\eta!}{(\eta-2)!}P_2(E_n,E_{n'}) \\ &= R_1(E_n)R_1(E_{n'})-T_2(E_n,E_{n'}).\end{aligned} \tag{H.12}$$

The previous result can be inserted in Eq. (H.11) renaming the energy levels as $E_n = E_1$ and $E_{n'} = E_2$. Taking this result and Eqs. (H.8) and (H.10), the ensemble average of the survival probability (H.7) takes the form

$$\langle S_P(t)\rangle = \left[1-\left\langle\frac{1}{P_R}\right\rangle\right]F(t)+\left\langle\frac{1}{P_R}\right\rangle, \tag{H.13}$$

where the time-dependent term can be divided into two terms

$$\begin{aligned}F(t) &= \int_{-\infty}^{+\infty} dE\langle\delta[E-(E_1-E_2)]\rangle e^{-iEt}, \\ &= f_1(t)+f_2(t).\end{aligned} \tag{H.14}$$

For the first term is found

$$\begin{aligned} f_1(t) &= \frac{1}{\eta(\eta-1)} \int_{-\infty}^{+\infty} \int_{-\infty}^{+\infty} dE_1 dE_2 R_1(E_1) R_1(E_2) e^{-i(E_1-E_2)t} \\ &= \frac{1}{\eta(\eta-1)} \left| \int_{-\infty}^{+\infty} dE\, R_1(E) e^{-iEt} \right|^2 \\ &\approx \frac{\eta}{\eta-1} \left| \int_{-\infty}^{+\infty} dE\, \rho(E) e^{-iEt} \right|^2 \\ &\approx \frac{\eta}{\eta-1} S_P^{\mathrm{st}}(t), \end{aligned} \tag{H.15}$$

where was considered

$$\begin{aligned} \frac{R_1(E)}{\eta} = \nu(E) &= \sum_n \delta(E-E_n) \\ &\approx \rho_0(E) = \sum_n |c_n|^2 \delta(E-E_n) \\ &\approx \rho(E), \end{aligned} \tag{H.16}$$

that is, the generalized level density $R_1(E)$ normalized to the total number of effective levels η was approximated to the envelope of the LDoS $\rho(E)$. On the other hand, for the second term is found

$$\begin{aligned} f_2(t) &= -\frac{1}{\eta(\eta-1)} \int_{-\infty}^{+\infty} \int_{-\infty}^{+\infty} dE_1 dE_2 T_2(E_1, E_2) e^{-i(E_1-E_2)t} \\ &= -\frac{1}{\eta-1} \int_{-\infty}^{+\infty} \int_{-\infty}^{+\infty} dy_1 dy_2 \widetilde{Y}_2(y_1, y_2) e^{-i(y_1-y_2)Dt} \\ &= -\frac{1}{\eta-1} \int_{-\infty}^{+\infty} dr\, \widetilde{Y}_2(r) e^{2\pi i r[Dt/(2\pi)]} \\ &= -\frac{1}{\eta-1} b_2\left(\frac{Dt}{2\pi}\right), \end{aligned} \tag{H.17}$$

where the two-level cluster function $T_2(E_1, E_2)$ was also normalized to the total number of effective levels η

$$\widetilde{T}_2(E_1, E_2) = \frac{T_2(E_1, E_2)}{\eta}, \tag{H.18}$$

and was considered the rescaled two-level cluster function

$$\widetilde{Y}_2(y_1, y_2) = \lim_{\eta \to +\infty} D^2 \widetilde{T}_2(E_1, E_2) \tag{H.19}$$

to the rescaled variables $y_i = E_i/D$, such that $\widetilde{Y}_2(r) = \widetilde{Y}_2(y_1, y_2)$ with $r = |y_1 - y_2|$.

Using Eqs. (H.15) and (H.17) in Eq. (H.14) is found the result

$$F(t) = \frac{1}{\eta - 1}\left[\eta S_P^{\mathrm{st}}(t) - b_2\left(\frac{Dt}{2\pi}\right)\right], \tag{H.20}$$

such that, by inserting it in Eq. (H.13) gives Eq. (4.36).

Appendix I

Properties of Coherent States

In this Appendix is exposed the property of the Glauber coherent states as states of minimum uncertainty. Furthermore, the expectation values of collective pseudo-spin operators under Bloch coherent states are developed.

I.1 States of Minimum Uncertainty

The creation-annihilation operators $\hat{a}^\dagger$ and $\hat{a}$ can be expressed in terms of the position and momentum operators of the quantum harmonic oscillator with unitary mass as

$$\hat{q} = \sqrt{\frac{\hbar}{2\omega}} \left(\hat{a}^\dagger + \hat{a} \right), \tag{I.1}$$

$$\hat{p} = i\sqrt{\frac{\hbar\omega}{2}} \left(\hat{a}^\dagger - \hat{a} \right), \tag{I.2}$$

which satisfy the commutation relation $[\hat{q}, \hat{p}] = i\hbar\hat{1}$. Under these variables, the generalized uncertainty principle, known as the

Schrödinger-Robertson uncertainty principle [49], takes the form

$$\sigma_q^2 \sigma_p^2 - \sigma_{pq}^4 \geq \frac{\hbar^2}{4}, \tag{I.3}$$

where each term is given by

$$\begin{aligned} \sigma_q^2 &= \langle\alpha|\hat{q}^2|\alpha\rangle - \langle\alpha|\hat{q}|\alpha\rangle^2 \\ &= \frac{\hbar}{2\omega}, \qquad \text{(I.4)} \\ \sigma_p^2 &= \langle\alpha|\hat{p}^2|\alpha\rangle - \langle\alpha|\hat{p}|\alpha\rangle^2 \\ &= \frac{\hbar\omega}{2}, \qquad \text{(I.5)} \\ \sigma_{pq}^2 &= \frac{1}{2}\langle\alpha|\hat{p}\hat{q} + \hat{q}\hat{p}|\alpha\rangle - \langle\alpha|\hat{p}|\alpha\rangle\langle\alpha|\hat{q}|\alpha\rangle \\ &= 0. \qquad \text{(I.6)} \end{aligned}$$

Using the latter explicit results, the Schrödinger-Robertson uncertainty principle becomes the Heisenberg's uncertainty principle and at the same time becomes an equality

$$\sigma_q \sigma_p = \frac{\hbar}{2}, \tag{I.7}$$

which implies that the Glauber coherent states are states of minimum uncertainty.

I.2 Expectation Values of the Collective Pseudo-Spin Operators

The expectation values of the collective pseudo-spin operators $\hat{J}_{x,y,z}$ and their corresponding raising-lowering operators $\hat{J}_{\pm} =$

$\hat{J}_x \pm i\hat{J}_y$ are given by

$$\begin{aligned}\langle z|\hat{J}_{x,y,z}|z\rangle &= j[\cos(\phi)\sin(\theta), \sin(\phi)\sin(\theta), -\cos(\theta)] \\ &= j\left(\frac{2\Re[z]}{1+|z|^2}, -\frac{2\Im[z]}{1+|z|^2}, \frac{|z|^2-1}{1+|z|^2}\right), \qquad \text{(I.8)} \\ \langle z|\hat{J}_{\pm}|z\rangle &= j\sin(\theta)e^{\pm i\phi} \\ &= j\left(\frac{2z^*}{1+|z|^2}, \frac{2z}{1+|z|^2}\right), \qquad \text{(I.9)}\end{aligned}$$

where the angular variables (ϕ, θ) are the azimuthal and zenith angles of the spherical coordinates, measuring the θ angle from the negative z axis. Moreover, were used the expressions

$$[\sin(\theta), \cos(\theta)] = \left(\frac{2|z|}{1+|z|^2}, \frac{1-|z|^2}{1+|z|^2}\right), \qquad \text{(I.10)}$$

which can be found from Eq. (C.4).

Appendix J

Quasiprobability Distributions of Coherent States

In this Appendix are exposed the explicit expressions for some quasiprobability distributions (Wigner and Husimi functions) of Glauber and Bloch coherent states.

J.1 Wigner Function of Coherent States

For an initial Glauber coherent state $|\alpha_0\rangle$ with parameter $\alpha_0 = \alpha(q_0, p_0)$ (see Eq. (2.29)), the Wigner function is given by a normal distribution

$$\begin{aligned} \mathcal{W}_{\alpha_0}(\alpha) &= \frac{j}{\pi} e^{-2|\alpha-\alpha_0|^2} \\ &= \frac{j}{\pi} e^{-j\Delta^2}, \end{aligned} \tag{J.1}$$

where

$$\Delta = \sqrt{(q-q_0)^2 + (p-p_0)^2}. \tag{J.2}$$

For an initial Bloch coherent state $|z_0\rangle$ with parameter $z_0 = z(\phi_0, \theta_0)$ (see Eq. (2.30)), the atomic angle variables can be mapped

to the atomic position-momentum variables $(\phi, \theta) \to (Q, P)$ using the transformation (C.6)), the Wigner function can be written as a sum of Legendre polynomials $P_k(x)$ [289]

$$\begin{aligned}\mathcal{W}_{z_0}(z) &= \frac{(2j)!}{4\pi} \sum_{k=0}^{2j} \sqrt{\frac{2k+1}{(2j-k)!(2j+k+1)!}} P_k[\cos(\Theta)] \\ &\approx \frac{j}{\pi} e^{-j\Theta^2},\end{aligned} \tag{J.3}$$

where Θ is the angle between two points (ϕ_0, θ_0) and (ϕ, θ) obtained from the relation

$$\cos(\Theta) = \cos(\theta)\cos(\theta_0) + \sin(\theta)\sin(\theta_0)\cos(\phi - \phi_0), \tag{J.4}$$

and furthermore, the Wigner function is very well approximated by a normal distribution on the Bloch sphere for large values of the system size j.

Thus, the Wigner function for initial Glauber-Bloch coherent states $|\mathbf{x}_0\rangle = |\alpha_0\rangle \otimes |z_0\rangle$ is just the product of the Wigner functions (J.1) and (J.3)

$$\begin{aligned}\mathcal{W}_{\mathbf{x}_0}(\mathbf{x}) &= \mathcal{W}_{\alpha_0}(\alpha)\mathcal{W}_{z_0}(z) \\ &\approx \left(\frac{j}{\pi}\right)^2 e^{-jD^2_{\mathcal{M}}(\mathbf{x},\mathbf{x}_0)},\end{aligned} \tag{J.5}$$

where

$$\begin{aligned}D_{\mathcal{M}}(\mathbf{x}, \mathbf{x}_0) &= \sqrt{\Delta^2(\alpha, \alpha_0) + \Theta^2(z, z_0)} \\ &= \sqrt{(q-q_0)^2 + (p-p_0)^2 + \Theta^2}\end{aligned} \tag{J.6}$$

is the phase-space separation.

J.2 Husimi Function of Coherent States

The unnormalized Husimi function for an initial Glauber coherent state $|\alpha_0\rangle$ with parameter $\alpha_0 = \alpha(q_0, p_0)$ (see Eq. (2.29)) and an initial Bloch coherent state $|z_0\rangle$ with parameter $z_0 = z(\phi_0, \theta_0)$

(see Eq. (2.30), the atomic angle variables can be mapped to the atomic position-momentum variables $(\phi, \theta) \to (Q, P)$ using the transformation (C.6)) is given by Eqs. (5.11) and (5.19)

$$\begin{aligned} \mathcal{Q}_{\alpha_0}(\alpha) &= e^{-|\alpha-\alpha_0|^2} \\ &= e^{-(j/2)\Delta^2}, \end{aligned} \tag{J.7}$$

$$\begin{aligned} \mathcal{Q}_{z_0}(z) &= \left[1 - \frac{|z-z_0|^2}{(1+|z|^2)(1+|z_0|^2)}\right]^{2j} \\ &\approx e^{-(j/2)\Theta^2}, \end{aligned} \tag{J.8}$$

where the Husimi function of the Bloch coherent state is well fitted by a normal distribution for large j, and the parameters Δ and Θ are given by Eqs. (J.2) and (J.4), respectively.

In this way, the unnormalized Husimi function for initial Glauber-Bloch coherent states $\hat{\rho}_{\mathbf{x}_0} = |\mathbf{x}_0\rangle\langle\mathbf{x}_0|$ with $|\mathbf{x}_0\rangle = |\alpha_0\rangle \otimes |z_0\rangle$ is given by the product of the Husimi functions (J.7) and (J.8)

$$\begin{aligned} \mathcal{Q}_{\mathbf{x}_0}(\mathbf{x}) &= \langle \mathbf{x}|\hat{\rho}_{\mathbf{x}_0}|\mathbf{x}\rangle \\ &= \mathcal{Q}_{\alpha_0}(\alpha)\mathcal{Q}_{z_0}(z) \\ &\approx e^{-(j/2)D^2_{\mathcal{M}}(\mathbf{x},\mathbf{x}_0)}, \end{aligned} \tag{J.9}$$

where $D_{\mathcal{M}}(\mathbf{x}, \mathbf{x}_0)$ is given by Eq. (J.6).

Appendix K

Random States in the Dicke Model

In this Appendix is exposed the general method to construct random states within energy intervals of the spectrum of the Dicke model, as well as the ensemble effective dimension related with the participation ratio.

K.1 Random States within an Energy Interval

A random state can be expanded in the energy eigenbasis of the Dicke Hamiltonian $\{|E_k\rangle\}$ (see Eq. (2.26)) as

$$|\Psi_{\mathrm{R}}\rangle = \sum_k c_k |E_k\rangle, \tag{K.1}$$

where the coefficients $c_k = \langle E_k|\Psi_{\mathrm{R}}\rangle$ can be defined as

$$c_k = \sqrt{\frac{r_k \rho(E_k)}{M\nu(E_k)}} e^{i\theta_k}, \tag{K.2}$$

where the weights r_k are sampled from an arbitrary distribution and the phases θ_k from a uniform distribution defined in the

interval $[0, \pi)$. The term $\rho(E)$ defines the envelope of the coefficient distribution (LDoS envelope of the initial state) contained within a selected interval of the energy spectrum, $\nu(E) = \nu(\epsilon)/j$ is the semiclassical density of sates given by Eq. (2.41), and $M = \sum_k r_k \rho(E_k)/\nu(E_k)$ is a normalization constant.

K.2 Ensemble Effective Dimension

For initial random states whose coefficients are defined by Eq. (K.2), the ensemble average of the inverse of the PR takes the form

$$\begin{aligned}\left\langle \frac{1}{P_R} \right\rangle &= \left\langle \sum_k |c_k|^4 \right\rangle \\ &= \left\langle \sum_k \frac{r_k^2 \rho^2(E_k)}{M^2 \nu^2(E_k)} \right\rangle \\ &= \left\langle \frac{r_k^2}{M^2} \right\rangle \sum_k \frac{\rho^2(E_k)}{\nu^2(E_k)} \\ &\approx \frac{\langle r_k^2 \rangle}{\langle r_k \rangle^2} \frac{1}{\eta},\end{aligned} \tag{K.3}$$

where was considered that the eigenenergies are statistically independent of the eigenstates, and the ensemble average was approximated as

$$\begin{aligned}\left\langle \frac{r_k^2}{M^2} \right\rangle &\approx \frac{\langle r_k^2 \rangle}{\langle M^2 \rangle} \\ &\approx \frac{\langle r_k^2 \rangle}{\langle r_k \rangle^2 [\sum_k \rho(E_k)/\nu(E_k)]^2}.\end{aligned} \tag{K.4}$$

Using the above expression the ensemble effective dimension can be defined as

$$\begin{aligned}\eta &= \frac{[\sum_k \rho(E_k)/\nu(E_k)]^2}{\sum_k \rho^2(E_k)/\nu^2(E_k)} \\ &\approx \frac{\nu_{\mathrm{c}}}{\int_{-\infty}^{+\infty} dE\, \rho^2(E)} \\ &\approx \frac{\langle r_k^2 \rangle}{\langle r_k \rangle^2} \left\langle \frac{1}{P_R} \right\rangle^{-1}, \end{aligned} \tag{K.5}$$

where the sum was changed for an integral $\sum_k \bullet \to \int dE\, \nu(E) \bullet$, the normalization condition of the LDoS envelope was used, and the semiclassical density of states was evaluated at the energy center of the LDoS envelope $\nu_{\mathrm{c}} = \nu(E_{\mathrm{c}})$.

Appendix L

Classical Limit of the Survival Probability

In this Appendix is exposed the complete derivation of the classical limit of the survival probability constructed with the truncated Wigner approximation.

L.1 Truncated Wigner Approximation

The Moyal bracket for two functions F and F' is defined as [290]

$$\begin{aligned}\{F, F'\}_{\mathrm{M}} &= \frac{2}{\hbar} F \sin\left[\frac{\hbar}{2}\left(\overleftarrow{\partial_{\mathbf{q}}}\overrightarrow{\partial_{\mathbf{p}}} - \overleftarrow{\partial_{\mathbf{p}}}\overrightarrow{\partial_{\mathbf{q}}}\right)\right] F' \\ &= \{F, F'\} + \mathcal{O}(\hbar^2),\end{aligned} \tag{L.1}$$

where the sine was Taylor expanded, such that, the first term is a Poisson bracket. Using this feature, the so-called Moyal equation [291], which governs the time evolution of the Wigner function, can be written as

$$\begin{aligned}\frac{\partial \mathcal{W}_\Psi(\mathbf{x}, t)}{\partial t} &= \{\mathcal{W}_\Psi(\mathbf{x}, t), h_{\mathrm{D}}(\mathbf{x})\}_{\mathrm{M}} \\ &= \{\mathcal{W}_\Psi(\mathbf{x}, t), h_{\mathrm{D}}(\mathbf{x})\} + \mathcal{O}(j^{-2}),\end{aligned} \tag{L.2}$$

where $\mathcal{W}_\Psi(\mathbf{x},t)$ is the time-dependent Wigner function of an arbitrary state $|\Psi\rangle$, $h_{\rm D}(\mathbf{x})$ is the classical Dicke Hamiltonian (2.38). By ignoring the j^{-2} order terms in this expression, the remaining equation is the classical Liouville equation. The latter choice defines the truncated Wigner approximation and yields the correct quantum evolution for small times.

Within this approximation, the Wigner function remains constant along classical trajectories in phase space, so its time dependence can be written in terms of the Hamiltonian flow $\varphi^t : \mathcal{M} \to \mathcal{M}$, which describes the time evolution of an initial condition $\mathbf{x}_0 \in \mathcal{M}$ as

$$\mathbf{x}(t) = \varphi^t(\mathbf{x}_0), \tag{L.3}$$

and satisfies the one-parameter group identities $\varphi^0 = \mathrm{Id}$, $\varphi^{-t} = (\varphi^t)^{-1}$, and $\varphi^{t_1+t_2} = \varphi^{t_2} \circ \varphi^{t_1}$. Thus, the Wigner function for any pair of times t_1 and t_2 satisfies the next relation

$$\mathcal{W}_\Psi[\varphi^{t_1}(\mathbf{x}_0), t_1] = \mathcal{W}_\Psi[\varphi^{t_2}(\mathbf{x}_0), t_2]. \tag{L.4}$$

In particular, taking $t_1 = 0$ and $t_2 = t$ is found

$$\mathcal{W}_\Psi(\mathbf{x},t) = \mathcal{W}_\Psi[\varphi^{-t}(\mathbf{x}), 0]. \tag{L.5}$$

L.2 Survival Probability and Wigner Function

The basic idea to write the survival probability in terms of their Wigner functions is to use the overlap property between two arbitrary quantum states $|\Psi\rangle$ and $|\Psi'\rangle$ [227]

$$|\langle\Psi|\Psi'\rangle|^2 = (2\pi\hbar)^I \int d\alpha\, \mathcal{W}_\Psi(\alpha)\mathcal{W}_{\Psi'}(\alpha), \tag{L.6}$$

where $\mathcal{W}_\Psi(\alpha)$ is the Wigner function of the arbitrary state $|\Psi\rangle$ in the overcomplete basis of coherent states $\{|\alpha\rangle\}$, and I represents the degrees of freedom of the system.

The Wigner function $\mathcal{W}_\Psi(\mathbf{x})$ of an arbitrary state $|\Psi\rangle$ defined in the overcomplete basis of Glauber-Bloch coherent states $\{|\mathbf{x}\rangle\}$

is given by Eq. (7.2), where $\mathbf{x} = (q, p; Q, P)$ are the coordinates of the four-dimensional phase space $\mathcal{M}$ of the Dicke model. In this way, the survival probability (4.26) can be written as

$$S_P(t) = (2\pi\hbar_{\text{eff}})^2 \int_{\mathcal{M}} d\mathbf{x}\, \mathcal{W}_\Psi(\mathbf{x}, 0)\mathcal{W}_\Psi(\mathbf{x}, t), \tag{L.7}$$

where $\hbar_{\text{eff}} = j^{-1}$. Using the TWA, the short-time dependence of the Wigner function can be written in terms of the Hamiltonian flow $\varphi^t : \mathcal{M} \to \mathcal{M}$ and the relation (L.5) for short times is found. Using the definitions $\mathcal{W}_\Psi(\mathbf{x}, 0) \equiv \mathcal{W}_\Psi(\mathbf{x})$ and $\mathcal{W}_\Psi(\mathbf{x}, t) = \mathcal{W}_\Psi[\varphi^{-t}(\mathbf{x}), 0] \equiv \mathcal{W}_\Psi[\varphi^{-t}(\mathbf{x})]$ in the above expression the Eq. (7.1) is found.

On the other hand, the classical limit of survival probability (7.1) can be rewritten as

$$\begin{aligned} \mathfrak{S}_P(t) &= \left\langle \mathcal{W}_\Psi[\varphi^{-t}(\mathbf{x})] \right\rangle_{\mathcal{W}_\Psi} \\ &\approx \frac{1}{M} \sum_{i=1}^{M} \mathcal{W}_\Psi[\varphi^{-t}(\mathbf{x}_i)], \end{aligned} \tag{L.8}$$

where the expectation value can be efficiently approximated using a Monte Carlo method provided that $\mathcal{W}_\Psi$ is everywhere positive and defined for initial Glauber-Bloch coherent states $|\Psi\rangle = |\mathbf{x}_0\rangle$ (see Eq. (J.5)). The points $\mathbf{x}_i \in \mathcal{M}$ are randomly sampled from the initial distribution $\mathcal{W}_{\mathbf{x}_0}(\mathbf{x})$, and M is a sufficiently large, albeit computationally accessible, integer.

Appendix M

Coherent States in the Dicke Model

In this Appendix is exposed the representation of the Glauber-Bloch coherent states in the energy eigenbasis of the Dicke Hamiltonian using the coherent basis.

M.1 Coherent States and the Coherent Basis

The coherent basis $\{|N; j, m_x\rangle\}$ allows to diagonalize the Dicke Hamiltonian and to find the eigenenergies and eigenstates. In this way, such eigenstates are represented in the coherent basis as

$$|E_k\rangle = \sum_{N,m_x} C^k_{N,m_x} |N; j, m_x\rangle, \tag{M.1}$$

where the coefficients $C^k_{N,m_x} = \langle N; j, m_x | E_k\rangle$ are found numerically [6].

On the other hand, the Glauber-Bloch coherent states $|\mathbf{x}\rangle = |\alpha\rangle \otimes |z\rangle$ have a representation in the energy eigenbasis of the

Dicke Hamiltonian $\{|E_k\rangle\}$ (see Eq. (2.26)) given by

$$|\mathbf{x}\rangle = \sum_k C_k(\mathbf{x})|E_k\rangle, \tag{M.2}$$

where $\mathbf{x} = (q, p; Q, P)$ are the coordinates of the four-dimensional phase space $\mathcal{M}$ of the Dicke model, and the coefficients $C_k(\mathbf{x}) = \langle E_k|\mathbf{x}\rangle$ can be represented at the same time in the coherent basis as

$$C_k(\mathbf{x}) = \sum_{N,m_x} (C^k_{N,m_x})^* C_{N,m_x}(\mathbf{x}), \tag{M.3}$$

and the coefficients $C_{N,m_x}(\mathbf{x}) = \langle N; j, m_x|\mathbf{x}\rangle$ are found using Eq. (B.6)

$$C_{N,m_x}(\mathbf{x}) = \frac{(\alpha - \alpha_{m_x})^N}{\sqrt{N!}} \langle \alpha_{m_x}|\alpha\rangle \langle j, m_x|z\rangle, \tag{M.4}$$

where $\alpha_{m_x} = -Gm_x$ and $G = 2\gamma/(\omega\sqrt{\mathcal{N}})$. Moreover, Eq. (5.10) gives directly the bosonic overlap $\langle \alpha_{m_x}|\alpha\rangle$, while Eq. (5.16) gives the atomic overlap

$$\langle j, m_x|w(z)\rangle = \sqrt{\begin{pmatrix} 2j \\ j + m_x \end{pmatrix}} \frac{w^{j+m_x}(z)}{(1 + |w(z)|^2)^j}, \tag{M.5}$$

where $w(z) = (1 + z)/(1 - z)$ is the rotated atomic parameter with $z = \tan(\theta/2)e^{-i\phi}$. In this way, using the latter results the Glauber-Bloch coherent states have an explicit representation in the energy eigenbasis using the coherent basis through the coefficients (M.3)

An analogous procedure can be derived using the coherent basis with well-defined parity $\{|N; j, m_x; p\rangle\}$, which gives the following coefficients

$$C_{k,p}(\mathbf{x}) = \sum_{N,m_x} (C^{k,p}_{N,m_x})^* C^p_{N,m_x}(\mathbf{x}), \tag{M.6}$$

where

$$C^p_{N,m_x}(\mathbf{x}) = \frac{C_{N,m_x}(\mathbf{x}) + p(-1)^N C_{N,-m_x}(\mathbf{x})}{\sqrt{2(1 + \delta_{m_x,0})}}. \tag{M.7}$$

Appendix N

Husimi Function in the Dicke Model

In this Appendix is exposed the Husimi function for eigenstates of the Dicke Hamiltonian. On the other hand, two methods of projection of the Husimi function are developed, one defined at a classical energy shell, and other one defined over all classical energy shells, such that, exact projections can be found using the Fock basis.

N.1 Husimi Function of Eigenstates

The unnormalized Husimi function for eigenstates $\hat{\rho}_k = |E_k\rangle\langle E_k|$ of the Dicke model can be written as

$$\begin{aligned} \mathcal{Q}_k(\mathbf{x}) &= \langle \mathbf{x}|\hat{\rho}_k|\mathbf{x}\rangle \\ &= |\langle E_k|\mathbf{x}\rangle|^2 \\ &= |C_k(\mathbf{x})|^2, \end{aligned} \tag{N.1}$$

where $C_k(\mathbf{x})$ are the coefficients of the Glauber-Bloch coherent states given by Eq. (M.3), which can be constructed numerically by diagonalizing the Dicke Hamiltonian (2.5) with the coherent basis $\{|N; j, m_x\rangle\}$.

N.2 Projection at a Classical Energy Shell

An arbitrary function $F(\mathbf{x})$, which depends on the coordinates $\mathbf{x} = (q, p; Q, P)$ of the four-dimensional phase space $\mathcal{M}$ of the Dicke model, can be projected in the atomic plane $Q - P$ at a classical energy shell $\epsilon = E/j$ as

$$\begin{aligned}\widetilde{F}_\epsilon(Q,P) &= \int\int dq\, dp\, \delta[h_{\mathrm{D}}(\mathbf{x}) - \epsilon] F(\mathbf{x}) \\ &= \int_{p_-}^{p_+} dp \frac{\sum_{q_\pm} F(q_\pm, p; Q, P)}{\sqrt{\Delta_\epsilon(p, Q, P)}}, \end{aligned} \tag{N.2}$$

where δ is the Dirac delta function given by Eq. (C.14) and were used its properties (C.15), $q_\pm$ are the two solutions of the second degree equation $h_{\mathrm{D}}(\mathbf{x}) - \epsilon = 0$, and $p_\pm$ are the two solutions of the second degree equation $\Delta_\epsilon(p, Q, P) = 0$. The term $\Delta_\epsilon(p, Q, P)$ is specified by Eqs. (C.17) and (C.18). With the latter definitions, the integral (N.2) over p can be computed with a Chebyshev-Gauss quadrature method [15].

N.3 Exact Projections of the Husimi Function

An advantage of using the Fock basis $\{|n, m_z\rangle\}$ to construct the Husimi function of an arbitrary state $\hat{\rho}$ is that closed expressions for the projected Husimi function can be found [250, 252]. The last property is equivalent to project the Husimi function over all available classical energy shells, since any trace of energy is erased from the projection. The Husimi functions projected in

both bosonic $q-p$ and atomic $Q-P$ planes are given by

$$\begin{aligned}\widetilde{\mathcal{Q}}_{\hat{\rho}}(q,p) =& \frac{1}{C_{\mathrm{A}}}\int\int dQ\, dP\, \mathcal{Q}(\mathbf{x}) \\ =& B(q,p)\sum_{n=0}^{n_{\max}}\sum_{n'=0}^{n_{\max}}\sum_{m_z=-j}^{j}(C^{\hat{\rho}}_{n,m_z})^* C^{\hat{\rho}}_{n',m_z}\times \\ & \times F^{\mathrm{B}}_n(q,p)[F^{\mathrm{B}}_{n'}(q,p)]^*, \qquad \text{(N.3)} \\ \widetilde{\mathcal{Q}}_{\hat{\rho}}(Q,P) =& \frac{1}{C_{\mathrm{B}}}\int\int dq\, dp\, \mathcal{Q}(\mathbf{x}) \\ =& A(Q,P)\sum_{n=0}^{n_{\max}}\sum_{m_z=-j}^{j}\sum_{m'_z=-j}^{j}(C^{\hat{\rho}}_{n,m_z})^* C^{\hat{\rho}}_{n,m'_z}\times \\ & \times F^{\mathrm{A}}_{m_z}(Q,P)[F^{\mathrm{A}}_{m'_z}(Q,P)]^*, \qquad \text{(N.4)}\end{aligned}$$

where the constants $C_{\mathrm{A}} = 4\pi/(2j+1)$ and $C_{\mathrm{B}} = 2\pi/j$ normalize the atomic and bosonic subspace, respectively. Moreover

$$F^{\mathrm{B}}_n(q,p) = \frac{1}{\sqrt{n!}}\left[\sqrt{\frac{j}{2}}(q+ip)\right]^n, \qquad \text{(N.5)}$$

$$F^{\mathrm{A}}_{m_z}(Q,P) = \sqrt{\binom{2j}{j+m_z}}\left(\frac{Q+iP}{\sqrt{4-Q^2-P^2}}\right)^{j+m_z}, \qquad \text{(N.6)}$$

and the amplitudes are given by $B(q,p) = e^{-(j/2)(q^2+p^2)}$ and $A(Q,P) = [1-(Q^2+P^2)/4]^{2j}$, respectively. The coefficients $C^{\hat{\rho}}_{n,m_z}$ of the state $\hat{\rho}$ are found numerically by diagonalizing the Dicke Hamiltonian (2.5) with the Fock basis.

Appendix O

Periodic Orbits in the Dicke Model

In this Appendix is exposed the monodromy method to find well-converged periodic orbits in the Dicke model, as well as the procedure to compute their Lyapunov exponent. Moreover, a scarring measure of quantum states caused by these periodic orbits is also exposed.

O.1 Monodromy Method for Periodic Orbits

The monodromy method is a Newton-Raphson-type algorithm that converges towards a periodic orbit given an initial guess for an initial condition and period [259, 260]. This type of algorithm has been extensively studied in several systems [251, 261].

The procedure begins with the guesses for an initial condition $\check{\mathbf{x}}$ and period $\check{T}$ of a given periodic orbit. Now, the objective is to obtain the initial condition $\mathbf{x} = \check{\mathbf{x}} + \Delta\mathbf{x}$ and period $T = \check{T} + \Delta T$ of a periodic orbit in the same energy shell as $\check{\mathbf{x}}$. Considering the fundamental matrix $\mathbf{\Phi}_{\mathbf{x}}(t)$ associated to the classical Dicke Hamiltonian $h_{\mathrm{D}}(\mathbf{x})$ (2.38) and the Hamiltonian flow $\varphi^t(\mathbf{x})$ which

satisfies $\mathbf{x}(t) = \varphi^t(\mathbf{x})$ [292], the following approximations to first order, where $||\Delta\mathbf{x}||$ and $|\Delta T|$ are small, can be made

$$\varphi^{\check{T}}(\check{\mathbf{x}} + \Delta\mathbf{x}) \approx \varphi^{\check{T}}(\check{\mathbf{x}}) + \mathbf{\Phi}_{\check{\mathbf{x}}}(\check{T})\Delta\mathbf{x}, \tag{O.1}$$

$$\varphi^{\Delta T}(\mathbf{x}) \approx \mathbf{x} + \Delta T\, \mathbf{\Sigma}\nabla h_{\mathrm{D}}(\mathbf{x}), \tag{O.2}$$

where

$$\mathbf{\Sigma} = \begin{pmatrix} 0 & 1 & 0 & 0 \\ -1 & 0 & 0 & 0 \\ 0 & 0 & 0 & 1 \\ 0 & 0 & -1 & 0 \end{pmatrix}, \tag{O.3}$$

and $\nabla h_{\mathrm{D}}(\mathbf{x})$ is the gradient of the classical Dicke Hamiltonian. Thus, the Hamiltonian flow takes the form

$$\begin{aligned} \varphi^{T}(\mathbf{x}) &= \varphi^{\check{T}+\Delta T}(\mathbf{x}) \\ &= \varphi^{\Delta T}[\varphi^{\check{T}}(\check{\mathbf{x}} + \Delta\mathbf{x})] \\ &\approx \varphi^{\check{T}}(\check{\mathbf{x}} + \Delta\mathbf{x}) + \Delta T\, \mathbf{\Sigma}\nabla h_{\mathrm{D}}[\varphi^{\check{T}}(\check{\mathbf{x}} + \Delta\mathbf{x})] \\ &\approx \varphi^{\check{T}}(\check{\mathbf{x}}) + \mathbf{\Phi}_{\check{\mathbf{x}}}(\check{T})\Delta\mathbf{x} + \Delta T\, \mathbf{\Sigma}\nabla h_{\mathrm{D}}(\check{\mathbf{x}}'), \end{aligned} \tag{O.4}$$

where $\check{\mathbf{x}}' = \varphi^{\check{T}}(\check{\mathbf{x}})$. The last equation allows to approximate the periodicity constriction $\mathbf{x} = \varphi^{T}(\mathbf{x})$ to first order as

$$\check{\mathbf{x}} + \Delta\mathbf{x} = \varphi^{\check{T}}(\check{\mathbf{x}}) + \mathbf{\Phi}_{\check{\mathbf{x}}}(\check{T})\Delta\mathbf{x} + \Delta T\, \mathbf{\Sigma}\nabla h_{\mathrm{D}}(\check{\mathbf{x}}'), \tag{O.5}$$

and in the same way the energy constriction $h_{\mathrm{D}}(\mathbf{x}) = h_{\mathrm{D}}(\check{\mathbf{x}})$ as

$$\nabla h_{\mathrm{D}}(\check{\mathbf{x}}') \cdot \Delta\mathbf{x} = 0. \tag{O.6}$$

Therefore, the constriction to stay in the same Poincaré section of constant variable P is given by

$$\mathbf{\Xi} \cdot \Delta\mathbf{x} = 0, \tag{O.7}$$

where $\mathbf{\Xi} = (q = 0, p = 0; Q = 0, P = 1)^{\top}$. The last constriction eliminates the movement along the Hamiltonian flow and

increases the stability of the algorithm. The previous linear constrictions (O.5), (O.6), and (O.7) can be written in matrix form as

$$\begin{pmatrix} 1-\boldsymbol{\Phi}_{\check{\mathbf{x}}}(\check{T}) & -\boldsymbol{\Sigma}\nabla h_{\mathrm{D}}(\check{\mathbf{x}}') \\ \nabla h_{\mathrm{D}}(\check{\mathbf{x}}')^{\top} & 0 \\ \boldsymbol{\Xi}^{\top} & 0 \end{pmatrix} \cdot \begin{pmatrix} \Delta\mathbf{x} \\ \Delta T \end{pmatrix} = \begin{pmatrix} \check{\mathbf{x}}' - \check{\mathbf{x}} \\ 0 \\ 0 \end{pmatrix}. \tag{O.8}$$

This overdetermined system of linear equations may be approximately solved by least squares using Moore-Penrose pseudoinversion. The solution for $\Delta\mathbf{x}$ and ΔT is not exact, but the process may be iterated with new guesses $\check{\mathbf{x}} + \Delta\mathbf{x}$ and $\check{T} + \Delta T$ that will converge to $\mathbf{x}$ and T if the initial guesses were good enough.

Given a stable stationary point $\mathbf{x}_{\mathrm{gs}} \in \mathcal{M}$ with energy $\epsilon_{\mathrm{gs}} = h_{\mathrm{D}}(\mathbf{x}_{\mathrm{gs}})$ and normal period T_{gs}, a continuous family of periodic orbits $\mathcal{O}_\epsilon$ can be found iteratively, whose existence is guaranteed [293]. Therefore, given $\mathcal{O}_\epsilon$ the objective is to find $\mathcal{O}_{\epsilon'}$ with $\epsilon' = \epsilon + \delta\epsilon$ close to ϵ. Thus, $\mathbf{x} \in \mathcal{O}_\epsilon$ is selected and the perturbation defined as $\delta\mathbf{x} = a\nabla h_{\mathrm{D}}(\mathbf{x})$, where a is a scalar such that $h_{\mathrm{D}}(\mathbf{x} + \delta\mathbf{x}) = \epsilon + \delta\epsilon$. For the first step, $\nabla h_{\mathrm{D}}(\mathbf{x}_{\mathrm{gs}}) = 0$, in which case any direction can be selected (the q direction is used here), and the stability of the initial stationary point will guarantee that the algorithm converges. Now, setting

$$\check{\mathbf{x}}' = \mathbf{x} + \delta\mathbf{x}, \tag{O.9}$$

$$\check{T}' = T + \delta T, \tag{O.10}$$

where

$$\delta T_k = \begin{cases} 0 & \text{if it is the first step} \\ (\epsilon' - \epsilon)\frac{T - T_{\mathrm{prev}}}{\epsilon - \epsilon_{\mathrm{prev}}} & \text{otherwise} \end{cases}, \tag{O.11}$$

and ϵ_{prev} and T_{prev} are the energy and period of the closest previously calculated orbit. Thus, $\check{T}'$ is linear extrapolation based on the behavior of the previous orbits.

Using the monodromy method the guesses $\check{\mathbf{x}}'$ and $\check{T}'$ can be corrected to obtain actual solutions $\mathbf{x}'$ and T', so that the desired periodic orbit is given by

$$\mathcal{O}_{\epsilon'} = \{\mathbf{x}'(t) \,|\, t \in [0, T']\}\,. \tag{O.12}$$

Although energy is constrained in the monodromy method, this is only to first order, so $\epsilon' = h_{\mathrm{D}}(\mathbf{x}')$ may not be exactly equal to $\epsilon + \delta\epsilon$. This is easily fixed by performing additional iterations with smaller $|\delta\epsilon|$ which converge to the desired energy.

O.2 Lyapunov Exponent of Periodic Orbits

For any point $\mathbf{x}$ in phase space, the associated maximum Lyapunov exponent can be calculated with the spectral norm of the fundamental matrix $\mathbf{\Phi}_{\mathbf{x}}(t)$, which is the square root of the maximum eigenvalue of the symmetric matrix $\mathbf{\Phi}_{\mathbf{x}}^{\dagger}(t)\mathbf{\Phi}_{\mathbf{x}}(t)$ [11,13,292]

$$\lambda = \lim_{t\to+\infty} \frac{1}{t} \ln ||\mathbf{\Phi}_{\mathbf{x}}(t)||. \tag{O.13}$$

If $\mathbf{x}$ corresponds to a periodic condition with period T, then Eq. (O.13) is greatly simplified. The so-called monodromy matrix associated to $\mathbf{x}$ is $M = \mathbf{\Phi}_{\mathbf{x}}(T)$. Then $\mathbf{\Phi}_{\mathbf{x}}(nT) = M^n$ for all positive integers n [292]. In this way, the Lyapunov exponent takes the form

$$\begin{aligned}
\lambda &= \lim_{n\to+\infty} \frac{1}{nT} \ln ||\mathbf{\Phi}_{\mathbf{x}}(nT)|| \\
&= \frac{1}{T} \lim_{n\to+\infty} \frac{1}{n} \ln ||M^n|| \\
&= \frac{1}{T} \lim_{n\to+\infty} \frac{1}{n} \ln ||e^{nA}|| \\
&= \frac{1}{T} \max_i (\ln |m_i|),
\end{aligned} \tag{O.14}$$

where $A = \ln(M)$ and the limit is equal to $\max_i[\Re(a_i)]$ [13]. That is, the maximum real part of the eigenvalues $a_i = \log(m_i)$ of the matrix A, where m_i are the eigenvalues of the matrix M.

Therefore, finding the maximum Lyapunov exponent of a periodic orbit $\mathcal{O}_\epsilon$ with period T reduces to computing the monodromy matrix M, which is done by simple numeric integration, and then taking the greatest of the norms of its eigenvalues divided by the period T.

O.3 Scarring Measure of Periodic Orbits

The scarring of an arbitrary state $\hat{\rho}$, caused by a given periodic orbit $\mathcal{O}_\epsilon$ with energy ϵ and period T, can be quantified defining the average

$$\begin{aligned}\langle \mathcal{Q}_{\hat{\rho}}(\mathbf{x})\rangle_{\mathcal{O}_\epsilon} &= \frac{1}{T}\int_0^T dt\, \mathcal{Q}_{\hat{\rho}}[\mathbf{x}(t)] \\ &= \mathrm{Tr}(\hat{\rho}\hat{\rho}_{\mathcal{O}_\epsilon}),\end{aligned} \tag{O.15}$$

where

$$\hat{\rho}_{\mathcal{O}_\epsilon} = \frac{1}{T}\int_0^T dt\, |\mathbf{x}(t)\rangle\langle\mathbf{x}(t)| \tag{O.16}$$

is a tubular Gaussian distribution around the periodic orbit $\mathcal{O}_\epsilon$ and the coherent state $|\mathbf{x}(t)\rangle$ is centered at $\mathbf{x}(t) \in \mathcal{O}_\epsilon$. The Husimi function of the state $\hat{\rho}_{\mathcal{O}_\epsilon}$ is described by the Husimi function (J.9)

$$\begin{aligned}\mathcal{Q}_{\mathcal{O}_\epsilon}(\mathbf{x}) &= \langle\mathbf{x}|\hat{\rho}_{\mathcal{O}_\epsilon}|\mathbf{x}\rangle \\ &= \frac{1}{T}\int_0^T dt\, e^{-(j/2)D^2_{\mathcal{M}}[\mathbf{x},\mathbf{x}_0(t)]},\end{aligned} \tag{O.17}$$

for any initial state $|\mathbf{x}_0(t)\rangle$ with $\mathbf{x}_0(t) \in \mathcal{O}_\epsilon$.

The way to compare the average (J.9) with a benchmark is to consider a completely delocalized state of the form

$$\begin{aligned}\hat{\rho}_\epsilon &= \frac{1}{\mathcal{V}_\epsilon}\int_{\mathcal{M}_\epsilon} d\mathbf{s}\, |\mathbf{x}\rangle\langle\mathbf{x}| \\ &= \frac{1}{\mathcal{V}_\epsilon}\int_{\mathcal{M}} d\mathbf{x}\, \delta[h_{\mathrm{D}}(\mathbf{x}) - \epsilon]|\mathbf{x}\rangle\langle\mathbf{x}|,\end{aligned} \tag{O.18}$$

which is composed of all coherent states within the classical energy shell $\epsilon = h_{\mathrm{D}}(\mathcal{O}_\epsilon)$, where $\mathcal{V}_\epsilon$ is given by Eq. (8.6), and δ is the Dirac delta function given by Eq. (C.14). The ratio between the average (O.15) for states $\hat{\rho}$ and $\hat{\rho}_\epsilon$ defines the scarring measure (9.7).

Appendix P

Localization Measures in Continuous Spaces

In this Appendix is exposed a scheme to define generalized localization measures in continuous spaces based in the generalized Rényi entropy.

P.1 Rényi Volume

The way to define a generalized localization measure in continuous spaces comes from the Rényi entropy of order α defined in a discrete basis $\{|\phi_n\rangle\}$ with dimension N, whose explicit expression is given by

$$S_\alpha = \frac{1}{1-\alpha} \ln \left(\sum_{n=1}^{N} p_n^\alpha \right), \tag{P.1}$$

$$\begin{aligned} S_1 &= \lim_{\alpha \to 1} S_\alpha \\ &= -\sum_{n=1}^{N} p_n \ln(p_n), \end{aligned} \tag{P.2}$$

where $\alpha \geq 0$ ($\alpha \neq 1$) and the term $p_n = |\langle \phi_n | \Psi \rangle|^2$ defines the probability to find an arbitrary state $|\Psi\rangle$ in an basis state $|\phi_n\rangle$

and satisfies the relation $\sum_n p_n = 1$. The limit case $\alpha = 1$ designs the well-known Shannon entropy. The exponential of the latter entropies define generalized localization measures in discrete spaces in the following form

$$e^{S_\alpha} = \left(\sum_{n=1}^{N} p_n^\alpha \right)^{1/(1-\alpha)} \in [1, N], \tag{P.3}$$

$$e^{S_1} = e^{-\sum_{n=1}^{N} p_n \ln(p_n)} \in [1, N], \tag{P.4}$$

which are known as generalized participation ratios of order α [93, 294]. The particular case $\alpha = 2$ gives the well-known participation ratio $P_R = e^{S_2}$ (see Eq. (4.31)).

The concept of localization in discrete bases can be extended to continuous bases which depend explicitly on a given parameter υ defined in a continuous space $\mathfrak{N}$ with volume

$$\mathcal{V}_\mathfrak{N} = \int_\mathfrak{N} d\mathcal{V}(\upsilon). \tag{P.5}$$

The procedure consists of replace the discrete probabilities by a distribution of probability $p_n \to \Phi(\upsilon)$ which is normalized $\int_\mathfrak{N} d\mathcal{V}(\upsilon)\, \Phi(\upsilon) = 1$ and the sums by integrals $\sum_n \bullet \to \int d\mathcal{V}(\upsilon) \bullet$. Taking the latter considerations can be found the Rényi volumes

$$\mathcal{V}_\alpha(\mathfrak{N}, \Phi) = \left[\int_\mathfrak{N} d\mathcal{V}(\upsilon)\, \Phi^\alpha(\upsilon) \right]^{1/(1-\alpha)} \in (0, \mathcal{V}_\mathfrak{N}], \tag{P.6}$$

$$\mathcal{V}_1(\mathfrak{N}, \Phi) = e^{-\int_\mathfrak{N} d\mathcal{V}(\upsilon)\, \Phi(\upsilon) \ln[\Phi(\upsilon)]} \in (0, \mathcal{V}_\mathfrak{N}]. \tag{P.7}$$

If the latter Rényi volumes are scaled by the volume of the continuous space (P.5), the Rényi occupation (10.1) bounded to the interval $(0, 1]$ is found.

When the continuous space $\mathfrak{N}$ is unbounded, its volume is infinite ($\mathcal{V}_\mathfrak{N} = \infty$) and the probability distribution $\Phi(\upsilon)$ is arbitrarily delocalized. For such cases, the Rényi occupation (10.1) must be defined within bounded subspaces $\mathcal{S} \subset \mathfrak{N}$ with finite volume $\mathcal{V}_\mathcal{S} < \mathcal{V}_\mathfrak{N}$.

Appendix Q

Rényi Occupation in the Dicke Model

In this Appendix are exposed two Rényi occupations defined in different bounded subspaces of the Dicke model, one defined in the atomic subspace, and other one defined at a classical energy shell.

Q.1 Rényi Occupation in the Atomic Subspace

The bounded atomic subspace $\mathcal{A}$ of the Dicke model is given by Eq. (10.5), and its phase-space volume is given by

$$\begin{aligned} \mathcal{V}_{\mathcal{A}} &= \int_{\mathcal{A}} dQ\, dP \\ &= 4\pi. \end{aligned} \tag{Q.1}$$

The selected probability distribution defined in the latter subspace is given by the exact projected Husimi function (N.4)

$$\begin{aligned}\Phi_{\hat{\rho}}(Q,P) &= \frac{1}{C_{\mathrm{A}}}\widetilde{\mathcal{Q}}_{\hat{\rho}}(Q,P) \\ &= \frac{1}{C}\int\int dq\,dp\,\mathcal{Q}_{\hat{\rho}}(\mathbf{x}),\end{aligned} \tag{Q.2}$$

where the constant

$$\begin{aligned}C &= \int_{\mathcal{M}} d\mathbf{x}\,\mathcal{Q}_{\hat{\rho}}(\mathbf{x}) \\ &= C_{\mathrm{A}}C_{\mathrm{B}}\end{aligned} \tag{Q.3}$$

ensures the normalization of the Husimi function in all phase space $\mathcal{M}$ of the Dicke model with coordinates $\mathbf{x} = (q,p;Q,P)$, where $C_{\mathrm{A}} = 4\pi/(2j+1)$ and $C_{\mathrm{B}} = 2\pi/j$. Using the probability distribution (Q.2) in Eq. (10.2) the Rényi occupations (10.3) and (10.4) can be found.

Q.2 Rényi Occupation at a Classical Energy Shell

The subspace of a classical energy shell $\mathcal{M}_\epsilon$ is given by Eq. (8.5) and its phase-space volume $\mathcal{V}_\epsilon$ is given by Eq. (8.6). The selected probability distribution defined in the latter subspace is given by the Husimi function normalized to the subspace of the classical energy shell $\epsilon = E/j$

$$\Phi_{\epsilon,\hat{\rho}}(\mathbf{x}) = \frac{1}{C_\epsilon}\mathcal{Q}_{\hat{\rho}}(\mathbf{x}), \tag{Q.4}$$

where the constant C_ϵ is given by Eq. (8.4). Using the probability distribution (Q.4) in Eq. (10.2) the Rényi occupations (10.6) and (10.7) can be found.

On the other hand, a useful way to represent the Rényi oc-

cupations (10.6) and (10.7) is as follows

$$\mathfrak{L}_\alpha(\epsilon,\hat{\rho}) = \left[\frac{\langle \mathcal{Q}^\alpha_{\hat{\rho}}(\mathbf{x})\rangle_\epsilon}{\langle \mathcal{Q}_{\hat{\rho}}(\mathbf{x})\rangle^\alpha_\epsilon}\right]^{1/(1-\alpha)}, \tag{Q.5}$$

$$\mathfrak{L}_1(\epsilon,\hat{\rho}) = \langle \mathcal{Q}_{\hat{\rho}}(\mathbf{x})\rangle_\epsilon e^{-\langle \mathcal{Q}_{\hat{\rho}}(\mathbf{x})\ln[\mathcal{Q}_{\hat{\rho}}(\mathbf{x})]\rangle_\epsilon/\langle \mathcal{Q}_{\hat{\rho}}(\mathbf{x})\rangle_\epsilon}, \tag{Q.6}$$

where the average is defined in the available phase space of the classical energy shell $\mathcal{M}_\epsilon$ and is given explicitly by

$$\begin{aligned}\langle F(\mathbf{x})\rangle_\epsilon &= \frac{1}{\mathcal{V}_\epsilon}\int_{\mathcal{M}_\epsilon} d\mathbf{s}\, F(\mathbf{x}) \\ &= \frac{1}{\mathcal{V}_\epsilon}\int_{\mathcal{M}} d\mathbf{x}\, \delta[h_{\mathrm{D}}(\mathbf{x})-\epsilon]F(\mathbf{x}),\end{aligned} \tag{Q.7}$$

where $F(\mathbf{x})$ is an arbitrary function which depends on the coordinates $\mathbf{x} = (q,p;Q,P)$ of the four-dimensional phase space $\mathcal{M}$ of the Dicke model, $\mathcal{V}_\epsilon$ is given by Eq. (8.6), and δ is the Dirac delta function given by Eq. (C.14).

Appendix R

Rényi Occupation of Maximally Delocalized States

In this Appendix is exposed a procedure to find the Rényi occupation of maximally delocalized states in Hilbert spaces with finite dimension.

R.1 Delocalization in Hilbert Spaces with Finite Dimension

In a Hilbert space with finite dimension $\mathcal{D}$, the average of the overlap of order α between to arbitrary states $|\Psi\rangle$ and $|\Psi'\rangle$ is given by [285, 295, 296]

$$\langle |\langle \Psi | \Psi' \rangle|^{2\alpha} \rangle_{\Psi} = \frac{\Gamma(\mathcal{D})\Gamma(\alpha+1)}{\Gamma(\mathcal{D}+\alpha)}, \tag{R.1}$$

where Γ is the gamma function given by Eq. (3.21) and the average is taken over all possible (normalized) states $|\Psi\rangle$.

Maximum delocalization in Hilbert spaces with finite dimension $\mathcal{D}$ is attained by random pure states. Thus, applying the

latter average to an ensemble of random sates $|\Psi\rangle = |\Psi_{\rm R}\rangle$ and using Glauber-Bloch coherent states $|\Psi'\rangle = |\mathbf{x}\rangle$ averaged in the bounded phase space $\mathcal{M}_\mathcal{D}$ associated to the finite Hilbert space, the relation takes the form

$$\begin{aligned}\langle\langle|\langle\Psi_{\rm R}|\mathbf{x}\rangle|^{2\alpha}\rangle_{\mathbf{x}\in\mathcal{M}_\mathcal{D}}\rangle_{\Psi_{\rm R}} &= \frac{\Gamma(\mathcal{D})\Gamma(\alpha+1)}{\Gamma(\mathcal{D}+\alpha)} \\ &\approx \langle|\langle\Psi_{\rm R}|\mathbf{x}\rangle|^{2\alpha}\rangle_{\mathbf{x}\in\mathcal{M}_\mathcal{D}}, \end{aligned} \tag{R.2}$$

where the approximation is taken considering that the variance of the average over the random states decreases when the finite dimension $\mathcal{D}$ grows.

In this way, when the dimension $\mathcal{D}$ is large enough, but remains finite, the Rényi occupation of a random state $\hat{\rho}_{\rm R} = |\Psi_{\rm R}\rangle\langle\Psi_{\rm R}|$ defined in the bounded phase space $\mathcal{M}_\mathcal{D}$ is given by

$$\begin{aligned}\mathfrak{L}_\alpha(\mathcal{M}_\mathcal{D}, \hat{\rho}_{\rm R}) &= \left[\frac{\langle|\langle\Psi_{\rm R}|\mathbf{x}\rangle|^{2\alpha}\rangle_{\mathbf{x}\in\mathcal{M}_\mathcal{D}}}{\langle|\langle\Psi_{\rm R}|\mathbf{x}\rangle|^{2}\rangle^{\alpha}_{\mathbf{x}\in\mathcal{M}_\mathcal{D}}}\right]^{1/(1-\alpha)} \\ &\approx \Gamma^{1/(1-\alpha)}(\alpha+1), \end{aligned} \tag{R.3}$$

which is independent of the dimension $\mathcal{D}$ and only depends on the order α. The last expression resembles the Rényi occupation of a random state defined at a classical energy shell given by Eq. (Q.5).

Bibliography

[1] R. H. Dicke, *Coherence in Spontaneous Radiation Processes*, Phys. Rev. **93**, 99 (1954).

[2] M. A. Bastarrachea-Magnani, S. Lerma-Hernández, and J. G. Hirsch, *Comparative quantum and semiclassical analysis of atom-field systems. I. Density of states and excited-state quantum phase transitions*, Phys. Rev. A **89**, 032101 (2014).

[3] M. A. Bastarrachea-Magnani, S. Lerma-Hernández, and J. G. Hirsch, *Comparative quantum and semiclassical analysis of atom-field systems. II. Chaos and regularity*, Phys. Rev. A **89**, 032102 (2014).

[4] Miguel Angel Bastarrachea-Magnani and Jorge G. Hirsch, *Peres lattices and chaos in the Dicke model*, J. Phys.: Conf. Ser. **512**, 012004 (2014).

[5] Miguel Angel Bastarrachea-Magnani, Baldemar López-del-Carpio, Sergio Lerma-Hernández, and Jorge G Hirsch, *Chaos in the Dicke model: quantum and semiclassical analysis*, Phys. Scr. **90**, 068015 (2015).

[6] M. A. Bastarrachea-Magnani, B. López-del-Carpio, J. Chávez-Carlos, S. Lerma-Hernández, and J. G. Hirsch, *Delocalization and quantum chaos in atom-field systems*, Phys. Rev. E **93**, 022215 (2016).

[7] J. Chávez-Carlos, M. A. Bastarrachea-Magnani, S. Lerma-Hernández, and J. G. Hirsch, *Classical chaos in atom-field systems*, Phys. Rev. E **94**, 022209 (2016).

[8] Miguel Angel Bastarrachea-Magnani, Baldemar López-del-Carpio, Jorge Chávez-Carlos, Sergio Lerma-Hernández, and Jorge G Hirsch, *Regularity and chaos in cavity QED*, Phys. Scr. **92**, 054003 (2017).

[9] S. Lerma-Hernández, J. Chávez-Carlos, M. A. Bastarrachea-Magnani, B. López-del-Carpio, and J. G. Hirsch, *Dynamics of Coherent States in Regular and Chaotic Regimes of the Non-Integrable Dicke Model*, AIP Conf. Proc. **1950**, 030002 (2017).

[10] Sergio Lerma-Hernández, Jorge Chávez-Carlos, Miguel A Bastarrachea-Magnani, Lea F Santos, and Jorge G Hirsch, *Analytical description of the survival probability of coherent states in regular regimes*, J. Phys. A: Math. Theor. **51**, 475302 (2018).

[11] Jorge Chávez-Carlos, B. López-del-Carpio, Miguel A. Bastarrachea-Magnani, Pavel Stránský, Sergio Lerma-Hernández, Lea F. Santos, and Jorge G. Hirsch, *Quantum and Classical Lyapunov Exponents in Atom-Field Interaction Systems*, Phys. Rev. Lett. **122**, 024101 (2019).

[12] S. Lerma-Hernández, D. Villaseñor, M. A. Bastarrachea-Magnani, E. J. Torres-Herrera, L. F. Santos, and J. G. Hirsch, *Dynamical signatures of quantum chaos and relaxation time scales in a spin-boson system*, Phys. Rev. E **100**, 012218 (2019).

[13] Saúl Pilatowsky-Cameo, Jorge Chávez-Carlos, Miguel A. Bastarrachea-Magnani, Pavel Stránský, Sergio Lerma-Hernández, Lea F. Santos, and Jorge G. Hirsch, *Positive quantum Lyapunov exponents in experimental systems with a regular classical limit*, Phys. Rev. E **101**, 010202(R) (2020).

[14] D Villaseñor, S Pilatowsky-Cameo, M A Bastarrachea-Magnani, S Lerma-Hernández, L F Santos, and J G Hirsch, *Quantum vs classical dynamics in a spin-boson system: manifestations of spectral correlations and scarring*, New J. Phys. **22**, 063036 (2020).

[15] Saúl Pilatowsky-Cameo, David Villaseñor, Miguel A. Bastarrachea-Magnani, Sergio Lerma-Hernández, Lea F. Santos, and Jorge G. Hirsch, *Ubiquitous quantum scarring does not prevent ergodicity*, Nat. Comm. **12**, 852 (2021).

[16] Saúl Pilatowsky-Cameo, David Villaseñor, Miguel A Bastarrachea-Magnani, Sergio Lerma-Hernández, Lea F Santos, and Jorge G Hirsch, *Quantum scarring in a spin-boson system: fundamental families of periodic orbits*, New J. Phys. **23**, 033045 (2021).

[17] D. Villaseñor, S. Pilatowsky-Cameo, M. A. Bastarrachea-Magnani, S. Lerma-Hernández, and J. G. Hirsch, *Quantum localization measures in phase space*, Phys. Rev. E **103**, 052214 (2021).

[18] Saúl Pilatowsky-Cameo, David Villaseñor, Miguel A. Bastarrachea-Magnani, Sergio Lerma-Hernández, Lea F. Santos, and Jorge G. Hirsch, *Identification of quantum scars via phase-space localization measures*, Quantum **6**, 644 (2022).

[19] Saúl Pilatowsky-Cameo, David Villaseñor, Miguel A. Bastarrachea-Magnani, Sergio Lerma-Hernández, and Jorge G. Hirsch, *Effective dimensions of infinite-dimensional Hilbert spaces: a phase-space approach*, arXiv:2111.09891 (2021).

[20] Toshiya Kinoshita, Trevor Wenger, and David S. Weiss, *A quantum Newton's cradle*, Nature **440**, 900 (2006).

[21] Jonathan Simon, Waseem S. Bakr, Ruichao Ma, M. Eric Tai, Philipp M. Preiss, and Markus Greiner, *Quantum simulation of antiferromagnetic spin chains in an optical lattice*, Nature **472**, 307 (2011).

[22] Michael Schreiber, Sean S. Hodgman, Pranjal Bordia, Henrik P. Lüschen, Mark H. Fischer, Ronen Vosk, Ehud Altman, Ulrich Schneider, and Immanuel Bloch, *Observation of many-body localization of interacting fermions in a quasirandom optical lattice*, Science **349**, 842 (2015).

[23] Adam M. Kaufman, M. Eric Tai, Alexander Lukin, Matthew Rispoli, Robert Schittko, Philipp M. Preiss, and Markus Greiner, *Quantum thermalization through entanglement in an isolated many-body system*, Science **353**, 794 (2016).

[24] Takaaki Monnai, *Generic Evaluation of Relaxation Time for Quantum Many-Body Systems: Analysis of the System Size Dependence*, J. Phys. Soc. Japan **82**, 044006 (2013).

[25] Sheldon Goldstein, Takashi Hara, and Hal Tasaki, *Time Scales in the Approach to Equilibrium of Macroscopic Quantum Systems*, Phys. Rev. Lett. **111**, 140401 (2013).

[26] Artur S. L. Malabarba, Luis Pedro García-Pintos, Noah Linden, Terence C. Farrelly, and Anthony J. Short, *Quantum systems equilibrate rapidly for most observables*, Phys. Rev. E **90**, 012121 (2014).

[27] Sheldon Goldstein, Takashi Hara, and Hal Tasaki, *Extremely quick thermalization in a macroscopic quantum system for a typical nonequilibrium subspace*, New J. Phys. **17**, 045002 (2015).

[28] Peter Reimann, *Typical fast thermalization processes in closed many-body systems*, Nat. Comm. **7**, 10821 (2016).

[29] Luis Pedro García-Pintos, Noah Linden, Artur S. L. Malabarba, Anthony J. Short, and Andreas Winter, *Equilibration Time Scales of Physically Relevant Observables*, Phys. Rev. X **7**, 031027 (2017).

[30] Thiago R de Oliveira, Christos Charalambous, Daniel Jonathan, Maciej Lewenstein, and Arnau Riera, *Equilibration time scales in closed many-body quantum systems*, New J. Phys. **20**, 033032 (2018).

[31] Luc Leviandier, Maurice Lombardi, Rémi Jost, and Jean Paul Pique, *Fourier Transform: A Tool to Measure Statistical Level Properties in Very Complex Spectra*, Phys. Rev. Lett. **56**, 2449 (1986).

[32] Hannes Bernien, Sylvain Schwartz, Alexander Keesling, Harry Levine, Ahmed Omran, Hannes Pichler, Soonwon Choi, Alexander S. Zibrov, Manuel Endres, Markus Greiner, Vladan Vuletić, and Mikhail D. Lukin, *Probing many-body dynamics on a 51-atom quantum simulator*, Nature **551**, 579 (2017).

[33] C. J. Turner, A. A. Michailidis, D. A. Abanin, M. Serbyn, and Z. Papić, *Weak ergodicity breaking from quantum many-body scars*, Nat. Phys. **14**, 745 (2018).

[34] Wen Wei Ho, Soonwon Choi, Hannes Pichler, and Mikhail D. Lukin, *Periodic Orbits, Entanglement, and Quantum Many-Body Scars in Constrained Models: Matrix Product State Approach*, Phys. Rev. Lett. **122**, 040603 (2019).

[35] Soonwon Choi, Christopher J. Turner, Hannes Pichler, Wen Wei Ho, Alexios A. Michailidis, Zlatko Papić, Maksym Serbyn, Mikhail D. Lukin, and Dmitry A. Abanin, *Emergent SU(2) Dynamics and Perfect Quantum Many-Body Scars*, Phys. Rev. Lett. **122**, 220603 (2019).

[36] C. J. Turner, J.-Y. Desaules, K. Bull, and Z. Papić, *Correspondence Principle for Many-Body Scars in Ultracold Rydberg Atoms*, Phys. Rev. X **11**, 021021 (2021).

[37] Eric J. Heller, *Bound-State Eigenfunctions of Classically Chaotic Hamiltonian Systems: Scars of Periodic Orbits*, Phys. Rev. Lett. **53**, 1515 (1984).

[38] Eric J. Heller, Qualitative Properties of Eigenfunctions of Classically Chaotic Hamiltonian Systems. In *Quantum Chaos and Statistical Nuclear Physics: Proceedings of the 2nd International Conference on Quantum Chaos and the 4th International Colloquium on Statistical Nuclear Physics, Held at Cuernavaca, México, January 6–10,*

1986, (eds. T. H. Seligman and H. Nishioka) (Springer-Verlag, Berlin, 1986).

[39] Eric J. Heller, Wavepacket dynamics and quantum chaology. In *Les Houches, Session LII, 1989. Chaos et Physique Quantique / Chaos and Quantum Physics* (eds. M.-J. Giannoni, A. Voros, and J. Zinn-Justin) (North-Holland, Amsterdam, 1991).

[40] B. V. Chirikov, F. M. Izrailev, and D. L. Shepelyansky, *Dynamical Stochasticity in Classical and Quantum Mechanics*, Sov. Sci. Rev. C **2**, 209 (1981).

[41] P. W. Anderson, *Absence of Diffusion in Certain Random Lattices*, Phys. Rev. **109**, 1492 (1958).

[42] Shmuel Fishman, D. R. Grempel, and R. E. Prange, *Chaos, Quantum Recurrences, and Anderson Localization*, Phys. Rev. Lett. **49**, 509 (1982).

[43] Patrick A. Lee and T. V. Ramakrishnan, *Disordered electronic systems*, Rev. Mod. Phys. **57**, 287 (1985).

[44] S. Fishman, *Anderson localization and quantum chaos maps*, Scholarpedia **5**, 9816 (2010).

[45] Rahul Nandkishore1 and David A. Huse, *Many-Body Localization and Thermalization in Quantum Statistical Mechanics*, Annu. Rev. Condens. Matter Phys. **6**, 15 (2015).

[46] Dmitry A. Abanin and Zlatko Papić, *Recent progress in many-body localization*, Ann. Phys. (Berlin) **529**, 1700169 (2017).

[47] Fabien Alet and Nicolas Laflorencie, *Many-body localization: An introduction and selected topics / Localisation à N corps: introduction et sujets choisis*, C. R. Physique **19**, 498 (2018).

[48] Dmitry A. Abanin, Ehud Altman, Immanuel Bloch, and Maksym Serbyn, *Colloquium: Many-body localization,*

thermalization, and entanglement, Rev. Mod. Phys. **91**, 021001 (2019).

[49] Andrei B. Klimov and Sergei M. Chumakov, *A Group-Theoretical Approach to Quantum Optics: Models of Atom-Field Interactions*, (Wiley-VCH Verlag GmbH & Co. KGaA, Weinheim, 2009).

[50] L. Allen and J. H. Eberly, *Optical Resonance and Two-Level Atoms*, (John Wiley & Sons, New York, 1975).

[51] Marlan O. Scully and M. Suhail Zubairy, *Quantum optics*, (Cambridge University Press, Cambridge, 1997).

[52] Michael Tavis and Frederick W. Cummings, *Exact Solution for an N-Molecule-Radiation-Field Hamiltonian*, Phys. Rev. **170**, 379 (1968).

[53] I. I. Rabi, *On the Process of Space Quantization*, Phys. Rev. **49**, 324 (1936).

[54] I. I. Rabi, *Space Quantization in a Gyrating Magnetic Field*, Phys. Rev. **51**, 652 (1937).

[55] E. T. Jaynes and F. W. Cummings, *Comparison of Quantum and Semiclassical Radiation Theories with Application to the Beam Maser*, Proc. IEEE **51**, 89 (1963).

[56] L. E. Reichl, *The Transition to Chaos: In Conservative Classical Systems: Quantum Manifestations*, (Springer-Verlag, New York, 1992).

[57] M. A. Bastarrachea-Magnani and J. G. Hirsch, *Numerical solutions of the Dicke Hamiltonian*, Rev. Mex. Fis. S **57**, 69 (2011).

[58] Miguel Angel Bastarrachea-Magnani and Jorge G. Hirsch, *Convergence in numerical solutions of the Dicke Hamiltonian*, AIP Conf. Proc. **1488**, 418 (2012).

[59] Miguel A Bastarrachea-Magnani and Jorge G Hirsch, *Efficient basis for the Dicke model: I. Theory and convergence in energy*, Phys. Scr. **T160**, 014005 (2014).

[60] Jorge G Hirsch and Miguel A Bastarrachea-Magnani, *Efficient basis for the Dicke model: II. Wave function convergence and excited states*, Phys. Scr. **T160**, 014018 (2014).

[61] R. Rossignoli and A. Plastino, *Quasispin seniority and the variational description of the nuclear free energy*, Phys. Rev. C **30**, 1360 (1984).

[62] L. Bakemeier, A. Alvermann, and H. Fehske, *Dynamics of the Dicke model close to the classical limit*, Phys. Rev. A **88**, 043835 (2013).

[63] A. Perelomov, *Generalized Coherent States and Their Applications*, (Springer-Verlag, Berlin, 1986).

[64] A D Ribeiro, M A M de Aguiar, and A F R de Toledo Piza, *The semiclassical coherent state propagator for systems with spin*, J. Phys. A: Math. Gen. **39**, 3085 (2006).

[65] Y. K. Wang and F. T. Hioe, *Phase Transition in the Dicke Model of Superradiance*, Phys. Rev. A **7**, 831 (1973).

[66] Klaus Hepp and Elliott H. Lieb, *On the Superradiant Phase Transition for Molecules in a Quantized Radiation Field: The Dicke Maser Model*, Ann. Phys. (New York) **76**, 360 (1973).

[67] F. T. Hioe, *Phase Transitions in Some Generalized Dicke Models of Superradiance*, Phys. Rev. A **8**, 1440 (1973).

[68] Klaus Hepp and Elliott H. Lieb, *Equilibrium Statistical Mechanics of Matter Interacting with the Quantized Radiation Field*, Phys. Rev. A **8**, 2517 (1973).

[69] Clive Emary and Tobias Brandes, *Quantum Chaos Triggered by Precursors of a Quantum Phase Transition: The Dicke Model*, Phys. Rev. Lett. **90**, 044101 (2003).

[70] Clive Emary and Tobias Brandes, *Chaos and the quantum phase transition in the Dicke model*, Phys. Rev. E **67**, 066203 (2003).

[71] M. Gross and S. Haroche, *Superradiance: An essay on the theory of collective spontaneous emission*, Phys. Rep. **93**, 301 (1982).

[72] Martin C. Gutzwiller, *Chaos in Classical and Quantum Mechanics*, (Springer-Verlag, New York, 1990).

[73] N. Skribanowitz, I. P. Herman, J. C. MacGillivray, and M. S. Feld, *Observation of Dicke Superradiance in Optically Pumped HF Gas*, Phys. Rev. Lett. **30**, 309 (1973).

[74] Kristian Baumann, Christine Guerlin, Ferdinand Brennecke, and Tilman Esslinger, *Dicke quantum phase transition with a superfluid gas in an optical cavity*, Nature **464**, 1301 (2010).

[75] D. Nagy, G. Kónya, G. Szirmai, and P. Domokos, *Dicke-Model Phase Transition in the Quantum Motion of a Bose-Einstein Condensate in an Optical Cavity*, Phys. Rev. Lett. **104**, 130401 (2010).

[76] K. Baumann, R. Mottl, F. Brennecke, and T. Esslinger, *Exploring Symmetry Breaking at the Dicke Quantum Phase Transition*, Phys. Rev. Lett. **107**, 140402 (2011).

[77] Helmut Ritsch, Peter Domokos, Ferdinand Brennecke, and Tilman Esslinger, *Cold atoms in cavity-generated dynamical optical potentials*, Rev. Mod. Phys. **85**, 553 (2013).

[78] J. Klinder, H. Keßler, M. Reza Bakhtiari, M. Thorwart, and A. Hemmerich, *Observation of a Superradiant Mott Insulator in the Dicke-Hubbard Model*, Phys. Rev. Lett. **115**, 230403 (2015).

[79] Alicia J. Kollár, Alexander T. Papageorge, Varun D. Vaidya, Yudan Guo, Jonathan Keeling, and Benjamin L. Lev, *Supermode-density-wave-polariton condensation with a Bose–Einstein condensate in a multimode cavity*, Nat. Comm. **8**, 14386 (2017).

[80] K. Härkönen, F. Plastina, and S. Maniscalco, *Dicke model and environment-induced entanglement in ion-cavity QED*, Phys. Rev. A **80**, 033841 (2009).

[81] J Cohn, A Safavi-Naini, R J Lewis-Swan, J G Bohnet, M Gärttner, K A Gilmore, J E Jordan, A M Rey, J J Bollinger, and J K Freericks, *Bang-bang shortcut to adiabaticity in the Dicke model as realized in a Penning trap experiment*, New J. Phys. **20**, 055013 (2018).

[82] A. Safavi-Naini, R. J. Lewis-Swan, J. G. Bohnet, M. Gärttner, K. A. Gilmore, J. E. Jordan, J. Cohn, J. K. Freericks, A. M. Rey, and J. J. Bollinger, *Verification of a Many-Ion Simulator of the Dicke Model Through Slow Quenches across a Phase Transition*, Phys. Rev. Lett. **121**, 040503 (2018).

[83] Markus P. Baden, Kyle J. Arnold, Arne L. Grimsmo, Scott Parkins, and Murray D. Barrett, *Realization of the Dicke Model Using Cavity-Assisted Raman Transitions*, Phys. Rev. Lett. **113**, 020408 (2014).

[84] Zhiqiang Zhang, Chern Hui Lee, Ravi Kumar, K. J. Arnold, Stuart J. Masson, A. L. Grimsmo, A. S. Parkins, and M. D. Barrett, *Dicke-model simulation via cavity-assisted Raman transitions*, Phys. Rev. A **97**, 043858 (2018).

[85] Tuomas Jaako, Ze-Liang Xiang, Juan José Garcia-Ripoll, and Peter Rabl, *Ultrastrong-coupling phenomena beyond the Dicke model*, Phys. Rev. A **94**, 033850 (2016).

[86] Daniele De Bernardis, Tuomas Jaako, and Peter Rabl, *Cavity quantum electrodynamics in the nonperturbative regime*, Phys. Rev. A **97**, 043820 (2018).

[87] Anton Öttl, Stephan Ritter, Michael Köhl, and Tilman Esslinger, *Hybrid apparatus for Bose-Einstein condensation and cavity quantum electrodynamics: Single atom detection in quantum degenerate gases*, Rev. Sci. Instrum. **77**, 063118 (2006).

[88] Mario A. Quiroz-Juárez, Jorge Chávez-Carlos, José L. Aragón, Jorge G. Hirsch, and Roberto de J. León-Montiel, *Experimental realization of the classical Dicke model*, Phys. Rev. Research **2**, 033169 (2020).

[89] Ferdinand Brennecke, Tobias Donner, Stephan Ritter, Thomas Bourdel, Michael Köhl, and Tilman Esslinger, *Cavity QED with a Bose–Einstein condensate*, Nature **450**, 268 (2007).

[90] Barry M. Garraway, *The Dicke model in quantum optics: Dicke model revisited*, Phil. Trans. R. Soc. A **369**, 1137 (2011).

[91] Anton Frisk Kockum, Adam Miranowicz, Simone De Liberato, Salvatore Savasta, and Franco Nori, *Ultrastrong coupling between light and matter*, Nat. Rev. Phys. **1**, 19 (2019).

[92] P. Forn-Díaz, L. Lamata, E. Rico, J. Kono, and E. Solano, *Ultrastrong coupling regimes of light-matter interaction*, Rev. Mod. Phys. **91**, 025005 (2019).

[93] Edward Ott, *Chaos in dynamical systems*, (Cambridge University Press, New York, 1993).

[94] G. L. Baker and J. P. Gollub, *Chaotic Dynamics: an introduction*, (Cambridge University Press, New York, 1996).

[95] Sandro Wimberger, *Nonlinear Dynamics and Quantum Chaos: An Introduction*, (Springer International Publishing, Switzerland, 2014).

[96] Herbert Goldstein, Charles Poole, and John Safko, *Classical Mechanics*, (Addison-Wesley, San Francisco, 2002).

[97] M. S. Santhanam, Sanku Paul, and J. Bharathi Kannan, *Quantum kicked rotor and its variants: Chaos, localization and beyond*, Phys. Rep. **956**, 1 (2022).

[98] L. Chierchia and J. N. Mather, *Kolmogorov-Arnold-Moser theory*, Scholarpedia **5**, 2123 (2010).

[99] A. N. Kolmogorov, *On the conservation of conditionally periodic motions under small perturbation of the Hamiltonian*, Dokl. Akad. Nauk SSR **98**, 527 (1954).

[100] J. Moser, *On invariant curves of area-preserving mappings of an annulus*, Nachr. Akad. Wiss. Göttingen, Math.-Phys. Kl. II **1**, 1 (1962).

[101] V. I. Arnold, *Proof of a theorem of A. N. Kolmogorov on the invariance of quasi-periodic motions under small perturbations of the Hamiltonian*, Russ. Math. Surv. **18**, 9 (1963).

[102] V. I. Arnold, *Small denominators and problems of stability of motion in classical and celestial mechanics*, Russ. Math. Surv. **18**, 85 (1963).

[103] V. I. Oseledets, *A multiplicative ergodic theorem. Characteristic Ljapunov, exponents of dynamical systems*, Trans. Moscow Math. Soc. **19**, 197 (1968).

[104] Michael Tabor, *Chaos and Integrability in Nonlinear Dynamics: An Introduction*, (John Wiley & Sons, New York, 1988).

[105] Giancarlo Benettin, Luigi Galgani, Antonio Giorgilli, and Jean-Marie Strelcyn, *Lyapunov Characteristic Exponents for smooth dynamical systems and for hamiltonian systems; a method for computing all of them. Part 1: Theory*, Meccanica **15**, 9 (1980).

[106] Giancarlo Benettin, Luigi Galgani, Antonio Giorgilli, and Jean-Marie Strelcyn, *Lyapunov Characteristic Exponents for smooth dynamical systems and for hamiltonian systems; A method for computing all of them. Part 2: Numerical application*, Meccanica **15**, 21 (1980).

[107] Boris. V. Chirikov, *A universal instability of many-dimensional oscillator systems*, Phys. Rep. **52**, 263 (1979).

[108] Ya. B. Pesin, *Characteristic Lyapunov exponents and smooth ergodic theory*, Russ. Math. Surv. **32**, 55 (1977).

[109] G. Benettin, C. Froeschle, and J. P. Scheidecker, *Kolmogorov entropy of a dynamical system with an increasing number of degrees of freedom*, Phys. Rev. A **19**, 2454 (1979).

[110] Joseph B. Keller, *Corrected Bohr-Bommerfeld Quantum Conditions for Nonseparable systems*, Ann. Phys. **4**, 180 (1958).

[111] A. Einstein, *Zum Quantensatz von Sommerfeld und Epstein*, Deut. Phys. Gesell. Verhandl. **19**, 82 (1917).

[112] Martin C. Gutzwiller, *Phase-Integral Approximation in Momentum Space and the Bound States of an Atom*, J. Math. Phys. **8**, 1979 (1967).

[113] Martin C. Gutzwiller, *Phase-Integral Approximation in Momentum Space and the Bound States of an Atom. II*, J. Math. Phys. **10**, 1004 (1969).

[114] Martin C. Gutzwiller, *Energy Spectrum According to Classical Mechanics*, J. Math. Phys. **11**, 1791 (1970).

[115] Martin C. Gutzwiller, *Periodic Orbits and Classical Quantization Conditions*, J. Math. Phys. **12**, 343 (1971).

[116] Martin C. Gutzwiller, The Semi-classical quantization of chaotic Hamiltonian systems. In *Les Houches, Session LII, 1989. Chaos et Physique Quantique / Chaos and Quantum Physics* (eds. M.-J. Giannoni, A. Voros, and J. Zinn-Justin) (North-Holland, Amsterdam, 1991).

[117] F. Revuelta, E. Vergini, R. M. Benito, and F. Borondo, *Short-periodic-orbit method for excited chaotic eigenfunctions*, Phys. Rev. E **102**, 042210 (2020).

[118] Giulio Casati and Boris Chirikov, *Quantum chaos: Between order and disorder*, (Cambridge University Press, New York, 1995).

[119] Hans-Jürgen Stöckmann, *Quantum Chaos: An Introduction*, (Cambridge University Press, New York, 1999).

[120] M. Hillery, R. F. O'Conell, M. O. Scully, and E. P. Wigner, *Distribution functions in physics: Fundamentals*, Phys. Rep. **106**, 121 (1984).

[121] M. V. Berry, *The Bakerian Lecture, 1987. Quantum chaology*, Proc. R. Soc. Lond. A **413**, 183 (1987).

[122] Michael Berry, *Quantum Chaology, Not Quantum Chaos*, Phys. Scr. **40**, 335 (1989).

[123] Fritz Haake, *Quantum Signatures of Chaos*, (Springer-Verlag, Berlin, 1991).

[124] Freeman J. Dyson, *Statistical Theory of Energy Levels of Complex Systems. I*, J. Math. Phys. **3**, 140 (1962).

[125] Freeman J. Dyson, *Statistical Theory of Energy Levels of Complex Systems. II*, J. Math. Phys. **3**, 157 (1962).

[126] Freeman J. Dyson, *Statistical Theory of Energy Levels of Complex Systems. III*, J. Math. Phys. **3**, 166 (1962).

[127] Freeman J. Dyson and Madan Lal Mehta, *Statistical Theory of Energy Levels of Complex Systems. IV*, J. Math. Phys. **4**, 701 (1963).

[128] Madan Lal Mehta and Freeman J. Dyson, *Statistical Theory of Energy Levels of Complex Systems. V*, J. Math. Phys. **4**, 713 (1963).

[129] M. L. Mehta, *Random Matrices and the Statistical Theory of Energy Levels*, (Academic Press, New York, 1967).

[130] T. A. Brody, J. Flores, J. B. French, P. A. Mello, A. Pandey, and S. S. M. Wong, *Random-matrix physics: spectrum and strength fluctuations*, Rev. Mod. Phys. **53**, 385 (1981).

[131] Thomas Guhr, Axel Müeller-Groeling, and Hans A. Weidenmüller, *Random matrix theories in quantum physics: common concepts*, Phys. Rep. **299**, 189 (1998).

[132] Eugene P. Wigner, *On the Statistical Distribution of the Widths and Spacings of Nuclear Resonance Levels*, Math. Proc. Cambridge Phil. Soc. **47**, 790 (1951).

[133] Charles E. Porter, *Statistical Theories of Spectra: Fluctuations*, (Academic Press, New York, 1965).

[134] Eugene P. Wigner, *Group Theory and Its Application to the Quantum Mechanics of Atomic Spectra*, (Academic Press, New York, 1959).

[135] O. Bohigas, M. J. Giannoni, and C. Schmit, *Characterization of Chaotic Quantum Spectra and Universality of Level Fluctuation Laws*, Phys. Rev. Lett. **52**, 1 (1984).

[136] O. Bohigas and M. J. Giannoni, *Level Density Fluctuations and Random Matrix Theory*, Ann. Phys. **89**, 393 (1975).

[137] T. H. Seligman, J. J. M. Verbaarschot, and M. R. Zirnbauer, *Quantum Spectra and Transition from Regular to Chaotic Classical Motion*, Phys. Rev. Lett. **53**, 215 (1984).

[138] T H Seligman and J J M Verbaarschot, *Fluctuations of quantum spectra and their semiclassical limit in the transition between order and chaos*, J. Phys. A: Math. Gen. **18**, 2227 (1985).

[139] T H Seligman, J J M Verbaarschot, and M R Zirnbauer, *Spectral fluctuation properties of Hamiltonian systems: the transition region between order and chaos*, J. Phys. A: Math. Gen. **18**, 2751 (1985).

[140] Y. Alhassid and M. Feingold, *Statistical fluctuation of matrix elements in regular and chaotic systems*, Phys. Rev. A **39**, 374 (1989).

[141] Harald Friedrich and Dieter Wintgen, *The hydrogen atom in a uniform magnetic field - an example of chaos*, Phys. Rep. **183**, 37 (1989).

[142] Felix M. Izrailev, *Simple models of quantum chaos: spectrum and eigenfunctions*, Phys. Rep. **196**, 299 (1990).

[143] Vladimir Zelevinsky, B. Alex Brown, Njema Frazier, and Mihai Horoi, *The nuclear shell model as a testing ground for many-body quantum chaos*, Phys. Rep. **276**, 85 (1996).

[144] T. A. Brody, *A Statistical Measure for the Repulsion of Energy Levels*, Nuo. Cim. **7**, 482 (1973).

[145] J. F. Shriner, Jr. and G. E. Mitchell, *Small sample size effects in statistical analyses of eigenvalue distributions*, Z. Phys. A: Had. Nuc. **342**, 53 (1992).

[146] Madan Lal Mehta, *Random Matrices*, (Academic Press, Boston, 1991).

[147] J. P. Pique, Y. Chen, R. W. Field, and J. L. Kinsey, *Chaos and Dynamics on 0.5-300-ps Time Scales in Vibrationally Excited Acetylene: Fourier Transform of Stimulated-Emission Pumping Spectrum*, Phys. Rev. Lett. **58**, 475 (1987).

[148] T. Guhr and H. A. Weidenmüller, *Correlations in anticrossing spectra and scattering theory. Analytical aspects*, Chem. Phys. **146**, 21 (1990).

[149] U. Hartmann, H. A. Weidenmüller, and T. Guhr, *Correlations in anticrossing spectra and scattering theory: numerical simulations*, Chem. Phys. **150**, 311 (1991).

[150] A. Delon, R. Jost, and M. Lombardi, *NO_2 jet cooled visible excitation spectrum: Vibronic chaos induced by the $\tilde{X}^2A_1 - \tilde{A}^2B_2$ interaction*, J. Chem. Phys. **95**, 5701 (1991).

[151] Joshua Wilkie and Paul Brumer, *Time-Dependent Manifestations of Quantum Chaos*, Phys. Rev. Lett. **67**, 1185 (1991).

[152] Y. Alhassid and R. D. Levine, *Spectral autocorrelation function in the statistical theory of energy levels*, Phys. Rev. A **46**, 4650 (1992).

[153] Y. Alhassid and N. Whelan, *Onset of Chaos and Its Signature in the Spectral Autocorrelation Function*, Phys. Rev. Lett. **70**, 572 (1993).

[154] M. Lombardi and T. H. Seligman, *Universal and nonuniversal statistical properties of levels and intensities for chaotic Rydberg molecules*, Phys. Rev. A **47**, 3571 (1993).

[155] A. Kudrolli, S. Sridhar, Akhilesh Pandey, and Ramakrishna Ramaswamy, *Signatures of chaos in quantum billiards: Microwave experiments*, Phys. Rev. E **49**, R11(R) (1994).

[156] H. Alt, H.-D. Gräf, T. Guhr, H. L. Harney, R. Hofferbert, H. Rehfeld, A. Richter, and P. Schardt, *Correlation-hole method for the spectra of superconducting microwave billiards*, Phys. Rev. E **55**, 6674 (1997).

[157] Laurent Michaille and Jean-Paul Pique, *Influence of Experimental Resolution on the Spectral Statistics Used to Show Quantum Chaos: The case of Molecular Vibrational Chaos*, Phys. Rev. Lett. **82**, 2083 (1999).

[158] T. Gorin and T. H. Seligman, *Signatures of the correlation hole in total and partial cross sections*, Phys. Rev. E **65**, 026214 (2002).

[159] Y. Alhassid, Yan V. Fyodorov, T. Gorin, W. Ihra, and B. Mehlig, *Fano interference and cross-section fluctuations in molecular photodissociation*, Phys. Rev. A **73**, 042711 (2006).

[160] E. J. Torres-Herrera and Lea F. Santos, *Extended nonergodic states in disordered many-body quantum systems*, Ann. Phys. (Berlin) **529**, 1600284 (2017).

[161] E. J. Torres-Herrera and Lea F. Santos, *Dynamical manifestations of quantum chaos: correlation hole and bulge*, Phil. Trans. R. Soc. A **375**, 20160434 (2017).

[162] Lea F. Santos and E. Jonathan Torres-Herrera, *Analytical expressions for the evolution of many-body quantum systems quenched far from equilibrium*, AIP Conf. Proc. **1912**, 020015 (2017).

[163] E. J. Torres-Herrera, Antonio M. García-García, and Lea F. Santos, *Generic dynamical features of quenched interacting quantum systems: Survival probability, density imbalance, and out-of-time-ordered correlator*, Phys. Rev. B **97**, 060303(R) (2018).

[164] A. del Campo, J. Molina-Vilaplana, L. F. Santos, and J. Sonner, *Decay of a thermofield-double state in chaotic quantum systems: From random matrices to spin systems*, Eur. Phys. J.: Spec. Top. **227**, 247 (2018).

[165] Eduardo Jonathan Torres-Herrera, and Lea F. Santos, *Signatures of chaos and thermalization in the dynamics of many-body quantum systems*, Eur. Phys. J.: Spec. Top. **227**, 1897 (2019).

[166] Mauro Schiulaz, E. Jonathan Torres-Herrera, and Lea F. Santos, *Thouless and relaxation time scales in many-body quantum systems*, Phys. Rev. B **99**, 174313 (2019).

[167] Juan Maldacena and Douglas Stanford, *Remarks on the Sachdev-Ye-Kitaev model*, Phys. Rev. D **94**, 106002 (2016).

[168] Efim B. Rozenbaum, Sriram Ganeshan, and Victor Galitski, *Lyapunov Exponent and Out-of-Time-Ordered Correlator's Growth Rate in a Chaotic System*, Phys. Rev. Lett. **118**, 086801 (2017).

[169] Koji Hashimoto, Keiju Murata, and Ryosuke Yoshii, *Out-of-time-order correlators in quantum mechanics*, JHEP **10**, 138 (2017).

[170] Ignacio García-Mata, Marcos Saraceno, Rodolfo A. Jalabert, Augusto J. Roncaglia, and Diego A. Wisniacki, *Chaos Signatures in the Short and Long Time Behavior*

of the Out-of-Time Ordered Correlator, Phys. Rev. Lett. **121**, 210601 (2018).

[171] Rodolfo A. Jalabert, Ignacio García-Mata, and Diego A. Wisniacki, *Semiclassical theory of out-of-time-order correlators for low-dimensional classically chaotic systems*, Phys. Rev. E **98**, 062218 (2018).

[172] Efim B. Rozenbaum, Sriram Ganeshan, and Victor Galitski, *Universal level statistics of the out-of-time-ordered operator*, Phys. Rev. B **100**, 035112 (2019).

[173] Silvia Pappalardi, Angelo Russomanno, Bojan Žunkovič, Fernando Iemini, Alessandro Silva, and Rosario Fazio, *Scrambling and entanglement spreading in long-range spin chains*, Phys. Rev. B **98**, 134303 (2018).

[174] Quirin Hummel, Benjamin Geiger, Juan Diego Urbina, and Klaus Richter, *Reversible Quantum Information Spreading in Many-Body Systems near Criticality*, Phys. Rev. Lett. **123**, 160401 (2019).

[175] Tianrui Xu, Thomas Scaffidi, and Xiangyu Cao, *Does Scrambling Equal Chaos?*, Phys. Rev. Lett. **124**, 140602 (2020).

[176] Koji Hashimoto, Kyoung-Bum Huh, Keun-Young Kim, and Ryota Watanabe, *Exponential growth of out-of-time-order correlator without chaos: inverted harmonic oscillator*, JHEP **11**, 068 (2020).

[177] R. J. Lewis-Swan, A. Safavi-Naini, J. J. Bollinger, and A. M. Rey, *Unifying scrambling, thermalization and entanglement through measurement of fidelity out-of-time-order correlators in the Dicke model*, Nat. Comm. **10**, 1581 (2019).

[178] L. A. Khalfin, *Contribution to the Decay Theory of a Quasi-Stationary State*, Sov. Phys. JETP **6**, 1053 (1958).

[179] Rodolfo A. Jalabert and Horacio M. Pastawski, *Environment-Independent Decoherence Rate in Classically Chaotic Systems*, Phys. Rev. Lett. **86**, 2490 (2001).

[180] Ph. Jacquod, P. G. Silvestrov, and C. W. J. Beenakker, *Golden rule decay versus Lyapunov decay of the quantum Loschmidt echo*, Phys. Rev. E **64**, 055203(R) (2001).

[181] Jiří Vaníček and Doron Cohen, *Survival probability and local density of states for one-dimensional Hamiltonian systems*, J. Phys. A: Math. Theor. **36**, 9591 (2003).

[182] T Gorin, T Prosen, and T H Seligman, *A random matrix formulation of fidelity decay*, New J. Phys. **6**, 20 (2004).

[183] Thomas Gorin, Tomaž Prosen, Thomas H. Seligman, and Marko Žnidarič, *Dynamics of Loschmidt echoes and fidelity decay*, Phys. Rep. **435**, 33 (2006).

[184] A. Goussev, R. A. Jalabert, H. M. Pastawski, and D. A. Wisniacki, *Loschmidt echo*, Scholarpedia **7**, 11687 (2012).

[185] F Leyvraz, A García, H Kohler, and T H Seligman, *Fidelity under isospectral perturbations: a random matrix study*, J. Phys. A: Math. Theor. **46**, 275303 (2013).

[186] C. F. Bharucha, K. W. Madison, P. R. Morrow, S. R. Wilkinson, Bala Sundaram, and M. G. Raizen, *Observation of atomic tunneling from an accelerating optical potential*, Phys. Rev. A **55**, R857(R) (1997).

[187] Steven R. Wilkinson, Cyrus F. Bharucha, Martin C. Fischer, Kirk W. Madison, Patrick R. Morrow, Qian Niu, Bala Sundaram, and Mark G. Raizen, *Experimental evidence for non-exponential decay in quantum tunnelling*, Nature **387**, 575 (1997).

[188] R. Shäfer, H.-J. Stöckmann, T. Gorin, and T. H. Seligman, *Experimental Verification of Fidelity Decay: From Perturbative to Fermi Golden Rule Regime*, Phys. Rev. Lett. **95**, 184102 (2005).

[189] Bernd Köber, Ulrich Kuhl, Hans-Jürgen Stöckmann, Arseni Goussev, and Klaus Richter, *Fidelity decay for local perturbations: Microwave evidence for oscillating decay exponents*, Phys. Rev. E **83**, 016214 (2011).

[190] Marco Távora, E. J. Torres-Herrera, and Lea F. Santos, *Inevitable power-law behavior of isolated many-body quantum systems and how it anticipates thermalization*, Phys. Rev. A **94**, 041603(R) (2016).

[191] Marco Távora, E. J. Torres-Herrera, and Lea F. Santos, *Power-law decay exponents: a dynamical criterion for predicting thermalization.*, Phys. Rev. A **95**, 013604 (2017).

[192] E. J. Torres-Herrera and Lea F. Santos, *Quench dynamics of isolated many-body quantum systems*, Phys. Rev. A **89**, 043620 (2014).

[193] E J Torres-Herrera, Manan Vyas, and Lea F Santos, *General features of the relaxation dynamics of interacting quantum systems*, New J. Phys. **16**, 063010 (2014).

[194] E. J. Torres-Herrera and Lea F. Santos, *Nonexponential fidelity decay in isolated interacting quantum systems*, Phys. Rev. A **90**, 033623 (2014).

[195] E. Schrödinger, *Der stetige Übergang von der Mikro- zur Makromechanik*, Naturwissenschaften **14**, 664 (1926).

[196] Wei-Min Zhang, Da Hsuan Feng, and Robert Gilmore, *Coherent states: Theory and some applications*, Rev. Mod. Phys. **62**, 867 (1990).

[197] Roy J. Glauber, *Photon Correlations*, Phys. Rev. Lett. **10**, 84 (1963).

[198] E. C. G. Sudarshan, *Equivalence of Semiclassical and Quantum Mechanical Descriptions of Statistical Light Beams*, Phys. Rev. Lett. **10**, 277 (1963).

[199] Roy J. Glauber, *The Quantum Theory of Optical Coherence*, Phys. Rev. **130**, 2529 (1963).

[200] Roy J. Glauber, *Coherent and Incoherent States of the Radiation Field*, Phys. Rev. **131**, 2766 (1963).

[201] John R. Klauder and Bo-Sture Skagerstam, *Coherent States: Applications in Physics and Mathematical Physics*, (World Scientific, Singapore, 1985).

[202] J. M. Radcliffe, *Some properties of coherent spin states*, J. Phys. A: Gen. Phys. **4**, 313 (1971).

[203] F. T. Arecci, Eric Courtens, Robert Gilmore, and Harry Thomas, *Atomic Coherent States in Quantum Optics*, Phys. Rev. A **6**, 2211 (1972).

[204] L. Mandel and E. Wolf, *Coherence and Quantum Optics: Proceedings of the Third Rochester Conference on Coherence and Quantum Optics held at the University of Rochester, June 21-23, 1972*, (Plenum Press, New York, 1973).

[205] Christopher Gerry and Peter Knight, *Introductory Quantum Optics*, (Cambridge University Press, New York, 2005).

[206] John R. Klauder, *Continuous-Representation Theory. I. Postulates of Continuous-Representation Theory*, J. Math. Phys. **4**, 1055 (1963).

[207] John R. Klauder, *Continuous-Representation Theory. II. Generalized Relation between Quantum and Classical Dynamics*, J. Math. Phys. **4**, 1058 (1963).

[208] Leon Cohen, *Generalized Phase-Space Distribution Functions*, J. Math. Phys. **7**, 781 (1966).

[209] Hai-Woong Lee, *Theory and application of the quantum phase-space distribution functions*, Phys. Rep. **259**, 147 (1995).

[210] Stephen M. Barnett and Paul M. Radmore, *Methods in Theoretical Quantum Optics*, (Oxford University Press, New york, 1997).

[211] Maximilian Schlosshauer, *Decoherence and the Quantum-to-Classical Transition*, (Springer-Verlag, Berlin Heidelberg, 2007).

[212] Pierre Meystre and Murray Sargent III, *Elements of Quantum Optics*, (Springer-Verlag, Berlin Heidelberg, 2007).

[213] D.F. Walls and Gerard J. Milburn, *Quantum Optics*, (Springer-Verlag, Berlin Heidelberg, 2008).

[214] Miguel Orszag, *Quantum Optics: Including Noise Reduction, Trapped Ions, Quantum Trajectories, and Decoherence*, (Springer-Verlag, Berlin Heidelberg, 2008).

[215] E. Wigner, *On the Quantum Correction For Thermodynamic Equilibrium*, Phys. Rev. **40**, 749 (1932).

[216] Kôdi Husimi, *Some Formal Properties of the Density Matrix*, Proc. Phys. Math. Soc. Japan **22**, 264 (1940).

[217] T. W. Anderson and D. A. Darling, *Asymptotic Theory of Certain "Goodness of Fit" Criteria Based on Stochastic Processes*, Ann. Math. Statist. **23**, 193 (1952).

[218] Asher Peres, *New Conserved Quantities and Test for Regular Spectra*, Phys. Rev. Lett. **53**, 1711 (1984).

[219] P. Ehrenfest, *Bemerkung über die angenäherte Gültigkeit der klassischen Mechanik innerhalb der Quantenmechanik*, Z. Phys. **45**, 455 (1927).

[220] P. G. Silvestrov and C. W. J. Beenakker, *Ehrenfest times for classically chaotic systems*, Phys. Rev. E **65**, 035208(R) (2002).

[221] Fausto Borgonovi, Felix M. Izrailev, and Lea F. Santos, *Exponentially fast dynamics of chaotic many-body systems*, Phys. Rev. E **99**, 010101(R) (2019).

[222] Fausto Borgonovi, Felix M. Izrailev, and Lea F. Santos, *Timescales in the quench dynamics of many-body quantum systems: Participation ratio versus out-of-time ordered correlator*, Phys. Rev. E **99**, 052143 (2019).

[223] G. P. Berman and G. M. Zaslavsky, *Condition of Stochasticity in Quantum Nonlinear Systems*, Phys. A **91**, 450 (1978).

[224] George M. Zaslavsky, *Stochasticity in quantum systems*, Phys. Rep. **80**, 157 (1981).

[225] Alfredo M. Ozorio de Almeida, *The Weyl representation in classical and quantum mechanics*, Phys. Rep. **295**, 265 (1998).

[226] A. B. Klimov, *Exact evolution equations for SU(2) quasidistribution functions*, J. Math. Phys. **43**, 2202 (2002).

[227] William B. Case, *Wigner functions and Weyl transforms for pedestrians*, Am. J. Phys. **76**, 937 (2008).

[228] T. Dittrich, E. A. Gómez, and L. A. Pachón, *Semiclassical propagation of Wigner functions*, J. Chem. Phys. **132**, 214102 (2010).

[229] Anatoli Polkovnikov, *Phase space representation of quantum dynamics*, Ann. Phys. **325**, 1790 (2010).

[230] Michael Berry, Semiclassical mechanics of regular and irregular motion. In *Les Houches, Session XXXVI, 1981. Comportement chaotique des systèmes déterministes / Chaotic Behavior of Deterministic Systems* (eds. G. Iooss, R. H. G. Helleman, and R. Stora) (North-Holland, Amsterdam, 1983).

[231] M. V. Berry, *Quantum scars of classical closed orbits in phase space*, Proc. R. Soc. Lond. A **423**, 219 (1989).

[232] A. I. Shnirelman, *Ergodic properties of eigenfunctions*, Usp. Mat. Nauk **29**, 181 (1974).

[233] Steven William McDonald, *Wave Dynamics of Regular and Chaotic Rays*, (Dissertation, Ph. D. in Physics, University of California, Berkeley, 1983).

[234] Steven W. McDonald and Allan N. Kaufman, *Spectrum and Eigenfunctions for a Hamiltonian with Stochastic Trajectories*, Phys. Rev. Lett. **42**, 1189 (1979).

[235] M. Shapiro and G. Goelman, *Onset of Chaos in an Isolated Energy Eigenstate*, Phys. Rev. Lett. **53**, 1714 (1984).

[236] Steven W. McDonald and Allan N. Kaufman, *Wave chaos in the stadium: Statistical properties of short-wave solutions of the Helmholtz equation*, Phys. Rev. A **37**, 3067 (1988).

[237] Eric J. Heller, *Quantum localization and the rate of exploration of phase space*, Phys. Rev. A **35**, 1360 (1987).

[238] E. B. Bogomolny, *Smoothed wave functions of chaotic quantum systems*, Physica D **31**, 169 (1988).

[239] D. Wintgen and A. Hönig, *Irregular Wave Functions of a Hydrogen Atom in a Uniform Magnetic Field*, Phys. Rev. Lett. **63**, 1467 (1989).

[240] Marek Kuś, Jakub Zakrzewski, and Karol Życzkowski, *Quantum scars on a sphere*, Phys. Rev. A **43**, 4244 (1991).

[241] G. M. D'Ariano, L. R. Evangelista, and M. Saraceno, *Classical and quantum structures in the kicked-top model*, Phys. Rev. A **45**, 3646 (1992).

[242] 0. Bohigas, S. Tomsovic, and D. Ullmo, *Manifestations of classical phase space structures in quantum mechanics*, Phys. Rep. **223**, 43 (1993).

[243] Oded Agam and Shmuel Fishman, *Quantum eigenfunctions in terms of periodic orbits of chaotic systems*, J. Phys. A: Math. Gen. **26**, 2113 (1993).

[244] Oded Agam and Shmuel Fishman, *Semiclassical Criterion for Scars in Wave Functions of Chaotic Systems*, Phys. Rev. Lett. **73**, 806 (1994).

[245] Kirsten Müller and Dieter Wintgen, *Scars in wavefunctions of the diamagnetic Kepler problem*, J. Phys. B: At. Mol. Opt. Phys. **27**, 2693 (1994).

[246] L. Kaplan and E. J. Heller, *Linear and Nonlinear Theory of Eigenfunction Scars*, Ann. Phys. **264**, 171 (1998).

[247] L. Kaplan and E. J. Heller, *Measuring scars of periodic orbits*, Phys. Rev. E **59**, 6609 (1999).

[248] D. A. Wisniacki, E. Vergini, R. M. Benito, and F. Borondo, *Scarring by Homoclinic and Heteroclinic Orbits*, Phys. Rev. Lett. **97**, 094101 (2006).

[249] Max D. Porter, Aaron Barr, Ariel Barr, and L. E. Reichl, *Chaos in the band structure of a soft Sinai lattice*, Phys. Rev. E **95**, 052213 (2017).

[250] M. A. M. de Aguiar, K. Furuya, C. H. Lewenkopf, and M. C. Nemes, *Particle-Spin Coupling in a Chaotic System: Localization-Delocalization in the Husimi Distributions*, EPL **15**, 125 (1991).

[251] M. A. M. de Aguiar, K. Furuya, C. H. Lewenkopf, and M. C. Nemes, *Chaos in a Spin-Boson System: Classical Analysis*, Ann. Phys. **216**, 291 (1992).

[252] K. Furuya, M. A. M. de Aguiar, C. H. Lewenkopf, and M. C. Nemes, *Husimi Distributions of a Spin-Boson System and the Signatures of Its Classical Dynamics*, Ann. Phys. **216**, 313 (1992).

[253] J. Keski-Rahkonen, A. Ruhanen, E. J. Heller, and E. Räsänen, *Quantum Lissajous Scars*, Phys. Rev. Lett. **123**, 214101 (2019).

[254] J Keski-Rahkonen, P J J Luukko, S Åberg, and E Räsänen, *Effects of scarring on quantum chaos in disordered quantum wells*, J. Phys.: Condens. Matter **31**, 105301 (2019).

[255] Mitsuyoshi Tomiya, Shoichi Sakamoto, and Eric J. Heller, *Periodic orbit scar in wavepacket propagation*, Int. J. Mod. Phys. C **30**, 1950026 (2019).

[256] Shriya Pai and Michael Pretko, *Dynamical Scar States in Driven Fracton Systems*, Phys. Rev. Lett. **123**, 136401 (2019).

[257] J. Schnack, H. Feldmeier, *Statistical properties of fermionic molecular dynamics*, Nuc. Phys. A **601**, 181 (1996).

[258] Toshikazu Sunada, Quantum Ergodicity. In *Progress in Inverse Spectral Geometry* (eds. Stig I. Andersson and Michel L. Lapidus) (Springer-Verlag, Basel, 1997).

[259] M. A. M. de Aguiar and C. P. Malta, *Isochronous and period doubling bifurcations of periodic solutions of non-integrable Hamiltonian systems with reflexion symmetries*, Physica D **30**, 413 (1988).

[260] M. Baranger, K. T. R. Davies, and J. H. Mahoney, *The Calculation of Periodic Trajectories*, Ann. Phys. **186**, 95 (1988).

[261] N. S. Simonović, *Calculations of periodic orbits: The monodromy method and application to regularized systems*, Chaos **9**, 854 (1999).

[262] Giulio Casati, B. V. Chirikov, and D. L. Shepelyansky, *Quantum Limitations for Chaotic Excitation of the Hydrogen Atom in a Monochromatic Field*, Phys. Rev. Lett. **53**, 2525 (1984).

[263] Giulio Casati, Boris V. Chirikov, Dimitri L. Shepelyansky, and Italo Guarneri, *Relevance of classical chaos in quantum mechanics: The hydrogen atom in a monochromatic field*, Phys. Rep. **154**, 77 (1987).

[264] R. Blümel and U. Smilansky, *Localization of Floquet States in the rf Excitation of Rydberg Atoms*, Phys. Rev. Lett. **58**, 2531 (1987).

[265] G. Casati, B. V. Chirikov, I. Guarneri, and F. M. Izrailev, *Band-random-matrix model for quantum localization in conservative systems*, Phys. Rev. E **48**, R1613(R) (1993).

[266] Fausto Borgonovi, Giulio Casati, and Baowen Li, *Diffusion and Localization in Chaotic Billiards*, Phys. Rev. Lett. **77**, 4744 (1996).

[267] Benjamin Batistić and Marko Robnik, *Semiempirical theory of level spacing distribution beyond the Berry–Robnik regime: modeling the localization and the tunneling effects*, J. Phys. A: Math. Theor. **43**, 215101 (2010).

[268] Benjamin Batistić and Marko Robnik, *Dynamical localization of chaotic eigenstates in the mixed-type systems: spectral statistics in a billiard system after separation of regular and chaotic eigenstates*, J. Phys. A: Math. Theor. **46**, 315102 (2013).

[269] Benjamin Batistić and Marko Robnik, *Quantum localization of chaotic eigenstates and the level spacing distribution*, Phys. Rev. E **88**, 052913 (2013).

[270] Benjamin Batistić, Črt Lozej, and Marko Robnik, *Statistical properties of the localization measure of chaotic eigenstates and the spectral statistics in a mixed-type billiard*, Phys. Rev. E **100**, 062208 (2019).

[271] Marko Robnik, Recent Advances in Quantum Chaos of Generic Systems. Wave Chaos of Mixed-Type Systems. In *Synergetics. A Volume in the Encyclopedia of Complexity and Systems Science* (eds. Axel Hutt and Hermann Haken) (Springer-Verlag, New York, 2020).

[272] Achilleas Lazarides, Arnab Das, and Roderich Moessner, *Fate of Many-Body Localization Under Periodic Driving*, Phys. Rev. Lett. **115**, 030402 (2015).

[273] Efim B. Rozenbaum and Victor Galitski, *Dynamical localization of coupled relativistic kicked rotors*, Phys. Rev. B **95**, 064303 (2017).

[274] Michele Fava, Rosario Fazio, and Angelo Russomanno, *Many-body dynamical localization in the kicked Bose-Hubbard chain*, Phys. Rev. B **101**, 064302 (2020).

[275] Colin Rylands, Efim B. Rozenbaum, Victor Galitski, and Robert Konik, *Many-Body Dynamical Localization in a Kicked Lieb-Liniger Gas*, Phys. Rev. Lett. **124**, 155302 (2020).

[276] L. L. Campbell, *Exponential Entropy as a Measure of Extent of a Distribution*, Z. Wahrscheinlichkeitstheorie verw. Geb. **5**, 217 (1966).

[277] Lou Jost, *Entropy and diversity*, Oikos **113**, 363 (2006).

[278] F. Jelinek, R. L. Mercer, L. R. Bahl, and J. K. Baker, *Perplexity—a measure of the difficulty of speech recognition tasks*, J. Acoust. Soc. Am. **62**, S63 (1977).

[279] Peter F. Brown, Vincent J. Della Pietra, Robert L. Mercer, Stephen A. Della Pietra, and Jennifer C. Lai, *An Estimate of an Upper Bound for the Entropy of English*, Comput. Ling. **18**, 31 (1992).

[280] J T Edwards and D J Thouless, *Numerical studies of localization in disordered systems*, J. Phys. C: Solid State Phys. **5**, 807 (1972).

[281] Y. Y. Atas and E. Bogomolny, *Multifractality of eigenfunctions in spin chains*, Phys. Rev. E **86**, 021104 (2012).

[282] Y. Y. Atas and E. Bogomolny, *Calculation of multi-fractal dimensions in spin chains*, Phil. Trans. R. Soc. A **372**, 20120520 (2014).

[283] T. Gorin, H. J. Korsch, and B. Mirbach, *Phase-space localization and level spacing distributions for a driven rotor with mixed regular/chaotic dynamics*, Chem. Phys. **217**, 145 (1997).

[284] Alfred Wehrl, *General properties of entropy*, Rev. Mod. Phys. **50**, 221 (1978).

[285] Sven Gnutzmann and Karol Życzkowski, *Rényi-Wehrl entropies as measures of localization in phase space*, J. Phys. A: Math. Gen. **34**, 10123 (2001).

[286] Qian Wang and Marko Robnik, *Statistical properties of the localization measure of chaotic eigenstates in the Dicke model*, Phys. Rev. E **102**, 032212 (2020).

[287] P. A. M. Dirac, *The Quantum Theory of the Emission and Absorption of Radiation*, Proc. Roy. Soc. A **114**, 243 (1927).

[288] Qing-Hu Chen, Yu-Yu Zhang, Tao Liu, and Ke-Lin Wang, *Numerically exact solution to the finite-size Dicke model*, Phys. Rev. A **78**, 051801(R) (2008).

[289] Popo Yang, Iván F Valtierra, Andrei B Klimov, Shin-Tza Wu, Ray-Kuang Lee, Luis L Sánchez-Soto, and Gerd Leuchs, *The Wigner flow on the sphere*, Phys. Scr. **94**, 044001 (2019).

[290] J. E. Moyal, *Quantum mechanics as a statistical theory*, Math. Proc. Camb. Phil. Soc. **45**, 99 (1949).

[291] Andrei B Klimov, José Luis Romero, and Hubert de Guise, *Generalized SU(2) covariant Wigner functions and some of their applications*, J. Phys. A: Math. Theor. **50**, 323001 (2017).

[292] Pierre Gaspard, *Chaos, scattering and statistical mechanics*, (Cambridge University Press, Cambridge, 1998).

[293] Alan Weinstein, *Normal Modes for Nonlinear Hamiltonian Systems*, Invent. Math. **20**, 47 (1973).

[294] N. C. Murphy, R. Wortis, and W. A. Atkinson, *Generalized inverse participation ratio as a possible measure of localization for interacting systems*, Phys. Rev. B **83**, 184206 (2011).

[295] M Kuś, J Mostowski, and F Haake, *Universality of eigenvector statistics of kicked tops of different symmetries*, J. Phys. A: Math. Gen. **21**, L1073 (1988).

[296] Kingsley R W Jones, *Entropy of random quantum states*, J. Phys. A: Math. Gen. **23**, L1247 (1990).